Study of B_s^0-meson Production and Measurement of B_s^0 Decays into a $D_s^{(*)-}$ and a Light Meson in e^+e^- Collisions at $\sqrt{s}$=10.87 GeV

THÈSE N^{O} 5213 (2012)

PRÉSENTÉE LE 20 JANVIER 2012

À LA FACULTÉ SCIENCES DE BASE
LABORATOIRE DE PHYSIQUE DES HAUTES ÉNERGIES
PROGRAMME DOCTORAL EN PHYSIQUE

ÉCOLE POLYTECHNIQUE FÉDÉRALE DE LAUSANNE

POUR L'OBTENTION DU GRADE DE DOCTEUR ÈS SCIENCES

PAR

Remi Léandre Albert LOUVOT

acceptée sur proposition du jury:

Prof. V. Savona, président du jury
Prof. O. Schneider, directeur de thèse
Dr G. Lanfranchi, rapporteur
Dr U. Langenegger, rapporteur
Dr K. Trabelsi, rapporteur

ÉCOLE POLYTECHNIQUE
FÉDÉRALE DE LAUSANNE

Suisse
2012

Résumé

Ce mémoire est consacré à l'étude expérimentale de la production des mésons B_s^0 produits par des collisions e^+e^- à la résonance $\Upsilon(5S)$ ($\sqrt{s} = 10.87$ GeV) ainsi qu'à des mesures faites avec des désintégrations complètement reconstruites du méson B_s^0 faisant intervenir un méson $D_s^{(*)-}$. Les données analysées ont été enregistrées au Japon entre juin 2005 et décembre 2009 avec le détecteur Belle situé auprès l'anneau de stockage KEKB. Elles représentent le plus grand échantillon jamais enregistré à la résonance $\Upsilon(5S)$.

Après avoir écrit une procédure moyennant les mesures existantes de la fraction des événements $\Upsilon(5S)$ produisant une paire de mésons $B_s^0\bar{B}_s^0$,

$$f_s = \sigma(e^+e^- \to B_s^{(*)}\bar{B}_s^{(*)})/\sigma(e^+e^- \to b\bar{b}) = (19.9 \pm 3.0)\%\,,$$

nous présentons une nouvelle mesure du rapport entre le nombre d'événements $\Upsilon(5S)$ produisant une paire de mésons $B_s^0\bar{B}_s^0$ et le nombre de ceux faisant intervenir une pairs de mésons $B\bar{B}$ non-étranges. Cette mesure, faite avec $121\ \text{fb}^{-1}$ de données à l'$\Upsilon(5S)$, utilise une nouvelle méthode basée sur les événements contenant deux leptons et sur la corrélation entre leur signe. Le résultat est

$$\sigma(e^+e^- \to B_s^{(*)}\bar{B}_s^{(*)})/\sigma(e^+e^- \to B^{(*)}\bar{B}^{(*)}(X)) = (38.6 \pm 3.8 \pm 4.1)\%\,,$$

où la première erreur contient l'erreur statistique et celle due aux autres paramètres physiques, et la deuxième erreur contient les incertitudes dues à la sélection et à la procédure du fit. L'erreur relative totale est plus petite que celle de la moyenne des autres mesures existantes (obtenue avec le fit mentionné ci-dessus) :

$$\sigma(e^+e^- \to B_s^{(*)}\bar{B}_s^{(*)})/\sigma(e^+e^- \to B^{(*)}\bar{B}^{(*)}(X)) = (26.3^{+5.2}_{-4.4})\%\,.$$

Nous reconstruisons aussi des désintégrations $B_s^0 \to D_s^-\pi^+$ dans un échantillon de $23.4\ \text{fb}^{-1}$. Avec ce signal très pur, nous obtenons la mesure la plus précise d'une désintégration exclusive du méson B_s^0 (l'erreur systématique dominante, celle due à la fraction f_s, est données séparément) :

$$\mathcal{B}(B_s^0 \to D_s^-\pi^+) = (3.60 \pm 0.33(\text{stat}) \pm 0.42(\text{syst}) \pm 0.54(f_s)) \times 10^{-3}\,,$$

avec la mesure la plus précise de la masse du méson B_s^*,

$$m(B_s^*) = 5416.4 \pm 0.4(\text{stat}) \pm 0.7(\text{syst})\ \text{MeV}/c^2\,,$$

et la deuxième mesure la plus précise de la masse du méson B_s^0,

$$m(B_s^0) = 5364.4 \pm 1.3(\text{stat}) \pm 0.7(\text{syst})\ \text{MeV}/c^2\,.$$

Avec le même signal, les fractions de la production des mésons excités B_s^* à l'$\Upsilon(5S)$ sont mesurées :

$$F_{B_s^*\bar{B}_s^*} = \sigma(e^+e^- \to B_s^*\bar{B}_s^*)/\sigma(e^+e^- \to B_s^{(*)}\bar{B}_s^{(*)}) = \left(90.1^{+3.8}_{-4.0}(\mathrm{stat}) \pm 0.2(\mathrm{syst})\right)\%\,,$$
$$F_{B_s^*\bar{B}_s^0} = \sigma(e^+e^- \to B_s^*\bar{B}_s^0)/\sigma(e^+e^- \to B_s^{(*)}\bar{B}_s^{(*)}) = \left(7.3^{+3.3}_{-3.0}(\mathrm{stat}) \pm 0.1(\mathrm{syst})\right)\%\,.$$

Ces analyses prolifiques sont étendues à quatre autres modes du B_s^0 dont les rapports de branchement sont mesurés :

$$\mathcal{B}(B_s^0 \to D_s^{\mp}K^{\pm}) = (2.4 \pm 1.1(\mathrm{stat}) {\pm} 0.3(\mathrm{syst}) \pm 0.4(f_s)) \times 10^{-4}\,,$$
$$\mathcal{B}(B_s^0 \to D_s^{*-}\pi^{+}) = (2.3 \pm 0.4(\mathrm{stat}) \pm 0.3(\mathrm{syst}) \pm 0.3(f_s)) \times 10^{-3}\,,$$
$$\mathcal{B}(B_s^0 \to D_s^{-}\rho^{+}) = (8.2 \pm 1.1(\mathrm{stat}) \pm 1.1(\mathrm{syst}) \pm 1.2(f_s)) \times 10^{-3}\,,$$
$$\mathcal{B}(B_s^0 \to D_s^{*-}\rho^{+}) = (11.5 \pm 2.0(\mathrm{stat}) \pm 1.6(\mathrm{syst}) \pm 1.7(f_s)) \times 10^{-3}\,.$$

Les trois désintégrations, $B_s^0 \to D_s^{*-}\pi^+$, $B_s^0 \to D_s^-\rho^+$ and $B_s^0 \to D_s^{*-}\rho^+$, sont observées pour la première fois, avec des significances excédant 8σ. La désintégration $B_s^0 \to D_s^{*-}\rho^+$ fait intervenir deux polarisations et nous présentons une mesure de sa fraction de polarisation longitudinale,

$$f_L(B_s^0 \to D_s^{*-}\rho^+) = 1.05^{+0.08}_{-0.10}(\mathrm{stat})^{+0.03}_{-0.04}(\mathrm{syst})\,,$$

qui est la première mesure de ce type pour une désintégration du méson B_s^0. Tous ces résultats sont en accord avec les prédictions de la théorie des saveurs lourdes et avec les mesures effectuées avec des désintégrations similaires du méson B^0.

Mots-clés : Physique des hautes énergies, KEK, Belle, modèle standard, méson B_s^0, $\Upsilon(5S)$, HQET, saveur lourde.

Abstract

This work is dedicated to the experimental study of B_s^0 production in e^+e^- collisions at the $\Upsilon(5S)$ resonance ($\sqrt{s} = 10.87$ GeV), as well as measurement with fully reconstructed B_s^0 decays involving one $D_s^{(*)-}$ meson. The analysed data sample was recorded between June 2005 and December 2009 with the Belle detector at the KEKB storage ring in Japan, and represents the largest statistics ever collected at the $\Upsilon(5S)$ resonance.

After having performed a fit of the current existing measurements of the fraction of $\Upsilon(5S)$ events producing a $B_s^0\bar{B}_s^0$ meson pair,

$$f_s = \sigma(e^+e^- \to B_s^{(*)}\bar{B}_s^{(*)})/\sigma(e^+e^- \to b\bar{b}) = (19.9 \pm 3.0)\%\,,$$

we perform a new measurement of the ratio between the $\Upsilon(5S)$ events producing a $B_s^0\bar{B}_s^0$ meson pair and those involving a non-strange $B\bar{B}$ meson pair, by implementing an alternative method based on sign correlations of dilepton events in 121 fb^{-1} of $\Upsilon(5S)$ data. The result is

$$\sigma(e^+e^- \to B_s^{(*)}\bar{B}_s^{(*)})/\sigma(e^+e^- \to B^{(*)}\bar{B}^{(*)}(X)) = (38.6 \pm 3.8 \pm 4.1)\%\,,$$

where the first quoted error includes the statistical uncertainty and the errors due to external physics parameters, and the second quoted error represents uncertainties due to the selection and to the fitting procedure. The total relative error is smaller than that of the average obtained from other existing measurements with the above-mentioned fit,

$$\sigma(e^+e^- \to B_s^{(*)}\bar{B}_s^{(*)})/\sigma(e^+e^- \to B^{(*)}\bar{B}^{(*)}(X)) = (26.3^{+5.2}_{-4.4})\%\,.$$

We also fully reconstruct $B_s^0 \to D_s^-\pi^+$ decays with a sample of 23.4 fb^{-1}. From this high-purity signal, we obtain the most precise measurement of a B_s^0 exclusive decay (the dominant systematic error, due to the f_s fraction, is quoted separately):

$$\mathcal{B}(B_s^0 \to D_s^-\pi^+) = (3.60 \pm 0.33(\mathrm{stat}) \pm 0.42(\mathrm{syst}) \pm 0.54(f_s)) \times 10^{-3}\,,$$

together with the world most precise measurement of the B_s^* mass,

$$m(B_s^*) = 5416.4 \pm 0.4(\mathrm{stat}) \pm 0.7(\mathrm{syst})\ \mathrm{MeV}/c^2\,,$$

and the second most precise measurement of the B_s^0 mass,

$$m(B_s^0) = 5364.4 \pm 1.3(\mathrm{stat}) \pm 0.7(\mathrm{syst})\ \mathrm{MeV}/c^2\,.$$

With the same signal, the production fractions of excited B_s^* mesons at the $\Upsilon(5S)$ are obtained:

$$F_{B_s^*\bar{B}_s^*} = \sigma(e^+e^- \to B_s^*\bar{B}_s^*)/\sigma(e^+e^- \to B_s^{(*)}\bar{B}_s^{(*)}) = \left(90.1^{+3.8}_{-4.0}(\text{stat}) \pm 0.2(\text{syst})\right)\%\,,$$
$$F_{B_s^*\bar{B}_s^0} = \sigma(e^+e^- \to B_s^*\bar{B}_s^0)/\sigma(e^+e^- \to B_s^{(*)}\bar{B}_s^{(*)}) = \left(7.3^{+3.3}_{-3.0}(\text{stat}) \pm 0.1(\text{syst})\right)\%\,.$$

These fruitful analyses are extended to four other B_s^0 modes which branching fractions are measured:

$$\mathcal{B}(B_s^0 \to D_s^{\mp}K^{\pm}) = (2.4 \pm 1.1(\text{stat}) \pm 0.3(\text{syst}) \pm 0.4(f_s)) \times 10^{-4}\,,$$
$$\mathcal{B}(B_s^0 \to D_s^{*-}\pi^+) = (2.3 \pm 0.4(\text{stat}) \pm 0.3(\text{syst}) \pm 0.3(f_s)) \times 10^{-3}\,,$$
$$\mathcal{B}(B_s^0 \to D_s^-\rho^+) = (8.2 \pm 1.1(\text{stat}) \pm 1.1(\text{syst}) \pm 1.2(f_s)) \times 10^{-3}\,,$$
$$\mathcal{B}(B_s^0 \to D_s^{*-}\rho^+) = (11.5 \pm 2.0(\text{stat}) \pm 1.6(\text{syst}) \pm 1.7(f_s)) \times 10^{-3}\,.$$

The three decays, $B_s^0 \to D_s^{*-}\pi^+$, $B_s^0 \to D_s^-\rho^+$ and $B_s^0 \to D_s^{*-}\rho^+$ decays are observed for the first time with significances in excess of 8σ. The $B_s^0 \to D_s^{*-}\rho^+$ decay involves two polarisations and we report a measurement of its longitudinal polarisation fraction,

$$f_L(B_s^0 \to D_s^{*-}\rho^+) = 1.05^{+0.08}_{-0.10}(\text{stat})^{+0.03}_{-0.04}(\text{syst})\,,$$

which is the first polarisation measurement of a B_s^0 decay. All these results are in agreement with expectations from heavy-flavour theory and B^0 counterparts.

Keywords: high-energy physics, KEK, Belle, Standard Model, B_s^0 meson, $\Upsilon(5S)$, HQET, heavy flavor.

à Émile Mezzadonna
(1920-2007)

Contents

Introduction

The Belle experiment [1], located at the interaction point of the KEKB asymmetric-energy e^+e^- collider [2], was designed for the study of B^+ and B^0 mesons produced in e^+e^- annihilation at a centre-of-mass (CM) energy corresponding to the mass of the $\Upsilon(4S)$ resonance ($\sqrt{s} \approx 10.58$ GeV). In addition to an unprecedented sample of ~ 800 millions of $B^0\bar{B}^0$ and B^+B^- pairs, the Belle collaboration has also recorded collisions at higher energies, opening the possibility to study the B_s^0 meson. The $\Upsilon(5S)$ resonance ($\sqrt{s} \approx 10.87$ GeV) is above the $B_s^0\bar{B}_s^0$ threshold and it was naturally expected that the B_s^0 meson could be studied with $\Upsilon(5S)$ data as well as the B mesons can with $\Upsilon(4S)$ data. The large potential of such $\Upsilon(5S)$ data, mainly due to the low multiplicities of charged and neutral particles and high reconstruction efficiencies, was quickly confirmed [3, 4] with the 2005 engineering run representing 1.86 fb^{-1} of integrated luminosity.

After a data sample of $23.4\,\mathrm{fb}^{-1}$ was collected at the $\Upsilon(5S)$ resonance, the Belle experiment became, and remained, the only experiment with a significant dataset at this energy. It was natural to start analysing B_s^0 mesons with these data by reconstructing decays that were expected to have large efficiencies and branching fractions. The first choice is naturally $B_s^0 \to D_s^-\pi^+$ which involves a Cabibbo-allowed $b \to c\bar{u}d$ transition, and which has only four charged particles in its three dominant final states. This analysis was extended to the flavor-independent $B_s^0 \to D_s^\mp K^\pm$ decay which is Cabibbo-suppressed but very similar to reconstruct. More challenging Cabibbo-allowed decays involving photons and neutral pions in their final states, such as $B_s^0 \to D_s^{*-}\pi^+$ and $B_s^0 \to D_s^{(*)-}\rho^+$, were also studied afterwards. The $B_s^0 \to D_s^-\pi^+$ decay is a primary normalisation mode at hadron colliders, where the absolute production rate of B_s^0 mesons is difficult to measure directly. Normalisation is especially crucial for the search of very rare B_s^0 decays, such as $B_s^0 \to \mu^+\mu^-$ [5, 6]. The Cabibbo-suppressed mode $B_s^0 \to D_s^\mp K^\pm$ produces very few events, but this flavour-independent mode is of high importance for measuring time-dependent CP-violating effects with B_s^0 mesons [7]. All these analyses, from which many interesting physical quantities have been measured, are described in Chapter 4 and in two Belle notes [8, 9]. They are published in two Letters [10, 11].

As the number of fully-reconstructed exclusive B_s^0 decay were increasing, it quickly became crucial to know more precisely the B_s^0 production fraction at the $\Upsilon(5S)$ energy in order to extract branching fractions with smaller systematic uncertainties. The CLEO and Belle collaborations published several measurements of the B_s^0 production made with very small data samples. These measurements are largely limited by systematic uncertainties, and repeating them on the large Belle sample wouldn't improve the precision. In order to extract the maximum from existing publications, we implemented a fit with all the known correlations between these measurements. It is described at the beginning of Chapter 3, and an earlier version of its result appeared in the Heavy-Flavour Averaging Group (HFAG) review [12]. The 15% uncertainty on this averaged fraction of B_s^0 events was still limiting severely our branching fractions, and we decided to make a new measurement of the B_s^0 production with a novel approach, proposed in Ref. [13] and based on dilepton events. This analysis, for which we had to implement new functions in the simulation software of the Belle experiment, is detailed in the second half of Chapter 3 and in two Belle notes [14, 15].

Before the description of these original analyses, a first chapter is dedicated to a summary of the standard model and to a theoretical review of the physics with $B_{(s)}$ mesons. The second chapter details the experimental setup which is composed of the KEKB accelerator and the Belle detector.

Chapter 1

The standard model of particle physics

The standard model is the current theoretical paradigm in particle physics. It originates from the works of Weinberg, Glashow and Salam [16–18] on electroweak interactions. Quantum chromodynamics and quarks have been first independently proposed by Gell-Mann [19] and Zweig [20] later on. This chapter is only a brief introduction to the standard model parts that are relevant to experimental particle physics. It is based on the textbook of Langacker [21] and several others [22, 23]. The CP violation is described following the extensive monographs by Bigi and Sanda [24] and Branco *et al.* [25].

1.1 Symmetries and conservation laws in physics

Symmetries have always played a very important role in physics theories. The conserved quantities in a mechanical problem have driven the development of mechanics, from Newton's first law to the analytical mechanics of Lagrange and Hamilton and, later, quantum mechanics. From Noether's theorem [26], these two concepts are linked. A constant quantity of motion is associated with any continuous symmetry of the problem. For instance, the conservation of energy and momentum is related to the invariance under space-time translations, the conservation of angular momentum is related to the invariance under rotations, the conservation of electric charge is related to the invariance of the quantum wave function under a complex phase shift, etc. While the symmetries involved in Noether's theorem are continuous (i.e. can be parametrised by a real number), three discrete symmetries play an important role in quantum field theory.

- Charge-conjugation

  The charge-conjugation operator C changes a particle into its anti-particle.

$$(\pi^+ \to \mu_R^+ \nu_L) \xrightarrow{C} (\pi^- \to \mu_R^- \bar{\nu}_L) \tag{1.1}$$

  Some neutral particles can be eigenstate of C, such as π^0, η, ρ^0, but not K^0 or B_s^0.

- Parity

The parity operator P reverses the space coordinates of a particle, and thus its helicity (defined as the projection of the spin direction on the momentum). It is not reducible to a rotation ($\det P = -1$).

$$(\pi^+ \to \mu_R^+ \nu_L) \xrightarrow{P} (\pi^+ \to \mu_L^+ \nu_R) \tag{1.2}$$

- Time-reversal

  The time-reversal operator T reverses the time coordinate of a particle.

It was thought that these three C, P and T symmetries were respected at the microscopic level. This is true for the strong and electromagnetic interactions. However it was discovered that the weak interaction violates maximally the parity [27, 28], and thus the charge-conjugation [29–31]. It is an experimental fact that there is only left-handed neutrinos and right-handed anti-neutrinos in Nature. The decay $\pi^+ \to \mu_L^+ \nu_R$ is forbidden. The CP symmetry is slightly violated by the weak interaction [32]. The combination of these three symmetries, CPT, is conserved by any Lorentz-invariant quantum field theory [33]. All experimental searches for CPT violation have given negative results. If CP is violated and CPT holds, the time-reversal symmetry T should also be violated in weak interactions. This has been confirmed by the CPLEAR collaboration [34]. As shown by Sakharov [35], CP violation is one of the three ingredients required to explain the baryogenesis, i.e. the excess of matter over anti-matter in the universe. For tests of discrete symmetries, see Ref. [36] or the most recent review in the latest Review of Particle Physics [37].

1.2 Fundamental forces

The standard model is a theory based on the local gauge group associated with three "charges", namely colour, chirality and hypercharge:

$$G_{\mathrm{SM}} = SU(3)_C \times SU(2)_L \times U(1)_Y \,. \tag{1.3}$$

The three components correspond to the three fundamental interactions which are mediated by force bosons.

1.2.1 Strong force

The strong force was first invoked to explain the cohesion of the nucleons (neutrons and protons) in the atomic nuclei. Its range is of the order of a nucleus size (~ 1 fm). The particles that decay strongly are called resonances and are characterised by a very short lifetime, of the order of 10^{-24} s. It is now known that the strong force is only a residual force from the colour interaction between the components (quarks and gluons) of the nucleon.

The colour interaction, sometimes called colour force, is described by Quantum ChromoDynamics (QCD), a quantum field theory based on the local colour gauge group $SU(3)_C$. Each quark carries one of the three colour "charges", conventionally named red (r), green (g) and blue (b). The force is mediated by eight massless gauge fields (gluons), G_μ^A ($A = 1, \ldots, 8$). A gluon carries a colour and an anti-colour, with strong isospin $\vec{I}_g = \vec{1} + \vec{1}$.

There are nine states $(1+3+5)$, but the colourless singlet $(I_g = 0)$ is excluded. This is motivated by the non observation of free gluons [23].

This interaction conserves P, C and the isotopic spin (strong isospin). It is hard to study at its fundamental level (quarks and gluons) because of the colour confinement [38], and only colourless composite particles can be experimentally studied. In addition, the coupling constant is close to unity, precluding precise calculations using perturbation methods.

1.2.2 Weak force and electromagnetic force

The weak interaction was first suggested by Fermi to explain the nuclear β decays [39]. In the late 1940's, Quantum ElectroDynamics (QED) was the first theory of electromagnetic interactions based on an Abelian local gauge invariance.

A non-Abelian local gauge group $SU(2)_L \times U(1)_Y$ is at the origin of the unification of the electromagnetic and weak interactions. This electroweak theory is the cornerstone of the standard model formulation. The electroweak force is mediated with three W^a_μ $(a = 1, 2, 3)$ and one B_μ gauge bosons. The weak force violates maximally the C and P symmetries, while CP violation is tiny.

The "charge" of a field under the $SU(2)_L$ group is the chirality. There are two chiralities, right (singlet) and left (doublet). Only the left-handed fermions interact with the weak gauge bosons, which is the base of the original $V-A$ theory [40, 41]. The transformation under the Poincarré group determines the chirality. For a massless particle, the chirality coincides with the helicity, which is defined as the projection of the spin on the momentum direction:

$$h = \frac{\vec{S} \times \vec{p}}{|\vec{p}|} \,. \tag{1.4}$$

By convention, a field with $h > 0$ $(h < 0)$ is right(left)-handed (Fig. 1.1).

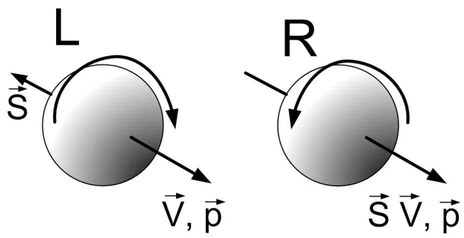

Figure 1.1: Left and right-handed particles.

The electromagnetic charge q is conserved. It is related to the $U(1)_Y$ hypercharge, Y, and the weak $SU(2)_L$ isospin, I_3, with the Gell-Mann–Nishijima formula [42, 43]:

$$q = I_3 + \frac{1}{2} Y \,. \tag{1.5}$$

1.2.3 Gravitation

There is no quantum theory of gravitation, and gravitation is therefore not included in the standard model Lagrangian density. For a review, see Refs. [44, 45]. This is undoubtedly a weak point of the model however the strength of this force is so small (Table 1.1) that, in practise, no gravitational effects have been observed so far in particle physics experiments.

Table 1.1: Gauge bosons and relative strengths of the three fundamental forces of the standard model and gravitation. The electromagnetic force relative strength is given by fine-structure constant at low energy, $\alpha = e^2/(4\pi\varepsilon_0\hbar c) \approx 1/137$. The weak force relative strength is evaluated from the ratio of the Δ and Σ baryon lifetimes, $\alpha_W/\alpha_s \approx \sqrt{\tau_\Lambda/\tau_\Sigma} \approx 4 \times 10^{-6}$. The gravitational force is evaluated from the ratio of the electromagnetic and the gravitational forces between two protons, $\alpha_G/\alpha \approx 4\pi\varepsilon_0 G_N(m_p/e)^2 = 8.1 \times 10^{-37}$.

Force	Carrier	Mass (GeV/c^2) [37]	Range	Relative strength [46]
Strong	8 gluons	0	10^{-15} m	1
Electromagnetic	γ	0	∞	10^{-2}
Weak (Charged)	$W^\pm$	80.399 ± 0.023	10^{-18} m	10^{-6}
Weak (Neutral)	Z^0	91.1876 ± 0.0021		
Gravitational	—	—	∞	10^{-38}

1.3 Fermions

Apart from the Higgs and the gauge bosons, the standard model contains fermions (spin-1/2 particles), divided in two categories[1], the colour triplets, called "quarks",

- left-handed quark $Q_L(3,2)_{+1/3}$, which is a $SU(2)_L$ doublet $(U_L\ D_L)^T$,
- right-handed up quark $U_R(3,1)_{+2/3}$, and
- right-handed down quark $D_R(3,1)_{-1/3}$;

and the colour singlets, called "leptons",

- left-handed $SU(2)_L$-doublet $L_L(1,2)_{-1/2}$; this is composed of left-handed charge lepton and its neutrino $(\nu\ l_L)^T$, and
- right-handed charged lepton $l_R(1,1)_{-1}$.

In the minimal standard model, no right-handed neutrinos are included. Right-handed neutrinos are not sensitive to any of the three forces of the standard model: they would be colour singlets and $SU(2)_L$ singlets without hypercharge.

The Dirac equation, $\left(i\hbar\partial\!\!\!/ - mc\right)\Psi = 0$ [47], which describes the motion of fermions in quantum mechanics, predicts that each fermion has an associated antiparticle with the same spin and mass but opposite electric charge.

The fermion pattern described above can be duplicated in several *families*. The number of families is denoted as N_F.

[1] We write the fields with their charged number for each of the three groups. For instance, the left-handed quark field, $Q_L(3,2)_{+1/3}$, is a triplet for $SU(3)_C$, a doublet for $SU(2)_L$ and has an hypercharge $Y = +1/3$.

1.4 Spontaneous symmetry breaking mechanism

In a Lagrangian density that respects the local gauge symmetry of Eq. (1.3), any fermionic field must be massless because a non-zero mass term would break the local symmetry because it connects the right-handed with the left-handed part of the field. Phenomenologically this is certainly incorrect because fermions obviously have a finite mass. This puzzle is solved by adding a left-handed complex scalar field to the theory $\phi(1,2)_{+1/2}$ with a quadratic potential ($\lambda > 0$)

$$V(\phi) = \mu^2 \phi^\dagger \phi + \lambda \left(\phi^\dagger \phi\right)^2 . \tag{1.6}$$

In the case $\mu^2 < 0$, the vacuum expectation value $\langle\phi\rangle_0$ is different from zero, but has a finite value

$$\langle\phi\rangle_0 = \sqrt{-\frac{\mu^2}{2\lambda}} \equiv \frac{\nu}{\sqrt{2}} . \tag{1.7}$$

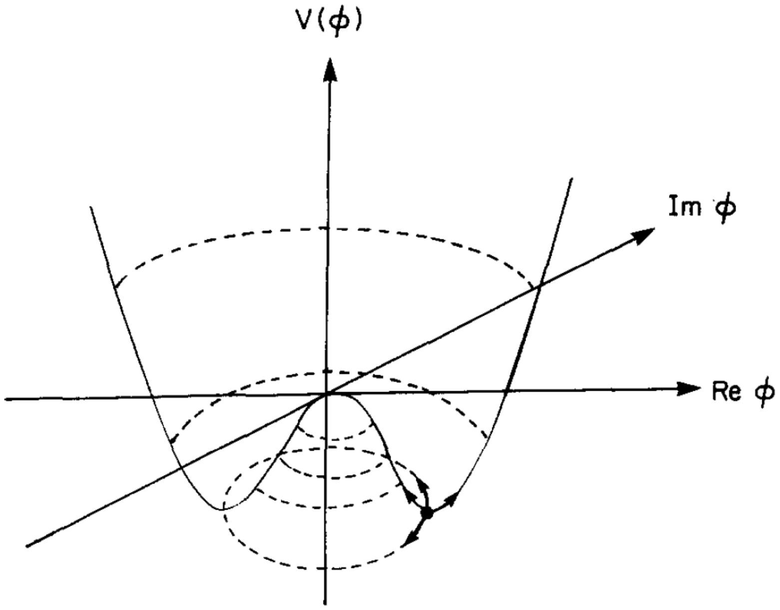

Figure 1.2: (Reproduced from Ref. [48]) The potential $V(\phi)$ as a function of the complex field ϕ. The minima of the potential are degenerated. The vacuum state is chosen to lie along the real direction. The two oscillation modes around this vacuum state are shown; the radial mode is the massive Higgs boson while the azimuthal mode is the massless Goldstone boson.

This non-zero vacuum expectation value spontaneously breaks the symmetry of the potential. When the complex field is quantised from its ground state $\langle\phi\rangle_0$, it has still four degrees of freedom, but one appears as a massive boson, the infamous Higgs boson, and the three others are massless. One can illustrate this mass effect from the shape of the potential (Fig. 1.2). A radial motion changes the potential (i.e. "the particle feels massive"), while an azimuthal motion does not change the level at all, and the movement is free (i.e. "the particle feels massless"). The mass less Goldstone bosons [49] do not appear when the unitary gauge is used to write the Lagrangian density. In this gauge the field ϕ and its conjugate $\tilde{\phi}$ are written as function of one real value defined by Eq. (1.7), ν, and one real scalar field, H:

$$\phi = \frac{1}{\sqrt{2}} \begin{pmatrix} 0 \\ \nu + H \end{pmatrix} , \ \tilde{\phi} = \frac{1}{\sqrt{2}} \begin{pmatrix} \nu + H \\ 0 \end{pmatrix} . \tag{1.8}$$

This mechanism leads to three massive bosons for the weak interactions which are combinations of the gauge bosons W_μ and B_μ. The weak charged currents are mediated by massive bosons $W_\mu^\pm$:

$$W_\mu^\pm = \frac{1}{\sqrt{2}} \left(W_\mu^1 \mp i W_\mu^2 \right) . \tag{1.9}$$

The massive neutral weak current boson Z_μ and the electromagnetic gauge field A_μ are a rotation of W_μ^3 and B_μ,

$$\begin{pmatrix} Z_\mu \\ A_\mu \end{pmatrix} = \begin{pmatrix} \cos\theta_W & -\sin\theta_W \\ \sin\theta_W & \cos\theta_W \end{pmatrix} \begin{pmatrix} W_\mu^3 \\ B_\mu \end{pmatrix} , \tag{1.10}$$

where θ_W is called the Weinberg angle [16]. It is related to the $SU(2)_L$ and $U(1)_Y$ coupling constants, g and g' respectively though

$$\cos\theta_W = \frac{g}{\sqrt{g^2 + g'^2}} , \tag{1.11}$$

$$\sin\theta_W = \frac{g'}{\sqrt{g^2 + g'^2}} . \tag{1.12}$$

A $U(1)_{EM}$ symmetry is preserved, corresponding to the well-known electromagnetic force carried by the photon, A_μ. This residual symmetry is crucial to preserve the electric charged conservation. The $U(1)_{EM}$ coupling constant correspond the electric charge unit,

$$e = \frac{g g'}{\sqrt{g^2 + g'^2}} . \tag{1.13}$$

The charges (in unit of e) of the fermions is given by Eq. (1.5).

With the field ϕ and $\tilde{\phi}$, it is possible to add new gauge invariant terms to the Lagrangian density, the so-called Yukawa couplings[2]

$$\bar{L}_l l_R \phi \, , \ \bar{Q}_L D_R \phi \, , \ \bar{Q}_L U_R \tilde{\phi} \, , \ \text{etc.} \tag{1.14}$$

Because of the spontaneous symmetry breaking in the electroweak part, the physical symmetry group of the standard model becomes

$$SU(3)_C \times U(1)_{\text{EM}} . \tag{1.15}$$

This mechanism has two important experimental consequences:

[2]Named after Hideki Yukawa, who proposed that the interaction between two nucleons (fermions) is mediated by a boson [50].

- As will be shown below, the fermion masses and CP violation naturally appear in the quark-related Yukawa terms of Eq. (1.14).
- A new massive boson appears in the theory. Intensive experimental efforts have been deployed for measuring this "Higgs" boson, which mass is expected in the $100 - 200\,\mathrm{GeV}/c^2$ range [51], but there is still no experimental evidence for its existence.

1.5 Physical Lagrangian density

The underlying fundamental principle in quantum field theory is that of minimal action, developed more than 200 years ago by Lagrange [52]. The action is the time-integrated Lagrangian where the Lagrangian is the difference between the kinematic and potential energies. In the framework of special relativity, it is convenient to use the Lagrangian density $\mathcal{L}$, instead of the Lagrangian, L, itself:

$$L = \int \mathcal{L}\,\mathrm{d}^3\vec{x}\,. \tag{1.16}$$

In this way, the action is the four-dimensional space-time integral of $\mathcal{L}$,

$$\mathcal{S} = \int L\,\mathrm{d}t = \int \mathcal{L}\,\mathrm{d}^4x\,. \tag{1.17}$$

A space-time invariant theory *simply* requires a Lorentz-invariant Lagrangian density. The Lagrangian density of the standard model is constructed from Lorentz- and gauge-invariant terms. For this purpose, it is useful to introduce the covariant derivative which is invariant under the local gauge group,

$$D_\mu = \partial_\mu - \overbrace{ig_S G^A_\mu \frac{\lambda^A}{2}}^{SU(3)_C} - \overbrace{igW^a_\mu \frac{\tau^a}{2}}^{SU(2)_L} - \overbrace{ig' B_\mu \frac{Y}{2}}^{U(1)_Y}\,, \tag{1.18}$$

where g_S, g and g' are the coupling constants of the $SU(3)_C$, $SU(2)_L$ and $U(1)_Y$ gauge groups, respectively. The product[3] between the Dirac matrices γ^μ and D_μ is usually written with the Feynman slash notation, $\not{D} = \gamma^\mu D_\mu$.

The total Lagrangian density, $\mathcal{L}_{\mathrm{SM}}$, contains the Lagrangian densities of the complex scalar field, the gauge fields (Yang-Mills), the fermion kinematics and the Yukawa couplings,

$$\mathcal{L}_{\mathrm{SM}} = \mathcal{L}_{\mathrm{Higgs}} + \mathcal{L}_{\mathrm{YM}} + \mathcal{L}_{\mathrm{kin}} + \mathcal{L}_{\mathrm{Y}}\,. \tag{1.19}$$

1.5.1 Complex scalar field

The Lagrangian density of a scalar field is

$$\mathcal{L}_{\mathrm{Higgs}} = (D_\mu\phi)^\dagger\,(D^\mu\phi) - V(\phi)\,. \tag{1.20}$$

After the spontaneous symmetry-breaking mechanism, ϕ is separated into a vacuum expectation value and a real scalar field H (Eq. (1.8)). The physical Lagrangian density is

[3] Einstein's convention [53] on implicit summation is used throughout this thesis.

therefore, after expanding the covariant derivative with only its $SU(2)_L$ component and introducing the Higgs mass, $m_H = \sqrt{-2\mu^2}$,

$$\begin{aligned}\mathcal{L}_{\text{Higgs}} = & \frac{g^2\nu^2}{4}W^{+,\mu}W^-_\mu\left(1+\frac{H}{\nu}\right)^2 + \frac{1}{2}\left(g^2+g'^2\right)\frac{\nu^2}{4}Z^\mu Z_\mu\left(1+\frac{H}{\nu}\right)^2 \\ & + \frac{1}{2}\left(\partial_\mu H\right)^2 - \frac{1}{2}m_H^2H^2 + \frac{m_H^2\nu^2}{8} - \frac{m_H^2}{2\nu}H^3 - \frac{m_H^2}{8\nu^2}H^4\,. \end{aligned} \tag{1.21}$$

It contains the $W^\pm$ and Z^0 mass terms, the interaction of the Z^0 and $W^\pm$ with the Higgs field (Z^0Z^0H, Z^0Z^0HH, W^+W^-H, W^+W^-HH vertices), and the self-interaction of the Higgs (HHH and $HHHH$ vertices). The masses of the $W^\pm$ and Z^0 are related to the vacuum expectation value of the complex field,

$$m_W = \frac{g\nu}{2}\,, \tag{1.22}$$

$$m_Z = \frac{\nu\sqrt{g^2+g'^2}}{2} = \frac{m_W}{\cos\theta_W}\,. \tag{1.23}$$

1.5.2 Yang-Mills Lagrangian term

The Yang-Mills [54] part contains the kinematic terms of the gauge fields themselves which involve the gauge curvatures[4]:

$$\mathcal{L}_{\text{YM}} = -\frac{1}{4}G^A_{\mu\nu}G^{\mu\nu A} - \frac{1}{4}W^a_{\mu\nu}W^{\mu\nu a} - \frac{1}{4}B_{\mu\nu}B^{\mu\nu}\,. \tag{1.24}$$

The $SU(3)_C$ part contains three- and four-gluon vertices, as for any non-Abelian local Gauge group. Similarly, when the $SU(2)_L \times U(1)$ part is expressed as function of the physical fields $W^\pm_\mu$, Z^0_μ and A_μ, it leads to additional terms representing 3- and 4-point gauge self-interactions ($W^+W^-Z^0$, $W^+W^-\gamma$, $W^+W^-W^+W^-$, $W^+W^-Z^0\gamma$, $W^+W^-Z^0Z^0$ and $W^+W^-\gamma\gamma$),

$$\begin{aligned}\mathcal{L}_{W3} = & -ig\cos\theta_W(\partial_\rho Z_\nu)W^+_\mu W^-_\sigma\,\mathcal{O}^{\rho\mu\nu\sigma} \\ & -ig\cos\theta_W(\partial_\rho W^+_\mu)Z_\nu W^-_\sigma\,\mathcal{O}^{\rho\sigma\mu\nu} \\ & -ig\cos\theta_W(\partial_\rho W^-_\sigma)Z_\nu W^+_\mu\,\mathcal{P}^{\rho\nu\mu\sigma} \\ & -ie(\partial_\rho A_\nu)W^+_\mu W^-_\sigma\,\mathcal{O}^{\rho\mu\nu\sigma} \\ & -ie(\partial_\rho W^+_\mu)A_\nu W^-_\sigma\,\mathcal{O}^{\rho\sigma\mu\nu} \\ & -ie(\partial_\rho W^-_\sigma)A_\nu W^+_\mu\,\mathcal{P}^{\rho\nu\mu\sigma}\,, \end{aligned} \tag{1.25}$$

$$\begin{aligned}\mathcal{L}_{W4} = & \frac{g^2}{4}W^+_\mu W^+_\nu W^-_\sigma W^-_\rho\,\mathcal{Q}^{\mu\nu\rho\sigma} \\ & -eg\cos\theta_W W^+_\mu Z_\nu A_\sigma W^-_\rho\,\mathcal{Q}^{\mu\rho\nu\sigma} \\ & -\frac{g^2\cos^2\theta_W}{2}W^+_\mu Z_\nu Z_\sigma W^-_\rho\,\mathcal{Q}^{\mu\rho\nu\sigma} \\ & -\frac{e^2}{2}W^+_\mu A_\nu A_\sigma W^-_\rho\,\mathcal{Q}^{\mu\rho\nu\sigma}\,, \end{aligned} \tag{1.26}$$

[4]The gauge curvature is defined as $F^i_{\mu\nu} = \partial_\mu F^i_\nu - \partial_\nu F^i_\mu - gc_{ijk}F^j_\mu F^k_\nu$, where g is the coupling constant and c_{ijk} are the structure constants of the Lie group (null for an Abelian group).

with the combinatorial factors depending only on the space-time metric $g^{\mu\nu}$:

$$\mathcal{O}^{\mu\nu\rho\sigma} = g^{\mu\nu}g^{\rho\sigma} - g^{\mu\sigma}g^{\rho\nu} , \tag{1.27}$$

$$\mathcal{P}^{\mu\nu\rho\sigma} = g^{\mu\nu}g^{\rho\sigma} - g^{\mu\rho}g^{\nu\sigma} , \tag{1.28}$$

$$\mathcal{Q}_{\mu\nu\rho\sigma} = 2g_{\mu\nu}g_{\rho\sigma} - g_{\mu\rho}g_{\nu\sigma} - g_{\mu\sigma}g_{\nu\rho} . \tag{1.29}$$

1.5.3 Fermion kinematic term

The kinematic term of the fermions is written as

$$\mathcal{L}_{\text{kin}} = i\sum_{j=1}^{N_F} \left(\bar{Q}_{Lj}\not{D}Q_{Lj} + \bar{U}_{Rj}\not{D}U_{Rj} + \bar{D}_{Rj}\not{D}D_{Rj} + \bar{L}_{Lj}\not{D}L_{Lj} + \bar{l}_{Rj}\not{D}l_{Rj}\right) . \tag{1.30}$$

When expressed in terms of physical fields, only the colour force remains in the covariant derivative

$$D_{QCD,\mu} = \partial_\mu - ig_S G^A_\mu \frac{\lambda^A}{2} , \tag{1.31}$$

and the Lagrangian density gets additional terms representing charged currents (CC), involving $W^\pm$ couplings, and neutral currents (NC), involving Z^0 and photon couplings:

$$\begin{aligned}\mathcal{L}_{\text{kin}} = i\sum_{j=1}^{N_F} & \bar{Q}_{Lj}\not{D}_{QCD}Q_{Lj} + \bar{U}_{Rj}\not{D}_{QCD}U_{Rj} + \bar{D}_{Rj}\not{D}_{QCD}D_{Rj} + \bar{L}_j\not{\partial}L_j + \bar{E}_j\not{\partial}E_j \\ & +\mathcal{L}_{CC,j} + \mathcal{L}_{NC,j} .\end{aligned} \tag{1.32}$$

The Lagrangian densities for the weak and electromagnetic currents are

$$\mathcal{L}_{CC,j} = \frac{g}{\sqrt{2}}\left(J^\mu_{+,j}W^-_\mu + J^\mu_{-,j}W^+_\mu\right) , \tag{1.33}$$

$$\mathcal{L}_{NC,j} = eJ^\mu_{q,j}A_\mu + \frac{g}{\cos\theta_W}\left(J^\mu_{3,j} - \sin^2\theta_W J^\mu_{q,j}\right)Z_\mu . \tag{1.34}$$

The charged currents connect only the left-handed fields:

$$J^\mu_{+,j} = \bar{U}_{Lj}\gamma^\mu D_{Lj} + \bar{l}_{Lj}\gamma^\mu\nu_j , \tag{1.35}$$

$$J^\mu_{-,j} = \bar{D}_{Lj}\gamma^\mu U_{Lj} + \bar{\nu}_j\gamma^\mu l_{Lj} , \tag{1.36}$$

$$J^\mu_{3,j} = \frac{1}{2}\left(\bar{U}_{Lj}\gamma^\mu U_{Lj} - \bar{D}_{Lj}\gamma^\mu D_{Lj} + \bar{\nu}_j\gamma^\mu\nu_j - \bar{l}_{Lj}\gamma^\mu l_{Lj}\right) . \tag{1.37}$$

The standard electromagnetic current, which does not depend on the chirality ($D_j = D_{Lj} + D_{Rj}$, etc.), reads

$$J^\mu_{q,j} = \frac{2}{3}\bar{U}_j\gamma^\mu U_j - \frac{1}{3}\bar{D}_j\gamma^\mu D_j - \bar{l}_j\gamma^\mu l_j . \tag{1.38}$$

This term contains all the interactions between fermions and the three forces: strong force (gluons), charged weak current ($W^\pm$), neutral weak current (Z^0) and electromagnetic interaction (γ).

1.5.4 Yukawa couplings

The Yukawa couplings between fermions and the Higgs field are the only terms that can connect fermions of different families:

$$\begin{aligned}\mathcal{L}_{\mathrm{Y}} &= -\frac{\sqrt{2}}{\nu}\left(\bar{\boldsymbol{L}}_{\boldsymbol{L}} M_l \boldsymbol{l}_{\boldsymbol{R}}\phi + \bar{\boldsymbol{Q}}_{\boldsymbol{L}} M_D \boldsymbol{D}_{\boldsymbol{R}}\phi + \bar{\boldsymbol{Q}}_{\boldsymbol{L}} M_U \boldsymbol{U}_{\boldsymbol{R}}\tilde{\phi} + \text{h.c.}\right) \qquad (1.39)\\ &= -\left(\bar{\boldsymbol{l}}_{\boldsymbol{L}} M_l \boldsymbol{l}_{\boldsymbol{R}}\left(1+\frac{H}{\nu}\right) + \bar{\boldsymbol{D}}_{\boldsymbol{L}} M_D \boldsymbol{D}_{\boldsymbol{R}}\left(1+\frac{H}{\nu}\right) + \bar{\boldsymbol{U}}_{\boldsymbol{L}} M_U \boldsymbol{U}_{\boldsymbol{R}}\left(1+\frac{H}{\nu}\right) + \text{h.c.}\right),\end{aligned}$$

where the fermionic fields (typeset in bold) are now vectors of dimension N_F containing the corresponding fermions from the N_F flavours. M_l, M_D and M_U are $N_F \times N_F$ matrices. In Eq. (1.39), mass terms arise from the spontaneous symmetry-breaking mechanism, as well as fermion couplings to the Higgs boson.

A priori, the complex $N_F \times N_F$ matrices are not diagonal. The singular value decomposition theorem proves the existence of two unitary matrices $T_{U,L}$ and $T_{U,R}$ such that $T_{U,L} M_U T^{\dagger}_{U,R} = M_U^{\mathrm{diag}}$ is real, positive and diagonal. Similarly, $T_{D,L}$ and $T_{D,R}$ are defined such like $T_{D,L} M_D T^{\dagger}_{D,R} = M_D^{\mathrm{diag}}$ is also real, positive and diagonal. Then, the fermionic mass eigenstates can be defined as $\boldsymbol{U}^{\boldsymbol{m}}_{\boldsymbol{L}} = T_{U,L}\boldsymbol{U}_{\boldsymbol{L}}$, $\boldsymbol{U}^{\boldsymbol{m}}_{\boldsymbol{R}} = T_{U,R}\boldsymbol{U}_{\boldsymbol{R}}$, $\boldsymbol{D}^{\boldsymbol{m}}_{\boldsymbol{L}} = T_{D,L}\boldsymbol{D}_{\boldsymbol{L}}$ and $\boldsymbol{D}^{\boldsymbol{m}}_{\boldsymbol{R}} = T_{D,R}\boldsymbol{D}_{\boldsymbol{R}}$. With this new basis, the neutral currents remain unchanged, the mass eigenstates are also eigenstates of the neutral electroweak interactions, therefore we do not expect flavour-changing neutral currents at tree level in the standard model. However, the charged weak currents $J_{\pm}$ are modified because

$$\bar{\boldsymbol{U}}_{\boldsymbol{L}}\gamma^{\mu}\boldsymbol{D}_{\boldsymbol{L}} = \bar{\boldsymbol{U}}^{\boldsymbol{m}}_{\boldsymbol{L}} T_{U,L} T^{\dagger}_{D,L}\gamma^{\mu}\boldsymbol{D}^{\boldsymbol{m}}_{\boldsymbol{L}} \neq \bar{\boldsymbol{U}}^{\boldsymbol{m}}_{\boldsymbol{L}}\gamma^{\mu}\boldsymbol{D}^{\boldsymbol{m}}_{\boldsymbol{L}}\,. \qquad (1.40)$$

expliciting the fact that mass and interaction eigenstates are not aligned.

It is not possible to diagonalise simultaneously M_D and M_U, unless a new unitary $N_F \times N_F$ matrix $V = T_{U,L} T^{\dagger}_{D,L}$ is inserted. This is the so-called Cabibbo-Kobayashi-Maskawa matrix [55]. It tells us that the gauge eigenstates and the mass eigenstates of the quarks are not the same. It can be shown [24] than this matrix has $N_F(N_F-1)/2$ angular parameters and $(N_F-1)(N_F-2)/2$ phase parameters. It is remarkable that only the Yukawa coupling of the quarks to the Higgs field breaks effectively the flavour symmetry (if the CKM matrix is not diagonal) in the quark sector. This is the domain of study of flavour physics, which intends to explore the phenomena associated with the CKM matrix (mixing between flavours, CP violation, etc.).

In the lepton sector, because of the absence of right-handed neutrinos, the lepton states can be redefined such that the matrix M_l is diagonal and nothing will change in the other part of the Lagrangian density. As a consequence, the lepton number is expected to be independently conserved for each family.

1.6 The three flavours: consequences for the CKM matrix

From experimental evidences, there are three flavour families ($N_F = 3$). The fermions of the three observed families are shown in Table 1.2 with their mass hierarchy. The CKM matrix, V, has thus three angular parameters θ_{12}, θ_{13}, θ_{23}, and one complex phase δ [56]. As will be shown below, this phase is the only source of CP violation in the standard model, and all the results are so far consistent with this view [57, 58]. The matrix can be explicitly written as a function of these four parameters:

$$
\begin{aligned}
V &= \begin{pmatrix} V_{ud} & V_{us} & V_{ub} \\ V_{cd} & V_{cs} & V_{cb} \\ V_{td} & V_{ts} & V_{tb} \end{pmatrix} \qquad (1.41) \\
&= \begin{pmatrix} c_{12}c_{13} & s_{12}c_{13} & s_{13}e^{-i\delta} \\ -s_{12}c_{23} - c_{12}s_{23}s_{13}e^{i\delta} & c_{12}c_{23} - s_{12}s_{23}s_{13}e^{i\delta} & s_{23}c_{13} \\ s_{12}s_{23} - c_{12}c_{23}s_{13}e^{i\delta} & -c_{12}s_{23} - s_{12}c_{23}s_{13}e^{i\delta} & c_{23}c_{13} \end{pmatrix} ,
\end{aligned}
$$

where $c_{ij} = \cos\theta_{ij}$, $s_{ij} = \sin\theta_{ij}$, and the matrix elements V_{ij} have row and column indices written as $i = u, c, t$ and $j = d, s, b$, respectively. An expansion in powers of the Cabibbo angle [59],

$$
\lambda = \sin\theta_{12} = 0.22543(77) \quad \text{(see Table 1.5)}\,, \tag{1.42}
$$

was proposed by Wolfenstein [60]:

$$
V = \begin{pmatrix} 1-\lambda^2/2 & \lambda & A\lambda^3\left(\rho - i\eta\right) \\ -\lambda & 1-\lambda^2/2 & A\lambda^2 \\ A\lambda^3\left(1-\rho-i\eta\right) & -A\lambda^2 & 1 \end{pmatrix} + \mathcal{O}\left(\lambda^4\right) . \tag{1.43}
$$

The Wolfenstein parameters are related to the three angles and the phase by the relations

$$
\lambda = s_{12}\,, \qquad A = \frac{s_{23}}{s_{12}^2}\,, \qquad \rho = \frac{s_{13}\cos\delta}{s_{12}s_{23}}\,, \qquad \eta = \frac{s_{13}\sin\delta}{s_{12}s_{23}}\,. \tag{1.44}
$$

The unitarity condition[5], $V^\dagger V = 1$, leads to six independent relations

$$
\sum_k V_{ki}V_{kj}^* = \delta_{ij}\,, \tag{1.45}
$$

Three of them ($i = j$) are related to the weak universality (same coupling constant for all fermionic fields):

$$
\sum_k |V_{ki}|^2 = 1\,,\ i = 1, 2, 3\,. \tag{1.46}
$$

The remaining three represent the so-called "unitary" triangles in the complex plane:

$$
(V^\dagger V)_{31} = \overbrace{V_{ud}V_{ub}^*}^{\mathcal{O}(\lambda^3)} + \overbrace{V_{cd}V_{cb}^*}^{\mathcal{O}(\lambda^3)} + \overbrace{V_{td}V_{tb}^*}^{\mathcal{O}(\lambda^3)} = 0 \tag{1.47}
$$

$$
(V^\dagger V)_{21} = \overbrace{V_{ud}V_{us}^*}^{\mathcal{O}(\lambda)} + \overbrace{V_{cd}V_{cs}^*}^{\mathcal{O}(\lambda)} + \overbrace{V_{td}V_{ts}^*}^{\mathcal{O}(\lambda^5)} = 0 \tag{1.48}
$$

$$
(V^\dagger V)_{32} = \overbrace{V_{us}V_{ub}^*}^{\mathcal{O}(\lambda^4)} + \overbrace{V_{cs}V_{cb}^*}^{\mathcal{O}(\lambda^2)} + \overbrace{V_{ts}V_{tb}^*}^{\mathcal{O}(\lambda^2)} = 0 \tag{1.49}
$$

[5]The second condition $VV^\dagger = 1$ provides six other relations. It can be shown that they are the same as those given by $V^\dagger V = 1$ at least up to the order λ^4.

Table 1.2: Fermions of the standard model, with their masses [37]. Each fermion has an anti-fermion with the same mass and opposite charge. The neutrinos have no mass in the standard model, one of the current experimental limit is $\sum m_\nu < 0.28$ eV at 95% C.L. [61].

		Family		
		1	2	3
Colour triplet (quark)	$q = +2/3$	up (u)	charm (c)	top (t)
	Mass (MeV/c^2)	2.5	1.3×10^3	172×10^3
	$q = -1/3$	down (d)	strange (s)	beauty (b)
	Mass (MeV/c^2)	5.1	101	4.2×10^3
Colour singlet (lepton)	$q = -1$	electron (e^-)	muon (μ^-)	tau (τ^-)
	Mass (MeV/c^2)	0.511	105.66	1.777×10^3
	$q = 0$ (neutrino)	ν_e	ν_μ	ν_τ
	Mass	0	0	0

Only Eq. (1.47) has its three terms of the same order in λ. In the next sections, the relationship between this equation and the B mesons will be made explicit. When normalised,

$$\frac{V_{ud}V_{ub}^*}{V_{cd}V_{cb}^*} + \frac{V_{td}V_{tb}^*}{V_{cd}V_{cb}^*} + 1 = 0\,, \tag{1.50}$$

the first relation is called "the" unitary triangle [62]. This unitarity condition is testable by measuring only one complex number corresponding to the non-trivial apex of the triangle[6] $\bar\rho + i\bar\eta$ (Fig. 1.3). The angles of the unitary triangle are traditionally named α, β, γ (recommended by the Particle Data Group) or ϕ_1, ϕ_2, ϕ_3 (used by the Japanese community). They are defined as functions of the CKM matrix elements:

$$\alpha = \phi_2 = \arg\left(-\frac{V_{tb}^*V_{td}}{V_{ub}^*V_{ud}}\right)\,, \tag{1.52}$$

$$\beta = \phi_1 = \arg\left(-\frac{V_{cb}^*V_{cd}}{V_{tb}^*V_{td}}\right)\,, \tag{1.53}$$

$$\gamma = \phi_3 = \arg\left(-\frac{V_{ub}^*V_{ud}}{V_{cb}^*V_{cd}}\right)\,. \tag{1.54}$$

The quasi-degenerated triangle of Eq. (1.49) is also very interesting because it is related to B_s^0 decays and new physics could greatly impact its angles. This B_s^0 unitary

[6] At the lowest order in λ, it coincides with the Wolfenstein's $\rho + i\eta$:

$$\rho + i\eta = \left(1 + \frac{\lambda^2}{2}\right)(\bar\rho + i\bar\eta) + \mathcal{O}(\lambda^4)\,. \tag{1.51}$$

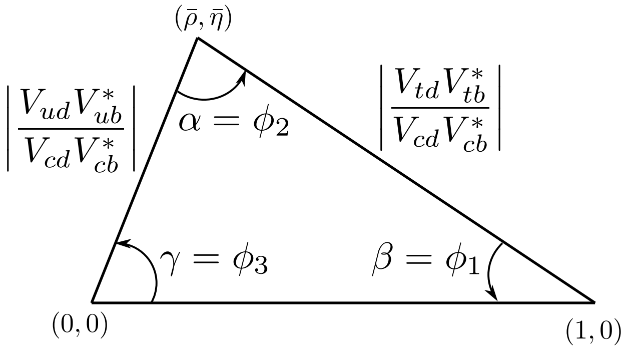

Figure 1.3: Definition of the angles of the unitary triangle.

triangle, similarly defined by its apex $\bar\rho_s + i\bar\eta_s$, can be drawn with Eq. (1.49). This triangle is expected to be very flat, but measurements [63, 64] of the angle

$$\beta_s = \arg\left(-\frac{V_{tb}^* V_{ts}}{V_{tb}^* V_{cs}}\right) \tag{1.55}$$

with $B_s^0 \to J/\psi\phi$ decays allows stringent tests of the unitary condition (Fig. 1.8).

The areas of the unitary triangles are all the same. This is a geometric interpretation of the unique phase of the matrix V. That area is phase invariant and correspond to half the Jarlskog invariant [65–67], defined as

$$J = c_{12}c_{23}c_{13}^2 s_{12}s_{23}s_{13}\sin\delta = A^2\lambda^6\eta\left(1 - \frac{\lambda^2}{2}\right) + \mathcal{O}(\lambda^{10})\,. \tag{1.56}$$

Without the phase δ, $J = 0$, and the unitary triangle is flat. $J \neq 0$ is a necessary condition to get CP violation.

1.7 Heavy meson phenomenology

1.7.1 Heavy quark effective theory

Isolated quarks have never been observed, and this fact is included in the SM by assuming that the physical particles are colourless. Thus, two kinds of *hadrons* are possible, the *mesons*, composed of a quark and an anti-quark, and the *baryons* composed of three quarks.

Sometimes seen as the "simplest non-trivial" hadrons [68], $\bar Q_q$ mesons, composed of a heavy anti-quark $\bar Q$, and a light quark q, are specially interesting in flavour physics. Their structure can be well approximated by an effective theory [69]. In such picture a $\bar Q_q$ meson can be described, in a very good approximation, as a $\bar Q$ quark at rest around which the light constituents (the "cloud") are in (relativistic) motion, like the hydrogen atom in atomic physics. In the heavy-quark effective theory (HQET), the mass of the light quark enters the calculation in an Taylor expansion in power of the parameter m_q/m_Q. This parameter is of the order of 0.1% for the B^0 and B^+ mesons, 0.3% for the $\bar D^0$ and D^- mesons, 2% for the B_s^0 meson and 8% for the D_s^- meson. The corrections are large (30%) for the B_c^+ meson, which is not expected to be precisely described by this approximation.

In this framework, it is natural to expect that all the species of B mesons, B^+, B^0, B^0_s and B_c^+, share similar properties at leading order.

Computations in HQET are considerably simplified because the heavy-quark spin does not interact when $m_Q \to \infty$. The spin-parity j^P of the cloud of the light quark is the same as a meson with a spin-less heavy anti-quark, $(j^P)_{\bar{Q}} = 0^-$. The cloud must have $(j^P)_q = l^{(-1)^l} \oplus \frac{1}{2}^+$, i.e. $(j^P)_q = \frac{1}{2}^+$ for a S-wave ($l = 0$) meson, $(j^P)_q = \frac{1}{2}^-$ or $\frac{3}{2}^-$ for a P-wave ($l = 1$) meson, etc. With the fermionic nature of the heavy quark ($(j^P)_{\bar{Q}} = \frac{1}{2}^-$), the spin-parity of the meson must satisfy $J^P = (j^P)_q \oplus (j^P)_{\bar{Q}}$, i.e. $P = (-1)^{l+1}$ and $J = (l \oplus \frac{1}{2}) \oplus \frac{1}{2}$. For $l = 0$, there is one S-wave doublet (0^-,1^-), for $l > 0$, there are two l-wave doublets $(l-1, l)$ and $(l, l+1)$ (Table 1.3). Finally, HQET calculations can be carried out by using the factorisation hypothesis [70, 71]. The part that can be computed with a perturbative approach is separated from the non-perturbative hadron structure which is described by a parton distribution function. Experimental measurements can provide insights about the limits of the factorisation view [72].

The mass splitting inside the doublets (called hyperfine splitting) is an effect of the finite heavy-quark mass [73]. For the S-wave doublet, the mass difference is expected to be [68, 74]

$$m_{B^*} - m_B = \frac{2\mu_G^2}{3m_b} + \mathcal{O}\left(\frac{\Lambda^3_{QCD}}{m_b^2}\right) \approx 50\ \mathrm{MeV}/c^2\,, \tag{1.57}$$

where $\Lambda_{QCD} \approx 1/R_{\mathrm{hadron}} \approx 200$ MeV [69] is the QCD scale and μ_G^2 is the matrix element of the chromomagnetic interaction operator. Of course, more subtle corrections can be added [75].

Most of the S-wave states for the charmed and strange mesons were experimentally established more than 20 years ago, in full agreement with the HQET picture: the two states for the charmed mesons, $D^{(*)0}$ and $D^{(*)+}$ [76, 77] (1976); the $D_s^{(*)+}$ meson [78] (1979). The discovery of bottom mesons followed, with the first evidence in 1981 [79, 80], the first exclusive B decay in 1983 [81], the excited B^* in 1985 [82]. Finally, the first evidences of the existence of the B^0_s and B^*_s mesons were published in 1990 [83].

It is remarkable that many P-wave states have also been measured. The four states of the $\bar{D}^0$ ($\bar{c}u$) system are established (Fig. 1.4) [84, 85]; two states, 0^+ and 2^+, of the D^- ($\bar{c}d$) system, have been seen [86, 87], while the spin is unknown for two other states [88, 89]. For the B mesons, the splitting is smaller (larger m_Q), but the CDF and DØ collaborations [90, 91] have reported 1^+ and 2^+ excited B^0 mesons. For the B^0_s mesons, the situation is quite similar, with the observation of 1^+ and 2^+ states from the two same experiments [92, 93].

The heavy quark symmetry is firmly established, and it is natural to expect the B^0_s meson to be as different from the B^0 meson than m_d/m_b is different from m_s/m_b. While one can think that the study of the B^0_s meson is not interesting, since it is expected to be very similar to the well-known B^0 particle, it can be exciting to precisely measure the B^0_s system in order to further test HQET, and a lot can be learnt from the discrepancies.

1.7.2 Neutral mesons

The pseudo-scalar neutral mesons reported in Table 1.4 can mix with their antiparticle before they decay. Figure 1.5 shows the two leading-order diagrams of a $B^0_q \to \bar{B}^0_q$ tran-

Table 1.3: Spin-parity of $\bar{Q}_q$ mesons. In the $m_Q \to \infty$ limit, the doublets are degenerated. The bottom part of the table presents the experimental observations [37]. The physical 1^+ states are an admixture of the two $(j_q = 1/2, J = 1)$ and $(j_q = 3/2, J = 1)$ states. There are no direct measurement of the spin-parity for many of these states. In the $\bar{c}s$ system, a 1^- meson, $D^*_{s1}(2700)^-$, has been observed, it is expected to be a D-wave meson ($l = 2$, $(j^P)_q = \frac{3}{2}^+$).

$l^{(-1)^l}$	S wave 0^+		P wave 1^-				...
$(j^P)_q$	$\frac{1}{2}^+$		$\frac{1}{2}^-$		$\frac{3}{2}^-$		...
J^P	0^-	1^-	0^+	1^+	1^+	2^+	...
$\bar{c}u$	$\bar{D}^0$	$\bar{D}^*(2007)^0$	$\bar{D}^*_0(2400)^0$	$\bar{D}_1(2420)^0$	$\bar{D}_1(2430)^0$	$\bar{D}^*_2(2460)^0$	
$\bar{c}d$	D^-	$D^*(2010)^-$	$D_0(2400)^-$	$D_1(2420)^-$		$D^*_2(2460)^-$	
$\bar{c}s$	D^-_s	D^{*-}_s	$D^*_{s0}(2317)^-$	$D_{s1}(2460)^-$	$D_{s1}(2536)^-$	$D^*_{s2}(2573)^-$	
$\bar{b}d$	B^0	B^{*0}		$B_1(5721)^0$		$B^*_2(5747)^0$	
$\bar{b}u$	B^+	B^{*+}					
$\bar{b}s$	B^0_s	B^*_s		$B_{s1}(5830)^0$		$B^*_{s2}(5840)^0$	
$\bar{b}c$	B^+_c						

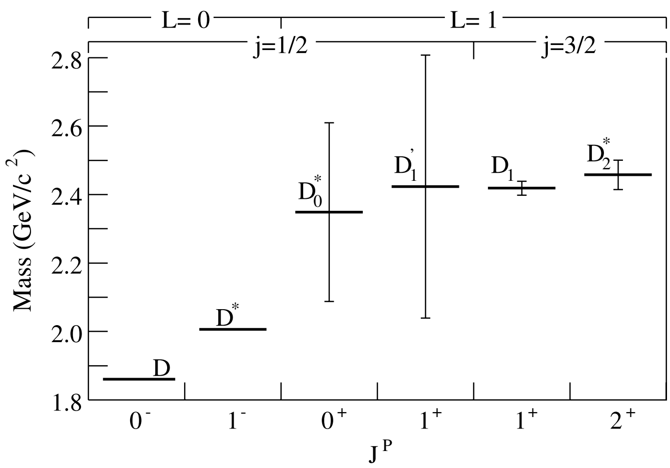

Figure 1.4: (Reproduced from Ref. [84]) Experimental spectrum [37] for the $\bar{c}u$ system. The vertical bars show the widths. The two physical 1^+ states are an admixture of the $j = 1/2$ and $j = 3/2$ $D_1^{(')}$ states, the mixing angle is of the order Λ_{QCD}/m_c [68].

sition. A lot of interesting phenomena arise from it because the properties (mass, flavour, CP eigenstates, etc.) of a neutral meson and its corresponding anti-meson are all distinct.

The time evolution of an oscillating meson P^0 is formalised using a vector in the Hilbert

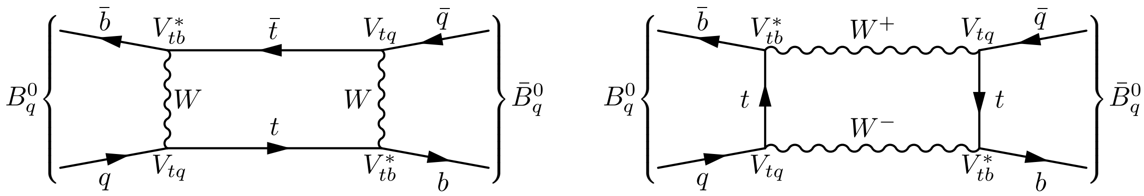

Figure 1.5: Leading order box diagrams involved in B mixing. Diagrams with loops involving the c or u quark also exist, but are suppressed with respect to the heavy t quark.

space restricted to the two-dimensional subspace composed of $|P^0\rangle$ and $|\bar{P}^0\rangle$,

$$|\psi(t)\rangle = \psi_1(t)\,|P^0\rangle + \psi_2(t)\,|\bar{P}^0\rangle \tag{1.58}$$

and by the non-Hermitian Hamiltonian H. In the Wigner-Weisskopf approximation [94, 95], the Hamiltonian can be decomposed into two Hermitian matrices,

$$H = M + i\Gamma\,, \tag{1.59}$$

representing the mass (free evolution) and the decay width, respectively. In case of CPT invariance, which is a general assumption in quantum field theory, the diagonal elements are equal: $M_{11} = M_{22}$ and $\Gamma_{11} = \Gamma_{22}$. The (complex) eigenvalues are

$$\mu_{H,L} \equiv m_{H,L} - \frac{i}{2}\Gamma_{H,L} = M_{11} - \frac{i}{2}\Gamma_{11} \pm \frac{q}{p}\left(M_{12} - \frac{i}{2}\Gamma_{12}\right) \tag{1.60}$$

with

$$\left(\frac{q}{p}\right)^2 = \frac{M_{12}^* - \frac{i}{2}\Gamma_{12}^*}{M_{12} - \frac{i}{2}\Gamma_{12}}\,. \tag{1.61}$$

The sign of q/p is conventionally chosen such that $m_H > m_L$. The eigenstates are written as

$$|P_H\rangle = p\,|P^0\rangle + q\,|\bar{P}^0\rangle\ , \tag{1.62}$$

$$|P_L\rangle = p\,|P^0\rangle - q\,|\bar{P}^0\rangle\ . \tag{1.63}$$

From the Schrödinger equation, $i\partial_t\,|\psi(t)\rangle = H\,|\psi(t)\rangle$, the eigenstates evolve as

$$|P_H(t)\rangle = e^{-i\mu_H t}\,|P_H\rangle = e^{-im_H t}e^{-\frac{1}{2}\Gamma_H t}\,|P_H\rangle\ , \tag{1.64}$$

$$|P_L(t)\rangle = e^{-i\mu_L t}\,|P_L\rangle = e^{-im_L t}e^{-\frac{1}{2}\Gamma_L t}\,|P_L\rangle\ , \tag{1.65}$$

where we have set $\hbar = c = 1$ for clarity. The states P_H and P_L are, in general, not orthogonal,

$$\langle P_H|P_L\rangle = |p|^2 - |q|^2 \neq 0\,; \tag{1.66}$$

they are CP eigenstates only if CP is a symmetry of the total Hamiltonian.

The width, Γ, and the mass, m, of P^0 are the arithmetic averages of the decay widths Γ_H and Γ_L, and the masses m_H and m_L, respectively. The inverse of Γ is defined as the P^0 lifetime[7]:

$$m = \frac{m_H + m_L}{2} \quad , \quad \Gamma = \frac{\Gamma_H + \Gamma_L}{2} = \frac{1}{\tau}\,. \tag{1.67}$$

[7]This convention is well suited for $B^0_{(s)}$ mesons, which have $\Gamma_H \approx \Gamma_L$.

The oscillation properties are summarised in two quantities, conventionally named

$$x = \frac{\Delta m}{\Gamma} \quad \text{and} \quad y = \frac{\Delta\Gamma}{2\Gamma}\,, \tag{1.68}$$

where $\Delta m = m_H - m_L$ and $\Delta\Gamma = \Gamma_L - \Gamma_H$.

A meson is created by strong interaction in a P^0 or $\bar{P}^0$ state. Let $\left|P^0(t)\right\rangle$ denote a state created as a P^0 at $t = 0$; it evolves as

$$\begin{aligned} \left|P^0(t)\right\rangle &= \frac{1}{2p}\left(|P_H(t)\rangle + |P_L(t)\rangle\right) \\ &= e^{-\Gamma t/2}e^{-imt}\left[\cos\left(\frac{\Gamma t}{2}(x+iy)\right)\left|P^0\right\rangle - i\frac{q}{p}\sin\left(\frac{\Gamma t}{2}(x+iy)\right)\left|\bar{P}^0\right\rangle\right], \end{aligned} \tag{1.69}$$

Similarly,

$$\begin{aligned} \left|\bar{P}^0(t)\right\rangle &= \frac{1}{2q}\left(|P_H(t)\rangle - |P_L(t)\rangle\right)\,, \\ &= e^{-\Gamma t/2}e^{-imt}\left[-i\frac{p}{q}\sin\left(\frac{\Gamma t}{2}(x+iy)\right)\left|P^0\right\rangle + \cos\left(\frac{\Gamma t}{2}(x+iy)\right)\left|\bar{P}^0\right\rangle\right]. \end{aligned} \tag{1.70}$$

For a P^0 created at time $t = 0$, the probability to have a $\bar{P}^0$ at time t is not zero, showing explicitly the $P^0 - \bar{P}^0$ oscillation. It is proportional to

$$\left|\left\langle \bar{P}^0 | P^0(t)\right\rangle\right|^2 = \left|\frac{q}{p}\right|^2 e^{-\Gamma t}\left|\sin\left(\frac{\Gamma t}{2}(x+iy)\right)\right|^2 = \frac{1}{2}\left|\frac{q}{p}\right|^2 e^{-\Gamma t}\left(\cosh\left(y\Gamma t\right) - \cos\left(x\Gamma t\right)\right)\,, \tag{1.71}$$

while the probability that it stays a P^0 is proportional to

$$\left|\left\langle P^0 | P^0(t)\right\rangle\right|^2 = e^{-\Gamma t}\left|\cos\left(\frac{\Gamma t}{2}(x+iy)\right)\right|^2 = \frac{1}{2}e^{-\Gamma t}\left(\cosh\left(y\Gamma t\right) + \cos\left(x\Gamma t\right)\right)\,. \tag{1.72}$$

The mixing properties of the neutral mesons (K^0, D^0, B^0 and B_s^0) are quite different, see Table 1.4 for experimental measurements. For the B^0 and B_s^0 systems, the formulae above can be simplified by assuming that CP violation is negligible, i.e.

$$\left|\frac{q}{p}\right| = 1\,. \tag{1.73}$$

The B^0 case can be further simplified with the assumption that the width of the B_H and B_L states are the same, i.e.[8]

$$y_d = 0\,. \tag{1.74}$$

For the B^0 meson, Eqs. (1.71) and (1.72) become

$$\left|\left\langle \bar{B}^0 | B^0(t)\right\rangle\right|^2 = \frac{1}{2}e^{-\Gamma_d t}\left(1 - \cos\left(x_d\Gamma_d t\right)\right)\,, \tag{1.75}$$

$$\left|\left\langle B^0 | B^0(t)\right\rangle\right|^2 = \frac{1}{2}e^{-\Gamma_d t}\left(1 + \cos\left(x_d\Gamma_d t\right)\right)\,. \tag{1.76}$$

[8]In the context of this thesis, the subscripts d and s refer to the B^0 and B_s^0 system, respectively.

Table 1.4: Properties of the neutral mesons: K^0 ($d\bar{s}$), D^0 ($c\bar{u}$), B^0 ($d\bar{b}$) and B_s^0 ($s\bar{b}$) [37]. The unit of Δmc^2 is $1\hbar/\text{ps} \sim 6.6 \times 10^{-10}\,\text{MeV}$.

Meson	K^0	D^0	B^0	B_s^0
Mass (MeV/c^2)	$497.614(24)$	1864.80 ± 0.14	5279.50 ± 0.30	5366.3 ± 0.6
Δmc^2 ($\hbar$/ps)	$0.5292(9)\times10^{-2}$	$(2.39^{+0.59}_{-0.63})\times10^{-2}$	0.507 ± 0.004	17.77 ± 0.12
τ_H (ps)	$5.116(21)\times10^4$	$(410.1\pm1.5)\times10^{-3}$	1.519 ± 0.007	$1.543^{+0.058}_{-0.060}$
τ_L (ps)	$89.53(5)$			$1.408^{+0.033}_{-0.030}$
$\Delta mc^2/\Gamma = x$		$(9.8^{+2.4}_{-2.6})\times10^{-3}$	0.771 ± 0.008	26.2 ± 0.5
$\lvert\Delta\Gamma/\Gamma\rvert = 2\,\lvert y\rvert$		$(1.66\pm0.32)\times10^{-2}$	0.010 ± 0.037	$0.092^{+0.051}_{-0.054}$
$\lvert\epsilon\rvert \approx \left\lvert\frac{1-q/p}{1+q/p}\right\rvert$	$2.228(11)\times10^{-3}$			
$\lvert q/p\rvert$		$0.86^{+0.18}_{-0.15}$	$1.0025(19)$	$1.0058(31)$

1.7.3 CP violation in heavy meson decays

CP violation of the order of 10^{-3} has been discovered in neutral kaons in 1964 [32] but has been understood and included in the standard model only ten years later, when Kobayashi and Maskawa proposed [55] a third family of quarks in order to have a 3×3 matrix with a complex phase that can provide the standard model with a source of CP violation (Sec 1.6). This implies large CP violation in neutral B mesons. CP violation can show up in three different ways: in decay amplitudes, in mixing amplitudes, and in the interference between mixing and decay amplitudes.

CP violation in decay (*direct CP* violation)

The direct CP asymmetry for a charged B decay to a final state f is defined as

$$a_{f^\pm}^{\text{decay}} = \frac{\Gamma(B^+ \to f^+) - \Gamma(B^- \to f^-)}{\Gamma(B^+ \to f^+) + \Gamma(B^- \to f^-)} = \frac{1 - \left|\bar{A}_{f^-}/A_{f^+}\right|^2}{1 + \left|\bar{A}_{f^-}/A_{f^+}\right|^2}\,, \tag{1.77}$$

where A are the decay amplitudes

$$A_{f^+} = \left\langle f^+\right| H^{\text{weak}} \left|B^+\right\rangle \text{ and} \tag{1.78}$$
$$\bar{A}_{f^-} = \left\langle f^-\right| H^{\text{weak}} \left|B^-\right\rangle\,. \tag{1.79}$$

For CP violation to appear, there should be at least two different contributing amplitudes (diagrams), A_j, with different strong (δ_j) and weak (ϕ_j) phases. In the case of two amplitudes: $A_{f^+} = \sum_{j=1}^2 a_j e^{i(\phi_j+\delta_j)}$ and $\bar{A}_{f^-} = \sum_{j=1}^2 a_j e^{i(-\phi_j+\delta_j)}$. The asymmetry is given by

$$a_{f^\pm}^{\text{decay}} = \frac{-2a_1a_2\sin(\delta_1-\delta_2)\sin(\phi_1-\phi_2)}{a_1^2+a_2^2+2a_1a_2\cos(\delta_1-\delta_2)\cos(\phi_1-\phi_2)}\,. \tag{1.80}$$

Hadronic uncertainties in a_i and strong phases make difficult the determination of the weak phases in measurements of direct CP-violating effects.

In the case of neutral B mesons, CP violation in mixing (see below) is negligible and the direct CP asymmetry for a flavour-specific final state is described in a similar way. Direct CP violation in $B^0 \to K^+\pi^-$ decays has been observed by both Belle [96]

$$a^{\rm decay}_{K^\pm\pi^\mp} = -0.094 \pm 0.020\,, \tag{1.81}$$

and BaBar [97]

$$a^{\rm decay}_{K^\pm\pi^\mp} = -0.107 \pm 0.019\,. \tag{1.82}$$

CP violation in mixing (*indirect CP violation*)

In semi-leptonic decays of neutral B mesons, the charge of the lepton indicates whether the B^0 was in a B^0 or a $\bar{B}^0$ state when it decayed. An asymmetry related to CP-violating effects in the mixing is constructed from the "wrong-sign" leptons,

$$a_{\rm SL}(B^0) = \frac{\Gamma(\bar{B}^0(t) \to l^+\nu X) - \Gamma(B^0(t) \to l^-\bar{\nu} X)}{\Gamma(\bar{B}^0(t) \to l^+\nu X) + \Gamma(B^0(t) \to l^-\bar{\nu} X)} = \frac{1-|q/p|^4}{1+|q/p|^4} = {\rm Im}\frac{\Gamma_{12}}{M_{12}}, \tag{1.83}$$

where $\Gamma(B^0(t) \to l^-\bar{\nu}X)$ ($\Gamma(\bar{B}^0(t) \to l^+\nu X)$ is the time-dependent decay rate of a produced B^0 ($\bar{B}^0$) decaying after a time t to a negative (positive) lepton. The asymmetry $a_{\rm SL}$ is not zero if the rate of the $B^0 \to \bar{B}^0$ transition differs from that of $\bar{B}^0 \to B^0$. This asymmetry is hard to measure because $|q/p|$ is very close to 1. So far, a non-zero asymmetry was only measured in the neutral kaon system [37]:

$$a_{\rm SL}(K^0) = (3.32 \pm 0.06) \times 10^{-3}\,. \tag{1.84}$$

CP violation in the interference of mixing and decay (*mixing-induced CP violation*)

As before, this CP asymmetry can occur only with neutral mesons. If the final state f is a CP eigenstate, the time-dependent asymmetry $a_{CP,f}(t)$

$$a_{CP,f}(t) = \frac{\Gamma(B^0(t) \to f) - \Gamma(\bar{B}^0(t) \to f)}{\Gamma(B^0(t) \to f) + \Gamma(\bar{B}^0(t) \to f)}\,, \tag{1.85}$$

is given by[9]

$$a_{CP,f}(t) = a^{\rm decay}_{CP,f}\cos(\Delta m t) + a^{\rm int}_{CP,f}\sin(\Delta m t)\,, \tag{1.86}$$

where $a^{\rm decay}_{CP,f}$ corresponds to the direct CP violation in the limit $|q/p| = 1$ and $a^{\rm int}_{CP,f}$ corresponds to CP violation in the interference between mixing and decay. It can be measured only with time-dependent studies, as the time-averaged asymmetry vanishes.

In terms of

$$\xi_f = \frac{q}{p}\frac{A(\bar{B}^0 \to f)}{A(B^0 \to f)}\,, \tag{1.87}$$

[9]In the Review of Particle Physics [37], the asymmetries are defined as $C_f = a^{\rm decay}_{CP,f}$ and $S_f = -a^{\rm int}_{CP,f}$

the direct and interference asymmetries read

$$a_{CP,f}^{\text{decay}} = \frac{1 - |\xi_f|^2}{1 + |\xi_f|^2} \tag{1.88}$$

and

$$a_{CP,f}^{\text{int}} = \frac{2\text{Im}\xi_f}{1 + |\xi_f|^2}\,. \tag{1.89}$$

A condition to get CP violation in the interference is that ξ_f must have an imaginary part.

For the CP-eigenstate $B^0 \to J/\psi K_S^0$ "golden" decay, the asymmetry can be expressed with the CKM matrix elements:

$$\xi_{J/\psi K_S^0} \approx -\frac{V_{tb}^* V_{td}}{V_{tb} V_{td}^*} \frac{V_{cb} V_{cs}^*}{V_{cb}^* V_{cs}} \frac{V_{us} V_{ud}^*}{V_{us}^* V_{ud}} = -e^{-2i\beta}\,. \tag{1.90}$$

The amplitudes are therefore directly related to the angleβ,

$$a_{CP,J/\psi K_S^0}^{\text{int}} = -\sin(2\beta) + \mathcal{O}(1\%) \ \text{ and} \tag{1.91}$$

$$a_{CP,J/\psi K_S^0}^{\text{decay}} = 0\,. \tag{1.92}$$

The B_s^0 counterpart of this mode, $B_s^0 \to J/\psi\phi$, can be used to measure $a_{CP,J/\psi\phi}^{\text{int}}$ in a similar way [63, 64]. In principle, a similar calculation for $B^0 \to \pi^+\pi^-$ leads to $\xi_{\pi^+\pi^-} \approx e^{2i\alpha}$. However, penguin contributions to the $B^0 \to \pi^+\pi^-$ decay are not negligible and the extraction of α is more complex. Belle [98] and BaBar [97] observed CP violation with a time-dependent analysis.

The study of CP violation in B meson decays is a long-standing source of research in high energy physics and more sophisticated methods for observing CP violation have been developed over the recent years, like the Dalitz-plot analysis [99, 100], the Atwood-Dunietz-Soni (ADS) [101, 102] or the Gronau-London-Wyler (GLW) [103, 104] methods. In addition to the B^0 mesons, B_s^0 mesons can provide crucial and independent measurements from its non-strange counterpart [7, 105]. See Ref. [106] for a review of physics achievements made with B meson decays.

1.8 Tests and limits of the standard model

1.8.1 Standard model parameters

The effective Lagrangian density of the standard model has 18 parameters:

- the coupling constants g_s, g and g', or [37]

$$\begin{aligned}
\alpha_s &= \frac{g_s^2}{4\pi} = 0.1184(7) && (\text{at } Q^2 = M_W^2)\,, \\
\alpha &= \frac{g^2 \sin^2\theta_W}{4\pi} = \frac{1}{137.04\ldots} && (\text{at } Q^2 = 0) \ \text{ and} \\
\sin\theta_W &= \frac{g'}{\sqrt{g^2 + g'^2}} = 0.23116(13)\,;
\end{aligned}$$

- the $W^{\pm}$ boson mass [37],

$$M_W = \frac{g\nu}{2} = 80.399 \pm 0.023 \text{ GeV}/c^2\,; \tag{1.93}$$

- the masses of the six quarks and three charged leptons (Table 1.2);
- the four parameters of the CKM quark-mixing matrix (Table 1.5) and
- the Higgs mass, which is still unknown.

All but the last one have been measured. So far, this model is very successful and has almost never been contradicted. The electroweak precision measurements show a remarkable consistency (Figs. 1.6 and 1.7).

1.8.2 The success of the CKM theory

The current constraints on the unitary triangle show an exceptional agreement with the CKM picture of CP violation (Fig. 1.8). The current values of the parameters of the CKM matrix are shown in Table 1.5. The constraints used to fit the unitary triangles (Fig. 1.8) include [58]:

- $\varepsilon_K = (2.229 \pm 0.010) \times 10^{-3}$, measured with the CP-violating decay $K^0_L \to \pi\pi$;
- $|V_{ub}| = (3.92 \pm 0.46) \times 10^{-3}$, measured with inclusive $B \to X_u l\bar{\nu}$ modes;
- $\Delta m_d c^2 = (0.507 \pm 0.005)\ \hbar/\text{ps}$, measured from B^0 mixing;
- $\Delta m_s c^2 = (17.77 \pm 0.12)\ \hbar/\text{ps}$, measured from B^0_s mixing;
- direct measurements of the three CKM angles, the most precise is β, $\sin 2\beta_{[c\bar{c}]} = 0.673 \pm 0.023$, measured from $b \to c\bar{c}q$ ($q = d, s$) decays.

The observation of CP violation and the confirmation of the CKM theory is undoubtedly the greatest success of the B factories. Their results [108, 109] are mentioned by the Nobel committee for the 2008 Nobel Price in physics awarded to Nambu, Kobayashi and Maskawa.

1.8.3 Beyond the standard model

However, the standard model as described here is certainly not the final story.

Several experimental evidences remain unexplained. The unitary triangle fit shows some tensions between best-fit values and direct measurements [110], the most serious case being the direct $\mathcal{B}(B^+ \to \tau^+\nu_\tau)$ measurements by Belle [111] and BaBar [112, 113]. Two surprising results have recently been reported by the Tevatron experiments, the large dilepton asymmetry reported by the DØ collaboration [114] and the intriguing 4.1σ-excess near $m \sim 140 \text{ GeV}/c^2$ reported by CDF [115], but excluded at 4.3σ level by DØ [116]. The existence of the Higgs bosons still need to be confirmed or excluded. For what concerns the SM Higgs, a definite answer is expected in the coming year from the LHC experiments which produce Higgs analysis results remarkably fast [117].

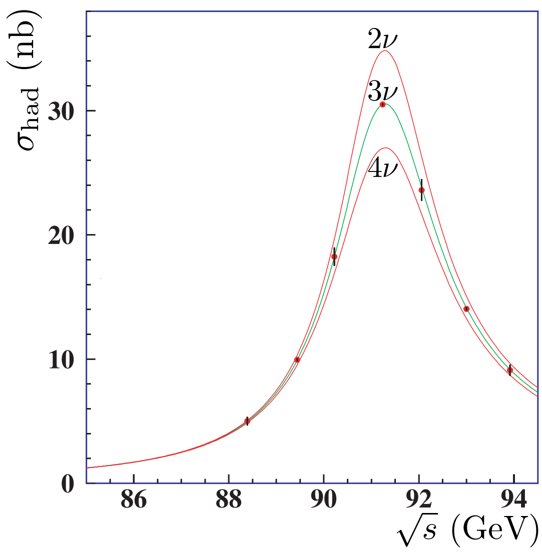

Figure 1.6: Measurement of the hadronic cross-section around the Z^0 resonance at LEP [51]. The error bars are multiplied by 10. The curves indicate the prediction of the standard model for 2, 3 and 4 species of standard-model neutrinos. The number of neutrino species is fitted to be $N_\nu = 2.9840 \pm 0.0082$.

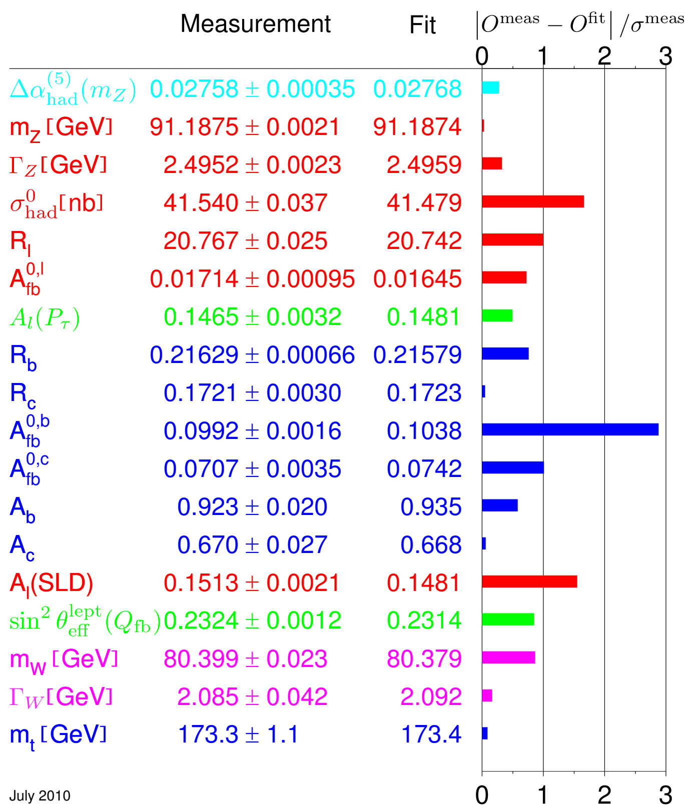

Figure 1.7: Summary of electroweak precision measurements: differences (in standard deviations) between single measurements and best fit values [51].

Table 1.5: Experimental status of the CKM matrix as of Summer 2010.

parameter	Fit result [58]
A	$0.812^{+0.013}_{-0.027}$
λ	0.22543 ± 0.00077
$\bar{\rho}$	0.144 ± 0.025
$\bar{\eta}$	$0.342^{+0.016}_{-0.015}$
$\bar{\rho}_s$	-0.0077 ± 0.0014
$\bar{\eta}_s$	$-0.01831^{+0.00083}_{-0.00087}$
α (°)	91.0 ± 3.9
β (°)	$21.76^{+0.92}_{-0.82}$
γ (°)	67.2 ± 3.9
J (10^{-3})	$2.96^{+0.18}_{-0.17}$

In the lepton sector, the well-established neutrino oscillations [118, 119] indicate that at least two neutrinos are massive, which is not accounted for in the SM. Neutrino masses can be included in the standard model by including "sterile" right-handed neutrinos. So far, there is no direct evidence for such neutrinos but they are not excluded by cosmological observations (Fig. 1.10). Proposals of extensions of the SM include flavour mixing in the lepton sector with the PMNS matrix [120], the leptonic counterpart of the quark-mixing CKM matrix.

The excess of baryons over anti-baryons in the early Universe is much too large to be explained only by the three-family CKM model [122, 123]. It is thus very plausible that there are other sources of CP violation [124]. The study of the cosmological microwave background shows that only a small fraction (4.6% [125]) of the Universe is made of standard model particles. Dark matter and dark energy are the main constituents, but nothing is known about their nature.

From a theoretical point of view, the standard model exhibits strange features. It is not well understood why there is no CP violation in the strong sector [126, 127]. The mass pattern of the components of the standard model, from the fermions (Table 1.2) and the Higgs boson to the Planck mass, $m_p = \sqrt{\hbar c/G_N} = 1.22089(6) \times 10^{19}\,\mathrm{GeV}/c^2$, is not understood at all as well as the large differences between the relative strengths of the various forces.

Extensions of the standard model have been proposed to resolve these problems: with a fourth quark family [128, 129], large extra-dimensions [130], warped extra-dimension (Randall-Sundrum models) [129, 131–133] or a form of supersymmetry (SUSY, CMSSM, mSUGRA, etc.) [134, 135], etc. The imagination of theorists is boundless. More fundamentally, the gravitational force should be present in a theory that aims at explaining the whole Universe; this is the goal of grand-unification theories [136].

The LHC experiments will restrain considerably the parameters space of the speculative

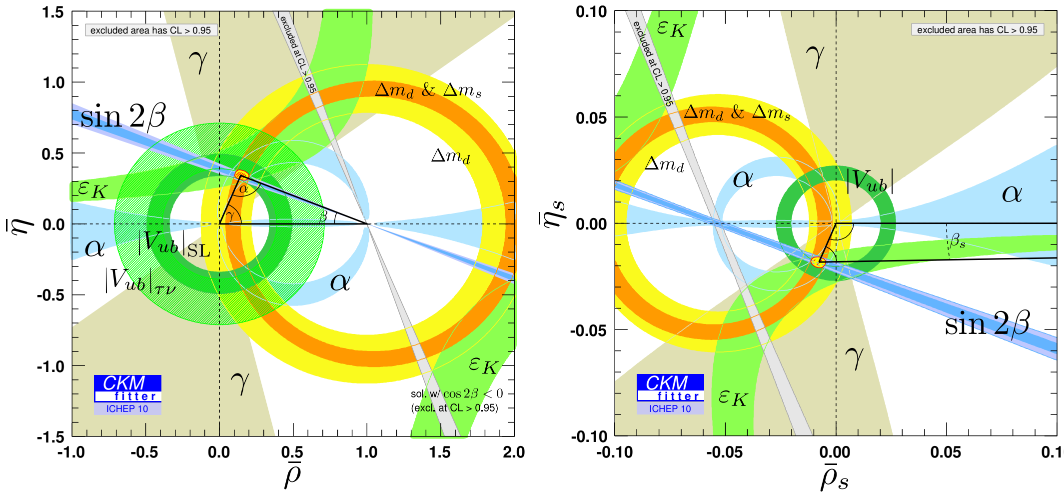

Figure 1.8: CKM fit results for two unitary triangles [58]. Note the difference between the scales.

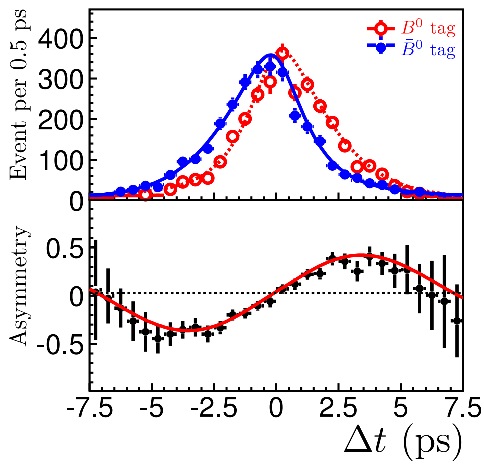

Figure 1.9: (Reproduced from Ref. [107]) Time-dependent yields and asymmetry of $B^0 \to J/\psi K^0$ and $\bar{B}^0 \to J/\psi \bar{K}^0$ decays at Belle. The fit result [107] is consistent with no direct CP violation, $a_{CP}^{\text{decay}} = 0.018 \pm 0.025$, but with mixing-induced CP violation, $a_{CP}^{\text{int}} = 0.642 \pm 0.035$.

standard model extensions. ATLAS and CMS are designed for direct searches of particles [137] taking further what the Tevatron experiments have started. On the other hand indirect tests via precision measurements are the goal of the LHCb experiment and the future super B factories (Belle II [138] and SuperB [139]). The b hadrons are very convenient [140, 141] for such studies and allow new physics phenomena to be probed at a larger energy scale than the direct searches which are limited by the collision centre-of-mass energy.

Because of the very successful start of LHC [142], important discoveries may happen in the coming years; new super B factories as well as possible new high energy e^+e^- linear collider will then be crucial to confirm them and perform precision measurements.

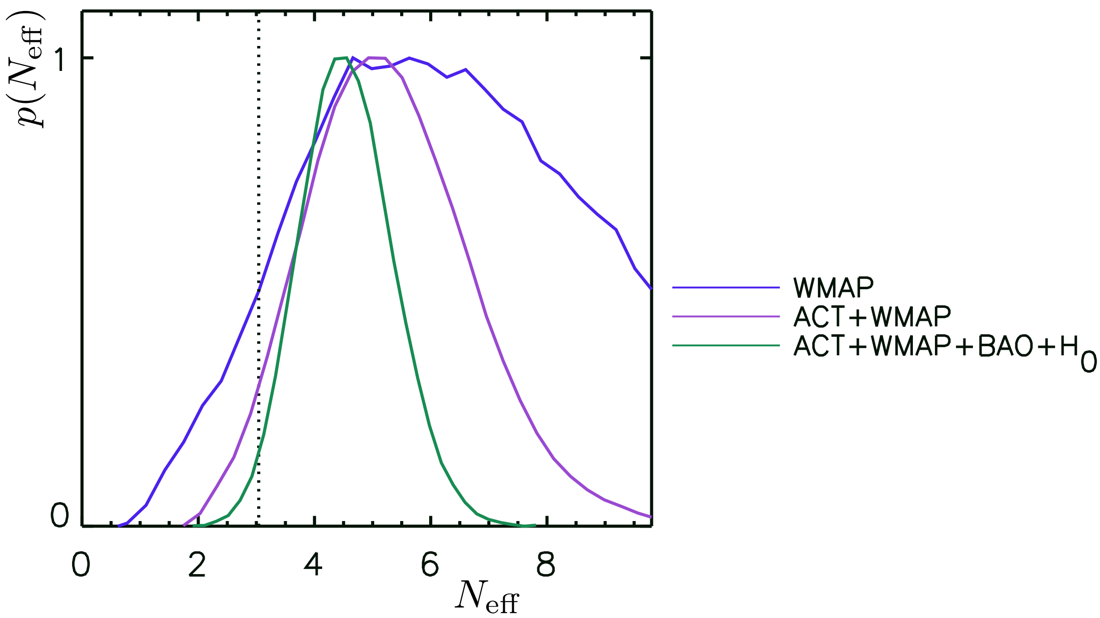

Figure 1.10: Marginal probability of the effective number of relativistic neutrino species $N_{\rm eff}$ from the observations of the Atacama cosmological telescope (ACT) [121]. Even though not the preferred value, the SM $N_{\rm eff} = 3$ is included in the 95% C.L. interval.

Chapter 2

The Belle experiment at KEKB

This chapter is dedicated to the description of the KEKB collider and the Belle detector. Standard particle detection and reconstruction techniques, as well as the $\Upsilon(5S)$ data sample, are also presented.

2.1 The KEKB accelerator and storage ring

The KEKB B factory [2] is an asymmetric electron-positron storage ring. It has one interaction point (IP) where the Belle detector stands (Fig. 2.1). It was designed for producing a large number of B mesons, with a design luminosity of 10 nb^{-1} per second. Two 3016m-long rings, a high-energy ring (HER) and a low-energy ring (LER), are installed in an 11m-deep tunnel at the High Energy Accelerator Research Centre (KEK) located near the city of Tsukuba (Japan). From a linear accelerator (Linac), an electron beam of energy $E_{\rm HER} = 8.0$ GeV is injected in the HER while a positron beam of energy $E_{\rm LER} = 3.5$ GeV is injected in the LER. The crossing angle between the two beams at the interaction point is $\theta_{\rm X} = \theta_{\rm LER} - \theta_{\rm HER}$ =22 mrad, where $\theta_{\rm HER}$ $(\pi + \theta_{\rm LER})$ is the angle between the centre-of-mass (CM) direction and the HER (LER) beam direction (Fig. 2.2). The non-zero crossing angle reduces the CM energy by about 1 MeV (0.01%). It will be shown in Sec. 2.3.1 that the CM energy is actually determined at this level of precision. The CM energy is designed to be close to that of the $\Upsilon(4S)$ resonance,

$$\sqrt{s} = \sqrt{2\,(1+\cos\theta_X)\,E_{\rm LER}E_{\rm HER}} = 10.58 \text{ GeV}\,,$$

while its boost,

$$\beta\gamma = \frac{E_{\rm HER}\cos\theta_{\rm HER} - E_{\rm LER}\cos\theta_{\rm LER}}{\sqrt{s}} = 0.42\,,$$

was chosen as a compromise between the data statistics for observing time-dependent CP violation and the acceptance for the analyses that don't require time information.

During its 10-year operation from 1999 to 2009 the KEKB accelerator performed very well and even above expectations (Table 2.1). Several improvements during that period increased the instantaneous luminosity up to 21 nb^{-1} per second. This has been achieved in 2009 following the installation, in 2006, of special devices called "crab cavities" [143] aiming at restoring head-on bunch collisions. This is done by rotating the bunches without

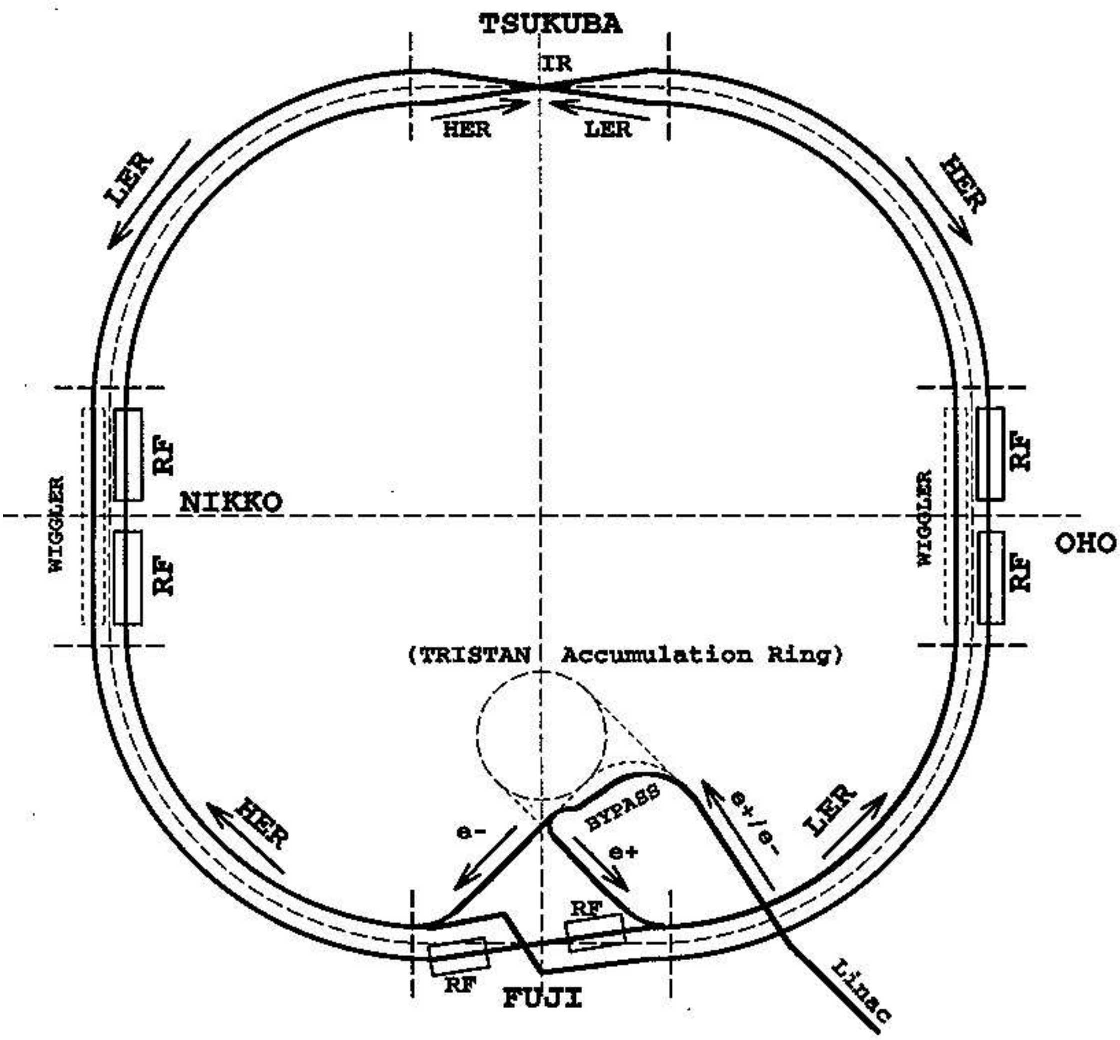

Figure 2.1: Sketch-plan of the KEKB collider. The Belle detector is installed at the interaction region (IR) in the "Tsukuba" hall.

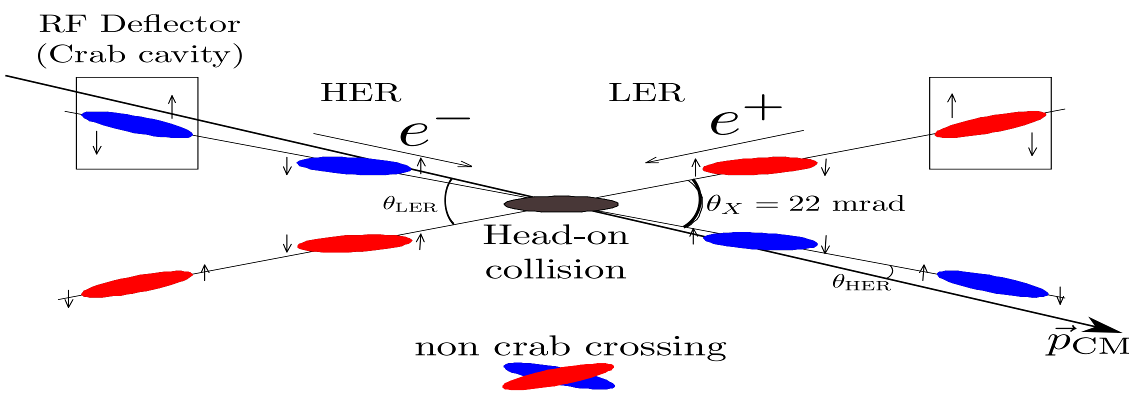

Figure 2.2: Definition of the beam angles, and sketch of crab crossing of bunches.

Table 2.1: Designed values of the KEKB parameters, compared with the achieved values, without and with the crab-crossing. β^* is the value of the β function (envelope of the betatron oscillations) at the interaction point.

Parameter	Design value [2]	Achieved values	
		June 2006	June 2009
Crab crossing	no	no	yes
Luminosity ($\mathrm{nb}^{-1}\mathrm{s}^{-1}$)	10	16.5	21.1
HER current (A)	1.1	1.2	1.2
LER current (A)	2.6	1.6	1.6
Number of bunches	4608	1388	1584
β_x^* (cm)	33	$56-59$	120
β_y^* (cm)	1	$0.59-0.65$	0.59

changing the beam angles ("crab-crossing" scheme, Fig. 2.2). A second important aspect is the introduction of continuous injection: the electrons and positons are injected during the data taking. The data taking is very efficient without the need to abort the beams every hour for a new injection[1]. Typical accelerator parameters are shown in Fig. 2.3, in the form of the summary of the run when the luminosity first reached $20\ \mathrm{nb}^{-1}$ per second.

The machine was stopped after it had delivered an integrated luminosity in excess of $1\ \mathrm{ab}^{-1}$, which was the goal set at the inception of the project. The Belle detector has recorded about $1040\ \mathrm{fb}^{-1}$ of data on tapes. While most of these data have been taken at the $\Upsilon(4S)$ energy, the KEKB accelerator also delivered collisions at higher energy by increasing the LER energy to $3.6\ \mathrm{GeV}$ and the HER energy to $8.2\ \mathrm{GeV}$, in order to reach the next bottomonium resonance, called $\Upsilon(5S)$. This energy is above the $B_s^0\bar{B}_s^0$ threshold and opened new physics opportunities for the Belle collaboration.

2.2 The Belle experiment

Located at the interaction point, the Belle detector [1] is a general-purpose 4π detector composed of many sub-detectors (see Fig. 2.4). The excellent performances of the particle identification and tracking system, and large angular coverage, make it very efficient to reconstruct B decays. A super-conducting solenoidal magnet producing a 1.5 T magnetic field is used for the momenta measurements.

The main sub-detectors,i.e. the silicon vertex detector (SVD), the central drift chamber (CDC), the aerogel Čerenkov counter (ACC), the time-of-flight system (TOF), the electromagnetic calorimeter (ECL), the extreme forward calorimeter (EFC) and the K_L^0 and $\mu^\pm$ detector (KLM), are described in the following sections. Cylindrical coordinates are generally used throughout this thesis, the positive z axis being defined along the CM boost

[1]In normal conditions, the run stops after an error or when the 8 hour limit is reached.

```
--------------------------------------------------
Belle Run Summary(v2.6) - Exp    69  Run  1140
--------------------------------------------------
Start Time: 2009 Jun 15, 11:26:48 took   22 sec to start
Stop  Time: 2009 Jun 15, 15:42:44 took 15356 sec
Stop Reason: FATAL from [TRG] (TT) BUSY in COPPER crate 1b at event 6122992
Expert shift:   R.Louvot
Non-Expert:     A.Kuzmin
BCG shift:      T.Nozaki
Run Mode:       Luminosity Run
Accelerator:     at start      at stop    Fill-number=18801  Status=Lp New Record!! > 20/nb/s
   HER current   1143.4 mA    1164.5 mA   8.2150 GeV  Lp New Record!! > 20/nb/s
   LER current   1599.7 mA    1617.2 mA   3.5941 GeV  Physics Run (Crab ON)
                             (CM-energy 10.8675 GeV)
   HER beamsiz 401.5/  2.0  456.5/  2.0 um (x/y)  life 158 min
   LER beamsiz 390.1/  2.3  416.7/  1.9 um (x/y)  life -200 min
   HER vacuum    2.6/  1.5    2.8/  1.7 x1e-8 Pa (average/upstream)
   LER vacuum    6.6/  1.5    8.1/  1.9 x1e-8 Pa (average/upstream)
   LER cont. inj. ON  (11.7 Hz  179590 times)   inj.veto ON (0)
Luminosity:     ECL        EFC        KEKB
   at start    177.96e32  164.81e32  137.27e32
   at stop     193.07e32  176.33e32  155.14e32
   peak/fill   199.99e32
```

Figure 2.3: Summary log of Run 1140 of Experiment 69. KEKB delivered for the first time an instantaneous luminosity larger than 20 /nb/s on June 15, 2009. A software limit at 20 /nb/s disturbed the online monitoring (last line). An offline recovery later confirmed that the luminosity actually exceeded 20 /nb/s. The record of 21.08 /nb/s was achieved two days later.

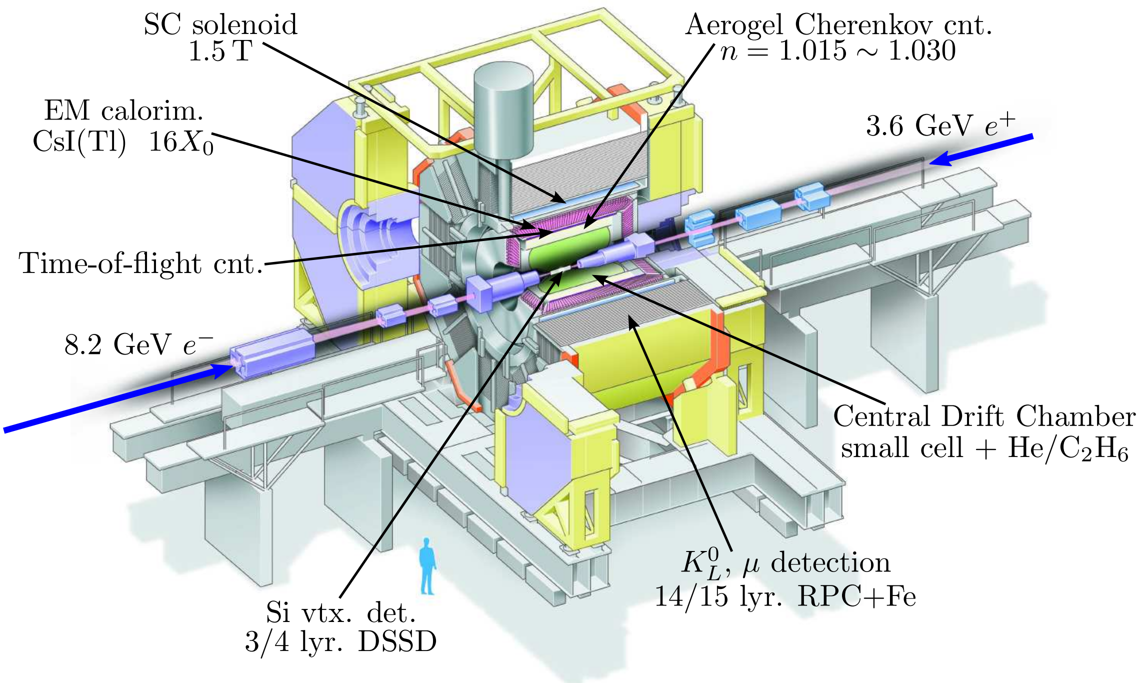

Figure 2.4: Perspective view of the Belle detector.

direction in the laboratory, with its the origin located at the nominal interaction point. More details can be found in Refs. [1, 144].

2.2.1 Silicon vertex detector

The silicon vertex detector is designed for tracking particles as close as possible to the interaction point. B mesons, which have $c\tau \approx 460\mu$m, fly approximately $\beta\gamma c\tau \approx 200\mu$m in the laboratory before they decay. The beam pipe has a reduced radius of 15 mm near the interaction point to place the SVD as close as possible to the point where the collisions take place. The SVD is the closest detector to the interaction region and subject to large radiation damage. After four years of data taking, the original SVD has been replaced [144–146]. We describe here the second version of the SVD (Fig. 2.5), which is relevant to our data sample.

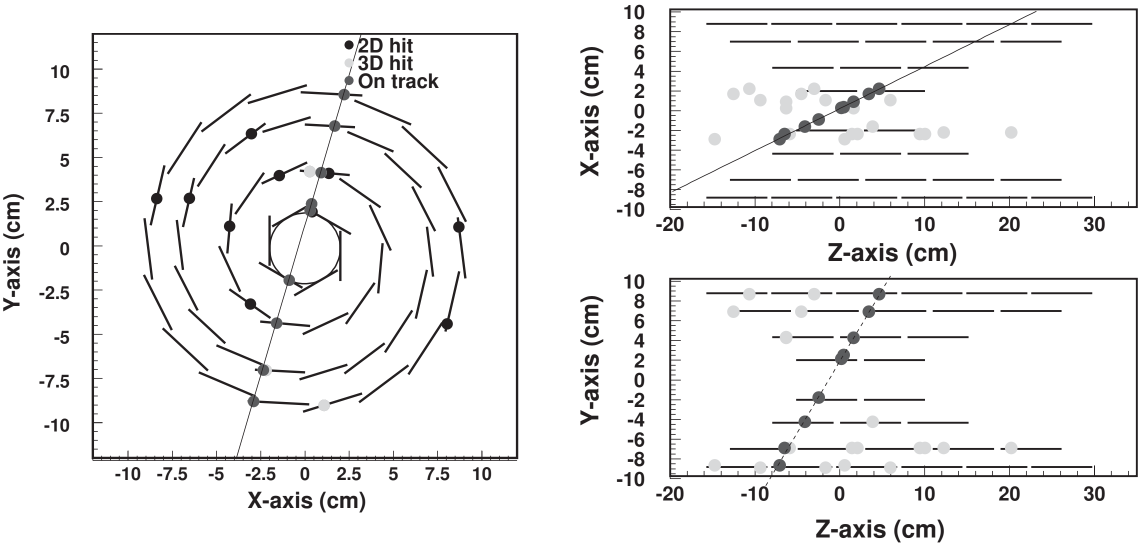

Figure 2.5: Schematic view of the Belle SVD detector with a reconstructed cosmic-ray track.

The SVD is composed of four concentric layers of double-sided silicon detector (DSSD) located at radii $r = 20.0, 43.5, 70.0$ and 88.0 mm, respectively. The polar coverage ($17^\circ < \theta < 150^\circ$) matches that of the CDC. A total of 110592 strips are read out by 864 independent radiation-hard ASICs[2] and the analog signals are then transmitted to the electronic hut where they are digitised and sent to the trigger system and the central Belle DAQ system. Very good performance has been achieved. The DAQ system is very stable in the standard Belle environment (trigger rate of 400 Hz) with an occupancy of 4%. The SVD was designed to handle a trigger rate up to 1.3 kHz with an occupancy of 5%. The achieved resolution is 12 μm in the r,ϕ plane, and 19 μm in the z direction. The SVD resolution is the key for precise time-dependent measurements because the position difference in the z direction between the decay points of the two B mesons is related to their proper lifetime difference ($\Delta z \approx \beta\gamma\Delta t$).

[2] *Application-specific integrated circuits.*

The SVD was also used for the trigger system in early days of data taking, well before the time when $\Upsilon(5S)$ data were recorded. We ignore this aspect of the SVD system here.

2.2.2 Central drift chamber

The central drift chamber is crucial for measuring charged tracks. It provides information about their trajectory (sign and momentum) and energy loss (dE/dx measurement). It has a large angular coverage, $17° < \theta < 150°$, from the inner radius of $r = 103.5$ mm to the outer radius of $r = 874$ mm (Fig. 2.6). The longest wires (at large r) are 2.4 m long. There are 50 cylindrical layers of wires and the maximal drift distance lies between 8 and 10 mm. About 3.5 tons of tension are applied by the wires on the CDC structure.

The CDC volume is filled with a mixture of helium and ethane (50% He, 50% C_2H_6). This gas has a large radiation length (640 m) in order to reduce multiple scattering. Its saturated drift speed of 4 cm/μs ensures a good quality dE/dx measurement (Fig. 2.7). The achieved relative track momentum resolution at start-up was $(1.64 \pm 0.04)\%$ in the range 4 to 5.2 GeV/c.

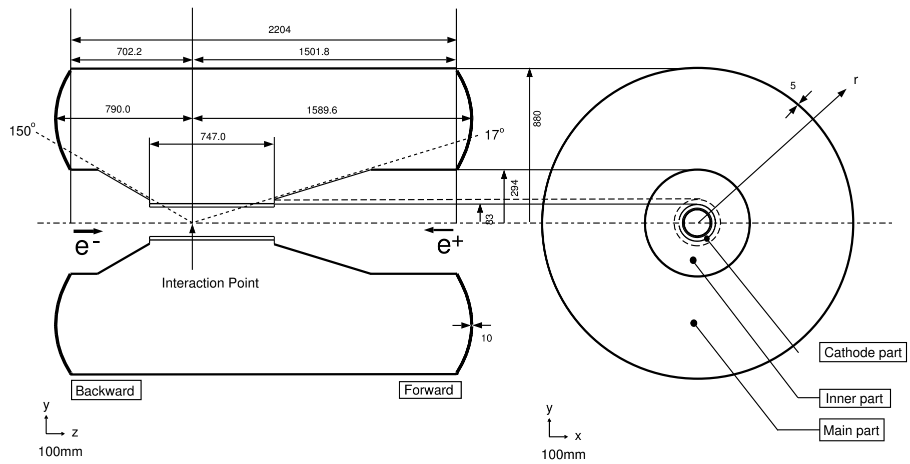

Figure 2.6: Layout of the CDC structure.

In the period of running we are interested in, the CDC was used in the trigger to identify tracks in the $r - \phi$ plane. The CDC trigger signal is formed from wire hits. Hit patterns are examined by a memory look-up table which latches with a period of 16 MHz. The CDC is divided in 6 concentric trigger layers and the CDC trigger system returns the number of short and long tracks and the maximum opening angle between two tracks when more than $135°$ (for the recognition of back-to-back event topology (Table 2.19)). The short (long) tracks are defined as tracks with hits in the three innermost (in all the six) layers and with $p \geq 200$ MeV/c (300 MeV/c).

2.2.3 Aerogel Čerenkov counters

An array of Čerenkov counters complement the particle identification system. It makes a good separation between $\pi^{\pm}$ and $K^{\pm}$, especially in regions out of reach for the CDC and TOF systems. It is composed of 960 modules with refractive index between $n = 1.01$

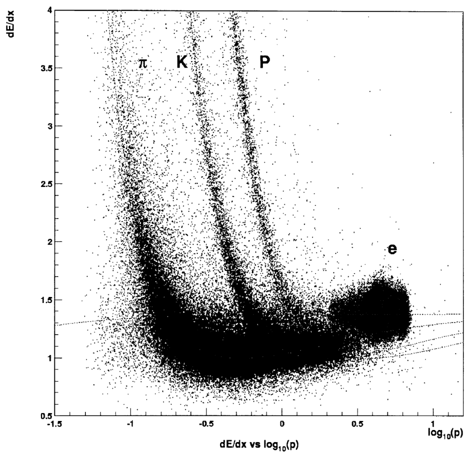

Figure 2.7: Truncated mean of the measured energy loss dE/dx (in arbitrary unit) as a function of the logarithm of the momentum (in GeV/c), in collision data. The dotted curves show the expectations for pions, kaons protons and electrons.

and 1.03 (Fig. 2.8). The active medium of a module is made of five tiles of silica aerogel stacked in a thin $12 \times 12 \times 12$ cm^3 box. The Čerenkov light is detected by two mesh-type photomultipliers. The ACC system is not used in the trigger. The light yields of the ACC modules are used in the computation of the electron-pion and kaon-pion separation likelihoods.

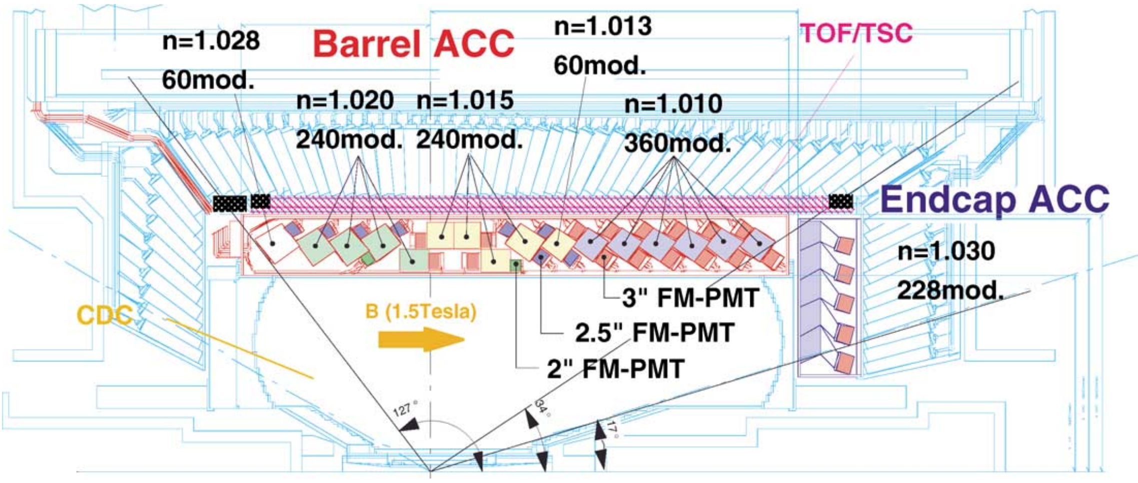

Figure 2.8: Side view of the ACC detector.

2.2.4 Time-of-flight system

Time-of-flight measurements are performed with scintillating plastic counters with a design time resolution of 100 ps. A very good time resolution enables efficient particle identification. This system also provides fast trigger signals. However, the trigger rate of

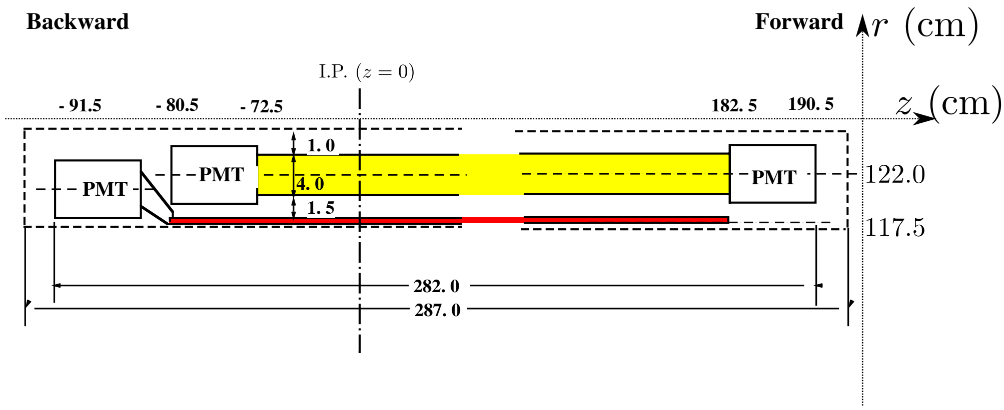

Figure 2.9: Dimensions and positions of the TOF (yellow) and TSC (red) modules. The TOF (TSC) modules are 4.0 (0.5) cm thick, 6.0 (12.0) cm wide and 255.0 (263.0) cm long.

the time-of-flight counter would be too high. Thin dedicated trigger scintillation counter (TSC) are added to the system (Fig. 2.9) to produce a fast trigger signal with a reasonable rate (below 70 kHz).

The whole TOF system contains 128 TOF and 64 TSC counters. The light guides are reduced as much as possible by using fine-mesh-dynode photo-multiplier directly mounted on the modules. The system has an angular coverage of $34° < \theta < 120°$. A charged particle needs to have a momentum larger than 0.28 GeV/c to reach the TOF counters. Above that limit, the TOF measurement is included in the algorithm of particle identification. Figure 2.10 shows the mass of the tracks including TOF and CDC signals. There is good agreement between simulation (with 100 ps TOF time resolution) and data.

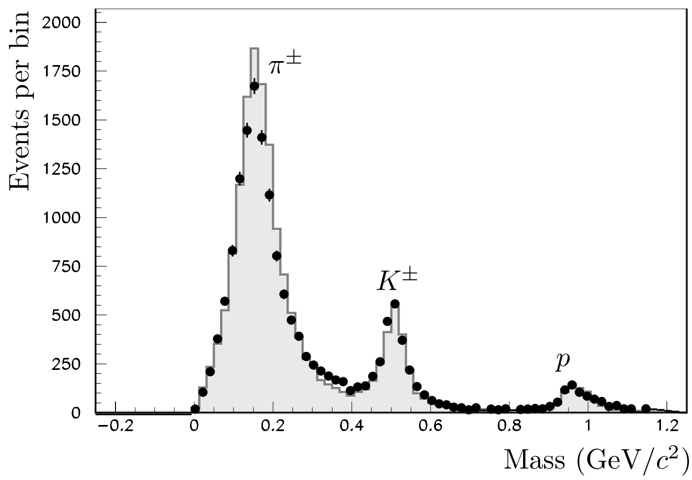

Figure 2.10: Distribution of the mass of hadron-event tracks, calculated as $m = P/c \times \sqrt{(cT/L)^2 - 1}$, where T is the time-of-flight from the TOF system, and the momentum P and path length L are obtained from the CDC. The MC simulation (histogram) assuming a resolution of 100 ps is compatible with data (points) .

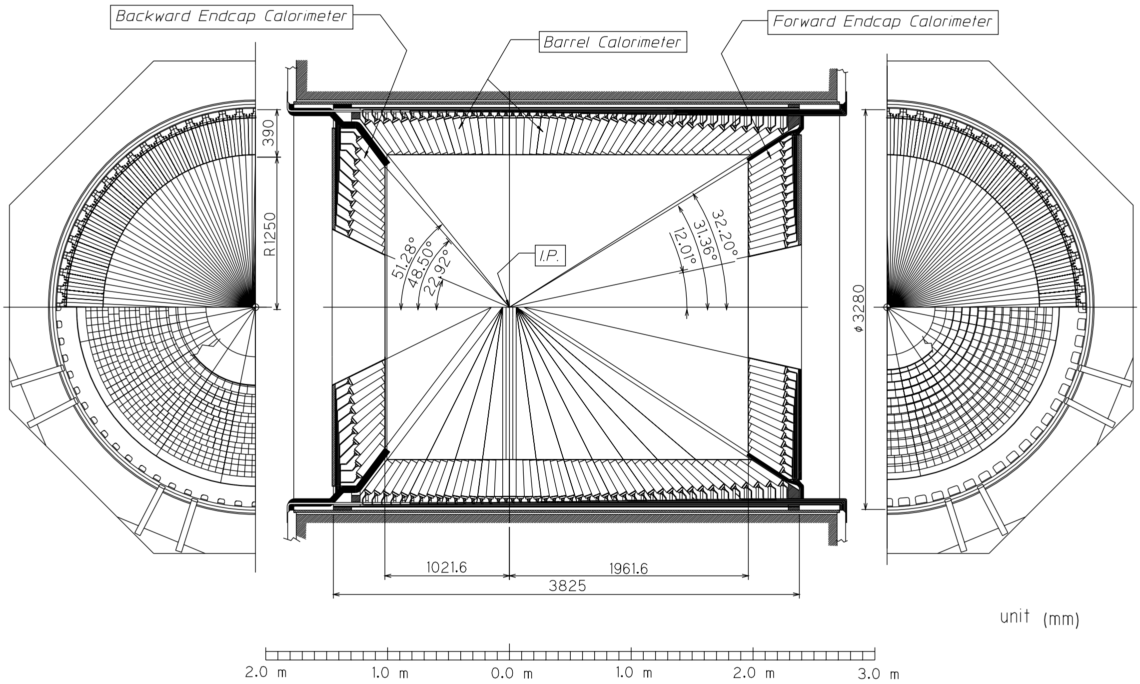

Figure 2.11: ECL layout.

2.2.5 Electromagnetic calorimetry

The electromagnetic calorimeter (ECL) is needed for measuring the energy and the position of electrons and photons. In the study of B decays, it is crucial to get photon measurements at low energies (below 500 MeV) because they ofter appear at the end of the decay chains. The high energies (up to 4 GeV) are also important because rare two-body decays like $B \to K^{*0}\gamma$ [147], $B^0 \to \pi^0\pi^0$ [148] are important milestones in B physics. In addition to the energy requirements, a good position resolution is required to identify high-energy neutral pions. The electromagnetic calorimeter is also important in combination with the hadronic calorimeter for photon and electron particle identification. It is crucial for luminosity measurements which are based on Bhabha and photo-production (Sec 2.3).

The electromagnetic calorimeter of Belle is a highly-segmented array of caesium iodide crystals doped with thallium, CsI(Tl). This material has several interesting properties like large photon yield, low hygroscopicity and mechanical stability. The ECL (Fig. 2.11) is composed of three parts: the central part or barrel (6624 crystals), the forward end-cap (1152 crystals) and the backward end-cap (960 crystals). The typical size of a crystal (cell) is 6×6 cm^2.

With time, radiation degrades the crystal transparency and the performances of the system. The barrel region receives 3 to 4 times less radiation than the end-cap regions (Fig. 2.12). In the most recent physics analyses, only the barrel region is used because of the deterioration of the data quality in the end-cap regions.

The ECL energy resolution achieved is about 2%; η and π^0 signals are shown in Fig. 2.14. ECL information, like the number of high-energy clusters, is also used by the

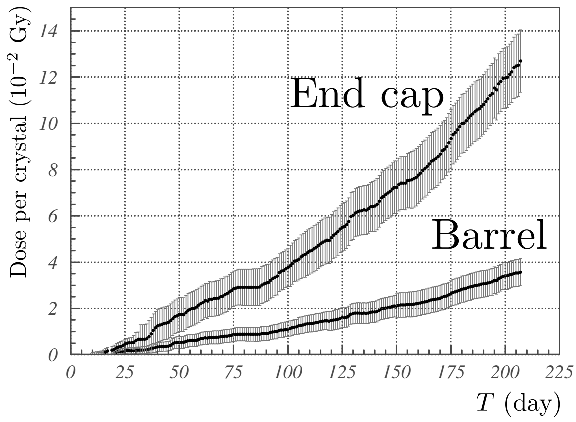

Figure 2.12: Radiation dose received by the end-cap and barrel parts of the ECL, during the first 200 days of the KEKB running.

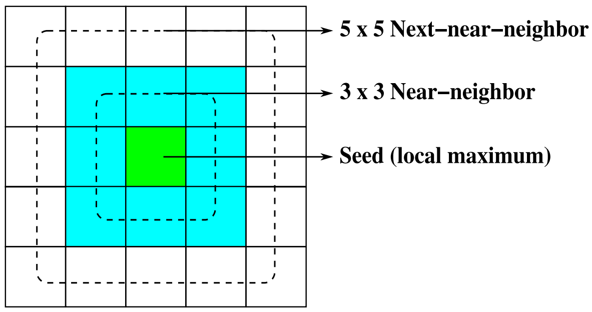

Figure 2.13: Definition of the ECL E_9/E_{25} quantity.

trigger. An important measurement used for photon and electron candidates is the ratio, E_9/E_{25}, between the energy deposited in the 3×3 crystals near the main signal and that deposited in the 5×5 crystals (Fig. 2.13).

2.2.6 Extreme-forward calorimeter

The extreme-forward calorimeter covers the small and large values of θ, from $6.4°$ to $11.5°$ and from $163.3°$ to $171.2°$. It was designed to improve the sensitivity to processes such as $B^+ \to \tau^+\nu_\tau$, and to provide tagging information for $\gamma\gamma$ physics. In addition, it provided important information for beam monitoring and luminosity measurements. This calorimeter is made with bismuth germanate (BGO, $Bi_4Ge_3O_{12}$) crystals. Each part of the detector is segmented into 160 cells (Fig. 2.15). The system is located in a harsh radiation area and wasn't used in recent analyses.

2.2.7 Solenoid and yoke

A magnetic field in the central part of the detector is required to curve the particle trajectories. The momentum of a track can be measured from its curvature. The subdetectors described above are located inside a cylindrical (3.4 m diameter $\times$ 4.4 m length) super-

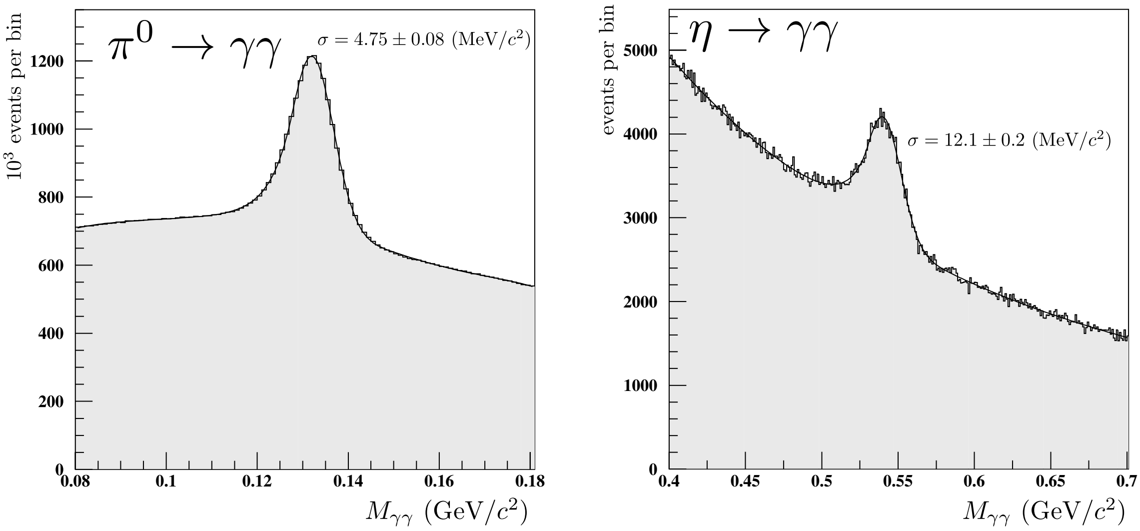

Figure 2.14: Mass distributions of photon pairs. Candidate photons are required to be in the barrel region with $E_\gamma > 30$ MeV. The π^0 and the η signals are clearing seen.

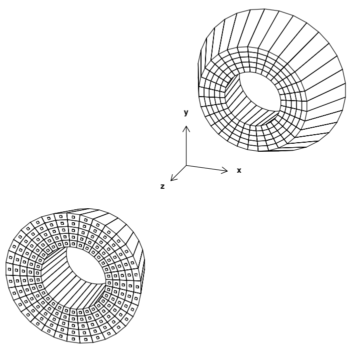

Figure 2.15: EFC isometric view.

conducting solenoid which provides a uniform magnetic field of 1.5 T. An early field map (Fig. 2.16) and calibration gave a magnetic field precision of about 0.25% as checked with the measured J/ψ mass. The 1132-ton iron yoke provides the structure of the detector, but it is designed for two other purposes: a return path for the magnetic flux and an absorber for K_L^0 and muons (see below).

2.2.8 *K*-long and muon system

Long-living neutral hadrons (such as K_L^0) and muons can only be detected in a very massive detector. This is the purpose of the K-long and muon (KLM) system located in the iron yoke.

It consists of successive layers of charged particle detectors (resistive plate counters, RPC) and iron plates (4.7 cm thick). In the central part (barrel), there are 15 layers of detectors and 14 of iron, providing approximately 3.9 interaction lengths (Fig. 2.17). The end caps are similarly instrumented. The neutral K_L^0 meson produces a hadronic

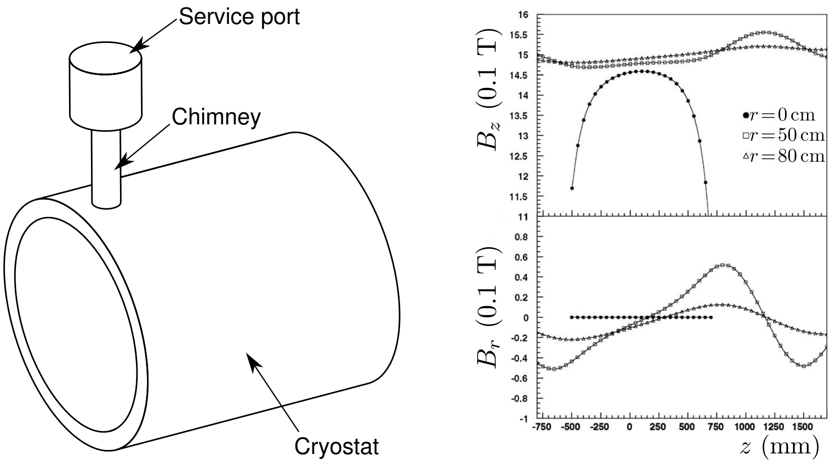

Figure 2.16: Overall view of the magnet and B field map.

shower when interacting in the iron, allowing for position detection. However, no useful measurement of its energy is possible because of the fluctuations of this shower. The muons easily go through all the detector and the hits in the RPC allow for energy and position measurements. Other charged particles, such as pions and kaons are stopped in the system and can easily be separated from muons.

The KLM information (presence of hits in the central/forward/backward regions) is sent to the trigger. The KLM provides efficient muon identification with more than 90% efficiency and less than 5% fake rate for $p_\mu > 1.5$ GeV/c. The K_L^0 detection is also performing well, with the expected rate of 0.5 per hadronic event (Fig. 2.18).

2.2.9 Trigger and data acquisition systems

An important part of the Belle experiment is the trigger and the data acquisition systems (DAQ, Fig. 2.19). Many events are not interesting for physics studies, like e^+e^- scattering (Bhabha interactions), beam-gas interactions, interactions in the beam pipe, cosmic rays, etc. The trigger is designed to ignore background as much as possible and keep inelastic e^+e^- interactions with high efficiency, within a very short decision time. The overall Belle trigger can work up to an output rate of 500 Hz.

A hardware "level 1" trigger (Fig. 2.20) has a designed latency (time to process one event) of 2.2 μs; the subdetector signals have a maximum latency of 1.85 μs in order to let 350 ns for the Global Decision Logic (GDL) to form the trigger signal. In total, the GDL receives and can combine up to 94 trigger signals. It delivers a 96-bit signal. For instance

```
(ncdr_short>2)&&(ncdr_full>0)&&e_low&&(nicl>1)&&tsc_ge1&&(!iveto35) ,
```

is a trigger signal used for the selection of hadronic events. It corresponds to at least three short and at least one long track in the CDC, at least two clusters in the ECL (one of them having more than 0.5 GeV), at least 1 hit in the TSC and no beam injection. If the event passes any of the trigger signals, all the subdetectors are read out and the selected event is sent to the event-builder farm (EFARM) and finally to the reconstruction farm (RFARM) before being saved to tape. Before $\sim$ 2007, a level-3 software trigger was rejecting events

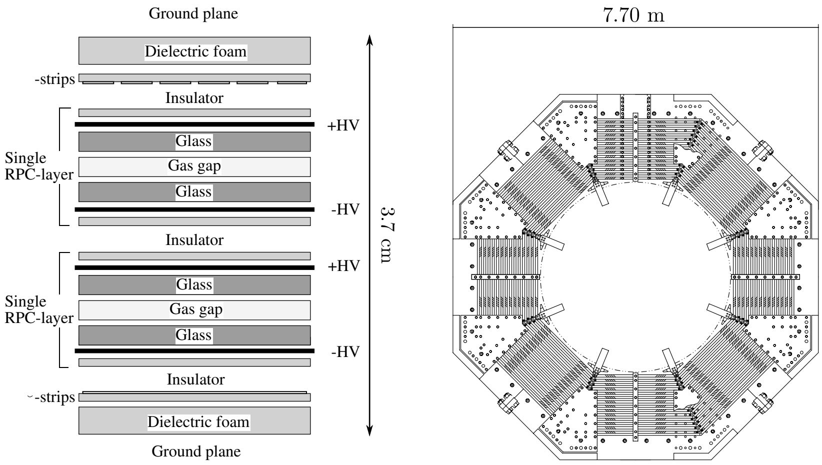

Figure 2.17: "KLM superlayer": double glass-electrode resistive plate counter module (right), situated between two iron plates of the yoke (left).

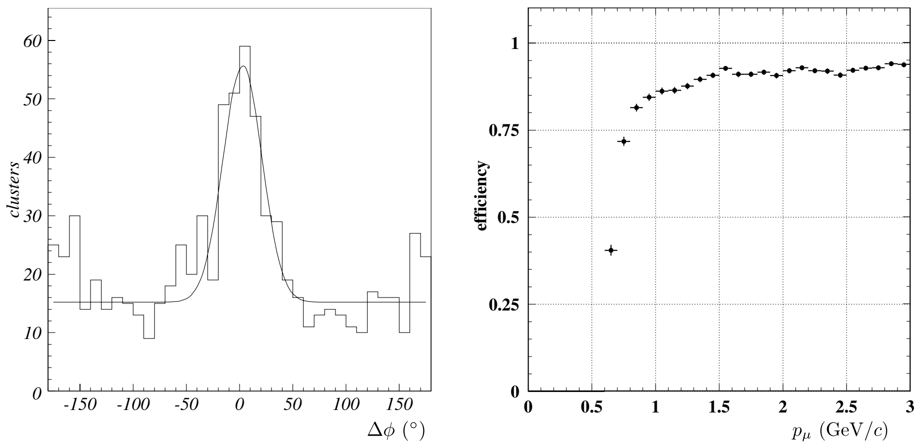

Figure 2.18: KLM performance. Left: difference in azimuthal angle between a KLM neutral cluster and the missing momentum, during a KEKB commissioning run. Right: muon detection efficiency as a function of momentum. The muon likelihood, made of SVD (if available), CDC and KLM information, is required to be larger than 0.66.

in the RFARM in order to save tape space and offline reprocessing time. This trigger was based on an ultra-fast track fitter. With the improvement of computing storages and performances, this level-3 trigger could be disabled in the last years of data taking.

Because of the continuous injection scheme, the events that are in coincidence with injection are not good for physics studies. A veto is sent by the accelerator to the trigger in order to forbid event recording at these moments (around 6 times per second).

The raw data are then reprocessed off-line and converted to physics data (4-momenta, likelihood values, etc.) to be stored on other tapes (data summary tape, DST).

At this stage, a classification is made between the different types of events. The study of B mesons are typically performed on the HadronBJ events, i.e. events passing the so-called

Table 2.2: Cross-section σ, efficiency ε, and visible cross-section $\sigma_{\text{vis}} = \sigma \times \varepsilon$, for e^+e^- processes at $\sqrt{s} = 10.58$ GeV [149]. $q\bar{q}$ events refers to light-quark production, $q = u, d, s, c$; QED refers to Bhabha scattering. The typical number of events per second is given for $L = 2 \times 10^{34}$ cm^{-2}s^{-1}. For comparison, the $b\bar{b}$ cross section at $\sqrt{s} = 10.87$ GeV is $\sigma = 0.3$ nb.

	$b\bar{b}$	$q\bar{q}$	$\tau^+\tau^-$	QED	$\gamma\gamma$	Beam-gas
σ (nb)	1.1	3.3	0.93	37.8	11.1	—
ε (%)	99.1	79.5	4.9	0.002	0.4	—
σ_{vis} (nb)	1.09	2.62	0.05	0.001	0.04	0.11
typical rate (Hz)	21.8	52.4	1.0	0.02	0.8	2.2

HadronB requirement or the J/ψ selections. These events are recorded on the mini-DST (mdst) which are read for physics analysis. In Table 2.2, the trigger efficiency for various e^+e^- processes is reported. At $\Upsilon(4S)$ energy, there are, each second, an average of 22 $e^+e^- \to b\bar{b}$ events recorded on tape together with 52 $e^+e^- \to q\bar{q}$ ($q = u, d, s, c$) continuum events. The latter are discriminated in the selection with the R_2 variable (see below). At the $\Upsilon(5S)$ energy, the $b\bar{b}$ events are about three times less frequent than at the $\Upsilon(4S)$ resonance.

Data samples are further reduced for specific purposes with tighter skimming criterias. Only the location of the qualified events are saved into index files. This procedure largely reduces the amount of data to be analysed. For instance, in Sec. 3.4, the index file for preselected dilepton events is used.

2.3 The Belle data set

The main Belle data used in this work are the collisions recorded at the $\Upsilon(5S)$ energy (Table 2.3). The whole $121\ \text{fb}^{-1}$ are used for the dilepton results presented in Chapter 3, while only the first $23.4\ \text{fb}^{-1}$ are used for the results of Chapter 4. A subset of so-called continuum data (Table 2.4), recorded at $60\ \text{MeV}$ below the $\Upsilon(4S)$ energy, was used for background subtraction in Chapter 3. The luminosity of these datasets is measured [150] with the processes $e^+e^- \to \gamma\gamma$ and $e^+e^- \to e^+e^-$ (Bhabha scattering), for which the ECL performances are crucial.

2.3.1 Determination of the centre-of-mass energy

As explained in Chapter 4, the B_s^0 and B_s^* masses can be determined with exclusive fully-reconstructed B_s^0 decays. The CM energy must be known, together with its uncertainy, to provide a correct measurement of the B_s^* mass.

The CM energy is determined with fully-reconstructed $\Upsilon(5S) \to \Upsilon(1S)(\to \mu^+\mu^-)\pi^+\pi^-$

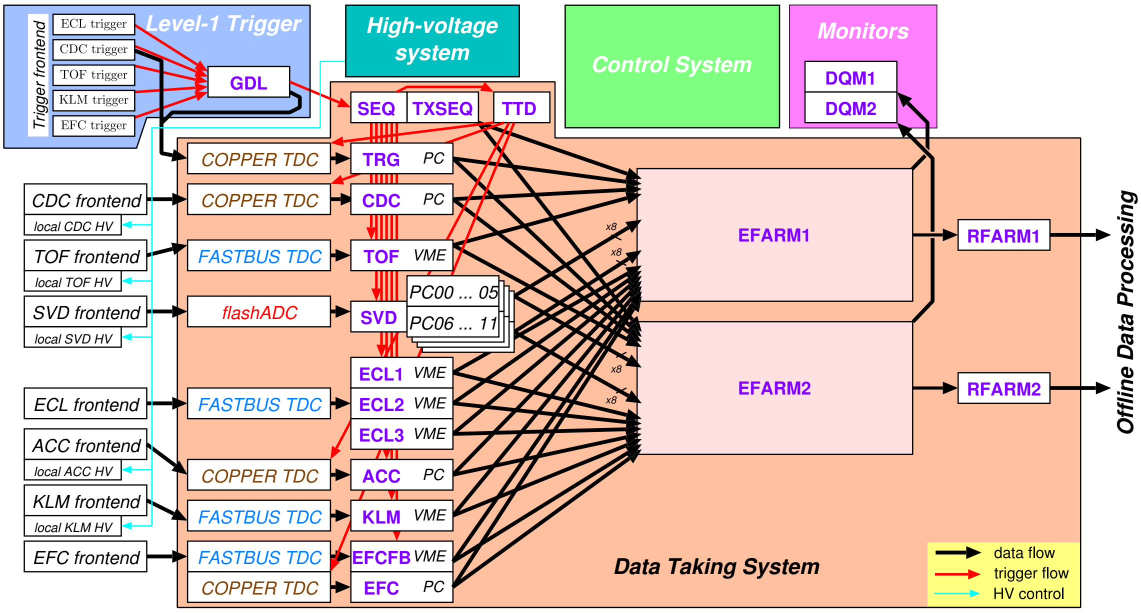

Figure 2.19: Block diagram of the online DAQ system.

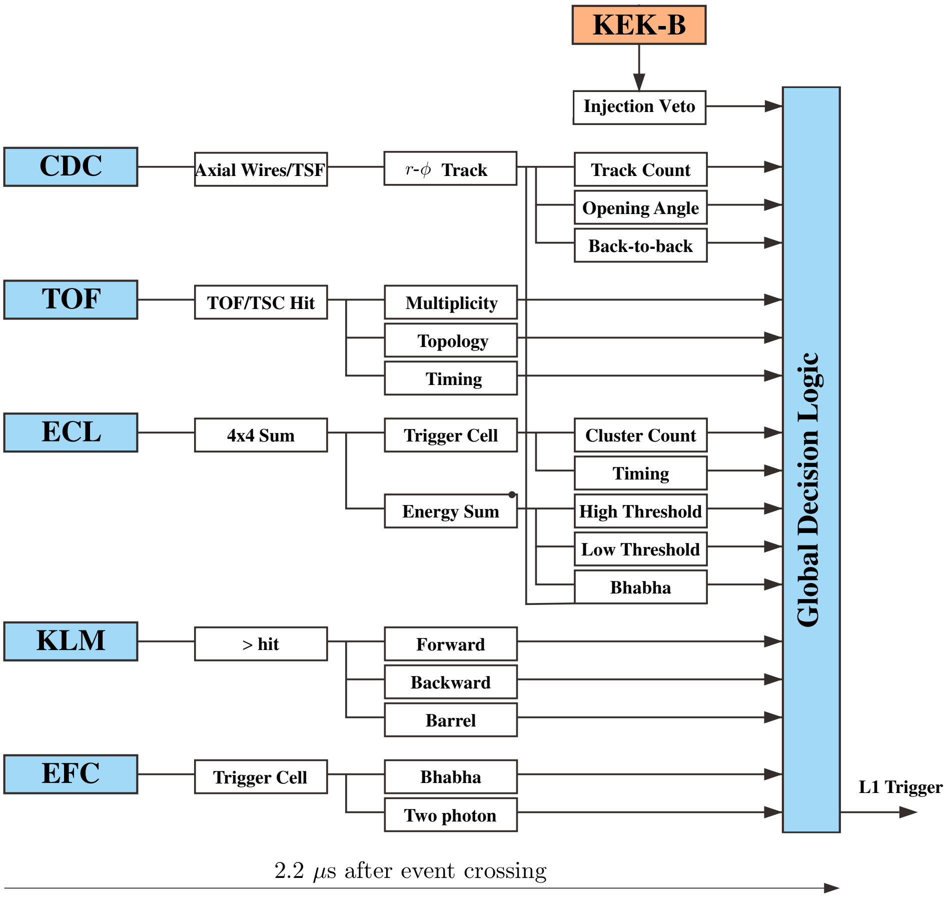

Figure 2.20: Belle level-1 trigger scheme.

Table 2.3: $\Upsilon(5S)$ data samples. The reduced $23.4\ \text{fb}^{-1}$ sample corresponds to the first two lines. Each Belle data-taking period is called an "experiment" and receives a unique integer number (increasing with time). An odd (even) number indicates a physics (calibration) experiment.

Date	Experiment	Run range(s)	L_{int} (fb^{-1})
June 2005	43	1013 – 1034	1.857
June 2006	53	1 – 272	21.513
Oct.-Dec. 2008	67	98 – 696	27.222
Apr.-June 2009	69	12 – 819, 892 – 1309	47.830
Oct.-Dec. 2009	71	27 – 221, 2001 – 2185, 2194 – 2244	22.938
	Total		**121.36 fb^{-1}**

Table 2.4: Continuum data samples used in Chapter 3.

Date	Exp.	Run range(s)	L_{int} (fb^{-1})
Spring 2005	43	559 – 604, 924 – 972	6.448
Autumn 2005	45	383 – 421	2.295
Autumn 2005	47	550 – 622	3.413
Winter 2006	49	553 – 706	2.567
Spring 2006	51	1312 – 1395, 1778 – 1805	4.878
Autumn 2006	55	793 – 853, 1579 – 1677	7.665
Autumn 2007	61	668 – 739	2.466
Spring 2008	63	618 – 679	5.212
Spring 2008	65	626 – 687	4.374
Autumn 2008	67	698 – 742	3.206
Spring 2009	69	823 – 887, 1311 – 1397	4.874
Autumn 2009	71	2249 – 2292	1.022
	Total		**48.420 fb^{-1}**

events [151, 152], by measuring the quantity $\Delta m = m_{\mu\mu\pi\pi} - m_{\mu\mu}$. Assuming[3] $m_{\mu\mu\pi\pi} = \sqrt{s}$, the CM energy is estimated as $\sqrt{s} = \Delta m + m_{\Upsilon(1S)}$ where $m_{\Upsilon(1S)}$ is the nominal $\Upsilon(1S)$ mass [37].

Δm is first measured in MC data, where $\sqrt{s}$ and the $\Upsilon(1S)$ mass are known without

[3] The radiative corrections, if any, are assumed to be the same for $\Upsilon(1S)$ and B_s^0 productions.

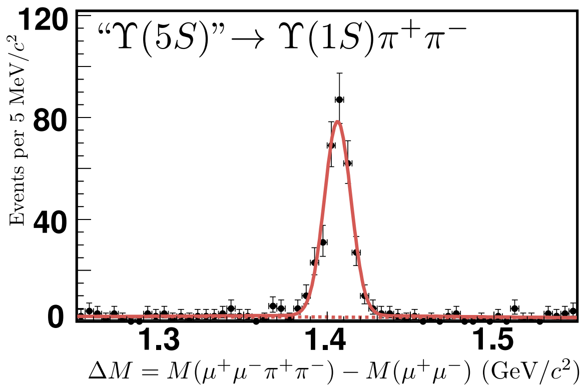

Figure 2.21: (Reproduced from Ref. [151]) $\Delta m = m_{\mu^+\mu^-\pi^+\pi^-} - m_{\mu^+\mu^-}$ distribution of $\Upsilon(5S) \to \Upsilon(1S)\pi^+\pi^-$ candidates selected in a $21.5\ \mathrm{fb}^{-1}$ $\Upsilon(5S)$ dataset (Experiment 53).

uncertainties; the central value of $m_{\mu\mu} = \sqrt{s} - \Delta m = 9460.5 \pm 0.1\ \mathrm{MeV}/c^2$ is $0.2 \pm 0.1\ \mathrm{MeV}/c^2$ larger than expected. In other terms, the CM energy measured with $\Delta m + m^{\mathrm{MC}}_{\Upsilon(1S)} = 10868.2 \pm 0.1\ \mathrm{MeV}/c^2$ is $0.2 \pm 0.1\ \mathrm{MeV}/c^2$ lower than the CM energy input value, 10.8684 GeV. A correction of $\delta = 0.2 \pm 0.1\ \mathrm{MeV}/c^2$ should be *added* to the result for the CM energy.

In $21.5\ \mathrm{fb}^{-1}$ of data (Experiment 53), representing 92% of the data used in Chapter 4, $\Delta m = 1406.5 \pm 0.5\ \mathrm{MeV}/c^2$ is measured (Fig. 2.21). Then, the corresponding CM energy is $\sqrt{s} = \Delta m + m^{\mathrm{PDG}}_{\Upsilon(1S)} + \delta = 10867.0 \pm 0.6\ \mathrm{MeV}$. The $0.6\ \mathrm{MeV}$ uncertainty is rounded to $1.0\ \mathrm{MeV}$ in order to include other possible systematics (e.g. momentum calibration: $\sim 0.2\ \mathrm{MeV}$). The final value is then

$$\sqrt{s} = 10867.0 \pm 1.0\ \mathrm{MeV}\,, \tag{2.1}$$

which can be compared with the official estimates obtained from the KEKB machine parameters, 10.869 GeV (Experiment 43, $1.86\ \mathrm{fb}^{-1}$) and 10.871 GeV (Experiment 53, $21.5\ \mathrm{fb}^{-1}$).

2.3.2 Continuum event rejection

At the $\Upsilon(5S)$ energy, for each interesting $e^+e^- \to b\bar{b}$ event, nine non-interesting continuum $e^+e^- \to q\bar{q}$ events ($q = u, d, s, c$) are recorded (Table 2.2). In the light-quark production process, a lot of energy is carried by the produced quarks. Because of momentum conservation, the quarks are traveling back-to-back in the centre-of-mass frame, forming two jets. In contrast, when a pair of B mesons is produced, most of the energy is converted into mass, and the products have small momenta. These events have a spherical shape.

The second Fox-Wolfram moment, $R_2 = H_2/H_0$ [153], is an observable that quantifies the event "jettiness" (Fig. 2.22). By setting a maximum value of R_2, most of the continuum events can be removed while keeping a maximum of $b\bar{b}$ events.

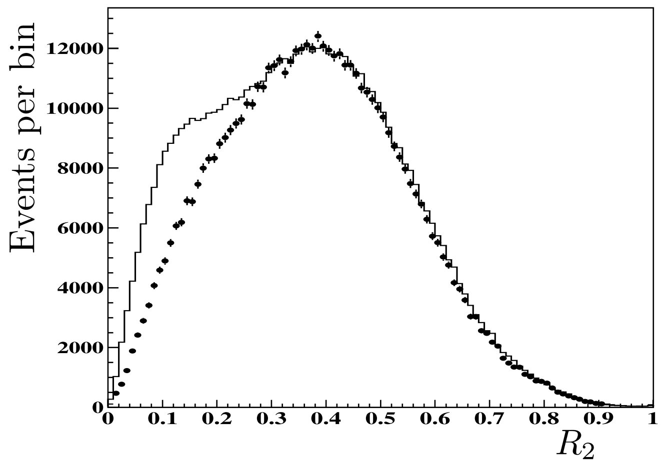

Figure 2.22: Distribution of the R_2 variable in $\Upsilon(5S)$ data (histogram) and in data below the open-beauty threshold (points) scaled to account for luminosity and energy differences (See Eq. (3.70) in next chapter). The event excess at low values is due to $e^+e^- \to B_{(s)}\bar{B}_{(s)}$ events.

2.3.3 Particle identification

Detected particles have to be correctly identified. Most of charged tracks are either protons, kaons, pions, muons or electons. Likelihood quantities are formed in order to discriminate between these five choices. The charged tracks have all some vertex requirements: they must have an impact parameter with respect to the interation point smaller than 0.5 cm in the radial direction (δr) and smaller than 3 cm in the beam axis direction (δz).

For distinguishing kaons from pions, a likelihood ratio,

$$\mathcal{R}_{K/\pi} = \frac{\mathcal{L}_K}{\mathcal{L}_K + \mathcal{L}_\pi}\,, \tag{2.2}$$

is computed with information coming from the ACC, TOF and CDC (dE/dx measurement) sub-detectors [154] where $\mathcal{L}_K$ ($\mathcal{L}_\pi$) is the likelihood for the kaon (pion) hypothesis. The limit is set at 0.6, i.e. a track with $\mathcal{R}_{K/\pi} < (>) 0.6$ is identified as a pion (kaon). The typical identification efficiencies of pions and kaons are above 80%, while the fake rate are below 10% [154].

For electrons and muons, electronic likelihoods $\mathcal{L}_e$ and $\mathcal{L}_\mu$ are formed and tracks with $\mathcal{L}_e(\mathcal{L}_\mu) > 0.8$ are identified as electrons (muons). The electrons are identified with charged tracks with matching ECL showers [155]. The muons are identified with charged tracks that have matching hits in the KLM [156].

Tables of efficiencies and fake rates are available for systematic uncertainties estimations [157–159]. The efficiency uncertainty of kaon indentification is 1.43% and 1.72% for pion.

The only detected neutral particles used in this work are the photons. Photon candidates are indentified from ECL showers with $E_\gamma > 50$ MeV, $E_9/E_{25} > 0.85$ and $17° < \theta_\gamma < 150°$ [160]. Tables for systematics uncertainties associated with photons are available [161]. Neutral pions are reconstructed from two photons, and contrained to have an invariant mass equal to the nominal π^0 mass (under an assumption for the π^0 production and decay point). The identification systematics uncertainties is detailed in Ref. [162]

2.4 Summary

The KEKB accelerator and the Belle detector are research instruments dedicated to the production and the detection of B mesons. Their performances are designed for precise studies of CP-violation in B decays. An increase of the centre-of-mass energy allowed for B_s^0 production, while the operation and trigger remained unchanged. The experience gained with the standard data at $\Upsilon(4S)$ could be used directly for the pioneering $\Upsilon(5S)$ runs.

Chapter 3

B_s^0 production at the $\Upsilon(5S)$

Because the $\Upsilon(5S)$ mass is substantially larger than the $B\bar{B}$ threshold, the production of bottom mesons at the $\Upsilon(5S)$ resonance is more complex than at the $\Upsilon(4S)$ resonance. In particular three different species of bottom mesons can be produced: B^+, B^0 and B_s^0. An important motivation to study B_s^0 production at the $\Upsilon(5S)$ is the possibility to determine the number of B_s^0 mesons present in the data sample, $N_{B_s^0}$, such as to enable the measurement of B_s^0 branching fractions: from the number of reconstructed B_s^0 events in a given channel, $N_{\rm rec}$, and the total efficiency, ε, the branching fraction can be obtained with the relation

$$\mathcal{B} = \frac{1}{N_{B_s^0}} \times \frac{N_{rec}}{\varepsilon} \,. \tag{3.1}$$

The study of B_s^0 production at the $\Upsilon(5S)$ is also interesting on its own right and is part of a much broader task: identifying and measuring all the $\Upsilon(5S)$ decay modes.

In this chapter, we review the existing measurements of the $\Upsilon(5S)$ branching fractions and combine all the available information to extract the best possible estimate of the fraction of B_s^0 events in $\Upsilon(5S)$ decays. Ideas for new measurements of this fraction are then presented. The one that appeared to be the most promising is then deployed as an analysis of the full $\Upsilon(5S)$ data sample, resulting in a new measurement.

3.1 Overview of e^+e^- collisions at the $\Upsilon(5S)$ energy

3.1.1 *b*-quark production

The heavy flavour quarks can be produced in electron-positron annihilation. They are always produced by pair of a quark and its antiquark (conservation of quark flavours by the strong interaction). At low energy, this pair can appear as a bound state, called quarkonium. Non-relativistic QCD describes well this type of systems. Charmoniun ($c\bar{c}$) and bottomonium ($b\bar{b}$) states have been extensively studied [163].

The Feynman diagram governing the creation of a pair of bottom mesons (B^+B^-, $B^0\bar{B}^0$, $B_s^0\bar{B}_s^0$, etc.) is presented in Fig. 3.1. At a centre-of-mass energy much below the Z^0 mass, the e^+e^- annihilation and the subsequent hadronisation of the $q\bar{q}$ pair are governed by the electromagnetic and strong interactions which conserve both parity and charge

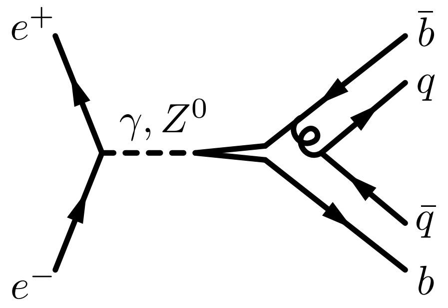

Figure 3.1: Leading-order Feynman diagram of an e^+e^- annihilation producing a bottom meson pair though a $b\bar{b}$ (Υ) resonance. At the $\Upsilon(4S)$ ($\Upsilon(5S)$) energy, q can be a u or d (u, d or s) quark. At energies much below the Z^0 mass, the virtual particle is dominantly a photon.

conjugation. The final state is a coherent quantum state with defined $C = C(\gamma) = -1$ and $P = P(\gamma) = -1$ eigenvalues.

To produce bottom mesons the minimum centre-of-mass energy of the collision must be larger than the open-beauty threshold[1], i.e.

$$\sqrt{s} > 2\, m_B\, c^2 \sim 10.56 \text{ GeV} \tag{3.2}$$

for creating B^+ and B^0 mesons, and

$$\sqrt{s} > 2\, m_{B_s^0}\, c^2 \sim 10.73 \text{ GeV} \tag{3.3}$$

for producing B_s^0 mesons in addition to B^+ and B^0 mesons.

In order to produce bottom mesons with maximum efficiency, it is better to run at a centre-of-mass energy where the process $e^+e^- \to b\bar{b}$ has a large cross section. The measurement reported on Fig. 3.2 show three distinct Υ resonances: $\Upsilon(4S)$, $\Upsilon(5S)$ and $\Upsilon(6S)$. The first resonance above the $B_s^0\bar{B}_s^0$ energy threshold is the $\Upsilon(5S)$.

The mass of the $\Upsilon(4S)$ resonance is remarkably convenient for the study of B mesons. It lies just above the $B\bar{B}$ threshold, but is too small to produce excited B^* mesons, or an extra particle. B meson pairs produced at the $\Upsilon(4S)$ mass are C-odd coherent B^+B^- and $B^0\bar{B}^0$ states. The B factories have been built to take advantage of this unique situation.

In contrast, the situation is more complex at the $\Upsilon(5S)$ resonance, but this is the price to pay to get B_s^0 mesons: its production cross-section is three times smaller and excited B^* and B_s^* states are also present. The collision can produce several types of $B_{(s)}$ pairs and up to two additional pions can also be produced in association with a $B\bar{B}$ pair. The types of events involving bottom meson pairs at the $\Upsilon(5S)$ energy are shown in Fig. 3.3, where their corresponding fractions are defined. The excited $B_{(s)}^*$ mesons decay electromagnetically to their ground state via the process $B_{(s)}^* \to B_{(s)}\gamma$.

The $b\bar{b}$ production cross-section[2], $\sigma(e^+e^- \to \Upsilon(5S))$, has been measured by subtracting the $e^+e^- \to q\bar{q}$ ($q = u, d, s, c$) component obtained just below the $\Upsilon(4S)$ resonance. With

[1]The notation B refers to the B^+ or B^0 mesons.

[2]Throughout this thesis, the notation $\Upsilon(5S)$ is used also for all the $b\bar{b}$ pair at $\Upsilon(5S)$ energy, including the non-resonant $b\bar{b}$ pairs.

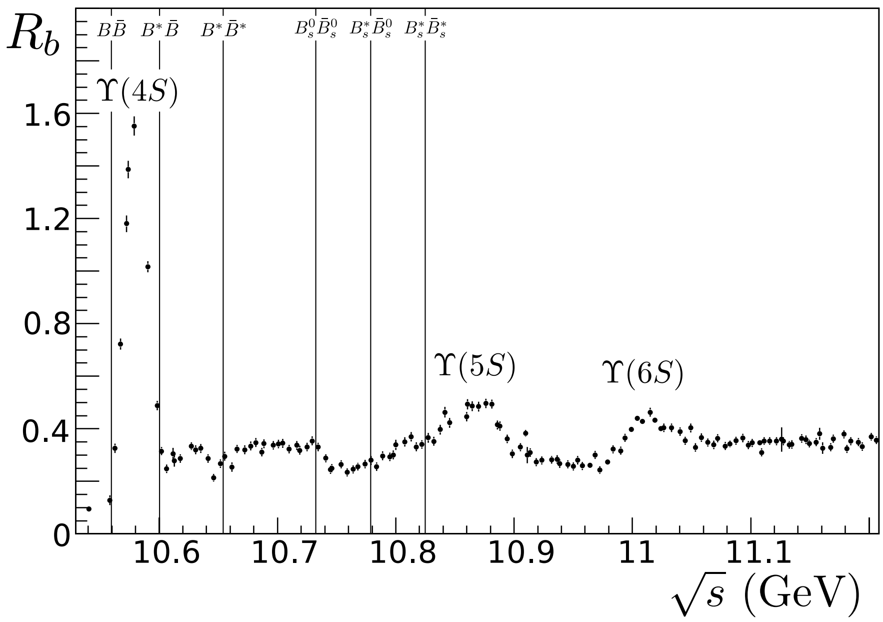

Figure 3.2: Energy scan in the $\Upsilon(4S) - \Upsilon(6S)$ region by Babar [164]. The normalised b-hadron cross-section, $R_b = \sigma(e^+e^- \to b\text{-hadrons})/\sigma(e^+e^- \to \mu^+\mu^-)$, is plotted against the centre-of-mass energy. Vertical lines shows the $B\bar{B}$, $B^*\bar{B}$, $B^*\bar{B}^*$, $B_s^0\bar{B}_s^0$, $B_s^*\bar{B}_s^0$ and $B_s^*\bar{B}_s^*$ energy thresholds, from left to right. In this energy range, $\sigma(e^+e^- \to \mu^+\mu^-) = \frac{4\pi\alpha^2}{3s}(\hbar c)^2 \approx 0.75$ nb.

$0.42\ \text{fb}^{-1}$, the CLEO collaboration reported [165]

$$\sigma(e^+e^- \to \Upsilon(5S)) = 0.301 \pm 0.039\ \text{nb}\,, \tag{3.4}$$

while the Belle measurement, with $1.86\ \text{fb}^{-1}$, is [3]

$$\sigma(e^+e^- \to \Upsilon(5S)) = 0.302 \pm 0.015\ \text{nb}\,. \tag{3.5}$$

The weighted average of these two measurements is chosen for our numerical calculations:

$$\sigma(e^+e^- \to \Upsilon(5S)) = 0.302 \pm 0.014\ \text{nb}\,. \tag{3.6}$$

3.1.2 Composition of the $\Upsilon(5S)$ events

The $\Upsilon(5S)$ events are divided into three categories:

1. events containing two strange bottom mesons, whose fraction is defined as

$$f_s = \frac{\sigma(e^+e^- \to B_s^{(*)}\bar{B}_s^{(*)})}{\sigma(e^+e^- \to \Upsilon(5S))}\,; \tag{3.7}$$

2. events containing two non-strange bottom mesons, whose fraction is defined as

$$f_{u,d} = \frac{\sigma(e^+e^- \to B^{(*)}\bar{B}^{(*)}(X))}{\sigma(e^+e^- \to \Upsilon(5S))}\,; \tag{3.8}$$

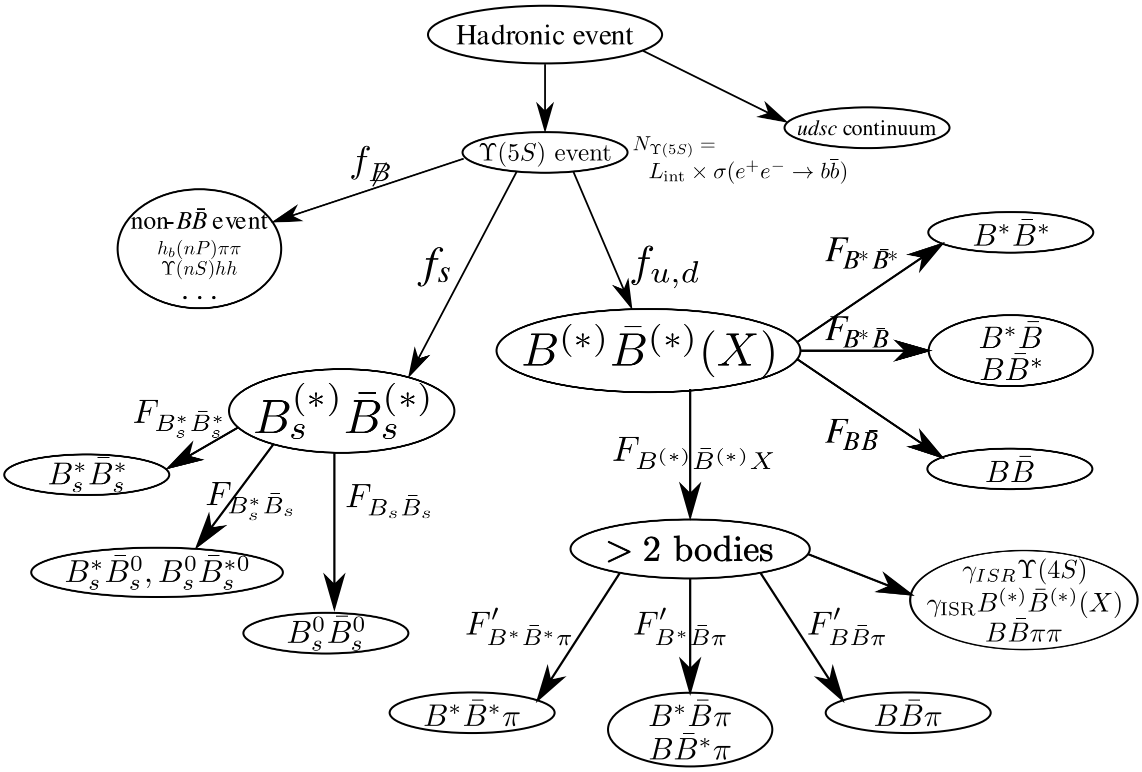

Figure 3.3: Classification of hadronic events produced in e^+e^- collisions at the $\Upsilon(5S)$ energy. The arrow labels define the fractions inside the categories. The subdivision of the non-strange B meson categories are driven by the experimental method to measure these fractions.

3. events containing no bottom meson, whose fraction is defined as

$$f_{\not B} = \frac{\sigma(e^+e^- \to \text{non-}B_{(s)}\bar{B}_{(s)})}{\sigma(e^+e^- \to \Upsilon(5S))} \,. \tag{3.9}$$

By definition, the sum of the three fraction equals unity,

$$f_s + f_{u,d} + f_{\not B} = 1 \,. \tag{3.10}$$

Three hadronisation modes with B_s^0 pairs are kinematically allowed[3], $\Upsilon(5S) \to B_s^0\bar{B}_s^0$, $\Upsilon(5S) \to B_s^*\bar{B}_s^0$ and $\Upsilon(5S) \to B_s^*\bar{B}_s^*$. As will be shown in Sec. 4.4.1, our study of $B_s^0 \to D_s^-\pi^+$ events provides measurements of the relative abundance of these modes:

$$F_{B_s^*\bar{B}_s^*} = \frac{\sigma(e^+e^- \to B_s^*\bar{B}_s^*)}{\sigma(e^+e^- \to B_s^{(*)}\bar{B}_s^{(*)})} = (90.1 \pm 3.9)\% \,, \tag{3.11}$$

$$F_{B_s^*\bar{B}_s^0} = \frac{\sigma(e^+e^- \to B_s^*\bar{B}_s^0)}{\sigma(e^+e^- \to B_s^{(*)}\bar{B}_s^{(*)})} = (7.3 \pm 3.2)\% \,, \tag{3.12}$$

$$F_{B_s^0\bar{B}_s^0} = 1 - F_{B_s^*\bar{B}_s^*} - F_{B_s^*\bar{B}_s^0} = (2.6 \pm 2.6)\% \,. \tag{3.13}$$

[3]Throughout this thesis, the notation $B_{(s)}^*\bar{B}_{(s)}$ refers to the two $B_{(s)}^*\bar{B}_{(s)}$ and $B_{(s)}\bar{B}_{(s)}^*$ states.

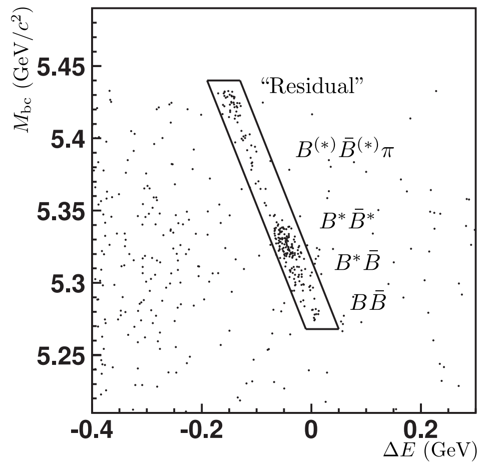

Figure 3.4: Scatter plot [166] of the beam-constrained mass $M_{\rm bc}$ and energy difference ΔE (defined later in Sec. 4.1) of $B^+ \to J/\psi K^+$ candidates in $23.4\,\mathrm{fb}^{-1}$ of $\Upsilon(5S)$ data, showing the signal region and its subregions.

This shows that most of the B_s^0 mesons are produced by the decay chain $\Upsilon(5S) \to B_s^*\bar{B}_s^*, B_s^* \to B_s^0\gamma$.

The $\Upsilon(5S)$ events can also contain a non-strange $B\bar{B}$ pair. Because of the significant energy release ($\sqrt{s} - 2\,m_B\,c^2 \approx 290$ MeV), excited B^* mesons can appear, as well as three- or four-body modes [167], as detailed in Fig. 3.4. The composition of these non-strange B meson events has been measured as follows by Belle [166]:

$$B^*\bar{B}^* \qquad \frac{\sigma(e^+e^- \to B^*\bar{B}^*)}{\sigma(e^+e^- \to \Upsilon(5S))} = f_{u,d} \times F_{B^*\bar{B}^*} = (37.5 \pm 3.6)\%\,, \tag{3.14}$$

$$B^*\bar{B} \qquad \frac{\sigma(e^+e^- \to B^*\bar{B})}{\sigma(e^+e^- \to \Upsilon(5S))} = f_{u,d} \times F_{B^*\bar{B}} = (13.7 \pm 1.7)\%\,, \tag{3.15}$$

$$B\bar{B} \qquad \frac{\sigma(e^+e^- \to B\bar{B})}{\sigma(e^+e^- \to \Upsilon(5S))} = f_{u,d} \times F_{B\bar{B}} = (5.5 \pm 1.0)\%\,, \tag{3.16}$$

$$B^{(*)}\bar{B}^{(*)}X \qquad \frac{\sigma(e^+e^- \to B^{(*)}\bar{B}^{(*)}X)}{\sigma(e^+e^- \to \Upsilon(5S))} = f_{u,d} \times F_{B^{(*)}\bar{B}^{(*)}X} = (17.5 \pm 2.1)\%\,, \tag{3.17}$$

$$B^*\bar{B}^*\pi \qquad \frac{\sigma(e^+e^- \to B^*\bar{B}^*\pi)}{\sigma(e^+e^- \to B^{(*)}\bar{B}^{(*)}X)} = F'_{B^*\bar{B}^*\pi} = (5.9 \pm 7.5)\%\,, \tag{3.18}$$

$$B^*\bar{B}\pi \qquad \frac{\sigma(e^+e^- \to B^*\bar{B}\pi)}{\sigma(e^+e^- \to B^{(*)}\bar{B}^{(*)}X)} = F'_{B^*\bar{B}\pi} = (41.6 \pm 11.8)\%\,, \tag{3.19}$$

$$B\bar{B}\pi \qquad \frac{\sigma(e^+e^- \to B\bar{B}\pi)}{\sigma(e^+e^- \to B^{(*)}\bar{B}^{(*)}X)} = F'_{B\bar{B}\pi} = (0.2 \pm 6.7)\%\,, \tag{3.20}$$

$$\text{residual} \qquad 1 - F'_{B^*\bar{B}^*\pi} - F'_{B^*\bar{B}\pi} - F'_{B\bar{B}\pi} = (52.3 \pm 15.5)\%\,. \tag{3.21}$$

About half of the events with more than two bodies are not three-body events. This surprisingly large fraction is interpreted as initial state radiation producing a $B\bar{B}$ pair at a lower centre-of-mass energy. The decay $e^+e^- \to B\bar{B}\pi\pi$ is also allowed, but the phase space ($\sim$ 37 MeV) is too small to give such a large fraction. In the following, we will

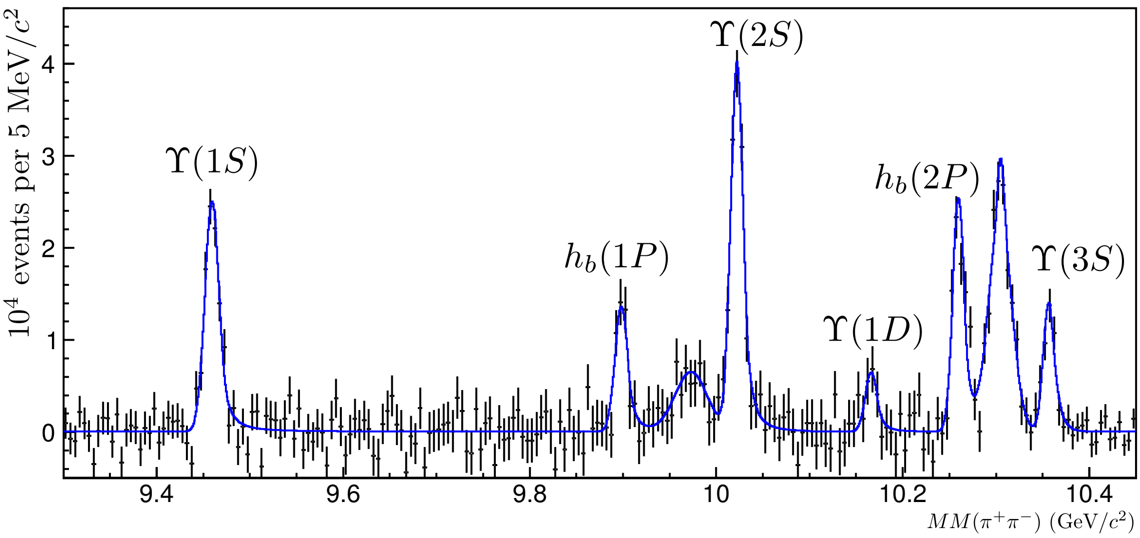

Figure 3.5: Background-subtracted experimental spectrum [172] of the missing mass in dipion events, $MM(\pi^+\pi^-) = \sqrt{\left(\sqrt{s} - E^*_{\pi^+\pi^-}\right)^2 - \vec{p}^{*2}_{\pi^+\pi^-}}$, at the $\Upsilon(5S)$ resonance, with a fit including known bottomonium resonances. Several of them, interpreted as being produced by $\Upsilon(5S) \to (b\bar{b})\pi^+\pi^-$ decays, are observed. The two unlabelled peaks near 9.98 and 10.32 GeV/c^2 correspond to the $\Upsilon(nS) \to \Upsilon(1S)\pi^+\pi^-$ ($n = 2, 3$) decays. The $\Upsilon(5S) \to \Upsilon(1D)\pi^+\pi^-$ signal, which has a statistical significance of only 2.4σ, is not included in our calculation of $f_{\not{B}}^{\min}$.

assume that the B^+ and B^0 mesons are produced in equal numbers[4], like at the $\Upsilon(4S)$ energy [12].

Finally, $b\bar{b}$ events can contain a bottomonium resonance below the open-beauty threshold. The fraction of these events without B meson, $f_{\not{B}}$, is expected to represent only a few percents and was often ignored in previous work[5]. Some of them, the $\Upsilon(5S) \to \Upsilon(nS)\pi^+\pi^-$ ($n = 1, 2, 3$) [151], $\Upsilon(5S) \to \Upsilon(1S)K^+K^-$ [151], and $\Upsilon(5S) \to h_b(nP)\pi^+\pi^-$ ($n = 1, 2$) [172] decays, have been observed by Belle (Fig. 3.5), from which the following

[4]However this assumption could be challenged in presence of an exotic resonance. For instance, a tetraquark component can enhance the $B^0\bar{B}^0$ pairs by a factor $\sigma(B^+B^-)/\sigma(B^0\bar{B}^0) \approx 0.8 \pm 0.1$. Indeed Ref. [168] reports $\sigma(B^+B^-)/\sigma(B^0\bar{B}^0) \approx 1 - 0.2/(\kappa^2 + 0.27)$ with $\kappa = 0.87 \pm 0.13$ [169]. See also Refs. [170, 171] for predictions from the tetraquark hypothesis.

[5]In $\Upsilon(4S)$ decays, they represent less than 4% (at 95% C.L.) [173] and the observed decays add up to ess than 0.03% [37].

branching fractions were extracted:

$$\mathcal{B}(\Upsilon(5S) \to \Upsilon(1S)\pi^+\pi^-) = (5.3 \pm 0.6) \times 10^{-3}\,, \tag{3.22}$$
$$\mathcal{B}(\Upsilon(5S) \to \Upsilon(2S)\pi^+\pi^-) = (7.6 \pm 1.2) \times 10^{-3}\,, \tag{3.23}$$
$$\mathcal{B}(\Upsilon(5S) \to \Upsilon(3S)\pi^+\pi^-) = (4.8 \pm 1.8) \times 10^{-3}\,, \tag{3.24}$$
$$\mathcal{B}(\Upsilon(5S) \to \Upsilon(1S)K^+K^-) = (6.1 \pm 1.8) \times 10^{-4}\,, \tag{3.25}$$
$$\frac{\mathcal{B}(\Upsilon(5S) \to h_b(1P)\pi^+\pi^-)}{\mathcal{B}(\Upsilon(5S) \to \Upsilon(2S)\pi^+\pi^-)} = 0.407 \pm 0.100\,, \tag{3.26}$$
$$\frac{\mathcal{B}(\Upsilon(5S) \to h_b(2P)\pi^+\pi^-)}{\mathcal{B}(\Upsilon(5S) \to \Upsilon(2S)\pi^+\pi^-)} = 0.78 \pm 0.19\,. \tag{3.27}$$

Summing these measured branching fractions, and adding also the contribution of similar decays but with pairs of neutral pions and kaons estimated from isospin invariance[6], yields[7]

$$\mathcal{B}(\Upsilon(5S) \to \Upsilon(nS)hh) = (2.8 \pm 0.3)\%\ , \ \text{for } n = 1, 2, 3,\ h = \pi, K\,, \tag{3.28}$$
$$\mathcal{B}(\Upsilon(5S) \to h_b(nP)\pi\pi) = (1.4 \pm 0.6)\%\ , \ \text{for } n = 1, 2\,, \tag{3.29}$$

with a grand total (taking into account correlated errors) of

$$\mathcal{B}^{\text{obs}}(\Upsilon(5S) \to (b\bar{b})hh) = f_{\not{B}}^{\text{min}} = (4.13 \pm 0.55)\% \tag{3.30}$$

for all observed decays involving a $b\bar{b}$ resonance below the open-beauty threshold. We take this as our lower limit for the fraction of bottomonium events at the $\Upsilon(5S)$, $f_{\not{B}}$.

3.2 Existing measurements of f_s and $f_{u,d}$

Several measurements of f_s and $f_{u,d}$ have been published. Most of them assumed no bottomonium production, i.e. $f_{\not{B}} = 0$. We average them at the end of this section without this assumption.

3.2.1 Measurements of $f_{u,d}$ with fully reconstructed B^0 and B^+ decays

$f_{u,d}$ can be measured by reconstructing B^0 and B^+ decay modes with reasonably large and well-known branching fractions, and assuming the numbers of charged and neutral non-strange B mesons to be equal. The CLEO collaboration applied this method on 0.42 fb^{-1} of $\Upsilon(5S)$ data and obtained [165, 174]

$$f_{u,d}^{(\text{CLEO})} = (58.9 \pm 10.0 \pm 9.2)\%\,, \tag{3.31}$$

which is presented in their articles to be equal to $(1 - f_s)$.

Another measurement with 23.4 fb^{-1} by Belle gave [166]

$$f_{u,d}^{(\text{Belle})} = (73.7 \pm 3.2 \pm 5.1)\%\,. \tag{3.32}$$

[6]Isospin conservation in the strong decay $\Upsilon(5S) \to (b\bar{b})\pi\pi$, where $(b\bar{b})$ is a bottomonium resonance, leads to a pair of pion with total isospin 0, hence $\mathcal{B}(\Upsilon(5S) \to (b\bar{b})\pi^+\pi^-) = 2 \times \mathcal{B}(\Upsilon(5S) \to (b\bar{b})\pi^0\pi^0)$; similarly $\mathcal{B}(\Upsilon(5S) \to (b\bar{b})K^+K^-) = \mathcal{B}(\Upsilon(5S) \to (b\bar{b})K^0\bar{K}^0)$.

[7]The decays $\Upsilon(5S) \to \Upsilon(nS)KK$ $(n = 2, 3)$ and $\Upsilon(5S) \to h_b(nP)KK$ $(n = 1, 2)$ are kinematically impossible at $\sqrt{s} \approx 10.865$ GeV.

3.2.2 Measurements of f_s with inclusive D_s^-, D^0 or ϕ production

All the other existing determinations of f_s or $f_{u,d}$ so far are based on the measurement of inclusive production rates in B and $\Upsilon(5S)$ decays using the formula

$$\frac{1}{2} \times \mathcal{B}_{\text{mult}}(\Upsilon(5S) \to AX) = f_s \times \mathcal{B}_{\text{mult}}(B_s^0 \to AX) + f_{u,d} \times \mathcal{B}_{\text{mult}}(B \to AX) + \frac{1}{2} \times f_{\not B} \times \mathcal{B}_{\text{mult}}(\Upsilon(5S) \to (b\bar{b})hh \to AX)\,, \quad (3.33)$$

where $\mathcal{B}_{\text{mult}}(P \to AX)$ is defined as the multiplicity of A in P decays:

$$\mathcal{B}_{\text{mult}}(P \to AX) = \sum_{i=1}^{\infty} i \times \mathcal{B}(P \to \text{“}i \text{ times } A\text{”} + \text{“anything without } A\text{”})\,. \quad (3.34)$$

The term $\frac{1}{2} \times f_{\not B} \times \mathcal{B}_{\text{mult}}(\Upsilon(5S) \to (b\bar{b})hh \to AX)$ is neglected, because the value of $f_{\not B}$ is only a few percents and the efficiency of the process $\Upsilon(5S) \to (b\bar{b})hh \to AX$ is much smaller than that of the $B_{(s)} \to AX$ modes.

Two quantities need to be measured, $\mathcal{B}_{\text{mult}}(B \to AX)$ (for instance at the $\Upsilon(4S)$ energy) and $\mathcal{B}_{\text{mult}}(\Upsilon(5S) \to AX)$. $\mathcal{B}_{\text{mult}}(B_s^0 \to AX)$ is a model-dependent estimate. f_s can be obtained through Eq. (3.33), with the approximation $f_{\not B} = 0$, i.e. $f_{u,d} = 1 - f_s$. Obviously this only works if $\mathcal{B}_{\text{mult}}(B \to AX)$ and $\mathcal{B}_{\text{mult}}(B_s^0 \to AX)$ are significantly different from each other; for example this methods is not expected to work with $A = J/\psi$.

This method was applied with $A = \phi$ and $A = D_s^-$ by the CLEO collaboration using $0.42\ \text{fb}^{-1}$ of $\Upsilon(5S)$ data; based on the model-dependent estimates $\mathcal{B}_{\text{mult}}(B_s^0 \to \phi X) = (16.1 \pm 2.4)\%$ [165] and $\mathcal{B}_{\text{mult}}(B_s^0 \to D_s^- X) = (92 \pm 11)\%$ [175], they get [165]:

$$f_s{}^{\phi(\text{CLEO})} = (24.6 \pm 2.9^{+11.0}_{-5.3})\%\,, \quad (3.35)$$

$$f_s{}^{D_s^-(\text{CLEO})} = (16.8 \pm 2.6^{+6.7}_{-3.4})\%\,. \quad (3.36)$$

On the other hand, Belle used $1.86\ \text{fb}^{-1}$ of $\Upsilon(5S)$ data with $A = D_s^-$ and $A = D^0$; based on the model-dependent estimates $\mathcal{B}_{\text{mult}}(B_s^0 \to D_s^- X) = (92 \pm 11)\%$ [175] and $\mathcal{B}_{\text{mult}}(B_s^0 \to D^0 X) = (8 \pm 7)\%$ [3, 175], the following more precise results were obtained [3]:

$$f_s{}^{D_s^-(\text{Belle})} = (17.9 \pm 1.4 \pm 4.1)\%\,, \quad (3.37)$$

$$f_s{}^{D^0(\text{Belle})} = (18.1 \pm 3.6 \pm 7.5)\%\,. \quad (3.38)$$

As seen in Eqs. (3.35)–(3.38) and explicited in Table 3.1, these measurements are largely dominated by systematic uncertainties. A way to get rid of the model dependence would be to measure $\mathcal{B}_{\text{mult}}(B_s^0 \to D_s^- X)$, $\mathcal{B}_{\text{mult}}(B_s^0 \to \phi X)$ and $\mathcal{B}_{\text{mult}}(B_s^0 \to D^0 X)$ in B_s^0-tagged events, which is currently out of reach (see Sec. 3.3.3).

3.2.3 Simultaneous fit of f_s, $f_{u,d}$ and $f_{\not B}$

This section describes our fit implementation for averaging the previously discussed $f_{u,d}$ and f_s measurements and taking all the known correlations into account. An earlier version of our fit results were included in the HFAG compilation of heavy flavour results [12]. A fit of the six existing measurements (Eqs. (3.31), (3.32) and (3.35) to (3.38)) allows

Table 3.1: Uncertainties affecting the CLEO and Belle determinations of f_s from the measurements of inclusive ϕ, D_s^- and D^0 production. The sign of the correlations are indicated as "±" or "∓".

Source	Uncertainty on f_s by analysis			
	CLEO [165]		Belle [3]	
	ϕ	D_s^-	D_s^-	D^0
Data statistics:				
– $0.42\ \mathrm{fb}^{-1}$ (CLEO) or $1.86\ \mathrm{fb}^{-1}$ (Belle)	±0.029	±0.026	±0.014	±0.036
Experimental systematics:				
– Estimate of number of $b\bar{b}$ events	∓0.068	∓0.036	∓0.015	±0.050
– Other experimental systematics	±0.058	±0.031	±0.013	±0.030
External measurements:				
– $\mathcal{B}_{\mathrm{mult}}(B \to \phi X) = (3.53 \pm 0.30)\%$ [165]	∓0.017	—	—	—
– $\mathcal{B}(D_s^- \to \phi\pi^-) = (4.4 \pm 0.6)\%$ [176]	—	∓0.026	∓0.027	—
– $\mathcal{B}_{\mathrm{mult}}(B \to D_s^- X) \times \mathcal{B}(D_s^- \to \phi\pi^-)$ $= (0.381 \pm 0.015)\%$ [175, 176]	—	∓0.008	∓0.003	—
– $\mathcal{B}_{\mathrm{mult}}(B \to D^0 X) \times \mathcal{B}(D^0 \to K^-\pi^+)$ $= (2.43 \pm 0.10)\%$ [176]	—	—	—	±0.040
Model-dependent estimates:				
– $\mathcal{B}_{\mathrm{mult}}(B_s^0 \to \phi X) = (16.1 \pm 2.4)\%$ [165]	∓0.046	—	—	—
– $\mathcal{B}_{\mathrm{mult}}(B_s^0 \to D_s^- X) = (92 \pm 11)\%$ [175]	—	∓0.022	∓0.024	—
– $\mathcal{B}_{\mathrm{mult}}(B_s^0 \to D^0 X) = (8 \pm 7)\%$ [3, 175]	—	—	—	±0.023
Total	0.106	0.064	0.043	0.083

the three fractions, f_s, $f_{u,d}$ and $f_{\not B}$, to float, but with their sum constrained to 1. In order to take into account the correlations induced by the external inputs and the experimental systematics, we recalculated the raw measurements of the efficiency-corrected signal yields for the four inclusive $\Upsilon(5S)$ modes. The event yield of the CLEO $f_{u,d}$ measurement is also directly used. Those quantities, reported in Table 3.2, are assumed to be fully uncorrelated.

A χ^2 quantity (defined in Table 3.2) is formed from the six raw measurements and the constraints from external parameters (Table 3.3); it is minimized by floating the three fractions and all external parameters with the Minuit software [178]. The branching fractions have been adjusted to their latest world averages, whenever available. Two constant factors are used to multiply the $B_s^0 \to \phi X$ and $B \to \phi X$ branching fractions in the inclusive ϕ CLEO analysis, $\alpha_s^\phi = 0.974$ and $\alpha_{u,d}^\phi = 0.964$ [165]; this is because the

Table 3.2: Raw measurements and χ^2 expression used in the fit for the fractions f_s, $f_{u,d}$ and $f_{\not{B}}$. See explanations in the text.

Raw measurement and its equivalent expressions		Value	Ref.
$M_\phi^{\rm CLEO}$	$N(\Upsilon(5S)\to\phi X)^{\rm CLEO}/(\varepsilon_{\phi X}^{\rm CLEO}\times\mathcal{B}(\phi\to K^+K^-))$ $\mathcal{B}(\Upsilon(5S)\to\phi X)\times N_{\Upsilon(5S)}^{\rm CLEO}$	$(16.4\pm 2.1)\times 10^3$	[165]
$M_{D_s^-}^{\rm CLEO}$	$N(\Upsilon(5S)\to D_s^- X)^{\rm CLEO}/(\varepsilon_{D_s^- X}^{\rm CLEO}\times\mathcal{B}(\phi\to K^+K^-))$ $\mathcal{B}(\Upsilon(5S)\to D_s^- X)\times\mathcal{B}(D_s^-\to\phi\pi^-)\times N_{\Upsilon(5S)}^{\rm CLEO}$	$(2.58\pm 0.39)\times 10^3$	[177] [165]
$M_{D_s^-}^{\rm Belle}$	$N(\Upsilon(5S)\to D_s^- X)^{\rm Belle}/(\varepsilon_{D_s^- X}^{\rm Belle}\times\mathcal{B}(\phi\to K^+K^-))$ $\mathcal{B}(\Upsilon(5S)\to D_s^- X)\times\mathcal{B}(D_s^-\to\phi\pi^-)\times N_{\Upsilon(5S)}^{\rm Belle}$	$(11.65\pm 0.79)\times 10^3$	[3]
$M_{D^0}^{\rm Belle}$	$N(\Upsilon(5S)\to D^0 X)^{\rm Belle}/\varepsilon_{D^0 X}^{\rm Belle}$ $\mathcal{B}(\Upsilon(5S)\to D^0 X)\times\mathcal{B}(D^0\to K^-\pi^+)\times N_{\Upsilon(5S)}^{\rm Belle}$	$(22.94\pm 1.11)\times 10^3$	[3]
$M_{BBX}^{\rm CLEO}$	$N(\Upsilon(5S)\to BB(X))^{\rm CLEO}$ $f_{u,d}\varepsilon_B^{\rm CLEO}(1+\sigma_{\mathcal{B}})N_{\Upsilon(5S)}^{\rm CLEO}$	53.2 ± 9.1	[174]
$M_{BBX}^{\rm Belle}$	$f_{u,d}(1+\sigma_{\mathcal{B}})$	$(73.7\pm 5.2)\%$	[166]

Global χ^2 expression:

$$\chi^2 = \left(\frac{M_\phi^{\rm CLEO} - 2N_{b\bar b}^{\rm CLEO}\left(f_s\mathcal{B}(B_s^0\to\phi X)\alpha_s^\phi + f_{u,d}\mathcal{B}(B\to\phi X)\alpha_{u,d}^\phi\right)}{\sigma(M_\phi^{\rm CLEO})}\right)^2$$

$$+\left(\frac{M_{D_s^-}^{\rm CLEO} - 2N_{b\bar b}^{\rm CLEO}\left(f_s\mathcal{B}(B_s^0\to D_s^- X)\mathcal{B}(D_s^-\to\phi\pi^-) + f_{u,d}\mathcal{B}(B\to D_s^- X, D_s^-\to\phi\pi^-)\right)}{\sigma(M_{D_s^-}^{\rm CLEO})}\right)^2$$

$$+\left(\frac{M_{D_s^-}^{\rm Belle} - 2N_{b\bar b}^{\rm Belle}\left(f_s\mathcal{B}(B_s^0\to D_s^- X)\mathcal{B}(D_s^-\to\phi\pi^-) + f_{u,d}\mathcal{B}(B\to D_s^- X, D_s^-\to\phi\pi^-)\right)}{\sigma(M_{D_s^-}^{\rm Belle})}\right)^2$$

$$+\left(\frac{M_{D^0}^{\rm Belle} - 2N_{b\bar b}^{\rm Belle}\left(f_s\mathcal{B}(B_s^0\to D^0 X)\mathcal{B}(D^0\to K^-\pi^+) + f_{u,d}\mathcal{B}(B\to D^0 X, D^0\to K^-\pi^+)\right)}{\sigma(M_{D^0}^{\rm Belle})}\right)^2$$

$$+\left(\frac{M_{BBX}^{\rm CLEO} - N_{b\bar b}^{\rm CLEO} f_{u,d}(1+\sigma_{\mathcal{B}})\varepsilon_B^{\rm CLEO}}{\sigma(M_{BBX}^{\rm CLEO})}\right)^2 + \left(\frac{M_{BBX}^{\rm Belle} - f_{u,d}(1+\sigma_{\mathcal{B}})}{\sigma(M_{BBX}^{\rm Belle})}\right)^2$$

$$+H(f_{\not{B}}^{\rm min} - f_{\not{B}})\left(\frac{f_{\not{B}} - f_{\not{B}}^{\rm min}}{\sigma(f_{\not{B}}^{\rm min})}\right)^2 + \left(\frac{1-(f_s+f_{u,d}+f_{\not{B}})}{\epsilon}\right)^2 + \left(\frac{\rho_{u,d}^s - f_s/f_{u,d}}{\epsilon}\right)^2$$

$+$ 12 individual Gaussian constraints on all the inputs of Table 3.3 (except $f_{\not{B}}^{\rm min}$)

Table 3.3: Independent external inputs used to fit f_s. The values derived from Ref. [37] (5th and 8th lines) are the product of the two separate branching fractions; their error is the quadratic *difference* between the two individual errors: in Ref. [37], the uncertainty of the second branching fraction is included in the uncertainty of the first. All but $f_{\not{B}}^{\min}$ are constrained separately in the χ^2 expression with a term $\left((x - x_0)/\sigma_0\right)^2$, where x is the variable used in the other χ^2 terms and $x_0 \pm \sigma_0$ is the value reported in this table.

Input	Value	Comment	Ref.
$N^{\mathrm{CLEO}}_{\Upsilon(5S)}$	$(1.27 \pm 0.01 \pm 0.16) \times 10^5$		[165]
$N^{\mathrm{Belle}}_{\Upsilon(5S)}$	$(5.61 \pm 0.03 \pm 0.29) \times 10^5$		[3]
$\varepsilon^{\mathrm{CLEO}}_{B}$	$(7.11 \pm 0.57) \times 10^{-4}$	adjusted	[165, 174]
$\sigma_{\mathcal{B}}$	0.00 ± 0.04	err. $\mathcal{B}(B^{0/+})$	[166, 174]
$\mathcal{B}(B \to D_s^- X, D_s^- \to \phi\pi^-)$	$(0.374 \pm 0.014)\%$	derived from	[37]
$\mathcal{B}(B_s^0 \to D_s^- X)$	$(92 \pm 11)\%$	model-dependent	[175]
$\mathcal{B}(D_s^- \to \phi\pi^-)$	$(4.5 \pm 0.4)\%$		[37]
$\mathcal{B}(B \to D^0 X, D^0 \to K^-\pi^+)$	$(2.43 \pm 0.11)\%$	derived from	[37]
$\mathcal{B}(B_s^0 \to D^0 X)$	$(8 \pm 7)\%$	model-dependent	[3, 175]
$\mathcal{B}(D^0 \to K^-\pi^+)$	$(3.87 \pm 0.05)\%$		[37]
$\mathcal{B}(B \to \phi X)$	$(3.43 \pm 0.12)\%$		[37]
$\mathcal{B}(B_s^0 \to \phi X)$	$(16.1 \pm 2.4)\%$	model-dependent	[165]
$f_{\not{B}}^{\min}$	$(4.13 \pm 0.55)\%$	Eq. (3.30)	[151, 172]

ϕ kinematic range is restricted to $x = p^*/E_{\mathrm{beam}} > 0.05$, which encompasses 97.4% and 96.4% of the ϕ coming from $B_s^0 \to \phi X$ and $B \to \phi X$ decays, respectively. Such formulation allows for the update of this analysis with the most recent world averages of $\mathcal{B}(B_{(s)} \to \phi X)$. A 4% uncertainty due to the branching fraction of the $B^{+/0}$ decays is common in the $f_{u,d}$ measurement of Belle and CLEO. This 4% error is subtracted (quadratically) from $f_{u,d}^{(\mathrm{Belle})}$ and $\varepsilon_B^{\mathrm{CLEO}}$ and added back with the $(1 + \sigma_{\mathcal{B}})$ factor in the χ^2. The fraction $f_{\not{B}}$ is constrained by its lower limit given by Eq. (3.30); this is done with an additional Gaussian term in the χ^2 only when $f_{\not{B}}$ is smaller than the central value of $f_{\not{B}}^{\min}$ (hence the presence of the Heaviside step function H in the χ^2 expression of Table 3.2). The value of the ratio $f_s/f_{u,d}$ (with its uncertainty) is also desired as an output of the fit procedure; therefore an additional free parameter representing this ratio, $\rho^s_{u,d}$, is included in the χ^2 expression and constrained to be equal to $f_s/f_{u,d}$.

This method has two advantages: the measurements are updated with the most recent PDG branching fractions and all the known correlations[8] between the inputs are correctly

[8]The relative small error of $\mathcal{B}(\phi \to K^+K^-)$, 1%, is small and therefore the correlation it introduces

handled. The alternative fitting method reported by the PDG [37] and by HFAG until 2009 [179] requires a linearisation of f_s around the original input parameters while this new method uses the exact formulae, and accounts for additional known correlations (the number of $b\bar{b}$ events for each experiment, etc.).

With the constraint $f_{\not B} = 0$, the minimisation fit returns a value of $\left(21.5^{+3.3}_{-3.0}\right)\%$ for $f_s = 1 - f_{u,d}$. The final results, obtained with $f_{\not B}$ allowed to float, are

$$f_s = (19.9 \pm 3.0)\,\%\,, \tag{3.39}$$

$$f_{u,d} = \left(75.9^{+2.7}_{-4.1}\right)\%\,, \tag{3.40}$$

$$f_{\not B} = \left(4.1^{+4.8}_{-0.5}\right)\%\,, \tag{3.41}$$

$$\rho^s_{u,d} = \frac{f_s}{f_{u,d}} = \left(26.3^{+5.2}_{-4.4}\right)\%\,. \tag{3.42}$$

The above average of f_s has a 15% relative uncertainty. It will be used for the B_s^0 branching fraction measurements presented in Chapter 4, for which it represents one of the main systematic uncertainties.

3.3 Other possible methods for measuring the B_s^0 production

3.3.1 Alternative with fully reconstructed B^0 and B^+ decays

We propose here a variant of the method described in Sec. 3.2.1, using two samples, one collected at the $\Upsilon(4S)$ resonance and another one collected at the $\Upsilon(5S)$ resonance. If we measure the yields of a specific exclusive B^+ or B^0 decay mode i in these two samples, called $Y_i^{\Upsilon(4S)}$ and $Y_i^{\Upsilon(5S)}$ respectively, then we expect

$$Y_i^{\Upsilon(4S)} = N_{b\bar{b}}^{\Upsilon(4S)} \times \mathcal{B}_i \times \epsilon_i^{\Upsilon(4S)}\,, \tag{3.43}$$

$$Y_i^{\Upsilon(5S)} = N_{b\bar{b}}^{\Upsilon(5S)} \times f_{u,d} \times \mathcal{B}_i \times \epsilon_i^{\Upsilon(5S)}\,, \tag{3.44}$$

where $N_{b\bar{b}}^{\Upsilon(4S)}$ and $N_{b\bar{b}}^{\Upsilon(5S)}$ are the number of $b\bar{b}$ events in the two analysed samples, $\mathcal{B}_i$ is the product of the branching fractions of the reconstructed mode i, and $\epsilon_i^{\Upsilon(4S)}$ and $\epsilon_i^{\Upsilon(5S)}$ are the total signal reconstruction efficiencies. Summing over many exclusive modes, taking the ratio of the two equations, and solving for f_s, we obtain, assuming $f_{\not B} = 0$,

$$f_s = 1 - \frac{N_{b\bar{b}}^{\Upsilon(4S)}}{N_{b\bar{b}}^{\Upsilon(5S)}} \times \frac{\sum_i Y_i^{\Upsilon(5S)}}{\sum_i Y_i^{\Upsilon(4S)}} \times \frac{\sum_i \mathcal{B}_i \epsilon_i^{\Upsilon(4S)}}{\sum_i \mathcal{B}_i \epsilon_i^{\Upsilon(5S)}}\,. \tag{3.45}$$

We examine in turn the uncertainty on each of the three fractions appearing in this expression, from right to left:

- In the limit where $\epsilon_i^{\Upsilon(4S)} = \epsilon_i^{\Upsilon(5S)}$, which should be a very good approximation if the selections are made "identical" in the two samples, the last fraction of the above expression is equal to 1 without error, i.e. the uncertainties on the branching fractions $\mathcal{B}_i$ become irrelevant (in practise, there might be small difference between the

between the inclusive ϕ and D_s^- analyses has been (safely) ignored.

efficiencies, leading to a fraction slightly different from 1 but which can in principle be obtained from Monte Carlo with a precision as good as desired).

- The uncertainty on the ratio of the total yields (second fraction in the above expression) will be dominated by the statistical uncertainty on the total yield at the $\Upsilon(5S)$, as long as the size of the $\Upsilon(5S)$ sample is much smaller than that of the $\Upsilon(4S)$ sample. Using modes which can be reconstructed with high purity such as[9] $B \to J/\psi K^{(*)}$, $B \to D^{(*)}\pi^+$ or $B \to D^{(*)}\rho^+$, the total efficiency $\sum_i \mathcal{B}_i \epsilon_i$ can be expected to be around 5×10^{-4}. With integrated luminosities of $100\ \text{fb}^{-1}$ and $800\ \text{fb}^{-1}$ at the $\Upsilon(5S)$ and $\Upsilon(4S)$ respectively, this would imply $\sum_i Y_i^{\Upsilon(5S)} \sim 20k$ events and $\sum_i Y_i^{\Upsilon(4S)} \sim 900k$ events, hopefully a total uncertainty not in excess of 1%. It should be noted that, for this measurement, it is not necessary to separate the yields from the different regions in the $\Delta E - M_{\text{bc}}$ plane. A fit of the invariant mass of the reconstructed B candidates, without constraint from the beam energy, would be enough to extract the total yield, similar to what has been done by CLEO [174]. Alternatively, a fit of a linear combination of M_{bc} and ΔE can do the same with a better resolution [166].

- The relative error achieved by Belle on $N_{b\bar{b}}^{\Upsilon(4S)}$ is 1.4%. However $N_{b\bar{b}}^{\Upsilon(5S)}$ presently has 4.8% uncertainty, limited by the luminosity precision. With some effort, it could be improved to 3% [180].

Putting everything together, we expect an uncertainty of $4 - 5\%$ on $(1 - f_s)$, hence of $\sim 16 - 20\%$ on f_s (if $f_s \sim 0.2$). Clearly the disadvantage of this method if that the nice relative precision obtained on $(1 - f_s)$ is diluted by a factor $1/f_s - 1 \sim 4$ when translated on a relative precision on f_s.

3.3.2 Measurement of f_s with multiple ϕ rates

The idea here is to measure the single, double and triple ϕ production rates, $\mathcal{B}(\Upsilon(5S) \to n\phi X)$ and $\mathcal{B}(\Upsilon(4S) \to n\phi X)$ where $n = 1, 2, 3$,to avoid the dependence on $\mathcal{B}(B_s^0 \to \phi X)$ which needs to be known precisely to obtain a reasonable uncertainty when using inclusive ϕ production (Sec. 3.2.2).

The definition of "inclusive rate" should be modified because the multiplicity of, say, two ϕ in B_s^0 decays is tricky to define. In this section, $\mathcal{B}(P \to nA\ X)$ is defined as the rate of P decaying with *at least* n particles A. This observable is easy to measure experimentally. The formula is then (note the lack of the factor i in front of the branching fraction):

$$\mathcal{B}(P \to nA\ X) = \sum_{i=n}^{\infty} \mathcal{B}(P \to \text{“}i \text{ times } A\text{”} + \text{“anything without } A\text{”}) \tag{3.46}$$

Following the same idea as in Sec. 3.2.2 and neglecting the ϕ production by non-$B_{(s)}\bar{B}_{(s)}$ events, we obtain three equations [14],

[9]See an example list in Table 1 of Ref. [174] but note that Belle efficiencies [166] are about 30% smaller than the ones quoted in Ref. [174].

$$\mathcal{B}\left(\Upsilon(5S)\to\phi\,X\right)=f_s\times\Big(2\,\mathcal{B}\left(B_s^0\to\phi\,X\right)\\ -\mathcal{B}\left(B_s^0\to\phi\,X\right)^2\Big)+f_{u,d}\times\mathcal{B}\left(\Upsilon(4S)\to\phi\,X\right)\,, \quad (3.47)$$

$$\mathcal{B}\left(\Upsilon(5S)\to 2\phi\,X\right)=f_s\times\Big(\mathcal{B}\left(B_s^0\to\phi\,X\right)^2+2\,\mathcal{B}\left(B_s^0\to 2\phi\,X\right)\\ -2\,\mathcal{B}\left(B_s^0\to\phi\,X\right)\mathcal{B}\left(B_s^0\to 2\phi\,X\right)\Big)\,,\\ +f_{u,d}\times\mathcal{B}\left(\Upsilon(4S)\to 2\phi\,X\right) \quad (3.48)$$

$$\mathcal{B}\left(\Upsilon(5S)\to 3\phi\,X\right)=f_s\times\Big(2\,\mathcal{B}\left(B_s^0\to 3\phi\,X\right)+2\,\mathcal{B}\left(B_s^0\to 2\phi\,X\right)\mathcal{B}\left(B_s^0\to\phi\,X\right)\\ -\mathcal{B}\left(B_s^0\to 2\phi\,X\right)^2-2\,\mathcal{B}\left(B_s^0\to 3\phi\,X\right)\mathcal{B}\left(B_s^0\to\phi\,X\right)\Big)\\ +f_{u,d}\times\mathcal{B}\left(\Upsilon(4S)\to 3\phi\,X\right)\,, \quad (3.49)$$

where again the $f_{\not B}$ contribution is ignored. This set of equations can be solved for f_s, $\mathcal{B}(B_s^0\to\phi\,X)$ and $\mathcal{B}(B_s^0\to 2\phi\,X)$, by measuring the six rates $\mathcal{B}(\Upsilon(nS)\to m\phi\,X$ ($n=4,5$, $m=1,2,3$) and assuming a value for $\mathcal{B}(B_s^0\to 3\phi\,X)$, which we know to be very small. One can imagine to continue to 4, 5, n ϕ rates, knowing $\mathcal{B}(B_s^0\to n\phi\,X)=0$ for $n>5$ (because of the B_s^0 mass).

The main advantage of this method is the reconstruction of only 2, 4 or 6 tracks in an event. The difficulties of this method concern the complexity of the equation set, which must be inverted (it can be done numerically). A fit was implemented in order to include all the possible correlations, simplified with $f_{u,d}=1-f_s$. The results are:

- if only f_s is a floating parameter (while $\mathcal{B}(B_s^0\to\phi\,X)$ and $\mathcal{B}(B_s^0\to 2\phi\,X)$ are fixed), the precision obtained on f_s is the same as the precision we get from the single-rate equation (Eq. (3.47)) alone,
- if the three parameters are free, f_s is less precise, and $\mathcal{B}(B_s^0\to\phi\,X)$ is much more imprecise than a direct measurement (Sec. 3.3.3).

Even though this idea of multiple ϕ rates looked interesting, it turns out that no good precision on f_s can be obtained. A similar method was proposed in Ref. [13] with D_s^- by measuring single, double, triple and quadruple rates. The corresponding equations can be found in Ref. [13], including categorization depending on the D_s^- charges. However, the D_s^- rates are lower, and many tracks have to be reconstructed leading to various problems (small efficiencies, large systematics from tracking, wrong MC efficiencies, etc.). Furthermore the difficulty observed with ϕ mesons does no provide much hope with D_s^- mesons.

3.3.3 Measurements on the recoil of fully reconstructed B_s^0 decays

An obvious way to get rid of the normalization uncertainty, i.e. of the need to estimate the number of B_s^0 mesons produced in the sample collected at the $\Upsilon(5S)$ resonance, is to perform branching fraction measurements in already tagged B_s^0 events. The method consists of selecting as many events as possible where a B_s^0 candidate can be fully reconstructed in any decay mode, and then counting, in this sub-sample of events, the number of other B_s^0 decays to a specific mode that can be reconstructed. Such method requires

Table 3.4: Minimal integrated luminosity $L_{\rm int}$ needed to measure various B_s^0 branching fractions with a statistical precision of 10% on the recoil of 20 fully reconstructed B_s^0 events per $\rm fb^{-1}$, based on rough assumptions for the branching fraction $\mathcal{B}$, the visible branching fraction $\mathcal{B}_{\rm vis}$, and the total reconstruction efficiency $\epsilon_{\rm rec}$.

Decay mode	$\mathcal{B}$	$\mathcal{B}_{\rm vis}/\mathcal{B}$	$\epsilon_{\rm rec}$	$L_{\rm int}$
$B_s^0 \to D_s^-(\phi\pi^-, K^{*0}K^-, K_S^0K^-)\pi^+$	0.37%	6.2%	26%	$84\ \rm ab^{-1}$
$B_s^0 \to D_s^-(\phi\pi^-, K^{*0}K^-, K_S^0K^-)X$	92%	6.2%	35%	$0.25\ \rm ab^{-1}$
$B_s^0 \to D^0(K^-\pi^+)X$	8%	3.9%	50%	$3.2\ \rm ab^{-1}$
$B_s^0 \to \phi X$	16%	49.2%	50%	$0.13\ \rm ab^{-1}$

very large statistics, but is thought to be the one leading ultimately to the smallest systematic uncertainty on B_s^0 branching fractions. Additionally, inclusive measurements of $\mathcal{B}(B_s^0 \to \phi X), \mathcal{B}(B_s^0 \to D^0 X)$ or $\mathcal{B}(B_s^0 \to D_s^- X)$ with this method would help removing the model-dependence of the previously-described inclusive method (Sec. 3.2.2).

As shown in Chapter 4, the numbers of $\Upsilon(5S) \to B_s^* \bar{B}_s^*$ events in which a B_s^0 decay can be fully reconstructed in a $23.4\ \rm fb^{-1}$ sample are 145^{+14}_{-13} for the $B_s^0 \to D_s^-\pi^+$ mode, $53.4^{+10.3}_{-9.6}$ for the $B_s^0 \to D_s^{*-}\pi^+$ mode, $92.2^{+14.2}_{-13.2}$ for the $B_s^0 \to D_s^-\rho^+$ mode, and 73^{+14}_{-13} for the $B_s^0 \to D_s^{*-}\rho^+$ mode, for a total of 368 ± 26 events, i.e. approximately 15 events per $\rm fb^{-1}$. It is probably relatively easy to add a few more modes (such as $B_s^0 \to D_s^- a_1^+$ and $B_s^0 \to D_s^{*-} a_1^+$) to reach 20 events per $\rm fb^{-1}$, i.e. a cross section of $\sigma = 20$ fb. Ignoring background for the sake of a rough estimation, the minimal integrated luminosity $L_{\rm int}$ needed to make, on the recoil of these fully reconstructed candidates, a measurement of a specific B_s^0 branching fraction $\mathcal{B}$ with a relative statistical precision $\delta\mathcal{B}/\mathcal{B}$ is then

$$L_{\rm int} = \frac{1}{\epsilon_{\rm rec}\,\sigma\,\mathcal{B}_{\rm vis}\,(\delta\mathcal{B}/\mathcal{B})^2}\,, \tag{3.50}$$

where $\epsilon_{\rm rec}$ is the total reconstruction efficiency and $\mathcal{B}_{\rm vis}$ is the visible branching fraction, i.e. the branching fraction $\mathcal{B}$ multiplied by the branching fractions of the subsequent decays of the B_s^0 decay products. Using Eq. (3.50) we give in Table 3.4 the integrated luminosities needed to measure a few B_s^0 branching fractions. As can be seen, a 10% measurement of $\mathcal{B}(B_s^0 \to \phi X)$ measurement should be reachable with the currently available $\Upsilon(5S)$ statistics at Belle ($121\ \rm fb^{-1}$), while the full statistics of a Super B factory is needed to perform a 10% measurement of $\mathcal{B}(B_s^0 \to D_s^-\pi^+)$ with this method.

3.4 Model-independent measurement of $f_s/f_{u,d}$ with dilepton sign correlations

While all the previous methods deal only with rates (branching fractions) measurements, we now use a new method with a completely different approach. The ratio $f_s/f_{u,d}$ can be extracted by taking advantage of another physical property to disentangle B_s^0 mesons from non-strange B mesons. This method, first proposed in Ref. [13], takes advantage of the difference between the slow $B^0-\bar{B}^0$ and the fast $B_s^0-\bar{B}_s^0$ oscillations. The sign of the lepton coming from a $B_{(s)}$ decay is used to determine the flavour of the meson when it decays. By counting the same-sign and opposite-sign lepton pairs, one can disentangle the contributions from B_s^0 mesons and B^0 mesons, and extract the ratio $f_s/f_{u,d}$. We performed detailed feasability studies from which we expected the relative error on f_s to lie between $5\,\%$ and $10\,\%$ [14]. This section describes a measurement of $f_s/f_{u,d}$ based on the dilepton sign correlation. It is obtained with the full data sample recorded by Belle at the $\Upsilon(5S)$ energy (121 fb^{-1}).

The Monte Carlo simulation procedure of dileptons events is described in Appendix A.2. Several MC samples are used in this analysis: one representing about 6×120 fb^{-1}, simulated with $f_s = 19.3\%$ and $f_{\not B} = 2.8\%$, and smaller additional datasets, representing about 20 fb^{-1} each, with f_s values ranging from 10% to 30%. The Monte Carlo generator had to be updated to simulate properly B^0 and B_s^0 mixing in $\Upsilon(5S)$ events; details are given in Appendix A.2.

3.4.1 Number of same-sign and opposite-sign dileptons from B^0, B^+ and B_s^0 semileptonic decays

The time-integrated probabilities that the two $B_{(s)}$ decay with the same flavour[10], $P_{SS}^{q,\eta} = \text{Prob}(B_q B_{q'}) + \text{Prob}(\bar{B}_q \bar{B}_{q'})$, or with opposite flavour, $P_{OS}^{q,\eta} = \text{Prob}(B_q \bar{B}_{q'}) + \text{Prob}(\bar{B}_q B_{q'})$ depend on the charge of the two $B_{(s)}$ mesons and, in case of two neutral $B_{(s)}^0$ mesons, the C eigenvalue, η, of the $B_{(s)}^0$ pair. These probabilities are reported in Table 3.5, while the detailed calculations are presented in Appendix A.1. It turns out that $\Upsilon(5S)$ events produce $B_{(s)}^0\bar{B}_{(s)}^0$ pairs that can be in a $C=+1$ or in a $C=-1$ state. The initial state is a virtual photon (Fig. 3.1) which has $C=-1$. The total final state, excluding the initial state radiation, must have the same $C=-1$ value from charge-conjugaison conservation of the electromagnetic and strong forces[11]. While a possible accompanying neutral pion has $C=+1$ and does not influence the C eigenvalue of the B pair, a photon coming from the electromagnetic decay a of $B_{(s)}^*$ changes the C value. If there is one excited $B_{(s)}^*$, the C value of the $B_{(s)}^0\bar{B}_{(s)}^0$ is $+1$, if there are two, the C value is -1. In the case of a four-body $\Upsilon(5S) \to B^0\bar{B}^0\pi^+\pi^-$ decay, the C eigenvalue of the pion pair depends on their relative orbital momentum, $l_{\pi\pi}$: $C(\pi\pi) = (-1)^{l_{\pi\pi}}$. The C parity of the $B^0\bar{B}^0$ pair is thus $(-1)^{l_{\pi\pi}+1}$. Considering that the phase space for this decay is very small, $\sqrt{s}-2(m_B+m_\pi)c^2 \approx 30\,\text{MeV}$, it is safe to assume $l_{\pi\pi}=0$ and $C(B^0\bar{B}^0) = -1$. A summary of the C eigenvalues of the $B_{(s)}^0\bar{B}_{(s)}^0$ pairs is given in Table 3.6.

Within the category of non-strange B events, the proportion of $B^0\bar{B}^0$, $B^0B^- + \bar{B}^0B^+$ and B^-B^+ events can be determined from isospin conservation in the strong decay of the null-isospin $\Upsilon(5S)$ particle.

In the case of a $\Upsilon(5S) \to B^{(*)}\bar{B}^{(*)}$ two-body decay, the isospin state of the $B\bar{B}$ pair

[10] $q = u, d, s$ and q is not necessarily equal to q' (for instance in the $\Upsilon(5S) \to B^0B^-\pi^+$ mode). The qq' pair is either uu, dd, ud or ss. Throughout this section, q' is omitted if $q = q'$.

[11] In case of initial state radiation, the only difference is that the $b\bar{b}$ pair is produce by a virtual photon with a smaller energy, but still with $C=-1$.

Table 3.5: Probabilities (in %) that the two $B_{(s)}$ mesons decay with the same or opposite flavours, using $x_d = 0.771 \pm 0.008$, $y_d = 0$, $x_s = 26.2 \pm 0.5$ and $y_s = \frac{1}{2}\left(0.092^{+0.051}_{-0.054}\right)$ [37].

(qq')	Type of pair		η	Same flavour, $P^{q,\eta}_{SS}$	Opposite flavour, $P^{q,\eta}_{OS}$
		C-even	$+1$	42.0 ± 0.4	58.0 ± 0.4
(d)	$B^0\bar{B}^0$	C-odd	-1	18.6 ± 0.2	81.4 ± 0.2
		incoherent	0	30.3 ± 0.3	69.7 ± 0.3
		C-even	$+1$	50.1 ± 0.0	49.9 ± 0.0
(s)	$B^0_s\bar{B}^0_s$	C-odd	-1	49.9 ± 0.0	50.1 ± 0.0
		incoherent	0	50.0 ± 0.0	50.0 ± 0.0
(ud)	$B^0B^-, \bar{B}^0B^+$	—		18.6 ± 0.2	81.4 ± 0.2
(u)	B^+B^-	—		0	100

Table 3.6: C parity of the $B^0_{(s)}\bar{B}^0_{(s)}$ pair in $\Upsilon(5S) \to B^0_{(s)}\bar{B}^0_{(s)}(X)$ events.

$\Upsilon(5S)$ decay modes with a $B^0_{(s)}\bar{B}^0_{(s)}$ pair	$C(B^0_{(s)}\bar{B}^0_{(s)})) = \eta$
$B^{*0}\bar{B}^{*0}$, $B^0\bar{B}^0$, $B^{*0}\bar{B}^{*0}\pi^0$, $B^0\bar{B}^0\pi^0$, $B^0\bar{B}^0\gamma_{\rm ISR}$, $B^0_sB^0_s$, $B^*_s\bar{B}^*_s$	-1
$B^{*0}\bar{B}^0$, $B^{*0}\bar{B}^0\pi^0$, $B^0_s\bar{B}^*_s$, $B^*_s\bar{B}^0_s$	$+1$
$B^0\bar{B}^0\pi^+\pi^-$	$(-1)^{l_{\pi\pi}+1} \approx -1$

is[12]

$$|0,0\rangle_{B\bar{B}} = \frac{1}{\sqrt{2}}\left(\left|B^+B^-\right\rangle - \left|B^0\bar{B}^0\right\rangle\right) . \tag{3.51}$$

Therefore half of the $B^{(*)}\bar{B}^{(*)}$ events are $B^{(*)0}\bar{B}^{(*)0}$ events and the other half are $B^{(*)+}B^{(*)-}$ events.

In the case of a $\Upsilon(5S) \to B^{(*)}\bar{B}^{(*)}\pi$ three-body decay, the total isospin of the $B\bar{B}$ system must be 1, since the pion has isospin 1. The three $B\bar{B}$ isospin states are

$$|1,+1\rangle_{BB} = \left|B^+\bar{B}^0\right\rangle , \tag{3.52}$$
$$|1,0\rangle_{BB} = \frac{1}{\sqrt{2}}\left(\left|B^+B^-\right\rangle + \left|B^0\bar{B}^0\right\rangle\right) , \tag{3.53}$$
$$|1,-1\rangle_{BB} = \left|B^0B^-\right\rangle . \tag{3.54}$$

[12]We use the notation $|I, I_3\rangle_{B\bar{B}}$, where I is the total isospin of the $B\bar{B}$ pair and I_3 its third component.

Combining this[13] with the pion must give an isospin-0 state:

$$|0,0\rangle_{B\bar{B}\pi} = \frac{1}{\sqrt{3}}\left(|1,1\rangle_{BB}\left|\pi^-\right\rangle - |1,0\rangle_{BB}\left|\pi^0\right\rangle + |1,-1\rangle_{BB}\left|\pi^+\right\rangle\right) \tag{3.55}$$
$$= \frac{1}{\sqrt{6}}\left(\sqrt{2}\left|B^+\bar{B}^0\pi^-\right\rangle + \sqrt{2}\left|B^0B^-\pi^+\right\rangle + \left|B^+B^-\pi^0\right\rangle + \left|B^0\bar{B}^0\pi^0\right\rangle\right).$$

Therefore two thirds of the three-body decays are $B^{(*)0}B^{(*)-}\pi^+$ or $\bar{B}^{(*)0}B^{(*)+}\pi^-$ events, one sixth are $B^{(*)+}B^{(*)-}\pi^0$ events, and one sixth are $B^{(*)0}\bar{B}^{(*)0}\pi^0$ events.

In the case of a four-body $\Upsilon(5S) \to B\bar{B}\pi\pi$ decay, there are two $|0,0\rangle_{B\bar{B}\pi\pi}$ singlet states, because two sub-spaces of dimension 1 exist ($\frac{1}{2}\otimes\frac{1}{2}\otimes 1\otimes 1 = 0\oplus 0\oplus 1\oplus 1\oplus 1\oplus 1\oplus 2\oplus 2\oplus 2\oplus 3$). With the different possibilities of combination, the two values for the proportion of $B^0B^- + \bar{B}^0B^+$ pairs have always their mean equal to $\frac{1}{3}$. The minimal value is 0, the maximal $\frac{2}{3}$.

We assume in the following that the non-strange B events are either two-body decays, $B^{(*)}\bar{B}^{(*)}$, three-body decays, $B^{(*)}\bar{B}^{(*)}\pi$, or initial-state radiation decays with a C-odd B pair[14] ($e^+e^- \to \gamma_{\rm ISR}B\bar{B}$, or $e^+e^- \to \gamma_{\rm ISR}B^*\bar{B}^*$).

The non-strange $B\bar{B}$ pairs are sub-divided into $B^0B^- + \bar{B}^0B^+$ pairs, representing

$$F_{ud} = \frac{2}{3}\times F_{B^{(*)}\bar{B}^{(*)}\pi(\pi)}\times\left(F'_{B^*\bar{B}^*\pi} + F'_{B^*\bar{B}\pi} + F'_{B\bar{B}\pi}\right) = (7.5\pm 2.8)\% \tag{3.56}$$

of all non-strange B pairs, and into $B^0\bar{B}^0$ and B^+B^- pairs, each representing

$$F_u = F_d = \frac{1-F_{ud}}{2} = (46.3\pm 1.4)\%\,. \tag{3.57}$$

Another quantity needed to express the number of dileptons is the semi-leptonic branching fractions of the B_q mesons, $\mathcal{B}(B_q \to Xl\nu_l)$ ($q = u,d,s$, $l = e^\pm$ or $\mu^\pm$). They are proportional to their respective lifetimes[15],

$$\mathcal{B}(B_q \to Xl\nu_l) = \frac{\Gamma_{\rm sl}}{\Gamma_q} = \frac{\Gamma_{\rm sl}\tau_q}{\hbar}\,, \tag{3.58}$$

assuming the same common semi-leptonic decay width[16], $\Gamma_{\rm sl}\approx 44\times 10^{-12}$ MeV, for the three B_q mesons. This has the advantage to replace the imprecise semi-leptonic branching fractions by the more precisely measured lifetimes.

The number of same-sign ($\Sigma = SS$) and opposite-sign ($\Sigma = OS$) dileptons ($l_1l_2 = ee$, $\mu\mu$, $e\mu$ or μe) can be written as

$$N_\Sigma^{l_1l_2,u,d} = \mathcal{N}\varepsilon_{\Sigma,u,d}^{l_1l_2}\left(F_d\tau_d^2P_\Sigma^d + F_{ud}\tau_u\tau_dP_\Sigma^{ud} + F_u\tau_u^2P_\Sigma^u\right)\,,\ \text{for } B\bar{B} \text{ pairs}\,, \tag{3.59}$$
$$N_\Sigma^{l_1l_2,s} = \mathcal{N}\frac{f_s}{f_{u,d}}\varepsilon_{\Sigma,s}^{l_1l_2}\tau_s^2P_\Sigma^s\,,\ \text{for } B_s^0\bar{B}_s^0 \text{ pairs}\,, \tag{3.60}$$

[13]If we first combine one B with the pion, and then combine them with the other B, the same result is obtained.

[14]In Ref. [166], it is calculated that 40% of initial state radiation are due $\Upsilon(5S)\to\Upsilon(4S)\gamma_{\rm ISR}$ followed by $\Upsilon(4S)\to B\bar{B}$.

[15]Because $y_s \neq 0$, the B_s^0 lifetime is defined as the inverse of the width averages (Eq. (1.68)), $\tau_s = 2\hbar/(\Gamma_{B_{sL}^0} + \Gamma_{B_{sH}^0})$.

[16]The measured semi-leptonic widths $\Gamma_{\rm sl} = \hbar\mathcal{B}(B_q \to Xl\nu_l)/\tau_q$ are equal to [37] $0.448(12)$, $0.441(11)$, $0.471(57)$ in unit of 10^{-10} MeV for the B^0, B^+ and B_s^0 respectively, see Ref. [181] for the B_s^0 semi-leptonic inclusive branching fraction.

where $\varepsilon^{l_1 l_2}_{\Sigma,u,d}$ and $\varepsilon^{l_1 l_2}_{\Sigma,s}$ are the total efficiencies of same- and opposite-sign dileptons $l_1 l_2$, and $\mathcal{N} = N_{\Upsilon(5S)}\Gamma^2_{\text{sl}} f_{u,d}/\hbar^2$ is a global normalisation. The probability to give a same-sign or opposite-sign lepton pair for $B^0_q\bar{B}^0_q$ pairs ($q = d, s$), P^q_Σ, receives contributions from C-odd ($B^*_q\bar{B}^*_q + B_q\bar{B}_q$) and C-even ($B^*_q\bar{B}_q$) pairs:

$$P^q_\Sigma = f^q_{C_+} P^{q,+1}_\Sigma + f^q_{C_-} P^{q,-1}_\Sigma \,. \tag{3.61}$$

Using Table 3.6, the fractions of C-even and C-odd $B^0\bar{B}^0$ pairs are found to be

$$f^d_{C_+} = \frac{\frac{1}{2}F_{B^*\bar{B}} + \frac{1}{6}F_{B^{(*)}\bar{B}^{(*)}X} \times F'_{B^*\bar{B}\pi}}{F_d} = 1 - f^d_{C_-} = (23.5 \pm 2.5)\% \,, \tag{3.62}$$

while for $B^0_s\bar{B}^0_s$ pairs the expression is simply

$$f^s_{C_+} = F_{B^*_s\bar{B}^0_s} = 1 - f^s_{C_-} = (7.3 \pm 3.2)\% \,. \tag{3.63}$$

As can be seen from Eqs. (3.59) and (3.60), the ratio $f_s/f_{u,d}$ can be extracted from the ratio between the number of same-sign signal events and that of opposite-sign signal events, $R = (N^{l_1l_2,u,d}_{SS} + N^{l_1l_2,s}_{SS})/(N^{l_1l_2,u,d}_{OS} + N^{l_1l_2,s}_{OS})$,

$$\frac{f_s}{f_{u,d}} = \frac{\varepsilon^{l_1l_2}_{SS,u,d}\left(F_d\tau^2_d P^d_{SS} + F_{ud}\tau_u\tau_d P^{ud}_{SS}\right) - R \times \varepsilon^{l_1l_2}_{OS,u,d}\left(F_d\tau^2_d P^d_{OS} + F_{ud}\tau_u\tau_d P^{ud}_{OS} + F_u\tau^2_u\right)}{R \times \varepsilon^{l_1l_2}_{OS,s}\tau^2_s P^s_{OS} - \varepsilon^{l_1l_2}_{SS,s}\tau^2_s P^s_{SS}} \,. \tag{3.64}$$

Because of the presence of background, we will extract $f_s/f_{u,d}$ from a fit instead of counting the signal events.

3.4.2 Dilepton selection and background

Dilepton candidates are retained from preselected dilepton events with $R_2 < 0.5$, following a selection inspired from other Belle dilepton analyses [182–184]. The preselection retains events with at least one pair of leptons (electron or muon candidates) which energy, $E_{l_1} + E_{l_2}$, is larger than 1.3 GeV in the laboratory frame . Charged tracks in the central ECL barrel, i.e. with a polar angle satisfying $30° < \theta_{\text{lab}} < 135°$, are selected as electron (muon) candidates if their electronic (muonic) likelihood $\mathcal{L}_e$ ($\mathcal{L}_\mu$) is larger than 0.8. The background dilepton candidates usually have a smaller momentum than the signal leptons (Fig. 3.6) and a minimum value for the centre-of-mass lepton momentum is set in order to increase the purity:

$$p^* > 1.2 \text{ GeV}/c \,. \tag{3.65}$$

If an event has two or more lepton candidates, the two leptons with the largest centre-of-mass momenta (p^*_1 and p^*_2) are kept for further analysis. By convention, $p^*_1 > p^*_2$. Requirements are applied on the invariant mass of the lepton pair in order to reduce backgrounds from J/ψ decays and pair-production:

- J/ψ veto: the event is rejected if the lepton pair is either a e^+e^- or a $\mu^+\mu^-$ OS pair with an invariant mass satisfying

$$-150 \text{ MeV}/c^2 < M_{e^+e^-} - M_{J/\psi} < 50 \text{ MeV}/c^2 \quad \text{or}$$

$$\left|M_{\mu^+\mu^-} - M_{J/\psi}\right| < 50 \text{ MeV}/c^2 \,,$$

  where $M_{J/\psi}$ is the nominal J/ψ mass [37];

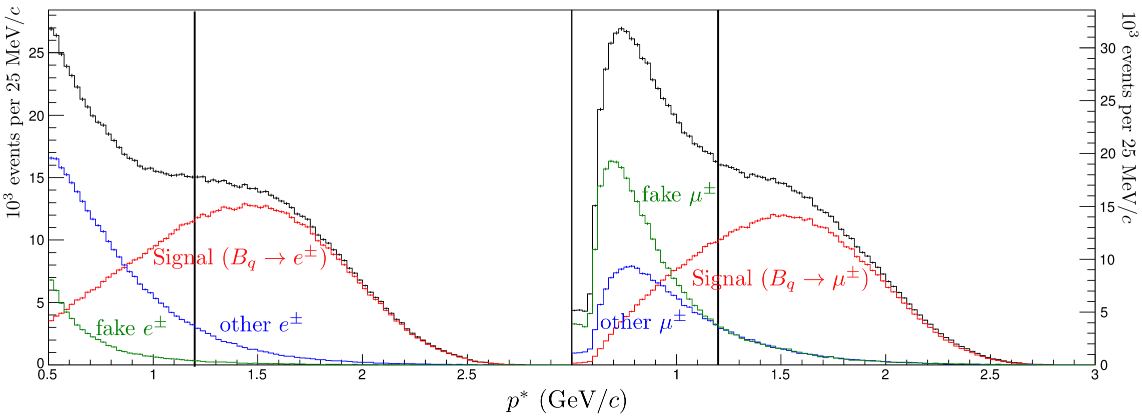

Figure 3.6: Electron (left) and muon (right) centre-of-mass momentum spectra with the contribution from $B_{(s)} \to Xl\nu$ decays (red), other true leptons (blue) and fake leptons (green). Only leptons with centre-of-mass momentum larger than 1.2 GeV/c are retained.

- to eliminate $\gamma \to e^+e^-$ conversions, an event with an OS e^+e^- pair is rejected if

$$M_{e^+e^-} < 200\,\mathrm{MeV}/c^2\,.$$

A requirement on the angle between the two leptons in the $\Upsilon(5S)$ centre-of-mass, $\cos\theta^*_{ll}$, is used to reject clone tracks (two tracks measured for the same lepton have $\cos\theta^*_{ll} \approx 1$) and back-to-back background which has small values of $\cos\theta^*_{ll}$ (Fig. 3.7):

$$\cos\theta^*_{l^+l^-} > -0.8\,, \tag{3.66}$$

$$\cos\theta^*_{l^\pm l^\pm} < 0.95\,, \quad \text{and} \tag{3.67}$$

$$\cos\theta^*_{\mu^\pm\mu^\pm} < 0.85\,. \tag{3.68}$$

In general, cuts have been made more efficient on the signal SS pairs because it is crucial to keep the smaller signal yields as high as possible.

Because leptons can be of two flavours (electron or muon), there are four types of pairs: dielectron, dimuon, and mixed pair with $p^*_e > p^*_\mu$ or $p^*_\mu > p^*_e$. The opposite-sign and same-sign candidates are selected separately. There are thus eight sets of candidates. The total signal efficiencies after this selection are reported in Table 3.7.

Not all selected candidates are composed of two signal leptons. The main background sources are identified to be lepton candidates from $e^+e^- \to u\bar{u}, d\bar{d}, s\bar{s}, c\bar{c}$ continuum.

The continuum can be subtracted using data recorded just below the $\Upsilon(4S)$ energy where $\sqrt{s} = 10.518$ GeV is insufficient to produce a pair of B mesons. Two adjustments are required due to the beam energy and the luminosity differences between those data and the on-resonance sample. The momenta of the candidates in continuum data are scaled assuming that the distribution of

$$x = \frac{p^*}{p^*_{\max}} \tag{3.69}$$

is the same at different energies, where $p^*_{\max} = \sqrt{E^{*2}_{\mathrm{b}} - m_l^2}$ is the centre-of-mass momentum that the considered particle l^- has in the reaction $e^+e^- \to l^+l^-$ (see Ref. [3]). The

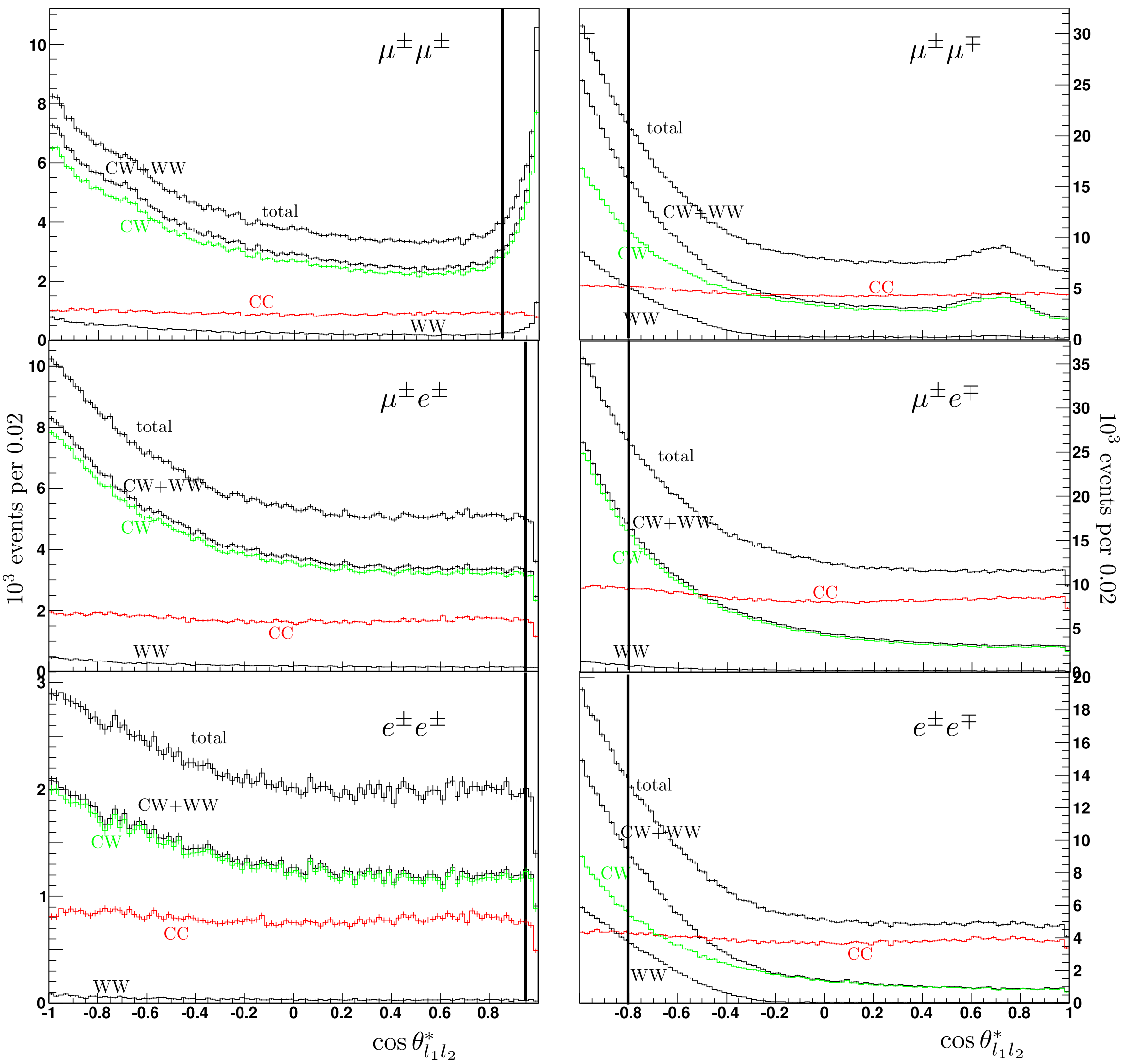

Figure 3.7: $\cos\theta^*_{ll}$ distributions for the generic $b\bar{b}$ MC, representing $480\ \mathrm{fb}^{-1}$. The sample is separated in background components, WW (small black histogram), CW (green histogram) and their sum, CW+WW (black histogram), and a signal component, CC (red histogram). The abbreviations CC, CW and WW correspond to the signal ("Correct Correct"), the background with one primary lepton ("Correct Wrong"), and the background with no primary lepton ("Wrong Wrong"), respectively. The cut values are indicated as vertical lines.

momenta measured in continuum data are therefore multiplied by

$$\frac{p_{\mathrm{max}}^{\Upsilon(5S)}}{p_{\mathrm{max}}^{\mathrm{cont}}} \approx \sqrt{\frac{s_{\Upsilon(5S)}}{s_{\mathrm{cont}}}} = \frac{10.864}{10.518} = 1.0329\,.$$

This value is the same, up to the fourth digit, for electrons and muons. The number of candidates is also scaled to account for integrated luminosity and energy differences. Considering the $1/s$ behaviour of the cross-section, the integrated luminosity ratio and a

Table 3.7: Dilepton efficiency (in %), $\varepsilon_{\Sigma,q}^{l_1 l_2}$, measured in the MC sample.

Σ		$l_1 l_2 = \mu\mu$	$l_1 l_2 = ee$	$l_1 l_2 = e\mu$	$l_1 l_2 = \mu e$
SS	$B_s^0 \bar{B}_s^0$, $q = s$	25.13±0.16	24.00±0.16	23.46±0.15	27.58±0.17
OS	$B_s^0 \bar{B}_s^0$, $q = s$	23.83±0.15	21.30±0.14	21.64±0.15	25.36±0.16
SS	$B\bar{B}$, $q = u, d$	30.06±0.16	28.13±0.15	28.11±0.15	32.19±0.16
OS	$B\bar{B}$, $q = u, d$	28.28±0.06	24.71±0.05	25.58±0.05	29.36±0.06

possible efficiency ratio different from 1, the number of events reconstructed in continuum data has to be rescaled by a factor

$$S = \frac{L_{\text{int}}^{\Upsilon(5S)}}{L_{\text{int}}^{\text{cont}}} \left(\frac{E_{\text{b}}^{*\text{cont}}}{E_{\text{b}}^{*\Upsilon(5S)}} \right)^2 \tilde{\varepsilon} \tag{3.70}$$

before being compared to the on-resonance data. In our case S is measured to be 2.463 ± 0.013 with $L_{\text{int}}^{\Upsilon(5S)} = 121.36\,\text{fb}^{-1}$ (Table 2.3), $L_{\text{int}}^{\text{cont}} = 48.42\,\text{fb}^{-1}$ (Table 2.4), and the ratio between efficiencies at $\sqrt{s_{\Upsilon(5S)}} = 10.867$ GeV and at $\sqrt{s_{\text{cont}}} = 10.518$ GeV is $\tilde{\varepsilon} = 1.007 \pm 0.003$ [3]. In this analysis, S will be a floating parameter of the fitting procedure. This is because it can be more precisely determined by the fit thanks to a region of the fit observables which contains only continuum events.

The other sources of background are due to lepton candidates from $\Upsilon(5S)$ events that are not signal. They include true leptons that are not produced in semileptonic $B_q \to X\,l\,\nu$ decays or candidates that are not leptons, mainly misidentified $K^\pm$ and $\pi^\pm$. A lepton candidate from an $\Upsilon(5S)$ decay is either a signal lepton (correct lepton), i.e. a lepton coming from a semi-leptonic decay B_q, or anything else (wrong lepton).

In summary, the selected candidates can belong to five different categories:

- the continuum;
- the background with two wrong leptons (WW);
- the background with one correct lepton and one wrong lepton (CW);
- the signal, which has two correct leptons (CC).

The leptons from B_s^0 and from $B^{+/0}$ have slightly different spectra and efficiencies. The signal and the CW background categories are therefore split between non-strange $B^{+/0}\bar{B}^{+/0}(X)$ events, CC($B\bar{B}$) and CW($B\bar{B}$), and $B_s^{(*)}\bar{B}_s^{(*)}$ events, CC($B_s^0\bar{B}_s^0$) and CW($B_s^0\bar{B}_s^0$).

3.4.3 Fitting procedure

The natural observable for a lepton is its centre-of-mass momentum, p^*. Instead of working with the variables p_1^* and p_2^*, we define two other observables that have smaller corre-

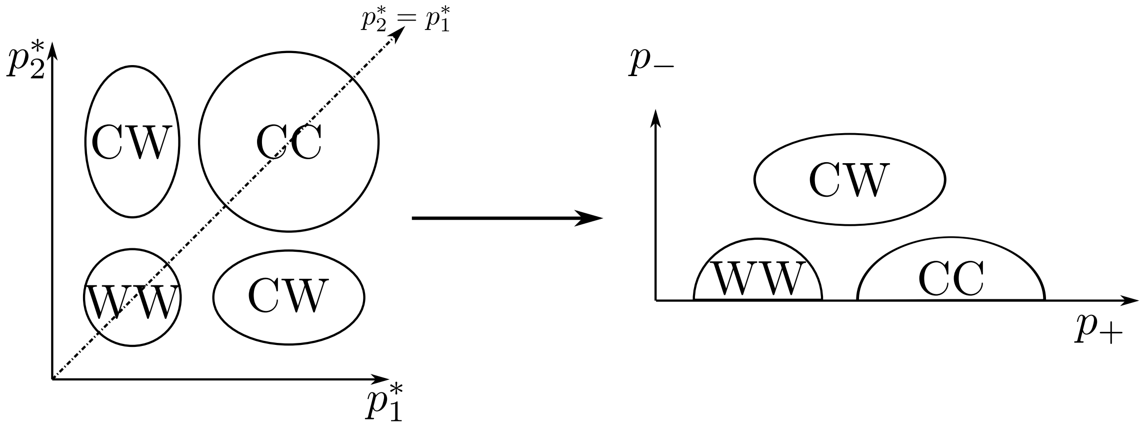

Figure 3.8: Sketch of the signal (CC) and background (CW+WW) regions in the (p_1^*, p_2^*) and (p_+, p_-) planes.

lation and are invariant under the swap of the two leptons (Fig. 3.8):

$$p_+ = p_1^* + p_2^* \,, \tag{3.71}$$
$$p_- = |p_1^* - p_2^*| \,. \tag{3.72}$$

A set of dilepton events is represented by two 2-dimensional (p_+, p_-) histograms, one for opposite-sign pairs and one for same-sign pairs. These histograms need to be fitted simultaneously in order to extract the number of OS and SS signal (CC) pairs both from events with and without B_s^0 production.

An extended binned maximum likelihood fit is implemented. The likelihood function for a histogram has the standard form of a Poissonian probability distribution with expected value ν_k for each of the K bins:

$$\mathcal{L}_\sigma^{l_1 l_2} = \prod_{k=1}^{K} e^{-\nu_k} \frac{\nu_k^{n_k}}{n_k!} \,, \tag{3.73}$$

where n_k (ν_k) is the observed (expected) number of events in bin k. When the histogram is fitted with C categories defined also as histograms[17], the expected number of events in bin k, ν_k, is parametrised as

$$\nu_k = \sum_{c=1}^{C} \nu^{(c)} \frac{n_k^{(c)}}{N_0^{(c)}} \,, \tag{3.74}$$

where $\nu^{(c)}$ is the expected number of events in category c (the ultimate goal of the procedure is to find the best-fit value of $\nu^{(c)}$), $n_k^{(c)}$ is the number of events in bin k of the histogram defining category c, and $N_0^{(c)}$ is the total number of events in the histogram

[17]An alternative method, which takes into account the statistical fluctuations in the MC histograms, has been proposed in Refs. [185–187]. We implemented such a complex likelihood, which gives very similar results. However the simplicity of Eq. (3.73) is preferred here because the number of events in our histograms is large enough to neglect the MC statistical uncertainties.

defining category c,

$$N_0^{(c)} = \sum_{k=1}^{K} n_k^{(c)} . \tag{3.75}$$

The fit has six components for each histogram:

- Continuum component: the shape is taken from off-resonance data with momentum scaling. The event yield scaling factor, S, which is common to all the histograms, is a free parameter of the fit.

- WW component: the shapes are taken from MC simulations. The yields, one for each histogram, are free parameters of the fit.

- Two CW components: the shapes are taken from MC simulations. The four CW yields can be expressed as

$$N_{OS}^{CW,s} = A^{CW} , \tag{3.76}$$

$$N_{OS}^{CW,u,d} = A^{CW} \times B_{OS}^{CW} \times \frac{f_{u,d}}{f_s} , \tag{3.77}$$

$$N_{SS}^{CW,s} = A^{CW} \times R^{CW} , \tag{3.78}$$

$$N_{SS}^{CW,u,d} = A^{CW} \times R^{CW} \times B_{SS}^{CW} \times \frac{f_{u,d}}{f_s} , \tag{3.79}$$

where A^{CW} is an overall normalisation factor and where

$$B_{\Sigma}^{CW} = \frac{N_{\Sigma}^{CW,u,d}}{N_{\Sigma}^{CW,s}} \times \frac{f_s}{f_{u,d}} , \quad \Sigma = OS, SS , \tag{3.80}$$

$$R^{CW} = \frac{N_{SS}^{CW,s}}{N_{OS}^{CW,s}} . \tag{3.81}$$

The three parameters B_{OS}^{CW}, B_{SS}^{CW} and R^{CW} are expected to be independent of $f_s/f_{u,d}$. This is confirmed using Monte Carlo simulation (see Table 3.8). In the fit to the data, they are fixed to their Monte Carlo values. The parameters A^{CW} and $f_s/f_{u,d}$ are free.

- CC (signal) components. The shapes are taken from MC simulations. The yields are related to external parameters and to $f_s/f_{u,d}$, which is free in the fit, by the relations of Eqs. (3.59) and (3.60).

The fit has 13 global floating parameters that are common to all the dilepton samples: $\mathcal{N}$, $f_s/f_{u,d}$, S, and ten others (six $B^{(*)}\bar{B}^{(*)}(X)$ fractions, three lifetimes and Δm_d, denoted as $y_j, j = 1 \ldots 10$) which have a Gaussian constraint to their measured value (see Table 3.9). For each dilepton sample $l_1 l_2$ ($l_1 = e, \mu$, $l_2 = e, \mu$), there are seven additional floating parameters (denoted as $x_i^{l_1 l_2}, i = 1 \ldots 7$) which all have a Gaussian constraint to values estimated from MC: four efficiencies, $\varepsilon_{\Sigma,s}^{l_1 l_2}$ and $\varepsilon_{\Sigma,u,d}^{l_1 l_2}$ (Table 3.7), and the B_{Σ}^{CW} and

Table 3.8: Parameters defining the CW yields (see Eqs. (3.76) to Eqs. (3.81)) as measured in MC samples for $\mu\mu$ (top left), ee (top right), $e\mu$ (bottom left) and μe (bottom right) pairs. The digits in parentheses are the statistical uncertainties. These parameters are found to be independent of the input value of f_s given in the first column. The mean values (over all MC samples) are used as input to the data fits.

f_s (%)	B_{SS}^{CW}	B_{OS}^{CW}	R^{CW}	B_{SS}^{CW}	B_{OS}^{CW}	R^{CW}
		$\mu\mu$			ee	
10.0	1.443(52)	1.144(35)	0.689(31)	1.644(96)	1.128(52)	0.610(44)
12.5	1.495(47)	1.180(31)	0.680(27)	1.535(75)	1.057(41)	0.615(37)
15.0	1.480(41)	1.184(28)	0.682(23)	1.650(74)	1.165(42)	0.633(34)
17.5	1.475(40)	1.206(28)	0.687(23)	1.600(69)	1.063(37)	0.601(31)
19.3	1.467 (8)	1.175 (5)	0.680 (4)	1.519(12)	1.072 (7)	0.635 (6)
20.0	1.515(37)	1.182(24)	0.661(19)	1.590(59)	1.109(34)	0.626(28)
22.5	1.514(36)	1.195(31)	0.642(27)	1.461(53)	1.046(31)	0.642(27)
25.0	1.498(34)	1.188(23)	0.681(18)	1.526(53)	1.105(32)	0.630(25)
27.5	1.506(33)	1.219(23)	0.684(17)	1.640(56)	1.104(31)	0.606(24)
30.0	1.530(38)	1.152(24)	0.649(18)	1.560(59)	1.092(35)	0.662(28)
Mean	1.476 (7)	1.177 (4)	0.678(4)	1.531(10)	1.077(6)	0.633(5)
χ^2/n.d.f.	7.3/9	7.2/9	5.6/9	12.8/9	9.8/9	4.2/9
χ^2 prob.	0.61	0.62	0.78	0.17	0.37	0.88
		$e\mu$			μe	
10.0	1.540(66)	1.151(41)	0.668(36)	1.661(86)	1.132(45)	0.588(37)
12.5	1.560(57)	1.087(33)	0.663(30)	1.501(63)	1.107(38)	0.655(34)
15.0	1.482(47)	1.161(32)	0.736(29)	1.540(58)	1.143(35)	0.641(19)
17.5	1.518(47)	1.123(30)	0.692(26)	1.508(55)	1.138(34)	0.648(28)
19.3	1.470 (9)	1.142 (6)	0.722 (5)	1.528(10)	1.088 (6)	0.619 (5)
20.0	1.497(41)	1.166(27)	0.707(23)	1.593(52)	1.098(29)	0.611(23)
22.5	1.450(39)	1.175(38)	0.736(24)	1.529(49)	1.154(30)	0.642(24)
25.0	1.429(36)	1.150(26)	0.751(23)	1.551(48)	1.126(28)	0.618(22)
27.5	1.460(36)	1.153(25)	0.712(21)	1.631(49)	1.067(25)	0.568(19)
30.0	1.474(41)	1.123(27)	0.688(22)	1.491(48)	1.102(30)	0.642(23)
Mean	1.472 (8)	1.143 (5)	0.719(4)	1.533(9)	1.094(5)	0.619(4)
χ^2/n.d.f.	6.7/9	6.5/9	12.1/9	9.2/9	11.9/9	12.7/9
χ^2 prob.	0.67	0.69	0.21	0.42	0.22	0.18

Table 3.9: Global physics parameters of the dilepton fits with external constraints.

Parameter	Constraint	Ref.
$F_{B^*\bar{B}^*}$	$(50.5 \pm 3.4)\%$	[166]
$F_{B^*\bar{B}}$	$(18.5 \pm 1.9)\%$	[166]
$F_{B\bar{B}}$	$(7.4 \pm 2.4)\%$	[166]
$F_{B^*\bar{B}^*\pi}$	$(5.9 \pm 7.5)\%$	[166]
$F_{B^*\bar{B}\pi}$	$(41.6 \pm 11.8)\%$	[166]
$F_{B\bar{B}\pi}$	$(0.2 \pm 6.7)\%$	[166]
τ_{B^+}	1.641 ± 0.008 ps	[37]
τ_{B^0}	1.519 ± 0.007 ps	[37]
$\tau_{B_s^0}$	1.472 ± 0.025 ps	[37]
Δm_d	$0.507 \pm 0.004\ \hbar/\mathrm{ps}$	[37]

R^{CW} parameters (Table 3.8). The total likelihood function is[18]

$$\mathcal{L} = \prod_{j=1}^{10} \exp -\frac{1}{2}\left(\frac{y_j - y_j^0}{\sigma(y_j^0)}\right)^2 \times \prod_{l_1 l_2 = ee,\mu\mu,e\mu,\mu e} \mathcal{L}^{l_1 l_2}\,, \tag{3.82}$$

where

$$\mathcal{L}^{l_1 l_2} = \prod_{\Sigma=SS,OS} \mathcal{L}_{\Sigma}^{l_1 l_2} \times \prod_{i=1}^{7} \exp -\frac{1}{2}\left(\frac{x_i^{l_1 l_2} - x_i^{l_1 l_2,0}}{\sigma(x_i^{l_1 l_2,0})}\right)^2 \tag{3.83}$$

is the likelihood function of $l_1 l_2$ pairs which is composed of two likelihood functions (Eq. (3.73)) for the histograms of SS and OS candidates. Of course, the fit can be restricted to less than four $l_1 l_2$ categories.

3.4.4 Tests of the fitting procedure

A test sample is made with data continuum ($20.43\,\mathrm{fb}^{-1}$ from Experiments 43, 51, 67, 69 and 71 with momentum scaling to the $\Upsilon(5S)$ energy) and MC $\Upsilon(5S) \to b\bar{b}$ events ($121\ \mathrm{fb}^{-1}$) in which $f_s = 19.3\%$ and $f_{\not{B}} = 2.8\%$, i.e.

$$\left(\frac{f_s}{f_{u,d}}\right)^{\text{MC input}} = 24.8\%\,. \tag{3.84}$$

This test sample is fitted with components determined from the following statistically-independent samples:

[18]The Gaussian constraint of a variable x to a value $x^0 \pm \sigma(x^0)$ is $\mathcal{L}_{\text{Gauss}} = e^{-\frac{1}{2}((x-x^0)/\sigma(x^0))^2}/\sqrt{2\pi\sigma(x^0)}$. The normalisation is ignored in our likelihood expressions.

Table 3.10: Dilepton fit results in MC samples generated with different values of $f_s/f_{u,d}$ and $f_{\not B}$ fixed to 2.8%. The quoted errors are mostly due to the statistical uncertainties of the MC samples, which are independent.

MC input $\frac{f_s}{f_{u,d}}$ (%)	$L_{\rm int}$ (/fb)	MC truth all $f_s/f_{u,d}$ (%)	Fit results ee $f_s/f_{u,d}$ (%)	$\mu\mu$ $f_s/f_{u,d}$ (%)	$e\mu$ $f_s/f_{u,d}$ (%)	μe $f_s/f_{u,d}$ (%)	all $f_s/f_{u,d}$ (%)	$ee+\mu\mu$ $f_s/f_{u,d}$ (%)
11.5	21	11.9 ± 0.3	14.1 ± 2.9	7.4 ± 3.8	4.4 ± 3.4	3.7 ± 2.7	9.9 ± 1.7	11.6 ± 2.2
14.8	19	14.8 ± 0.3	—	—	—	—	13.1 ± 1.8	—
18.3	21	18.0 ± 0.3	—	—	—	—	15.6 ± 1.8	—
22.0	19	21.8 ± 0.4	—	—	—	—	18.2 ± 2.1	—
24.8	121	25.3 ± 0.2	24.5 ± 1.1	24.3 ± 1.3	25.3 ± 1.3	22.1 ± 1.1	24.3 ± 0.3	24.9 ± 1.0
25.9	23	25.4 ± 0.4	24.0 ± 2.8	20.9 ± 3.6	22.6 ± 3.6	14.8 ± 2.8	23.2 ± 2.1	22.9 ± 2.2
30.1	21	30.1 ± 0.5	33.7 ± 5.3	26.9 ± 4.0	24.8 ± 4.0	25.9 ± 3.4	28.4 ± 1.9	30.1 ± 2.6
34.6	21	34.1 ± 0.4	34.3 ± 3.3	29.1 ± 4.1	23.0 ± 3.9	26.7 ± 3.3	29.1 ± 1.9	32.2 ± 2.7
39.5	21	38.6 ± 0.5	37.1 ± 3.5	37.3 ± 4.5	32.1 ± 4.3	27.2 ± 3.5	33.5 ± 1.8	37.3 ± 2.7
44.6	19	44.0 ± 0.5	43.6 ± 4.7	43.8 ± 6.0	25.9 ± 5.1	32.2 ± 4.5	37.1 ± 2.3	43.8 ± 3.6

- for the continuum: $28\ \text{fb}^{-1}$ of off-resonance data from Experiments 45, 47, 49, 55, 61, 63 and 65 with momentum scaling;
- for the CC, CW and WW components: MC samples representing more than $500\ \text{fb}^{-1}$.

In the fit, the ten parameters of Table 3.9 are set to their MC input values, without uncertainty[19]. The fit converges well to the expected values (see line $f_s/f_{u,d} = 24.8\%$ of Table 3.10). As an example, Fig. 3.9 presents the projections on p_+ and p_- for the fit of dimuon events.

Further tests using MC samples generated with f_s values ranging from 10% to 30% have been performed (Table 3.10). The results for electron-muon pairs exhibit significant deviations from the input values. This puzzle couldn't be resolved and these pairs are therefore excluded from the final data fit.

Finally, a fit on the $\Upsilon(4S)$ data (Experiment 55, $72\ \text{fb}^{-1}$) is performed, where $f_s = 0$ is expected. For this fit, the B_s^0 and $B_{u,d}$ signal components are defined with a common shape and efficiency, taken from MC simulations at the $\Upsilon(4S)$ energy. The CW components are not separated between B_s^0 and $B_{u,d}$ contributions, and their yields are free parameters. The fit returns

$$f_s/f_{u,d} = (-2.8 \pm 0.5)\%\,.$$

The significant deviation from 0 is taken as an estimate of the effect of possible inaccuracies in the MC description of the shapes. It will be added as a systematic error.

[19]In practise, the total likelihood of Eq. (3.82) is used with arbitrary small values of $\sigma(y_j^0)$.

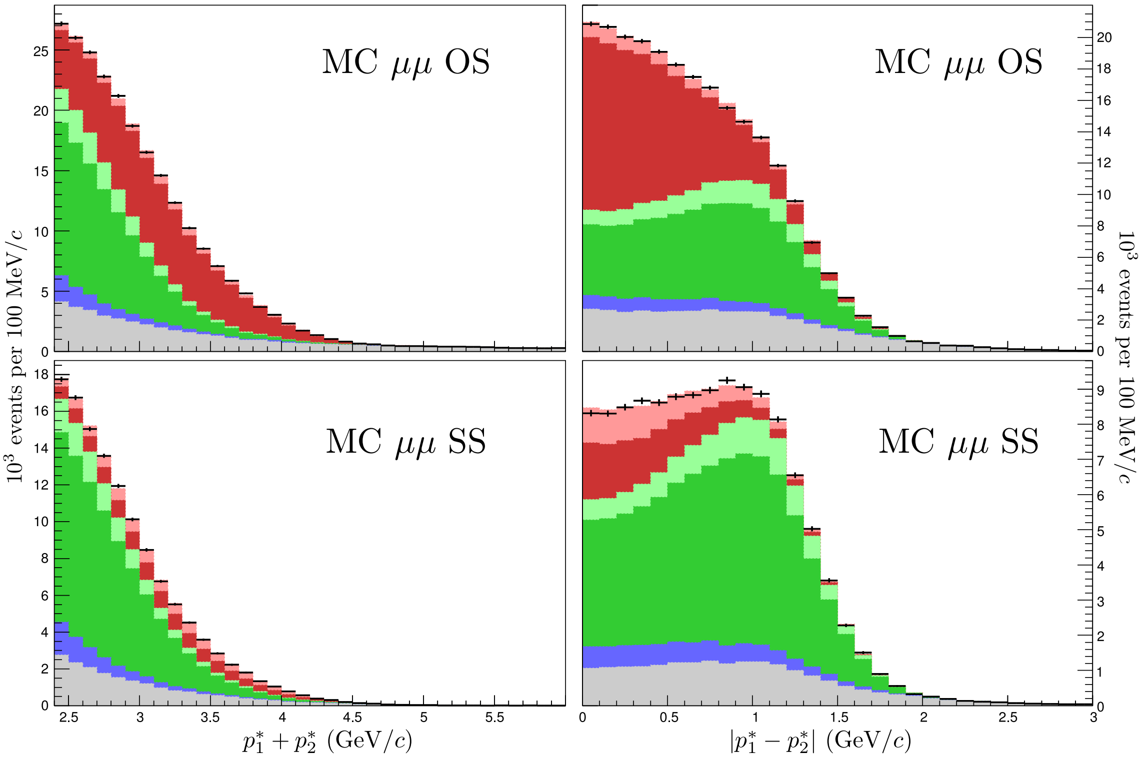

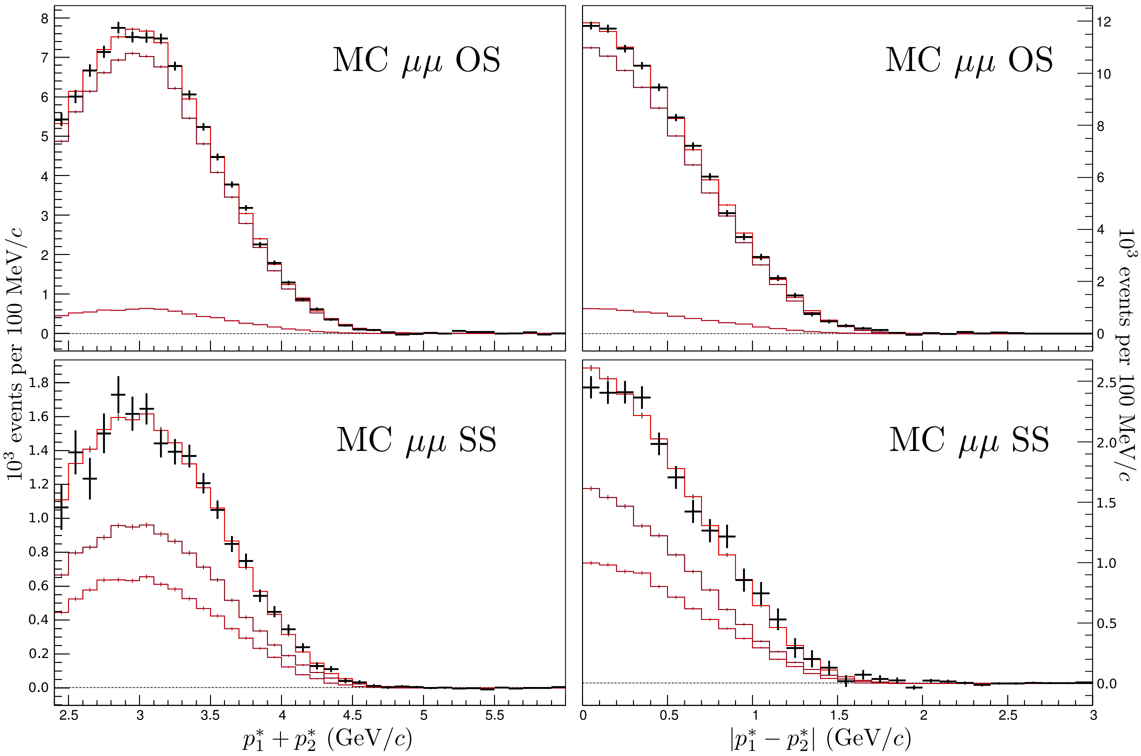

Figure 3.9: Top: Distributions of $p_+ = p_1^* + p_2^*$ (left) and $p_- = |p_1^* - p_2^*|$ (right) for SS and OS dimuon candidates in the MC sample described in the text. The points show the MC data. The total histograms show the result of the fit described in the text, which includes the following components, shown as cumulative histograms from bottom to top: continuum (grey), WW (blue), CW from $B\bar{B}$ (dark green), CW from $B_s^0\bar{B}_s^0$ (light green), CC from $B\bar{B}$ (dark red) and CC from $B_s^0\bar{B}_s^0$ (light red). Bottom: same distributions after background subtraction; the histograms show the CC component from $B_s^0\bar{B}_s^0$ (light red, smaller yield), the CC component from $B\bar{B}$ (dark red, larger yield) and their sum.

3.4.5 Fit result

Even though it is still not understood why the fitter does not recover correct $f_s/f_{u,d}$ value in MC samples for mixed electron-muon pairs, we decided to analyse the dielectron and dimuon samples in the experimental data. A common fit including only dielectron and dimuon pairs is performed on the $121\ \mathrm{fb}^{-1}$ of $\Upsilon(5S)$ data. The floating parameters which are constrained to an existing measurement converge to the correct value and error. The fit value for the continuum normalisation is $S = 2.305 \pm 0.007$. This is 0.158 ± 0.015 less than the estimated value of Eq. (3.70); it can be due to a deficient estimate of the efficiency ratio $\tilde{\varepsilon}$. The value of $f_s/f_{u,d}$ is measured to be

$$f_s/f_{u,d} = (38.6 \pm 3.8(\mathrm{fit}))\,\% \,. \tag{3.85}$$

The largest correlation coefficient between $f_s/f_{u,d}$ and another fit parameters is measured to be -0.86 for the correlation between $f_s/f_{u,d}$ and the B_s^0 lifetime. This shows the extreme sensitivity of this analysis to the B_s^0 lifetime.

The histogram and projections are presented on Figs. 3.10 and 3.11. The quoted error on $f_s/f_{u,d}$ includes all the external parameter uncertainties. It is larger than in the fits of MC samples, because the external parameters (Table 3.9) are constrained to their current world averages, not to their MC input values with negligible uncertainty. The individual contribution to the total error returned by the fit are estimated by taking the quadratic difference between the nominal error and that obtained when each group of external parameters in turn is fixed with a negligible uncertainty (Table 3.11). The absolute statistical error is estimated to be $\pm 1.0\%$, so it is only a small fraction of the error returned by the fit. This is in agreement with MC expectations: the statistical uncertainty on the $21\ \mathrm{fb}^{-1}$ MC sample with $f_s/f_{u,d} = 39.5\%$ is $\pm 2.7\%$ (Table 3.10), i.e. $2.7\%/\sqrt{6} = 1.1\%$ for $121\ \mathrm{fb}^{-1}$.

As a consistency check, the fit is again performed only on dielectron pairs, resulting in $f_s/f_{u,d} = (31.8 \pm 2.6)\%$, and only on dimuon pairs, resulting in $f_s/f_{u,d} = (45.4 \pm 3.8)\,\%$. Ignoring the systematic correlation betweem them, these two results differ already by 3σ. After the discrepancy seen in $e\mu$ and μe MC pairs, this is probably another sign that the fitting procedure is not well under control.

3.4.6 Systematic uncertainties and final result

The uncertainties on the input parameters like the $\Upsilon(5S)$ branching fractions, B_q lifetimes, mixing parameter, etc. are already included in the fit result. Several additional sources of systematic uncertainties are estimated:

- Possible differences in the PID performance between data and MC lead to an uncertainty of $\pm 0.2\%$; this is estimated by using the official Belle tables of the measured efficiency ratio between data and MC in several bins of the momentum and polar angle of the leptons in the laboratory frame. Alternative MC shapes are constructed by weighting each MC event by its corresponding efficiency ratio. Because the ratios are not constant, the resulting shapes are effectively different from those used in the nominal fit.

- The effect of the R_2 requirement is estimated by running the fit again with $R_2 < 0.4$ and $R_2 < 0.6$, $f_s/f_{u,d}$ moves by $\pm 1.6\%$.

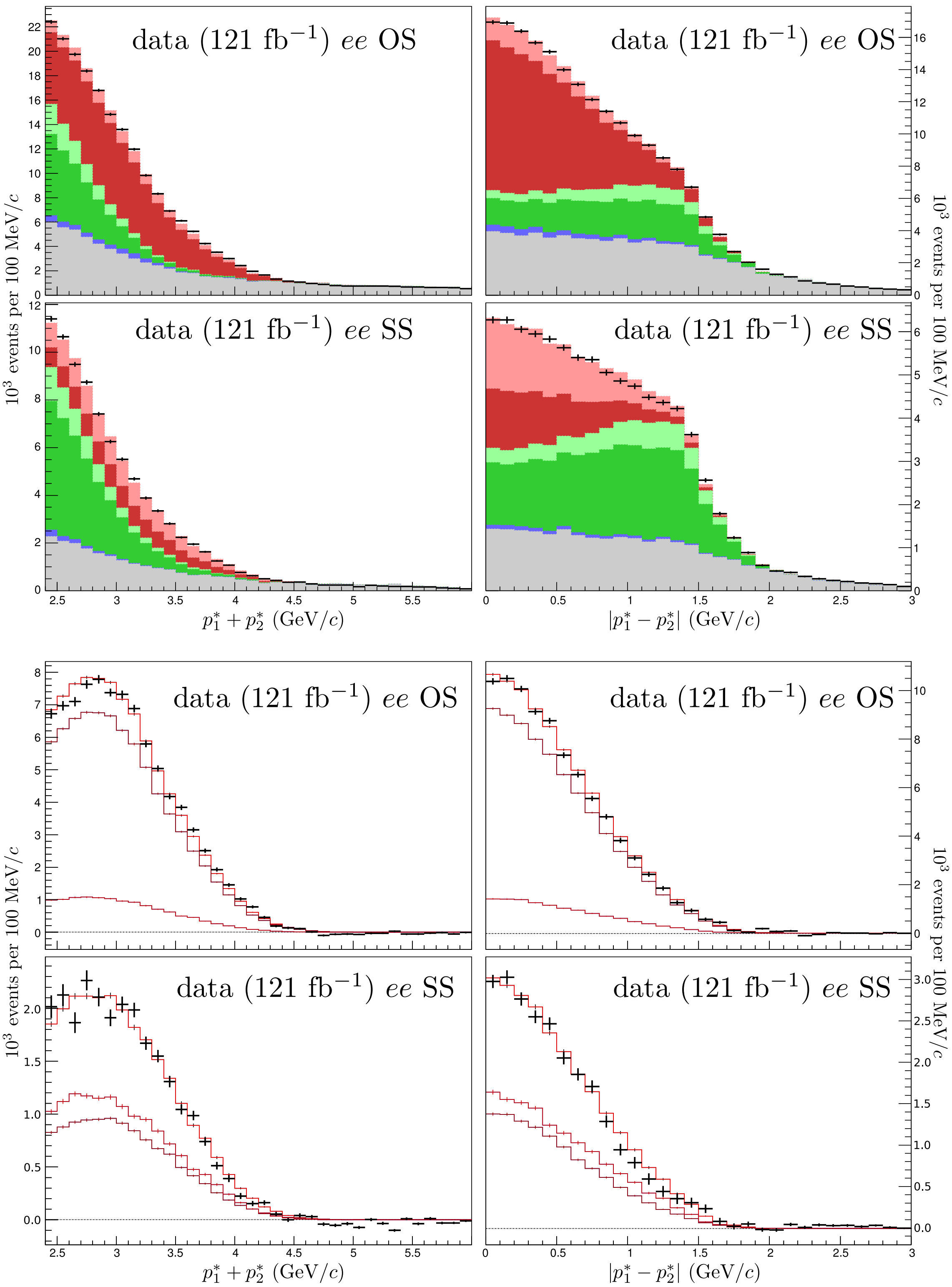

Figure 3.10: Top: Distributions of $p_+ = p_1^* + p_2^*$ (left) and $p_- = |p_1^* - p_2^*|$ (right) for SS and OS dielectron candidates in 121 fb^{-1} of $\Upsilon(5S)$ data. The points show the data. The total histograms show the result of the fit described in the text, which includes the following components, shown as cumulative histograms from bottom to top: continuum (grey), WW (blue), CW from $B\bar{B}$ (dark green), CW from $B_s^0\bar{B}_s^0$ (light green), CC from $B\bar{B}$ (dark red) and CC from $B_s^0\bar{B}_s^0$ (light red). Bottom: same distributions after background subtraction; the histograms show the CC component from $B_s^0\bar{B}_s^0$ (light red, smaller OS or larger SS yield), the CC component from $B\bar{B}$ (dark red, larger OS or smaller SS yield) and their sum.

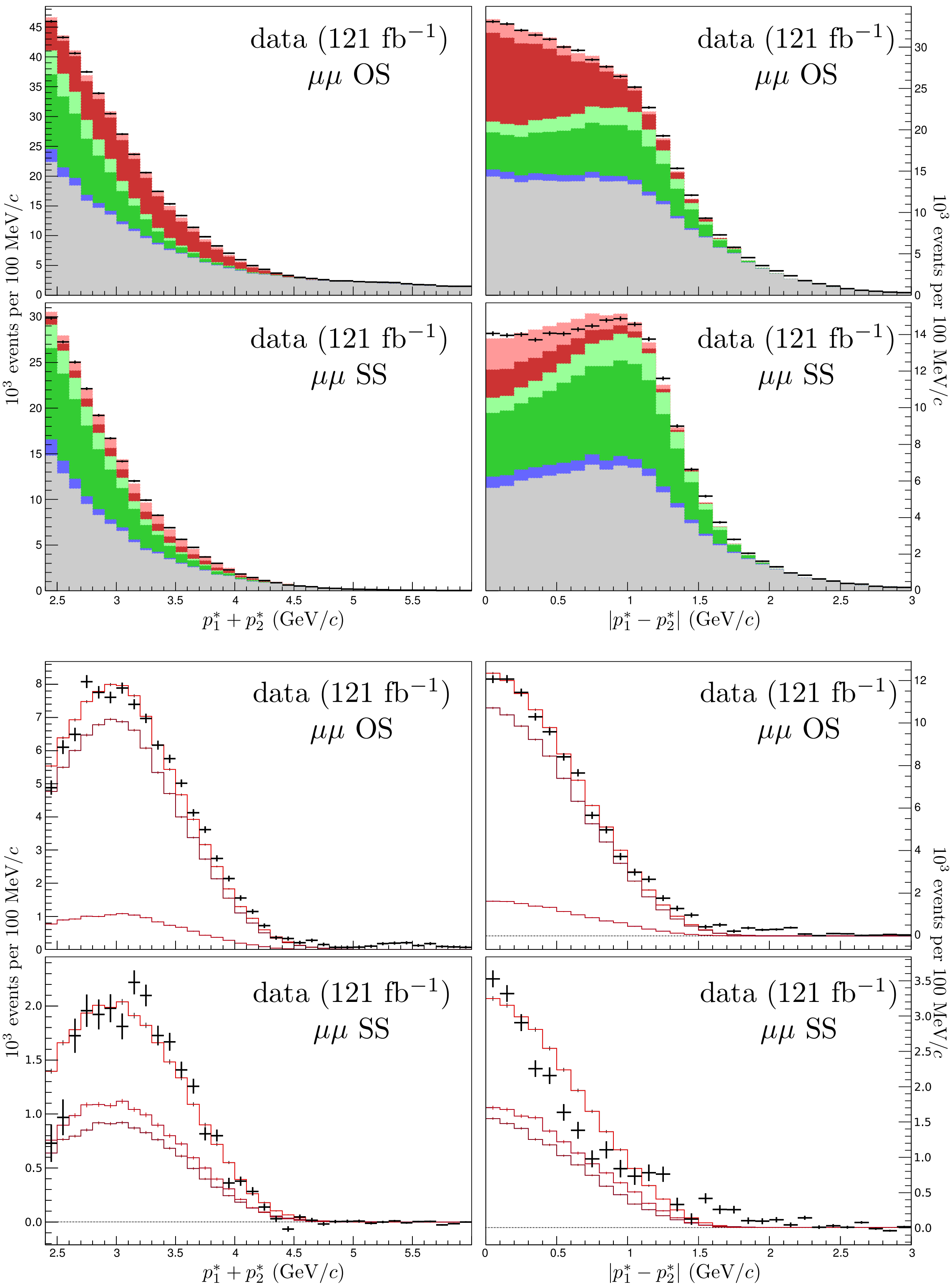

Figure 3.11: Top: Distributions of $p_+ = p_1^* + p_2^*$ (left) and $p_- = |p_1^* - p_2^*|$ (right) for SS and OS dimuon candidates in 121 fb^{-1} of $\Upsilon(5S)$ data. The points show the data. The total histograms show the result of the fit described in the text, which includes the following components, shown as cumulative histograms from bottom to top: continuum (grey), WW (blue), CW from $B\bar{B}$ (dark green), CW from $B_s^0\bar{B}_s^0$ (light green), CC from $B\bar{B}$ (dark red) and CC from $B_s^0\bar{B}_s^0$ (light red). Bottom: same distributions after background subtraction, the histograms show the CC component from $B_s^0\bar{B}_s^0$ (light red, smaller OS or larger SS yield), the CC component from $B\bar{B}$ (dark red, larger OS or smaller SS yield) and their sum.

- The effect of the lower bound of the lepton momenta is estimated by selecting leptons with $p^*_{\min} > 1.0$ or 1.3 GeV/c. $f_s/f_{u,d}$ moves by $\pm 1.0\%$.
- The binning effects are measured to be of the order of $\pm 2.0\%$, by repeating the fit with smaller and larger bins.
- The fit on $\Upsilon(4S)$ data returns $f_s/f_{u,d} = (-2.8 \pm 0.5)\%$ while 0 is expected. We choose to add a conservative $\pm 3\%$ systematic uncertainty to account for the possible discrepancy between MC and data momentum distributions.

The above effects are combined in quadrature to yield a $\pm 4.1\%$ additional absolute systematic error on $f_s/f_{u,d}$. The errors are summarized in Table 3.11, where they are compared with rough predictions from a prior feasibility study [14]. While the fit uncertainties are in reasonable agreement with expectations, taking into account differences between prediction assumptions and the actual analysis conditions, the other systematic uncertainties are a significant contribution to the total error. Our preliminary result is

$$f_s/f_{u,d} = (38.6 \pm 3.8 \pm 4.1)\% \,. \tag{3.86}$$

This is somewhat larger than the average of previous model-dependent measurements, $(26.3^{+5.2}_{-4.4})\%$ (Eq. (3.42)), but still consistent with it at the 1.6σ level.

3.5 Summary and discussion

Understanding the composition of the data sample recorded at $\Upsilon(5S)$ energy is crucial for B_s^0 studies. The current knowledge of f_s is dominated by model-dependent studies of inclusive ϕ and $D_{(s)}$ rates. A novel method based on dilepton events as witnesses of $B^0_{(s)}$ meson oscillations has been implemented. After several checks, which were not all fully satisfactory, the first preliminary result based on this model-independent method has been obtained. The dilepton method suffers from a poor signal purity and the fact that the fitting procedure require high quality spectrum for defining its components. Better rejection of the CW component would help increasing the signal purity. A selection restricted to the region in the $(\cos\theta^*_{l_1 l_2}, m_{l_1 l_2})$ plane where the signal lies may be a strategy to test further. The measurement is affected by the poor knowledge of the $B^{(*)}\bar{B}^{(*)}(X)$ fractions at $\Upsilon(5S)$. They have only been measured in $23.4\ \mathrm{fb}^{-1}$ of data and their uncertainties are mainly statistical: new measurements with the existing $121\ \mathrm{fb}^{-1}$ of data would help decreasing the error on $f_s/f_{u,d}$, as well as measurements including the Δz information. .

The relative precision ($\sim 15\%$) is worse than expectations, but better than that on the average of all the other existing measurements described at the beginning of this chapter (Eq. (3.42)). The errors on these measurements are dominated by systematic uncertainties; the better precision with dileptons is not due to the fact that a larger data sample was used. The main advantage of the dilepton method is its low theoretical uncertainty, i.e. the absence of model-dependent estimates. In addition it yields a result that is completely independent of all previous measurements.

A version of the fit descibed in Sec. 3.2.3 with the dilepton result added as an additional

Table 3.11: Summary of errors on $f_s/f_{u,d}$, compared with the predictions of the feasibility study of Ref. [14]. The latter were based on a counting experiment (see Eq. (3.64)), ignored the existence of background, and assumed that the $B^{(*)}\bar{B}^{(*)}(X)$ fractions would be measured with $121\ \mathrm{fb}^{-1}$, while values used in this analysis were obtained with $23.4\ \mathrm{fb}^{-1}$ only.

Source	Error on $f_s/f_{u,d}$ (absolute, in %)	Error on $f_s/f_{u,d}$ (relative, in %)	Prediction [14] Relative error (in %)
Statistics	1.0	2.5	1.8
MC statistics	0.1	0.3	0.0
$B^{(*)}\bar{B}^{(*)}(X)$ fractions	3.0	7.8	2.7
$B_{(s)}$ lifetimes, Δm_d	2.0	5.3	4.5
Total fit error	3.8	9.8	6.2
Binning	2.0		
R_2 cut	1.6		
Momentum cut	1.0		
Shape description	3.0		
PID	0.2		
Total other systematics	4.1		
Total	5.6	14.5	

Gaussian constraint on the ratio $f_s/f_{u,d}$ gives the following averages:

$$f_s = \left(23.4^{+2.3}_{-2.4}\right)\%\,, \tag{3.87}$$
$$f_{u,d} = \left(72.5^{+2.3}_{-2.8}\right)\%\,, \tag{3.88}$$
$$f_{\not{B}} = \left(4.1^{+3.4}_{-0.5}\right)\%\,, \tag{3.89}$$
$$\rho^s_{u,d} = \frac{f_s}{f_{u,d}} = \left(32.3^{+4.3}_{-4.1}\right)\%\,. \tag{3.90}$$

The relative uncertainty on the averaged f_s has decreased from 15% (Eq. (3.39)) to 10% (Eq. (3.87)).

Chapter 4

Measurements with exclusive $B_s^0 \to D_s^{(*)-} h^+$ $(h = \pi, K, \rho)$ decays

This chapter is dedicated to the measurements performed with $B_s^0 \to D_s^{(*)-}\pi^+$, $B_s^0 \to D_s^{(*)-}\rho^+$ and $B_s^0 \to D_s^{\mp}K^{\pm}$ decays fully reconstructed in $23.4\ \mathrm{fb}^{-1}$ of $\Upsilon(5S)$ data. These analyses are published[1] in two Letters [10, 11] reproduced in Appendix C. After a description of the B_s^0 observables and of the selection of the B_s^0 candidates, the second half of this chapter is dedicated to the fitting procedure and to the extraction of the branching fractions of these five B_s^0 modes. In addition, the following physics parameters are measured: the B_s^0 and B_s^* masses, the fractions $F_{B_s^*\bar{B}_s^*}$, $F_{B_s^*\bar{B}_s^0}$ and $F_{B_s^0\bar{B}_s^0}$ (Eqs. (3.11) to (3.13)) and the longitudinal polarisation fraction of the $B_s^0 \to D_s^{*-}\rho^+$ decay.

4.1 Expectation values of the ΔE and M_{bc} variables for B_s^0 signal

The B_s^0 signals are observed through two *standard* variables, the energy difference

$$\Delta E = E^*_{B_s^0} - E^*_{\mathrm{b}} \tag{4.1}$$

and the beam-constrained mass

$$M_{\mathrm{bc}} = \sqrt{E^{*2}_{\mathrm{b}}/c^4 - \vec{p}^{\,*2}_{B_s^0}/c^2}\,, \tag{4.2}$$

where $E^*_{B_s^0}$ and $\vec{p}^{\,*}_{B_s^0}$ are the energy and momentum of the reconstructed B_s^0 meson in the e^+e^- centre-of-mass frame, and E^*_{b} is the beam energy in the same frame[2]. As shown on Fig. 4.1, the B_s^0 signals appear in three distinct regions of the $(M_{\mathrm{bc}}, \Delta E)$ plane, depending on whether the B_s^0 originates from a $B_s^*\bar{B}_s^*$, a $B_s^*\bar{B}_s^0$ or a $B_s^0\bar{B}_s^0$ event.

[1]The branching fractions presented in this section are obtained using our f_s average of all published measurements (Eq. (3.39)) and slightly differ from those in the publications, where other f_s values were used.

[2]Unless specified otherwise, every kinematic variable is expressed in this frame.

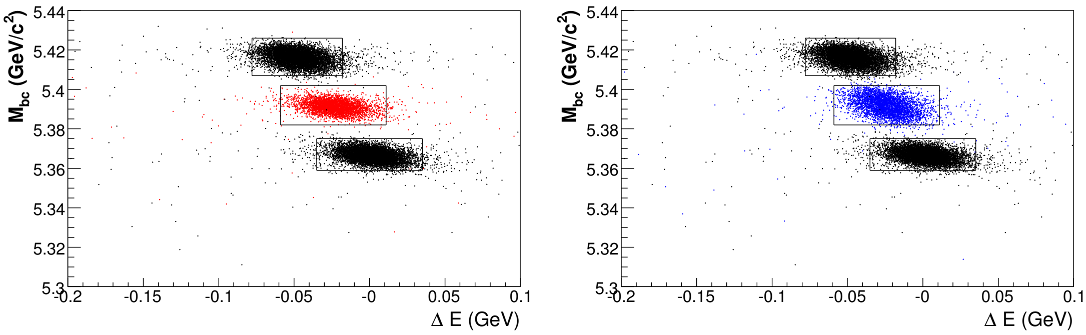

Figure 4.1: Expected two-dimensional distribution in the $(M_{\rm bc}, \Delta E)$ plane for fully reconstructed $B_s^0 \to D_s^- \pi^+$ signal decays in a Monte Carlo sample of $\Upsilon(5S)$ events. The three signal regions, indicated with rectangular boxes, correspond to $\Upsilon(5S) \to B_s^* \bar{B}_s^*$, $\Upsilon(5S) \to B_s^* \bar{B}_s^0$ and $\Upsilon(5S) \to B_s^0 \bar{B}_s^0$ events, from top to bottom, respectively. The two plots differ only for the middle $B_s^* \bar{B}_s^0$ region: on the left (right) plot, the red (blue) points represent the $B_s^0 \to D_s^- \pi^+$ signal produced without (though) an intermediate B_s^* meson.

The B_s^* signal cannot be reconstructed because the photon emitted in the $B_s^* \to B_s^0 \gamma$ has insufficient energy to be efficiently detected. Because of the small energy of the emitted photon, the momentum of the B_s^0 is assumed to be approximately the same as the B_s^* momentum. With this assumption and with the four-momentum conservation during the decays of the $\Upsilon(5S)$ and B_s^* particles, the $M_{\rm bc}$ and ΔE mean values of the B_s^0 signal depend only on the B_s^* and B_s^0 masses, $m_{B_s^*}$ and $m_{B_s^0}$, and on the beam energy, $E_{\rm b}^* = \sqrt{s}/2$. The reconstructed B_s^0 signal in $\Upsilon(5S) \to B_s^* \bar{B}_s^*$ decays has[3]

$$\langle \Delta E \rangle_{B_s^* \bar{B}_s^*} = \sqrt{\left(E_{\rm b}^{*2} - m_{B_s^*}^2 c^4\right) + m_{B_s^0}^2 c^4} - E_{\rm b}^* \,, \tag{4.3}$$

$$\langle M_{\rm bc} \rangle_{B_s^* \bar{B}_s^*} = m_{B_s^*} \,, \tag{4.4}$$

The reconstructed B_s^0 signal in $\Upsilon(5S) \to B_s^* \bar{B}_s^0$ decays has[4]

$$\langle \Delta E \rangle_{B_s^* \bar{B}_s^0} = -\frac{(m_{B_s^*}^2 - m_{B_s^0}^2) c^4}{4 \times E_{\rm b}^*} \,, \tag{4.5}$$

$$\langle M_{\rm bc} \rangle_{B_s^* \bar{B}_s^0} = \left(\frac{m_{B_s^*}^2 + m_{B_s^0}^2}{2} - \left(\frac{m_{B_s^*}^2 - m_{B_s^0}^2}{4 \times E_{\rm b}^* / c^2} \right)^2 \right)^{1/2} . \tag{4.6}$$

In $\Upsilon(5S) \to B_s^* \bar{B}_s^0$ decays, the $M_{\rm bc}$ and ΔE distributions depend, in principle, on whether or not the reconstructed B_s^0 was produced through an intermediate B_s^* excited meson. While a slight difference is seen in the distributions (Fig. 4.1), the $M_{\rm bc}$ and ΔE central

[3] Using $E_{B_s^*}^* = E_{\rm b}^*$, $p_{B_s^*}^* \approx p_{B_s^0}^*$ and hence $E_{B_s^0}^* \approx \sqrt{p_{B_s^*}^{*2} c^2 + m_{B_s^0}^2 c^4}$.

[4] The momentum conservation in the $\Upsilon(5S)$ decay gives $p_{B_s^*}^{*2} = p_{\bar{B}_s^0}^{*2}$, while the energy conservation is written as $E_{B_s^*} + E_{\bar{B}_s^0} = 2E_{\rm b}^*$. Therefore, the former is equivalent to $E_{B_s^*}^{*2} - m_{B_s^*}^2 c^4 = E_{\bar{B}_s^0}^{*2} - m_{B_s^0}^2 c^4$. An expression for $E_{B_s^0}$ can be found by substituting $E_{B_s^*}^*$ by $(2E_{\rm b}^* - E_{\bar{B}_s^0})$.

Table 4.1: $M_{\rm bc}$ fit results in signal MC with generated B_s^0 and B_s^* particles (before detector simulation), and with reconstructed $B_s^0 \to D_s^- \pi^+$ candidates (after detector simulation).

Beam-constrained mass		Mean value (MeV/c^2)	σ (MeV/c^2)
Generated B_s^*	$\sqrt{E_{\rm b}^{*2}/c^4 - p_{B_s^*}^{*{\rm MC}^2}/c^2}$	5416.91 ± 0.03	2.59 ± 0.02
Generated B_s^0	$\sqrt{E_{\rm b}^{*2}/c^4 - p_{B_s^0}^{*{\rm MC}^2}/c^2}$	5417.01 ± 0.03	3.45 ± 0.02
Reconstructed B_s^0	$\sqrt{E_{\rm b}^{*2}/c^4 - p_{B_s^0}{}^{*2}/c^2}$	5417.07 ± 0.04	3.71 ± 0.03

Table 4.2: Expected $M_{\rm bc}$ and ΔE mean values for the three signal regions, computed from Eqs. (4.4) to (4.7) using the values of MC input for B_s^0 and B_s^* masses. These are compared to the fitted mean values in the MC, given with their statistical errors.

Region	Observable		MC input	fitted value on MC
$B_s^*\bar{B}_s^*$	$M_{\rm bc}$	(MeV/c^2)	5416.60	5417.02 ± 0.04
	ΔE	(MeV)	-49.3	-49.0 ± 0.2
$B_s^* B_s^0$	$M_{\rm bc}$	(MeV/c^2)	5391.85	5392.37 ± 0.04
	ΔE	(MeV)	-24.6	-24.3 ± 0.2
$B_s^0\bar{B}_s^0$	$M_{\rm bc}$	(MeV/c^2)	5367.10	5367.39 ± 0.03
	ΔE	(MeV)	0	0.5 ± 0.2

values for these two cases are the same when $p_{B_s^*}^{*2}$ is approximated by $p_{B_s^0}^{*2}$ in the $B_s^* \to B_s^0\gamma$ decay. The reconstructed B_s^0 signal in $\Upsilon(5S) \to B_s^0\bar{B}_s^0$ decays is the simplest case because each B_s^0 takes half of the energy, $E_{B_s^0}^* = E_{\rm b}^*$,

$$\langle \Delta E \rangle_{B_s^0\bar{B}_s^0} = 0\,, \tag{4.7}$$
$$\langle M_{\rm bc} \rangle_{B_s^0\bar{B}_s^0} = m_{B_s^0}\,. \tag{4.8}$$

In order to quantify the systematic effect on the $M_{\rm bc}$ peak position due to the approximation $p_{B_s^*}^* \approx p_{B_s^0}^*$ in $B_s^* \to B_s^0\gamma$ decays, we measured the central value of the $M_{\rm bc}$ distributions in MC events for which we know the true B_s^* momentum. As shown in Table 4.1, there is a 0.10 ± 0.04 MeV/c^2 difference, at generator level, between the mean of the $M_{\rm bc}$ distribution and that of $\sqrt{E_{\rm b}^{*2} - p_{B_s^*}^{*2}}$. The systematic uncertainty on the $M_{\rm bc}$ peak position measurement (due to this approximation) is estimated to be ± 0.14 MeV/c^2.

A comparison, in MC data, between input and central values of the $M_{\rm bc}$ and ΔE distributions has been performed. Fits on MC signal sample can provide an experimental confirmation of the validity of these formulae. The central values of $M_{\rm bc}$ and ΔE distributions are measured in MC with Gaussian fits, Table 4.2 presents the results of such tests. The difference observed for $M_{\rm bc}$ in the $B_s^*\bar{B}_s^*$ region, 0.42 ± 0.04 MeV/c^2, is significant and cannot be explained by the ± 0.14 MeV$/c^2$ uncertainty due to $p^*_{B_s^*} \approx p^*_{B_s^0}$ approximation. An additional systematic of ± 0.44 MeV$/c^2$ will be added to the B_s^* mass result (Sec. 4.7.2). Because $\sim 90\%$ of the signal is concentrated in the $B_s^*\bar{B}_s^*$ region, the small discrepancies in the $B_s^*\bar{B}_s^0$ and $B_s^0\bar{B}_s^0$ region will not affect the results. Indeed, we are confident that the parametrisation of the signal $M_{\rm bc}$ and ΔE mean values returns the correct B_s^0 and B_s^* masses.

4.2 Reconstruction and selection of B_s^0 candidates

4.2.1 Preselection

The B_s^0 decays are fully reconstructed from their final state particles. The charged tracks are identified as pions or kaons, as described in Sec. 2.3.3.

The $\rho^\pm$ candidates are reconstructed via the $\rho^+ \to \pi^0\pi^+$ mode. The π^0 candidates are reconstructed via the $\pi^0 \to \gamma\gamma$ mode and the photon energies are fitted, assuming the π^0 decay point, such that the diphoton invariant mass, $M_{\gamma\gamma}$, equals the nominal π^0 mass (see Sec. 2.3.3).

The D_s^- candidates are formed in three different modes. The first one is $D_s^- \to \phi\pi^-$. The ϕ candidates are reconstructed via the $\phi \to K^+K^-$ mode using a pair of oppositely charged kaons with an invariant mass near the nominal ϕ mass. The D_s^- candidates are formed by adding a charged pion to the kaon pair. The second D_s^- mode is $D_s^- \to K^{*0}K^-$. The K^{*0} candidates[5] are formed with a kaon and a pion of opposite charges. The strong decay of the K^{*0} imposes that the kaon, added to the K^{*0} to form a D_s^- candidate, must have an opposite charge with respect to that coming from the K^{*0} decay. The third D_s^- mode is $D_s^- \to K_S^0K^-$. The K_S^0 candidates are reconstructed via the decay $K_S^0 \to \pi^+\pi^-$. The selection [188, 189] consists of two oppositely charged tracks (without $\mathcal{R}_{K/\pi}$ requirement) passing cuts on the z distance of the two tracks, $z_{\rm dist}$, on the distance in the $r-\phi$ plane of the K_S^0 vertex from the interaction point (IP), $r_{K_S^0}$, on the angle between the reconstructed K_S^0 and the line between the IP and the K_S^0 vertex, $\Delta\phi$, and the smallest impact parameter among the two daughters, dr. The requirements on these four variables depend on the number of K_S^0 daughters having a track with SVD hits (Table 4.3). The D_s^- candidate is formed by adding a charged kaon to the pion pair.

The D_s^{*-} candidates are reconstructed via the $D_s^{*-} \to D_s^-\gamma$ mode with a D_s^- candidate and a photon.

The B_s^0 candidates are formed with a D_s^- or a D_s^{*-} candidate and a π^+, K^+ or ρ^+ candidate within the ranges $M_{\rm bc} > 5.3$ GeV$/c^2$ and $\Delta E \in [-0.3, 0.4]$ GeV.

The invariant mass of the intermediate mesons, calculated from the final state particles, is required to be close to the expected nominal masses. The invariant mass distributions are shown in Figs. 4.2 and 4.3. From the resolutions (measured in MC with a Gaussian fit) and the known proper widths (for ϕ and K^{*0} resonances only), mass windows are defined as shown in Table 4.4. These windows correspond to standard choices. The K^{*0} channel is affected by a lot of background, therefore a tight window is chosen. The D_s^- mass requirements are not the same for all the B_s^0 modes: due to a large expected signal and low background in the $B_s^0 \to D_s^-\pi^+$ channel, a wide mass range is allowed; the expected signal

[5] also known as $K^*(892)^0$.

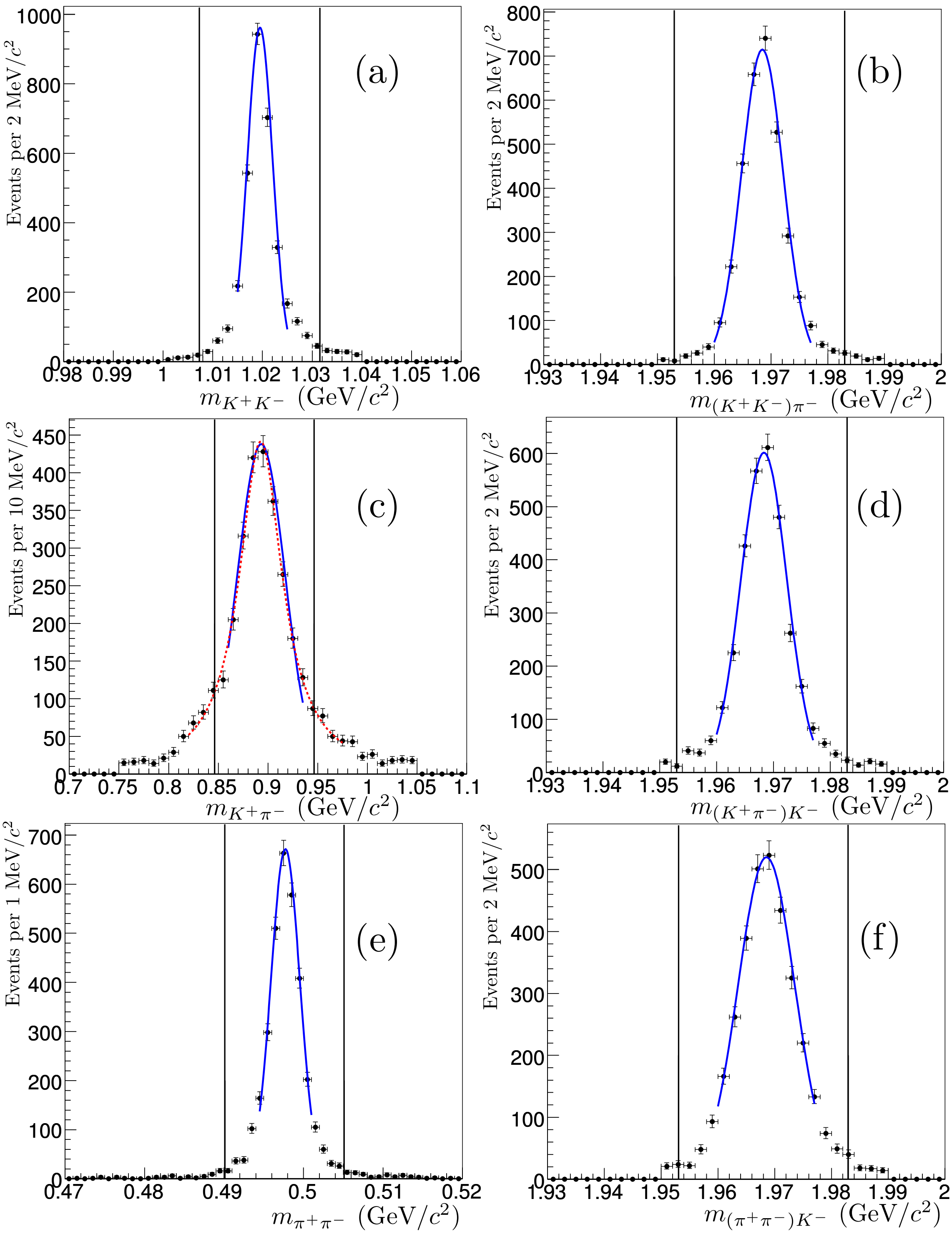

Figure 4.2: Invariant mass distributions of $\phi \to K^+K^-$ (a), $D_s^- \to \phi\pi^-$ (b), $K^{*0} \to K^+\pi^-$ (c), $D_s^- \to K^{*0}K^-$ (d), $K_S^0 \to \pi^+\pi^-$ (e), $D_s^- \to K_S^0 K^-$ (f) candidates in signal MC, with Gaussian fits (blue solid curves). The dotted red curve on the $K^{*0} \to K^+\pi^-$ distribution (c) is a fit with a Breit-Wigner function. The vertical lines show the selected mass ranges (see Table 4.4).

Table 4.3: Geometrical requirements on the K_S^0 candidates.

Category	dr (cm)	$\Delta\phi$ (rad)	$z_{\rm dist}$ (cm)	$r_{K_S^0}$ (cm)
Both daughters with hits in SVD	> 0.03	< 0.35	< 2	> 0.08
Only one daughter with hits in SVD	> 0.10	< 0.40	< 40	< 9.0
No daughter with hits in SVD	> 0.10	< 0.05	< 6.5	> 1.5

Table 4.4: Branching fractions [37] and mass windows (defined by their central values [37] and half widths) of selected mesons. The three D_s^- mass windows correspond to the $B_s^0 \to D_s^- \pi^+$, $B_s^0 \to D_s^\mp K^\pm$ and other B_s^0 analyses, respectively.

Decay	$\mathcal{B}$ (%)	Mass	Mass window (MeV/c^2)	
$\pi^0 \to \gamma\gamma$	98.823(34)	m_{π^0}	135.0	± 13
$\rho^+ \to \pi^+\pi^0$	99.955(5)	m_ρ	775.5	± 100
$K_S^0 \to \pi^+\pi^-$	69.20(5)	$m_{K_S^0}$	497.6	± 7.5
$\phi \to K^+K^-$	48.9(5)	m_ϕ	1019.5	± 12
$K^{*0} \to K^+\pi^-$	$\frac{2}{3} \times 99.761(21)$	$m_{K^{*0}}$	895.9	± 50
$D_s^{*-} \to D_s^-\gamma$	94.2(7)	$m_{D_s^{*-}} - m_{D_s^-}$	143.8	± 13
$D_s^- \to \phi\pi^-$	2.32 ± 0.14			
$D_s^- \to K^{*0}K^-$	2.60 ± 0.15	$m_{D_s^-}$	1968.5	$\pm 15/\pm 8/\pm 10$
$D_s^- \to K_S^0 K^-$	1.02 ± 0.06			

of the $B_s^0 \to D_s^\mp K^\pm$ channel is tiny, and background is reduced by choosing a tighter D_s^- window (optimised as explained below). An intermediate ± 10 MeV/c^2 window is chosen for the other modes where the background is mainly originating from neutral particle reconstruction.

4.2.2 Background study and optimised continuum rejection

Further selection requirements are applied in order to reduce the continuum events that are selected together with the signals.

Signal Monte Carlo events were fully simulated, using EvtGen [190] as decay generator and GEANT [191] for simulating the interactions in the Belle detector. For each studied B_s^0 decay mode and for each $\Upsilon(5S)$ production mode ($B_s^*\bar{B}_s^*$, $B_s^*\bar{B}_s^0$, $B_s^0\bar{B}_s^0$), 30k events were generated: 10k for each D_s^- channel ($\phi\pi^-$, $K^{*0}K^-$, $K_S^0K^-$). The two polarisations of the $B_s^0 \to D_s^{*-}\rho^+$ decay are simulated separately. The signal MC samples are used to measure the reconstruction efficiencies needed for continuum rejection optimisation and branching fraction extractions, and to determine fit shapes (see next section). The

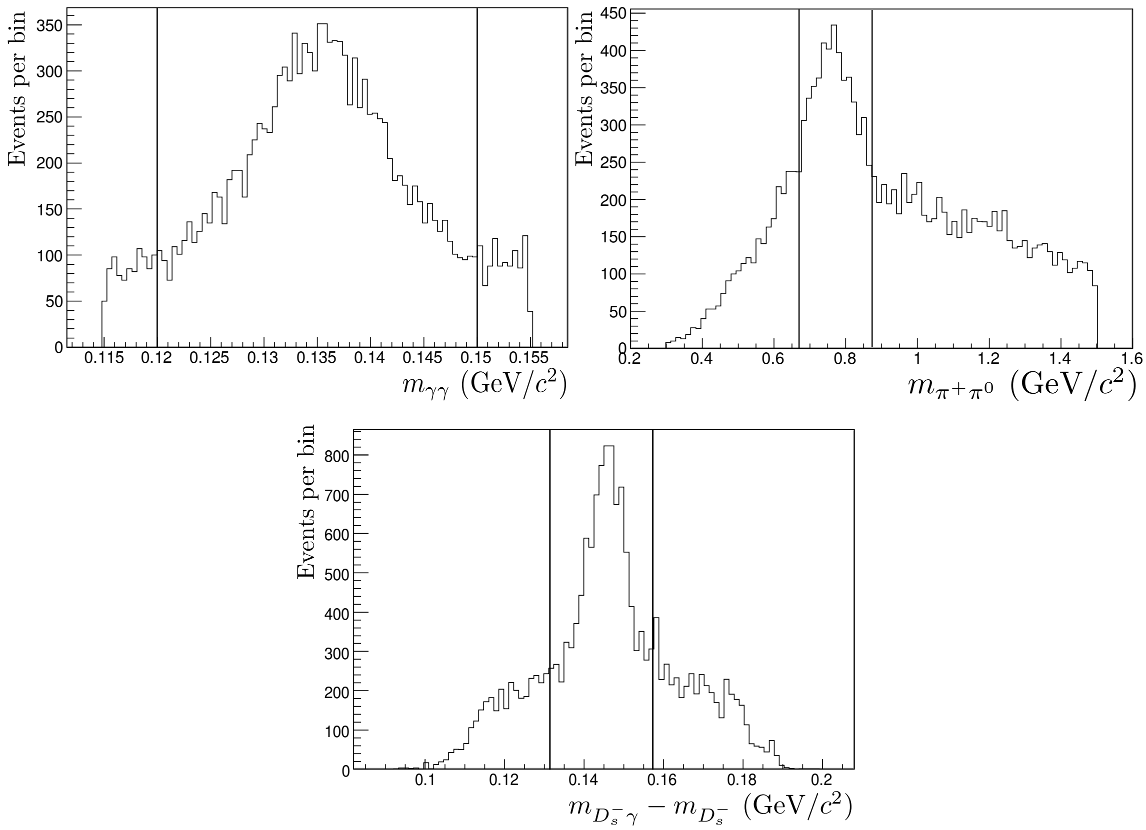

Figure 4.3: Top: Invariant mass distributions of $\pi^0 \to \gamma\gamma$ (left) and $\rho^+ \to \pi^+\pi^0$ (right) candidates in signal MC. Bottom: Distribution of the invariant mass difference $m(D_s^-\gamma) - m(D_s^-)$ for D_s^{*-} candidates in signal MC. The vertical lines show the selected mass ranges (see Table 4.4).

standard deviations of the MC distributions (see Table 4.12 below) are also used to define the three signal regions in $M_{\rm bc}$ and ΔE. The signal regions will be used for background rejection optimisation and for monitoring the fit result. They are defined as $\pm 2.5\sigma$ intervals around the expected values and are shown as rectangles in the $(M_{\rm bc}, \Delta E)$ scatter plots. For the $B_s^*\bar{B}_s^*$ signal, the $M_{\rm bc}$ region is defined as $5.407 < M_{\rm bc} < 5.426$ GeV/c^2, while the ΔE region is defined as $-80 < \Delta E < -17$ MeV, $-84 < \Delta E < -9$ MeV, $-144 < \Delta E < 16$ MeV and $-139 < \Delta E < 32$ MeV for the $B_s^0 \to D_s^-\pi^+$ (and $B_s^0 \to D_s^\mp K^\pm$), $B_s^0 \to D_s^{*-}\pi^+$, $B_s^0 \to D_s^-\rho^+$ and $B_s^0 \to D_s^{*-}\rho^+$ modes, respectively.

The preselections have also been run on a MC sample meant to reproduce a realistic inclusive $\Upsilon(5S)$ sample and representing approximately three times the data statistics. This is used to study possible physics background in the $(M_{\rm bc}, \Delta E)$ plane (as an example, see Fig. 4.4 for the $B_s^0 \to D_s^-\pi^+$ selection). Besides the signal, which lies as expected, several other B_s^0 decays contaminate the distributions. The contaminations from B_s^0 decays that have been identified are summarised in Table 4.5. No further cuts are applied to reduce specifically these contaminations.

$B_s^0 \to D_s^{*-}(\to D_s^-\gamma)\pi^+$ events are sometimes reconstructed as $B_s^0 \to D_s^-\pi^+$ candidates, without photon. This makes a negative shift along the ΔE axis. The same hap-

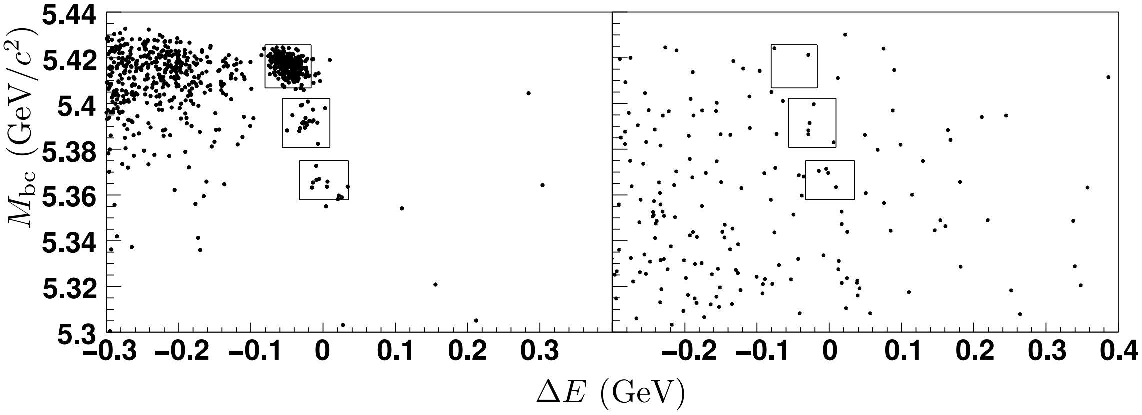

Figure 4.4: $M_{\rm bc}$ and ΔE distributions of $B_s^0 \to D_s^-\pi^+$ candidates in a generic $e^+e^- \to b\bar{b}$ MC sample representing 71 fb^{-1}. The left (right) plot contains only events with a pair of B_s^0 (non-strange B) mesons. The three boxes represent the $B_s^*\bar{B}_s^*$, $B_s^*\bar{B}_s^0$ and $B_s^0\bar{B}_s^0$ signal regions, from top to bottom. On the left plot, the contamination from true $B_s^0 \to D_s^{*-}\pi^+$ decays can clearly be seen at low ΔE values.

Table 4.5: Cross-contamination between the studied B_s^0 modes.

Analysis	Contamination from
$B_s^0 \to D_s^-\pi^+$	$B_s^0 \to D_s^{*-}\pi^+$
$B_s^0 \to D_s^\mp K^\pm$	$B_s^0 \to D_s^-\pi^+$, $B_s^0 \to D_s^{*-}\pi^+$
$B_s^0 \to D_s^{*-}\pi^+$	$B_s^0 \to D_s^-\pi^+$, $B_s^0 \to D_s^-\rho^+$
$B_s^0 \to D_s^-\rho^+$	$B_s^0 \to D_s^{*-}\rho^+$
$B_s^0 \to D_s^{*-}\rho^+$	—

pens with ρ modes: $B_s^0 \to D_s^{*-}\rho^+$ events appear as $B_s^0 \to D_s^-\rho^+$ candidates with lower ΔE values. $B_s^0 \to D_s^-\rho^+$ events are also sometimes selected as $B_s^0 \to D_s^{*-}\pi^+$ candidates without the π^0, giving again candidates with lower ΔE values. $B_s^0 \to D_s^-\pi^+$ events contaminate the $B_s^0 \to D_s^{*-}\pi^+$ sample when they are associated with random photon coming from the decay of the other B_s^0. These events exhibit too large ΔE values. The Cabibbo-suppressed $B_s^0 \to D_s^\mp K^\pm$ events are contaminated by the $B_s^0 \to D_s^{(*)-}\pi^+$ events which are selected when the pion is misidentified as a kaon. Unfortunately, the kaon fake rate and the Cabibbo-suppression factor are of the same order, making the signal and these backgrounds of comparable magnitudes. However they are not located in the same regions of the $(M_{\rm bc}, \Delta E)$ plane, even though there is an overlap between those regions. In addition to the specific above-mentioned B_s^0 contaminations, there are background events that are due to B decays. As can be seen in Fig. 4.4, this background is very low and spread over all the $(M_{\rm bc}, \Delta E)$ plane.

Finally the main source of background events comes from $e^+e^- \to q\bar{q}$ ($q = u, d, s, c$)

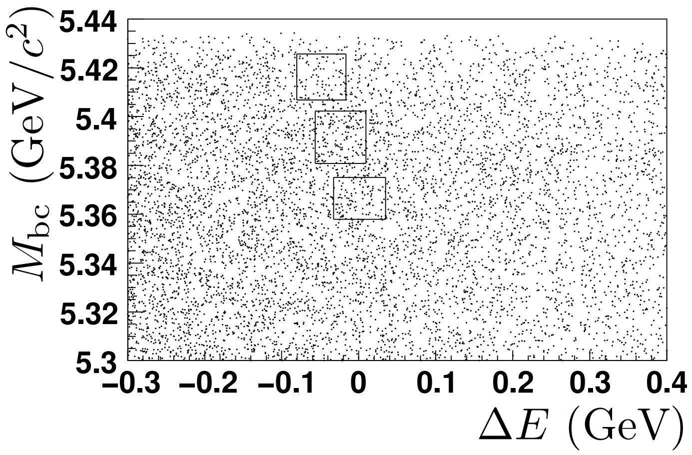

Figure 4.5: $M_{\rm bc}$ and ΔE scatter plot of $B_s^0 \to D_s^- \pi^+$ candidates in a continuum MC sample representing $66~\mathrm{fb}^{-1}$. The three boxes shows the signal region.

events. We processed a MC sample of such events representing $66~\mathrm{fb}^{-1}$. This background is continuously spread over the whole $(M_{\rm bc}, \Delta E)$ plane (see Fig. 4.5 as an example), hence its name of continuum. Topology differences between the continuum and the signal are exploited in order to reduce the background. This can be done in several ways:

- A cut can be applied on the second Fox-Wolfram moment, $R_2 = H_2/H_0$ [153]. This quantity is smaller for spherical events ($e^+e^- \to b\bar{b}$, signal) than for jet-like events (continuum).
- The so-called KSFW method [192, 193] is based on a Fisher discriminant [194] made of 16 Fox-Wolfram moments and the missing momentum. This sophisticated technique has been applied in $\Upsilon(4S)$ analyses and is expected to yield a better signal significance than a selection based only on R_2; however the improvement is not very significant in $\Upsilon(5S)$ analyses. In addition, it requires the background to be well described in the MC, which is not the case at the $\Upsilon(5S)$ energy.
- A requirement on the decay angle can be applied in any scalar-to-vector-scalar decay. As detailed in Appendix B, the angular distribution is not uniform for such a decay. The decays $D_s^- \to \phi\pi^-$, $D_s^- \to K^{*0}K^-$, $B_s^0 \to D_s^-\rho^+$ and $B_s^0 \to D_s^{*-}\pi^+$ all fall into this category. The decay angle, θ, is defined as the angle between the momenta of the mother and one of the vector's daughters in the vector rest frame. The first three decays have a $\cos^2\theta$ distribution, while $B_s^0 \to D_s^{*-}\pi^+$ has a $1-\cos^2\theta$ distribution: the difference is due to the D_s^{*-} emitting a photon, while the other intermediate vector mesons decay into two pseudo-scalar particles. As shown below, adding conditions on the decay angles has a very small impact on the signal significance.

Three rejections strategies have been tested with MC samples: R_2 requirement, R_2 and decay angle requirements, and KSFW requirements. In each case, the cut values are chosen such as to maximise a figure of merit defined as

$$S = \frac{N_{\rm sig}}{\sqrt{N_{\rm sig} + N_{\rm back}}} \,. \tag{4.9}$$

Table 4.6: Continuum rejection cuts for the five B_s^0 modes, together with their efficiencies (with respect to the preselection) on signal, $\varepsilon_{\rm sig}$, and continuum, $\varepsilon_{\rm cont}$. The cut on $\cos\theta_{D_s^-}$ is only applied to the $D_s^- \to \phi\pi^-$ and $D_s^- \to K^{*0}K^-$ channels.

Mode	Selection requirements	$\varepsilon_{\rm sig}$ (%)	$\varepsilon_{\rm cont}$ (%)
$B_s^0 \to D_s^-\pi^+$	$R_2 < 0.5, \lvert\cos\theta_{D_s^-}\rvert > 0.20$	95	57
$B_s^0 \to D_s^\mp K^\pm$	$R_2 < 0.4, \lvert\cos\theta_{D_s^-}\rvert > 0.35$	85	27
$B_s^0 \to D_s^{*-}\pi^+$	$R_2 < 0.5$	93	60
$B_s^0 \to D_s^-\rho^+$	$R_2 < 0.35$	82	31
$B_s^0 \to D_s^{*-}\rho^+$	$R_2 < 0.35$	86	36

$N_{\rm sig}$ and $N_{\rm back}$ stand for the expected number of signal and total background events, respectively, and are measured in the dominant signal region, $B_s^*\bar{B}_s^*$, of the $(M_{\rm bc}, \Delta E)$ plane. $N_{\rm sig}$ is evaluated under specific branching fraction assumptions from the efficiencies measured with signal MC as the sum of the correctly reconstructed signal, $N_{\rm sig}^{\rm good}$, and the incorrectly reconstructed signal, $N_{\rm sig}^{\rm bad}$. The expected number of continuum events is estimated from the continuum MC sample. When the region of other peaking backgrounds overlaps with the signal region, the number of peaking background events is also evaluated and added to $N_{\rm back}$. For the $B_s^0 \to D_s^\mp K^\pm$ analysis, the number of contaminating $B_s^0 \to D_s^-\pi^+$ events is obtained from the efficiency measured with $B_s^0 \to D_s^-\pi^+$ MC, but is corrected for the known discrepancy in $\pi^\pm$ fake-rate between the real data and the simulated data. There are approximately twice more misidentified pions (i.e. true pions identified as kaons) in the real data than in the MC.

Several optimisations have been performed for the low-signal $B_s^0 \to D_s^\mp K^\pm$ mode: in addition to the R_2 and $\cos\theta_{D_s^-}$ requirements, the D_s^- mass window has also been optimised (Fig. 4.6). The kaon identification cut has been checked as well but no improvement can be obtained by tightening the $\mathcal{R}_{K/\pi}$ requirement imposed in the preselection.

The final requirements for the different B_s^0 modes are summarised in Table 4.6. Except for $B_s^0 \to D_s^-\pi^+$ and $B_s^0 \to D_s^\mp K^\pm$, where $\cos\theta_{D_s^-}$ is also used, the background rejection is based solely on the R_2 quantity because of its simplicity and its low systematic uncertainty. Tables 4.7 to 4.10 show the efficiencies, signal yields, background yields, figures of merit, and signal-to-background ratios as measured in the above-mentioned MC samples for the five B_s^0 decays. The expectations are normalised to the data statistics, i.e. $23.4\ {\rm fb}^{-1}$.

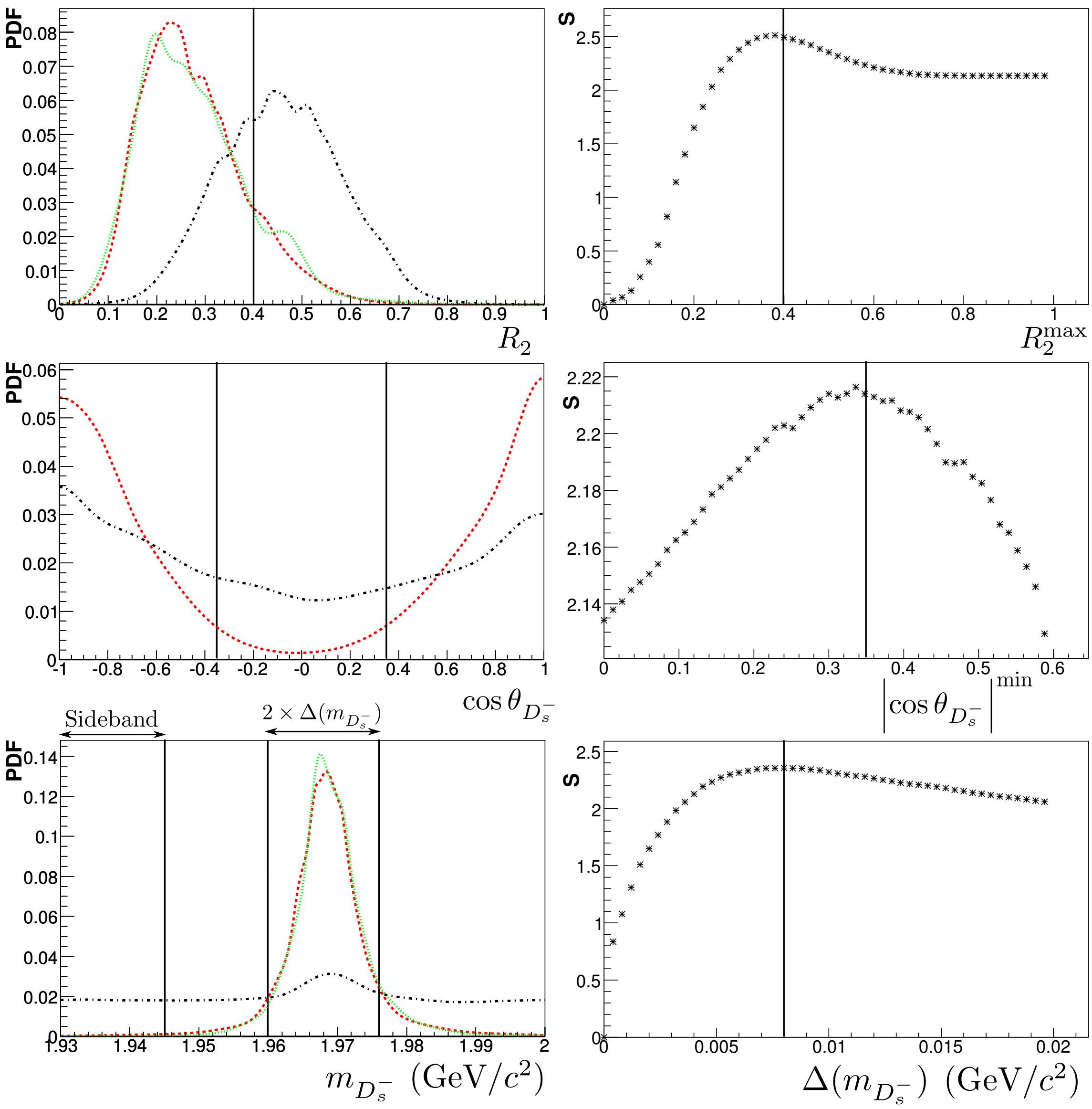

Figure 4.6: From top to bottom: optimisation of the R_2, $\cos\theta_{D_s^-}$ and D_s^- mass cuts for the $B_s^0 \to D_s^{\mp}K^{\pm}$ selection. Right: distribution of the cut variable for signal (red dashes) signal, $B_s^0 \to D_s^-\pi^+$ background (green dots) and continuum (blue dash-dots), normalised to the same area. Left: figure of merit, S, as a function of the cut value. The vertical lines show the chosen cut values.

Table 4.7: Expected signal efficiencies (ε), signal yields (N_{sig}), background yields (N_{back}), figures of merit (S), and signal-to-background ratios in the three signal regions for the $B_s^0 \to D_s^- \pi^+$ selection. The values before the continuum rejection are shown for comparison. The following assumptions are made: $\mathcal{B}(B_s^0 \to D_s^- \pi^+) = 3.0 \times 10^{-3}$, $F_{B_s^* \bar{B}_s^*} = 0.93$ [4] and $F_{B_s^* B_s^0} = 0.06$.

Signal region	D_s^- mode	ε (%)	N_{sig}	N_{back}	S	$N_{\text{sig}}/N_{\text{back}}$
$B_s^* \bar{B}_s^*$	$\phi\pi^-$	29.1	50	5.1±1.4	6.7	9.8
	$K^{*0}K^-$	22.0	43	16.7±2.5	5.6	2.6
	$K_S^0 K^-$	29.0	35	6.2 ± 1.5	5.5	5.6
	All		128	28 ± 3	10.2	4.6
Mass cuts only	All		135	49 ± 4	10.0	2.8
$B_s^* \bar{B}_s^0$	$\phi\pi^-$	29.6	3.3	13 ± 2	0.8	0.3
	$K^{*0}K^-$	21.6	2.7	28 ± 3	0.5	0.1
	$K_S^0 K^-$	28.9	2.3	11 ± 2	0.6	0.2
	All		8.3	51 ± 4	1.1	0.2
Mass cuts only	All		8.7	79 ± 5	0.9	0.1
$B_s^0 \bar{B}_s^0$	$\phi\pi^-$	28.9		12 ± 2		
	$K^{*0}K^-$	21.4	< 0.6	16 ± 2	<0.3	<0.1
	$K_S^0 K^-$	29.3		10 ± 2		
	All		1.4	35 ± 4	0.2	0.04
Mass cuts only	All		1.4	61 ± 5	0.2	0.02

Table 4.8: Expected signal efficiencies (ε), signal yields (N_{sig}), background yields (N_{back}), figures of merit (S), and signal-to-background ratios in the $B_s^* \bar{B}_s^*$ signal region for the $B_s^0 \to D_s^\mp K^\pm$ selection. The values before the continuum rejection are shown for comparison. The following assumptions are made: $\mathcal{B}(B_s^0 \to D_s^- \pi^+) = 3.5 \times 10^{-3}$, $F_{B_s^* \bar{B}_s^*} = 0.90$ and $\mathcal{B}(B_s^0 \to D_s^\mp K^\pm) = 3.7 \times 10^{-4}$.

D_s^- mode	ε (%)	N_{sig}	$N_{\text{back}} = N_{udsc} + N_{D_s^- \pi^+}$	S	$N_{\text{sig}}/N_{\text{back}}$
$\phi\pi^-$	20.6	4.3	2.4=1.6+0.8	1.7	1.8
$K^{*0}K^-$	15.5	3.6	3.5=2.8+0.7	1.4	1.0
$K_S^0 K^-$	21.4	3.2	2.2=1.8+0.2	1.4	1.5
All		11.1	8.2=6.3+1.9	2.5	1.4
Mass cuts only		13.1	25.7=23.4+2.3	2.1	0.5

Table 4.9: Expected signal efficiencies (ε), signal yields ($N_{\rm sig}$), background yields ($N_{\rm back}$), figures of merit (S), and signal-to-background ratios in the $B_s^*\bar{B}_s^*$ signal region for the $B_s^0 \to D_s^{*-}\pi^+$ selection. The values for alternative continuum rejection cuts (and without any) are shown for comparison. The following assumptions are made: $\mathcal{B}(B_s^0 \to D_s^{*-}\pi^+) = 3.3 \times 10^{-3}$, $F_{B_s^*\bar{B}_s^*} = 0.901$ and $\mathcal{B}(B_s^0 \to D_s^-\rho^+) = 7.0 \times 10^{-3}$.

D_s^- mode	ε (%)	$N_{\rm sig}^{\rm good}$ / $N_{\rm sig}^{\rm bad}$	N_{udsc} / $N_{B_s^0\to D_s^-\rho^+}$	$N_{\rm sig}$	$N_{\rm back}$	S	$N_{\rm sig}/N_{\rm bkg}$
$\phi\pi^-$	13.4	23.2±0.7	2.6±0.1	24.7±0.7	3.3±0.2	4.7	7.6
	0.8	1.5±0.2	0.7±0.2				
$K^{*0}K^-$	10.5	22.3±0.7	4.6±0.2	23.7±0.7	5.3±0.3	4.4	4.4
	0.7	1.4±0.2	0.7±0.2				
$K_S^0K^-$	13.9	11.5±0.3	2.3±0.1	12.0±0.3	2.5±0.2	3.2	4.7
	0.7	0.5±0.1	0.3±0.1				
All		57.0±1.0	9.5±0.2	60.4±1.1	11.1±0.4	7.1	5.4
		3.4±0.3	1.6±0.3				
Mass cut only				65.2±1.2	18.6±0.7	7.1	3.5
Mass cuts, $R_2 < 0.5$ and $\lvert\cos\theta_{D_s^-}\rvert > 0.3$				62.5±1.1	12.5±0.5	7.2	5.0
Mass cuts and KSFW				61.4±1.1	8.6 ±0.3	7.3	7.2

Table 4.10: Expected signal efficiencies (ε), signal yields ($N_{\rm sig}$), background yields ($N_{\rm back}$), figures of merit (S), and signal-to-background ratios in the $B_s^*\bar{B}_s^*$ signal region for the $B_s^0 \to D_s^-\rho^+$ (top) and $B_s^0 \to D_s^{*-}\rho^+$ (bottom) selection. The values for alternative continuum rejection cuts (and without any) are shown for comparison. The following assumptions are made: $\mathcal{B}(B_s^0 \to D_s^{*-}\pi^+) = 3.3 \times 10^{-3}$, $\mathcal{B}(B_s^0 \to D_s^-\rho^+) = \mathcal{B}(B_s^0 \to D_s^{*-}\rho^+) = 7.0 \times 10^{-3}$ and $F_{B_s^*\bar{B}_s^*} = 0.90$.

D_s^- mode	ε (%)	$N_{\rm sig}^{\rm good}$ $N_{\rm sig}^{\rm bad}$	N_{udsc} $N_{B_s^0\to D_s^{*-}\pi^+}$ $N_{B_s^0\to D_s^{*-}\rho^+}$	$N_{\rm sig}$	$N_{\rm back}$	S	$N_{\rm sig}/N_{\rm back}$
$\phi\pi^-$	5.1 0.7	19.1±0.9 2.5±0.3	5.7±0.3 1.3±0.2 2.4±0.3	21.6±0.9	9.4±0.4	3.9	2.3
$K^{*0}K^-$	3.9 0.6	17.8±0.9 2.7±0.4	12.1±0.5 1.0±0.2 2.6±0.3	20.5±1.0	15.7±0.6	3.4	1.3
$K_S^0K^-$	5.1 0.7	9.2±0.4 1.3±0.2	5.3±0.3 0.6±0.1 1.7±0.2	10.5±0.4	7.6±0.3	2.5	1.4
All		46.1±1.3 6.5±0.5	23.1±0.6 2.9±0.2 6.7±0.5	52.6±1.4	32.7±0.8	5.7	1.6
Mass cuts only				63.8±1.6	105±3	4.9	0.6
Mass cuts, $R_2 < 0.35$, $\lvert\cos\theta_{D_s^-}\rvert > 0.4$ and $\lvert\cos\theta_{B_s^0}\rvert > 0.3$				49.8±1.4	24.6±0.7	5.8	2.0

D_s^- mode	ε (%)	$N_{\rm sig}^{\rm good}$ $N_{\rm sig}^{\rm bad}$	N_{udsc} $N_{B_s^0\to D_s^-\rho^+}$	$N_{\rm sig}$	$N_{\rm back}$	S	$N_{\rm sig}/N_{\rm bkg}$
$\phi\pi^-$	3.2 0.7	11.2±0.6 2.3±0.3	2.9±0.2 0.8±0.2	13.5±0.7	3.8±0.3	3.2	3.5
$K^{*0}K^-$	2.2 0.5	9.4±0.6 2.3±0.3	5.3±0.3 1.1±0.2	11.7±0.7	6.5±0.4	2.7	1.8
$K_S^0K^-$	3.2 0.6	5.3±0.3 0.9±0.1	2.6±0.2 0.5±0.1	6.3±0.3	3.1±0.2	2.0	2.0
All		25.9±1.0 5.6±0.5	10.9±0.5 2.3±0.3	31.5±1.1	13.5±0.6	4.7	2.3
Mass cuts only				36.5±1.1	37.5±1.3	4.2	1.0
Mass cuts, $R_2 < 0.35$ and $\lvert\cos\theta_{D_s^-}\rvert > 0.3$				31.9±1.1	15.1±0.6	4.7	2.1

4.2.3 Best candidate selection

After the selection described above, several candidates in the same event may fall in the range $M_{\rm bc} > 5.3$ GeV$/c^2$ and $-0.3 < \Delta E < 0.4$ GeV. A further selection is implemented in order to keep no more than one candidate per event and per B_s^0 decay mode of interest. The goal is to keep the candidate that is most likely to be signal without introducing a bias in the $M_{\rm bc}$ and ΔE distributions.

This best candidate selection is based on the quality of the $D_s^{(*)-}$ and its associated light meson. The choice of the best pion is based on the $\mathcal{R}_{K/\pi}$ value[6]. The quality of an intermediate meson is based on its invariant mass and is summarised in one quantity, χ^2, defined as:

- for D_s^-:

$$\chi^2\left(D_s^-\right) = \left(\frac{m_{D_s^-} - m_{D_s^-}^{\rm PDG}}{\sigma_{m_{D_s^-}}}\right)^2 \tag{4.10}$$

  where $\sigma_{m_{D_s^-}} = 3.6$ MeV$/c^2$ is the D_s^- mass resolution and $m_{D_s^-}^{\rm PDG} = 1968.5$ MeV$/c^2$ is the nominal D_s^- mass [37];

- for D_s^{*-}:

$$\chi^2\left(D_s^{*-}\right) = \left(\frac{\left(m_{D_s^{*-}} - m_{D_s^-}\right) - \left(m_{D_s^{*-}}^{\rm PDG} - m_{D_s^-}^{\rm PDG}\right)}{\sigma_{m_{D_s^{*-}} - m_{D_s^-}}}\right)^2 + \chi^2\left(D_s^-\right) \tag{4.11}$$

  where $\sigma_{m_{D_s^{*-}} - m_{D_s^-}} = 5.1$ MeV$/c^2$ is the resolution of the photon used to form the D_s^{*-} and $m_{D_s^{*-}}^{\rm PDG} - m_{D_s^-}^{\rm PDG} = 143.8$ MeV$/c^2$ is the nominal mass difference [37];

- for π^0:

$$\chi^2\left(\pi^0\right) = \left(\frac{m_{\pi^0} - m_{\pi^0}^{\rm PDG}}{\sigma_{\pi^0}}\right)^2 \tag{4.12}$$

  where $\sigma_{\pi^0} = 6.5$ MeV$/c^2$ is the π^0 mass resolution and $m_{\pi^0}^{\rm PDG} = 135$ MeV$/c^2$ the nominal π^0 mass [37].

The ρ meson width is too large to use a χ^2 in the same way as above. We therefore choose the best candidate as the combination of the best π^0, based on $\chi^2(\pi^0)$, and the best charged pion. The best-candidate requirements, summarised in Table. 4.11, do not introduce biases in $M_{\rm bc}$ and ΔE.

[6] For the $B_s^0 \to D_s^- \pi^+$ and $B_s^0 \to D_s^\mp K^\pm$ modes (for which there are more than one candidate in less than 1% of the events), the best $K^\pm$ and π^- candidates are based on their momentum in the laboratory frame. It was implemented in this way for the original analysis [8, 10], but a choice based on $\mathcal{R}_{K/\pi}$ would have been better.

Table 4.11: Best candidate selection.

Mode	Choice of the candidate with...
$B_s^0 \to D_s^- \pi^+$	min $\chi^2(D_s^-)$ then max p_{π^+}
$B_s^0 \to D_s^\mp K^\pm$	min $\chi^2(D_s^-)$ then max $p_{K^\pm}$
$B_s^0 \to D_s^{*-} \pi^+$	min $\chi^2(D_s^{*-})$ then min $\mathcal{R}_{K/\pi}$ for the fast π^+
$B_s^0 \to D_s^- \rho^+$	min $(\chi^2(D_s^-) + \chi^2(\pi^0))$ then min $\mathcal{R}_{K/\pi}$ for the π^+ from the ρ^+
$B_s^0 \to D_s^{*-} \rho^+$	min $(\chi^2(D_s^{*-}) + \chi^2(\pi^0))$ then min $\mathcal{R}_{K/\pi}$ for the π^+ from the ρ^+

4.3 Fitting method and definition of PDF shapes

For each B_s^0 mode, an extended unbinned maximum likelihood fit [185], implemented using RooFit [195, 196], is used to extract the signal yield, as well as other physics parameters, from the sample of selected candidates. The fit is performed along two dimensions, $M_{\rm bc}$ and ΔE, except for the $B_s^0 \to D_s^{*-}\rho^+$ mode where two additional observables, the polarisation angles $\cos\theta_{D_s^{*-}}$ and $\cos\theta_{\rho^+}$ of the D_s^{*-} and the ρ^+, are included in the fit.

The two-dimensional fitting function, $\mathcal{P}(M_{\rm bc}, \Delta E)$, is defined as a linear combination of probability density functions (PDFs) for background and signal components. The analytical PDF of the signal in each of the three regions is determined from MC simulation. Despite a tiny correlation, the $M_{\rm bc}$ and ΔE distributions are fitted separately with a sum of Gaussian functions with common mean value. Physically, this can be explained by the presence of several contributions to the resolution. In case a distribution is asymmetric (mainly for the modes involving a ρ^+), the so-called Novosibirsk function (See for instance Ref. [197]),

$$f(x) = \exp\left[-\frac{1}{2}\left(\frac{\ln^2\left(1+\Lambda\left(x-x_0\right)\right)}{\tau^2}+\tau^2\right)\right], \tag{4.13}$$

is used, where x_0 is the mean and where $\Lambda = \sinh(\tau\sqrt{\ln 4})/(\sigma \ln 4)$ contains the width, σ, and the asymmetry parameter, τ.

The six mean values for $M_{\rm bc}$ and ΔE distributions are related to two physics parameters of the fit: the B_s^0 and B_s^* masses (Eqs. (4.4) to (4.7)). These parameters are left free in the fit, except for the $B_s^0 \to D_s^\mp K^\pm$ mode where the statistics are too small.

The MC resolutions (PDF widths) may not be exactly the same as in reality[7]. In order to calibrate the resolution on $M_{\rm bc}$ and ΔE, two scale factors, $\rho_{M_{\rm bc}}$ and $\rho_{\Delta E}$, are applied on the MC values. Table 4.12 shows the MC resolutions as well as the correction factors. The uncertainty of these factors, when fixed, is propagated as a systematic error. The resolution in $M_{\rm bc}$ is almost the same for the five modes; the scale factor measured with $B_s^0 \to D_s^-\pi^+$ events is chosen and fixed for the other modes. Concerning ΔE resolution scale factors, those of the $B_s^0 \to D_s^\mp K^\pm$ and $B_s^0 \to D_s^{*-}\pi^+$ modes are fixed at the value

[7] In principle, if the resolution can be perfectly understood, any difference between data and expectations can be used to set a limit on the B_s^* width; one of the difficulties of such a measurement is to relate correctly the width of the $M_{\rm bc}$ peak, in the $B_s^*\bar{B}_s^*$ region, to the B_s^* proper width.

Table 4.12: MC signal resolutions in ΔE and $M_{\rm bc}$, together with their corresponding scale factor. The resolutions and scale factors are the same for the three $B_s^*\bar{B}_s^*$, $B_s^*\bar{B}_s^0$ and $B_s^0\bar{B}_s^0$ production modes.

Mode	$\sigma_{\Delta E}$ (MeV)	$\sigma_{M_{\rm bc}}$ (MeV/c^2)	$\rho_{\Delta E}$	$\rho_{M_{\rm bc}}$	
$B_s^0 \to D_s^-\pi^+$	13.0 ± 0.1	3.57 ± 0.03	1.06 ± 0.08	1.05 ± 0.08	free
$B_s^0 \to D_s^{\mp}K^{\pm}$	11.3 ± 0.1	3.91 ± 0.04	1.06 ± 0.08	1.05 ± 0.08	fixed
$B_s^0 \to D_s^{*-}\pi^+$	14.6 ± 0.2	3.65 ± 0.04	1.06 ± 0.08	1.05 ± 0.08	fixed
$B_s^0 \to D_s^-\rho^+$	18.3 ± 1.4	3.9 ± 0.1	1.12 ± 0.06	1.05 ± 0.08	fixed
$B_s^0 \to D_s^{*-}\rho^+$	24.9 ± 1.4	3.9 ± 0.1	1.12 ± 0.06	1.05 ± 0.08	fixed

Table 4.13: Example of fitted parameters of the continuum PDF for $B_s^0 \to D_s^-\pi^+$ and $B_s^0 \to D_s^{\mp}K^{\pm}$ candidates selected in MC continuum. In all fits to the real data, the beam energy is fixed to its measured value, while c_1 and ξ are left free.

	$B_s^0 \to D_s^-\pi^+$	$B_s^0 \to D_s^{\mp}K^{\pm}$
c_1 (/GeV)	-0.44 ± 0.01	-0.13 ± 0.08
$E_{\rm b}^*$ (MeV)	5434.8 ± 0.2	fixed to MC input (5434.5)
ξ	-20.9 ± 0.9	-17.2 ± 3.6

measured with the $B_s^0 \to D_s^-\pi^+$ fit[8]. For the B_s^0 modes involving a ρ^+, the ρ^+ dominates the ΔE resolution, as seen in the $B^0 \to D_s^{*-}\rho^+$ analysis [200]. The scale factor obtained from $B^0 \to D^{*-}\rho^+$, 1.12 ± 0.02 [200] is chosen and fixed in the $B_s^0 \to D_s^{(*)-}\rho^+$ fits, with an additional 5% relative uncertainty to encompass possible differences between B^0 and B_s^0 decays.

The PDFs for contaminating B_s^0 backgrounds are defined with analytical shapes exactly in the same way as for the signal, except for the $B_s^0 \to D_s^{*-}\pi^+$ background in the $B_s^0 \to D_s^-\pi^+$ and $B_s^0 \to D_s^{\mp}K^{\pm}$ analyses where the non-parametric kernel estimation method [201] is used. Unlike for the signal, the mean values are fixed parameters unrelated to any physical quantity.

The PDF of the continuum background is the product of a linear function describing the ΔE dependence and a so-called Argus function describing the $M_{\rm bc}$ dependence. The Argus function is defined as [96, 202]

$$f(x) = x\sqrt{1-x^2}e^{-\xi(1-x^2)}\,, \tag{4.14}$$

with $x = M_{\rm bc}c^2/E_{\rm b}^*$. It has two parameters, ξ and the end point which is taken here as the

[8] The common scale factor between $B_s^0 \to D_s^-\pi^+$ and $B_s^0 \to D_s^{*-}\pi^+$ is confirmed by the consistency between the scale factors measured with $B^0 \to D_s^{*+}D^-$, 1.08 ± 0.05 [198, 199], and with our $B_s^0 \to D_s^-\pi^+$ fit.

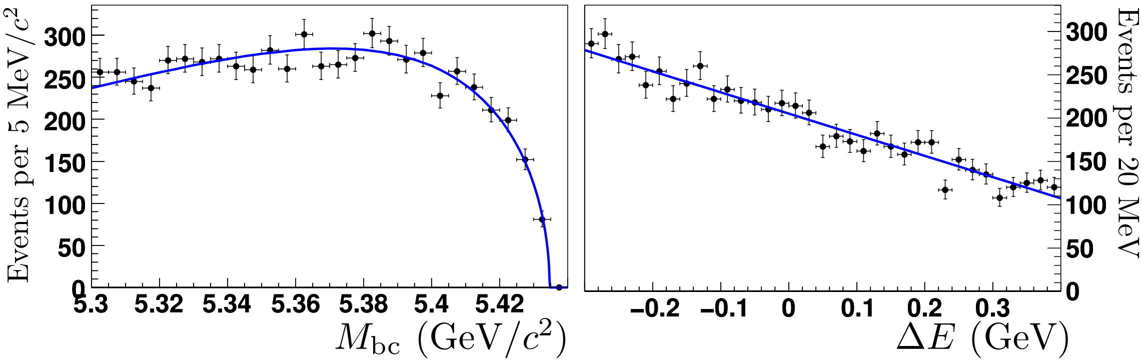

Figure 4.7: $M_{\rm bc}$ and ΔE distributions of $B_s^0 \to D_s^- \pi^+$ candidates in a continuum MC sample representing $66\ {\rm fb}^{-1}$. The histograms are fitted (blue curve) as described in the text. The situation is similar for all the studied B_s^0 modes with varying levels of background.

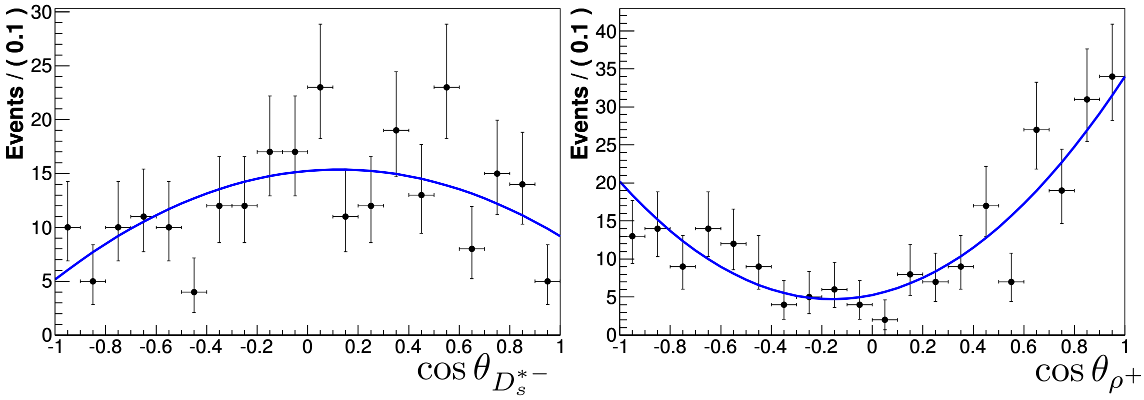

Figure 4.8: $\cos\theta_{\rho^+}$ and $\cos\theta_{D_s^{*-}}$ distributions of $B_s^0 \to D_s^{*-}\rho^+$ candidates falling outside a wide signal region.

beam energy, $E_{\rm b}^*$. The third parameter of the PDF is the ΔE slope, c_1. In the fits to the data, the beam energy, $E_{\rm b}^*$, is fixed to its measured value (see Sec. 2.3.1), while c_1 and ξ are left free. This shape describes well the continuum in all the studied B_s^0 modes. A fit example from MC is given in Fig. 4.7, while numerical parameters are shown in Table 4.13. The background from non-strange B events is scattered and flat enough to be described by the continuum PDF.

The four-dimensional fitting function for the $B_s^0 \to D_s^{*-}\rho^+$ mode is formed by multiplying the two-dimensional $\mathcal{P}(M_{\rm bc}, \Delta E)$ function with quadratic (continuum shape) or polynomial functions (up to order five for signal) for the angular part of the PDFs. It has been checked that quadratic functions describe well the data outside the signal region (Fig. 4.8).

4.4 $B_s^0 \to D_s^-\pi^+$ and $B_s^0 \to D_s^\mp K^\pm$ analyses

The $B_s^0 \to D_s^-\pi^+$ decay is the standard candle of B_s^0 decays. It has a large branching fraction, and only four charged particles in the final state. The experimental study of the Cabibbo-suppressed $B_s^0 \to D_s^\mp K^\pm$ mode is very similar; the only difference is the particle identification of the fast track (kaon instead of pion).

4.4.1 $B_s^0 \to D_s^-\pi^+$ fit results

The fitting function for the $B_s^0 \to D_s^-\pi^+$ sample is composed of three signal PDFs ($\mathcal{P}_{B_s^*\bar{B}_s^*}$, $\mathcal{P}_{B_s^*\bar{B}_s^0}$ and $\mathcal{P}_{B_s^0\bar{B}_s^0}$ for the three $B_s^*\bar{B}_s^*$, $B_s^*\bar{B}_s^0$ and $B_s^0\bar{B}_s^0$ signals), one PDF for the continuum background ($\mathcal{P}_{udsc}$), and one PDF for the $B_s^0 \to D_s^{*-}\pi^+$ background ($\mathcal{P}_{D_s^{*-}}$):

$$\begin{aligned}\mathcal{P}\left(\Delta E, M_{\mathrm{bc}}\right) = N_{\mathrm{sig}}^{B_s^*\bar{B}_s^*} \times \mathcal{P}_{B_s^*\bar{B}_s^*} + N_{\mathrm{sig}}^{B_s^*\bar{B}_s^0} \times \mathcal{P}_{B_s^*\bar{B}_s^0} + N_{\mathrm{sig}}^{B_s^0\bar{B}_s^0} \times \mathcal{P}_{B_s^0\bar{B}_s^0} \\ + N_{udsc} \times \mathcal{P}_{udsc} + N_{D_s^{*-}} \times \mathcal{P}_{D_s^{*-}}\,. \end{aligned} \tag{4.15}$$

The $B_s^0 \to D_s^-\pi^+$ fit is the only one from which the branching fraction is extracted using the three production modes $\Upsilon(5S) \to B_s^{(*)}\bar{B}_s^{(*)}$. To do that, the signal yields of Eq. (4.15), $N_{\mathrm{sig}}^{B_s^*\bar{B}_s^*}$, $N_{\mathrm{sig}}^{B_s^*\bar{B}_s^0}$ and $N_{\mathrm{sig}}^{B_s^0\bar{B}_s^0}$, are directly related to three other free parameters of the fit corresponding to the physical quantities, $\mathcal{B}(B_s^0 \to D_s^-\pi^+)$, $F_{B_s^*\bar{B}_s^*}$ and $F_{B_s^*\bar{B}_s^0}$ with the relations

$$N_{B_s^*\bar{B}_s^*} = N_{B_s^0} \times \mathcal{B}(B_s^0 \to D_s^-\pi^+) \times F_{B_s^*\bar{B}_s^*} \times \left(\sum \varepsilon\mathcal{B}\right)_{B_s^0\to D_s^-\pi^+}^{B_s^*\bar{B}_s^*}\,, \tag{4.16}$$

$$N_{B_s^*\bar{B}_s^0} = N_{B_s^0} \times \mathcal{B}(B_s^0 \to D_s^-\pi^+) \times F_{B_s^*\bar{B}_s^0} \times \left(\sum \varepsilon\mathcal{B}\right)_{B_s^0\to D_s^-\pi^+}^{B_s^*\bar{B}_s^0}\,, \tag{4.17}$$

$$N_{B_s^0\bar{B}_s^0} = N_{B_s^0} \times \mathcal{B}(B_s^0 \to D_s^-\pi^+) \times \left(1 - F_{B_s^*\bar{B}_s^*} - F_{B_s^*\bar{B}_s^0}\right) \times \left(\sum \varepsilon\mathcal{B}\right)_{B_s^0\to D_s^-\pi^+}^{B_s^0\bar{B}_s^0} \tag{4.18}$$

where the quantities $\sum\varepsilon\mathcal{B}$ are the sums over the three D_s^- modes of the product of the efficiency (Table 4.7) and the D_s^- total branching fraction (Table 4.4). As expected, their values are very similar in the three signal regions:

$$\left(\sum \varepsilon\mathcal{B}\right)_{B_s^0\to D_s^-\pi^+}^{B_s^*\bar{B}_s^*} = (15.8 \pm 0.2(\varepsilon) \pm 1.0(\mathcal{B})) \times 10^{-3}\,, \tag{4.19}$$

$$\left(\sum \varepsilon\mathcal{B}\right)_{B_s^0\to D_s^-\pi^+}^{B_s^*\bar{B}_s^0} = (15.8 \pm 0.2(\varepsilon) \pm 1.0(\mathcal{B})) \times 10^{-3}\,, \tag{4.20}$$

$$\left(\sum \varepsilon\mathcal{B}\right)_{B_s^0\to D_s^-\pi^+}^{B_s^0\bar{B}_s^0} = (15.6 \pm 0.2(\varepsilon) \pm 1.0(\mathcal{B})) \times 10^{-3}\,, \tag{4.21}$$

where the first error is due to the efficiency (statistical error in signal MC), and the second, to the D_s^- branching fraction. The number of B_s^0 in the sample,

$$N_{B_s^0} = 2 \times L_{\mathrm{int}} \times \sigma(e^+e^- \to \Upsilon(5S)) \times f_s = (2.57 \pm 0.41) \times 10^6\,, \tag{4.22}$$

is obtained from the integrated luminosity, L_{int} (Table 2.3), the $\Upsilon(5S)$ cross section, $\sigma(e^+e^- \to \Upsilon(5S))$ (Eq. (3.6)), and f_s (Eq. (3.39)). $\sum\varepsilon\mathcal{B}$ and $N_{B_s^0}$ are fixed in the fit and are sources of systematics uncertainties for the branching fraction result.

The results of the maximisation of the extended likelihood function on the data are shown in Table 4.14 and in Fig. 4.9. The correlation between $F_{B_s^* \bar{B}_s^*}$ and $F_{B_s^* B_s^0}$, -76.7%, leads to the following value for the third fraction :

$$F_{B_s^0 \bar{B}_s^0} = 1 - F_{B_s^* \bar{B}_s^*} - F_{B_s^* B_s^0} = \left(2.6^{+2.6}_{-2.5}\right)\% \,. \tag{4.23}$$

Table 4.14: Results of the fit to the $B_s^0 \to D_s^- \pi^+$ candidates, with statistical uncertainties only.

Fit parameter	Value
$\mathcal{B}(B_s^0 \to D_s^- \pi^+)$	$(3.60 \pm 0.33(\mathrm{stat})) \times 10^{-3}$
$F_{B_s^* \bar{B}_s^*}$	$(90.1^{+3.8}_{-4.0})\%$
$F_{B_s^* \bar{B}_s^0}$	$(7.3^{+3.3}_{-3.0})\%$
$m_{B_s^0}$	$5364.4 \pm 1.3\ \mathrm{MeV}/c^2$
$m_{B_s^*}$	$5416.4 \pm 0.4\ \mathrm{MeV}/c^2$
Yields	
$N_{\mathrm{sig}}^{B_s^* \bar{B}_s^*}$	145^{+14}_{-13}
$N_{\mathrm{sig}}^{B_s^* \bar{B}_s^0}$	$11.8^{+5.8}_{-5.0}$
$N_{\mathrm{sig}}^{B_s^0 \bar{B}_s^0}$	$4.0^{+4.6}_{-3.7}$
$N_{\mathrm{sig}}^{\mathrm{all}}$	161 ± 15

4.4.2 Check of the $B_s^0 \to D_s^- \pi^+$ fit

With a simplified fitting function (composed only of $B_s^* \bar{B}_s^*$ signal PDF, continuum background, and $B_s^0 \to D_s^{*-} \pi^+$ background), we generated fast MC samples (each with 700 continuum events, 40 $B_s^0 \to D_s^{*-} \pi^+$ events, and between 0 and 200 signal events) to check the absence of bias on the fitted number of signal events. Figure 4.10 shows the result of this test.

4.4.3 Distribution of the angle between the B_s^0 momentum and beam axis

The decay $\Upsilon(5S) \to B_s^* \bar{B}_s^*$ is of the type vector $\to$ vector vector. Therefore, the angle between the B_s^0 momentum in the CM frame with respect to the beam axis, $\theta^*_{B_s^0}$, is not trivially distributed[9]. Taking advantage of the large $B_s^0 \to D_s^- \pi^+$ peak in the $B_s^* \bar{B}_s^*$ region, we extract the $\theta^*_{B_s^0}$ distribution using the ${}_s\mathcal{P}lot$ procedure [203]. Figure 4.11 presents the distribution obtained for the $B_s^* \bar{B}_s^*$ signal. It has been checked that the efficiency does not depend on this angle. A fit of this distribution with the function $1 + a \times \cos^2 \theta^*_{B_s^0}$ returns

$$a = -0.59^{+0.18}_{-0.16} \,. \tag{4.24}$$

[9] The angular distribution is flat in the generic $b\bar{b}$ MC in which a pure phase-space decay model is used.

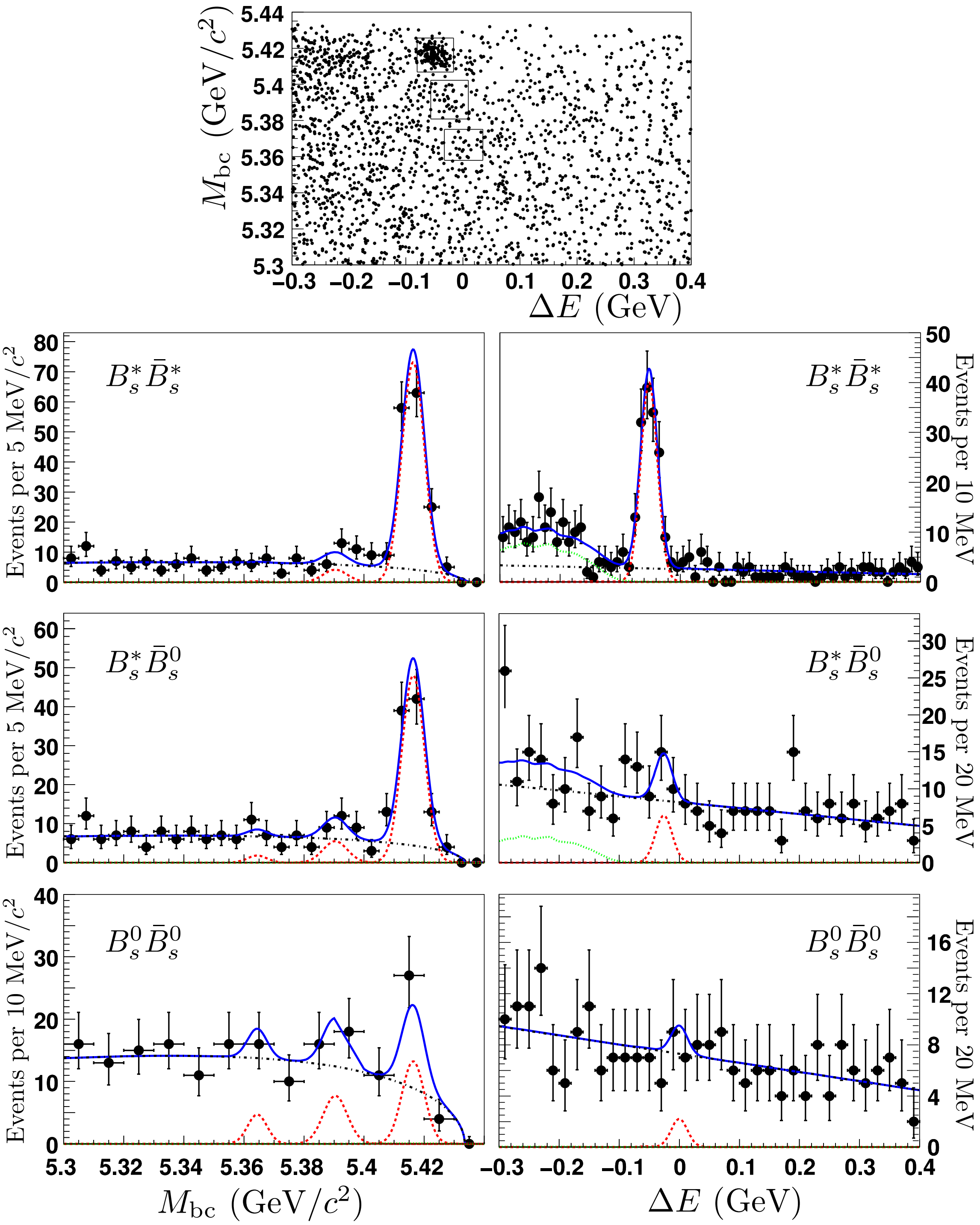

Figure 4.9: Scatter plot: $(M_{\rm bc}, \Delta E)$ distribution of the selected $B_s^0 \to D_s^- \pi^+$ candidates. The boxes show the signal region ($B_s^* \bar{B}_s^*$, $B_s^* \bar{B}_s^0$ and $B_s^0 \bar{B}_s^0$, from top to bottom). Histograms: projections on the on the $B_s^* \bar{B}_s^*$, $B_s^* \bar{B}_s^0$ and $B_s^0 \bar{B}_s^0$ (from top to bottom) signal regions. The $M_{\rm bc}$ distributions (left) are shown in the ΔE range of the signal region, and the ΔE distributions (right) are shown in the $M_{\rm bc}$ range of the signal region. The blue curves show the fitted function, while the red-dashed (black-dash-dotted, green-dotted) curves show the signal (continuum, $B_s^0 \to D_s^{*-} \pi^+$) component of the fit.

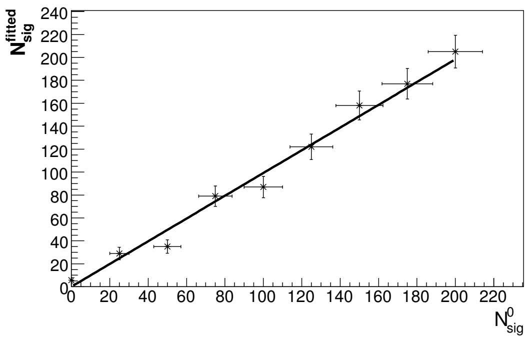

Figure 4.10: Fitted $B_s^0 \to D_s^- \pi^+$ signal yield as a function of the true number of signal events, for simplified fast MC samples. A straight line fit through the origin gives a slope of 0.99 ± 0.04.

This value is compatible with expectations from a calculation assuming that the initial state virtual photon is polarized along the beam direction and that there is no spin-dependent interaction: $a = -0.27$ [204]. With selected continuum events, the fit result is $a = -0.08 \pm 0.08$, in full agreement with the expected $a = 0$.

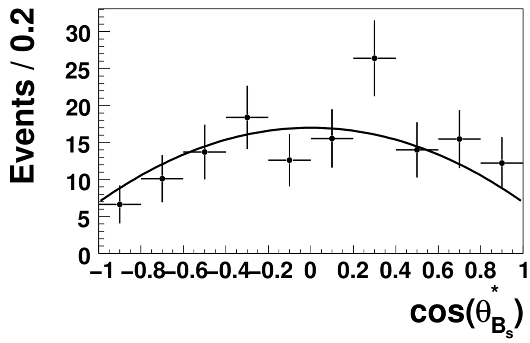

Figure 4.11: ${}_sPlot$ distribution of $\cos\theta^*_{B_s^0}$ in the CM frame, for $B_s^0 \to D_s^- \pi^+$ signal in the $B_s^* \bar{B}_s^*$ region.

4.4.4 $B_s^0 \to D_s^{\mp} K^{\pm}$ fit result

The $B_s^0 \to D_s^{\mp} K^{\pm}$ mode has a branching fraction one order of magnitude smaller than $B_s^0 \to D_s^- \pi^+$ [205], therefore only the $B_s^* \bar{B}_s^*$ signal region is included in the fit. The total fit function, $\mathcal{P}(M_{\rm bc}, \Delta E)$, has four components, namely the signal PDF ($\mathcal{P}_{\rm sig}$), the two $B_s^0 \to D_s^{(*)-}\pi^+$ background PDFs, and the continuum background PDF ($\mathcal{P}_{udsc}$): The total PDF is

$$\mathcal{P} = N_{B_s^0 \to D_s^{\mp} K^{\pm}} \times \mathcal{P}_{\rm sig} + N_{B_s^0 \to D_s^- \pi^+} \times \left(\mathcal{P}_{B_s^0 \to D_s^- \pi^+} + r \times \mathcal{P}_{B_s^0 \to D_s^{*-} \pi^+} \right) + N_{udsc} \times \mathcal{P}_{udsc} \,. \quad (4.25)$$

The $B_s^0 \to D_s^{*-} \pi^+$ event yield is made proportional to the $B_s^0 \to D_s^- \pi^+$ yield, with a ratio, r, which is fixed from the same fit, but with the $B_s^0 \to D_s^{\mp} K^{\pm}$ candidates selected

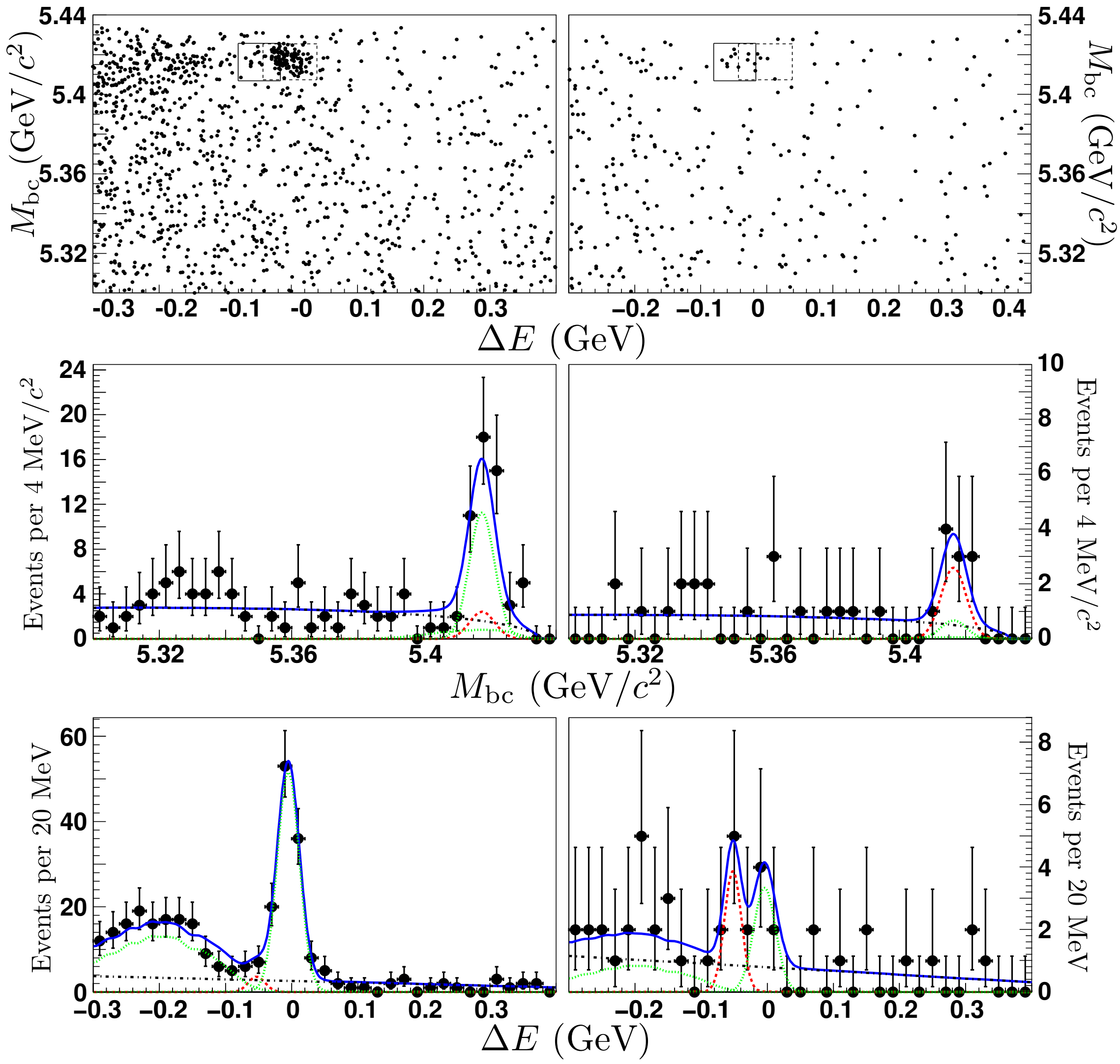

Figure 4.12: Top: $M_{\rm bc}$ and ΔE distributions of selected $B_s^0 \to D_s^{\mp} K^{\pm}$ candidates; the solid (dotted) box shows the region of the $B_s^0 \to D_s^{\mp} K^{\pm}$ ($B_s^0 \to D_s^- \pi^+$) signal in the $B_s^* \bar{B}_s^*$ production mode. Middle: $M_{\rm bc}$ distribution in the ΔE range of the $B_s^* \bar{B}_s^*$ signal region. Bottom: ΔE distribution in the $M_{\rm bc}$ range of the $B_s^* \bar{B}_s^*$ signal region. The left (right) plots are for the candidates selected without (with) kaon identification requirements. The blue curves show the total fitted function, while the red-dashed (green-dotted, black-dash-dotted) curves show the signal ($B_s^0 \to D_s^{(*)-} \pi^+$, continuum) component of the fit.

without kaon identification requirements (Fig. 4.12 left). All the charged tracks are seen as potential kaon candidates. As a result, many true $B_s^0 \to D_s^{(*)-}\pi^+$ events are selected. The three yields, $N_{B_s^0\to D_s^\mp K^\pm}$, $N_{B_s^0\to D_s^-\pi^+}$ and N_{bg}, but also r, are allowed to float. From MC studies, 112 $B_s^0 \to D_s^-\pi^+$ events and 6.6 $B_s^0 \to D_s^\mp K^\pm$ events are expected. The fit results are in agreement, yielding $N_{B_s^0\to D_s^-\pi^+} = 113^{+11}_{-12}(\mathrm{stat})$ and $N_{B_s^0\to D_s^\mp K^\pm} = 6.1^{+4.4}_{-3.6}(\mathrm{stat})$. The $B_s^0 \to D_s^{*-}\pi^+$ contribution has a yield of $183^{+33}_{-31}(\mathrm{stat})$. The ratio is measured to be

$$r = \frac{N_{B_s^0\to D_s^{*-}\pi}}{N_{B_s^0\to D_s^-\pi^+}} = 1.63 \pm 0.23\,. \tag{4.26}$$

In the following nominal fit with kaon identification requirements (Fig. 4.12 right), there are five free parameters: $N_{B_s^0\to D_s^-\pi^+}$, N_{udsc}, $N_{B_s^0\to D_s^\mp K^\pm}$ and the two parameters for the shape of the continuum background (ξ and c_1). The best-fit $B_s^0 \to D_s^\mp K^\pm$ signal yield is

$$N_{B_s^0\to D_s^\mp K^\pm} = 6.7^{+3.4}_{-2.7}\,. \tag{4.27}$$

The statistical significance of the $B_s^0 \to D_s^\mp K^\pm$ signal is 3.6σ. The continuum shape is compatible with the MC expectations. Using the relation

$$N(B_s^0 \to D_s^\mp K^\pm) = N_{B_s^0} \times F_{B_s^*\bar{B}_s^*} \times \mathcal{B}(B_s^0 \to D_s^\mp K^\pm) \times \left(\sum \varepsilon\mathcal{B}\right)_{B_s^0\to D_s^\mp K^\pm}, \tag{4.28}$$

$$\left(\sum \varepsilon\mathcal{B}\right)_{B_s^0\to D_s^\mp K^\pm} = (11.2 \pm 0.2(\varepsilon) \pm 0.7(\mathcal{B})) \times 10^{-3}\,, \tag{4.29}$$

the above signal yield (Eq. (4.27)) and the previously-obtained value for $F_{B_s^*\bar{B}_s^*}$, the following branching fraction measurement is obtained

$$\mathcal{B}(B_s^0 \to D_s^\mp K^\pm) = (2.4 \pm 1.1(\mathrm{stat})) \times 10^{-4}\,. \tag{4.30}$$

4.4.5 Fit of $B_s^0 \to D_s^\mp K^\pm$ candidates in the D_s^- sideband

To make sure that the $B_s^0 \to D_s^\mp K^\pm$ peak is not an experimental effect, a window for the mass of the D_s^- candidate is chosen far from the nominal D_s^- mass, $1968.45(33)$ MeV$/c^2$ [37], in the sideband of the distribution (see Fig.4.6):

$$1.930 < m_{D_s^-} < 1.945 \text{ GeV}/c^2\,. \tag{4.31}$$

With the data candidates in this window, the nominal fit returns $N_{B_s^0\to D_s^\mp K^\pm} = 2.2^{+3.0}_{-2.2}$, $N_{B_s^0\to D_s^-\pi^+} = 0.0^{+2.2}_{-1.3}$, $N_{udsc} = 261^{+17}_{-16}$. This validates the absence of signal in this D_s^- mass range.

4.5 $B_s^0 \to D_s^{*-}\pi^+$ and $B_s^0 \to D_s^-\rho^+$ analyses

The $B_s^0 \to D_s^{*-}\pi^+$ and $B_s^0 \to D_s^-\rho^+$ candidates are fitted in a way similar to $B_s^0 \to D_s^-\pi^+$. The likelihood fit is implemented including several components: three signal PDFs for the three signal regions, a continuum background PDF and the PDFs for backgrounds from

Table 4.15: Best fit values for $B_s^0 \to D_s^{*-}\pi^+$ (left) and $B_s^0 \to D_s^-\rho^+$ (right) signals. The results are quoted with the statistical uncertainties and the uncertainties coming from the fixed parameters of the fit. The statistical significances of the $B_s^*\bar{B}_s^*$ signals are both larger than 8σ.

Parameter	Fit results	
	$B_s^0 \to D_s^{*-}\pi^+$	$B_s^0 \to D_s^-\rho^+$
Signal yields		
$N_{B_s^*\bar{B}_s^*}$	$53.4^{+10.3+2.4}_{-9.4\ -2.6}$	$92.2^{+14.2+4.3}_{-13.2-4.2}$
$N_{B_s^*\bar{B}_s^0}$	$-1.9^{+4.0}_{-2.9} \pm 0.5$	$-4.0^{+5.2}_{-3.7} \pm 1.4$
$N_{B_s^0\bar{B}_s^0}$	$2.9^{+3.9+0.3}_{-3.0-0.2}$	$-3.0^{+5.7+0.4}_{-4.0-0.5}$
$m_{B_s^0}$ (MeV/c^2)	$5364.4^{+5.5+0.6}_{-3.4-0.8}$ MeV/c^2	$5372.3^{+4.2}_{-4.1} \pm 0.7$ MeV/c^2
$m_{B_s^*}$ (MeV/c^2)	$5416.7 \pm 0.6^{+0.2}_{-0.1}$ MeV/c^2	$5416.1 \pm 0.7 \pm 0.1$ MeV/c^2

other B_s^0 decays. The $B_s^0 \to D_s^{*-}\pi^+$ fit has a $B_s^0 \to D_s^-\pi^+$ and $B_s^0 \to D_s^-\rho^+$ components, while the $B_s^0 \to D_s^-\rho^+$ fit has only a $B_s^0 \to D_s^{*-}\rho^+$ component. The fit results are presented in Table 4.15 and in Fig. 4.13.

The ratios of the signal yields[10], e.g. $N_{B_s^*\bar{B}_s^*}/(N_{B_s^*\bar{B}_s^*}+N_{B_s^*\bar{B}_s^0}+N_{B_s^0\bar{B}_s^0})$, are compatible with the fractions $F_{B_s^*\bar{B}_s^*}$, $F_{B_s^*\bar{B}_s^0}$ and $F_{B_s^0\bar{B}_s^0}$ measured in the $B_s^0 \to D_s^-\pi^+$ analysis. In the $B_s^0 \to D_s^{*-}\pi^+$ results, the fitted number of $B_s^0 \to D_s^-\pi^+$ background events is 30 ± 9 while 31 events were expected from the MC studies.

In the $B_s^0 \to D_s^-\rho^+$ results, the B_s^0 mass is 10.1 ± 3.2 MeV/c^2 larger than the one obtained from the $B_s^0 \to D_s^-\pi^+$ fit. A similar deviation is seen for the $B_s^0 \to D_s^{*-}\rho^+$ fit discussed below.

The numbers of signal events in the $B_s^*\bar{B}_s^*$ region are related to the branching fractions via the relations

$$N(B_s^0 \to D_s^{*-}\pi^+) = N_{B_s^0} \times F_{B_s^*\bar{B}_s^*} \times \mathcal{B}(B_s^0 \to D_s^{*-}\pi^+) \times \left(\sum \varepsilon\mathcal{B}\right)_{B_s^0 \to D_s^{*-}\pi^+}, \quad (4.32)$$

$$N(B_s^0 \to D_s^-\rho^+) = N_{B_s^0} \times F_{B_s^*\bar{B}_s^*} \times \mathcal{B}(B_s^0 \to D_s^-\rho^+) \times \left(\sum \varepsilon\mathcal{B}\right)_{B_s^0 \to D_s^-\rho^+}, \quad (4.33)$$

where $N_{B_s^0}$ is the number of B_s^0 in the sample (Eq. (4.22)) and the quantities $\sum \varepsilon\mathcal{B}$ are the total signal efficiencies measured with MC, weighted by the sub-decay branching fractions:

$$\left(\sum \varepsilon\mathcal{B}\right)_{B_s^0 \to D_s^{*-}\pi^+} = (9.13 \pm 0.15(\varepsilon) \pm 0.59(\mathcal{B})) \times 10^{-3}, \quad (4.34)$$

$$\left(\sum \varepsilon\mathcal{B}\right)_{B_s^0 \to D_s^-\rho^+} = (4.40 \pm 0.10(\varepsilon) \pm 0.28(\mathcal{B})) \times 10^{-3}. \quad (4.35)$$

The branching fraction results are

$$\mathcal{B}(B_s^0 \to D_s^{*-}\pi^+) = (2.3 \pm 0.4(\mathrm{stat})) \times 10^{-3}, \quad (4.36)$$

$$\mathcal{B}(B_s^0 \to D_s^-\rho^+) = (8.2 \pm 1.1(\mathrm{stat})) \times 10^{-3}. \quad (4.37)$$

[10] Efficiencies differences between signal regions can be neglected for qualitative comparison.

In order to check that the contribution of non resonant $B_s^0 \to D_s^- \pi^+ \pi^0$ decays to the $B_s^0 \to D_s^- \rho^+$ result is negligible, we select the candidates without any requirement on the ρ^+ mass. A simplified fitting procedure, including only continuum background and $B_s^* \bar{B}_s^*$ components, is then applied, and the ρ mass distribution for the signal in the $B_s^* \bar{B}_s^*$ region is extracted with the ${}_sPlot$ method [203]. On Fig. 4.14, one can see that the ρ^+ mass shape of the signal MC describes the data reasonably well, leaving little room for a non resonant component.

4.6 $B_s^0 \to D_s^{*-} \rho^+$ analysis

4.6.1 Fit results

The $B_s^0 \to D_s^{*-} \rho^+$ decay involves three vector mesons and consequently has two polarisations which lead to two distinguishable distributions of the D_s^{*-} and ρ^+ decay angles (Appendix B). With two additional observables, the polarisation angles $\cos\theta_{D_s^{*-}}$ and $\cos\theta_{\rho^+}$, it is possible to measure the longitudinal polarisation fraction, $f_{\rm L}$ of the $B_s^0 \to D_s^{*-} \rho^+$ decay, in addition to its branching fraction. Figures 4.15 and 4.16 show the angular distributions in MC for transverse and longitudinal signal events. The theoretical angular PDFs are in agreement with simulated distributions, the difference being due to non-uniform detector inefficiencies.

To avoid unnecessary complication, no signal components for the $B_s^* \bar{B}_s^0$ and $B_s^0 \bar{B}_s^0$ regions are included in the final fit which contains three components, the longitudinal and transverse signals, and the continuum. The two relevant parameters are the longitudinal and transverse signal yields.

The best fit values, obtained from the selected $B_s^0 \to D_s^{*-} \rho^+$ candidates (Fig. 4.17), are

$$N^{\rm L}_{B_s^* \bar{B}_s^*} = 81.3^{+16.0}_{-14.9}\,, \tag{4.38}$$
$$N^{\rm T}_{B_s^* \bar{B}_s^*} = -3.5^{+8.0}_{-6.1}\,, \tag{4.39}$$
$$m_{B_s^0} = 5379.2^{+7.0}_{-6.6}\ {\rm MeV}/c^2\,, \tag{4.40}$$
$$m_{B_s^*} = 5415.7 \pm 0.8\ {\rm MeV}/c^2\,. \tag{4.41}$$

The fitted distributions are shown in Fig. 4.18. A negative fluctuation of the signal yield of transverse events is observed. The fitted B_s^0 mass is $14.8 \pm 6.7\ {\rm MeV}/c^2$ (2.2σ) larger than the one obtained in the $B_s^0 \to D_s^- \pi^+$ analysis. This situation is the same as for the $B_s^0 \to D_s^- \rho^+$ fit.

As done above for the other modes, we extract the branching fraction and the fraction of longitudinal events by using:

$$N^{\rm L}_{B_s^* \bar{B}_s^*} = N^{\rm L}(B_s^0 \to D_s^{*-} \rho^+) = N_{B_s^0} \times F_{B_s^* \bar{B}_s^*} \times \mathcal{B}(B_s^0 \to D_s^{*-} \rho^+) \times f_{\rm L} \times \varepsilon_{\rm L} \tag{4.42}$$
$$N^{\rm T}_{B_s^* \bar{B}_s^*} = N^{\rm T}(B_s^0 \to D_s^{*-} \rho^+) = N_{B_s^0} \times F_{B_s^* \bar{B}_s^*} \times \mathcal{B}(B_s^0 \to D_s^{*-} \rho^+) \times (1 - f_{\rm L}) \times \varepsilon_{\rm L}\,. \tag{4.43}$$

where $\varepsilon_{\rm L}$, $\varepsilon_{\rm T}$ are the total signal efficiencies weighted by the sub-decay branching frac-

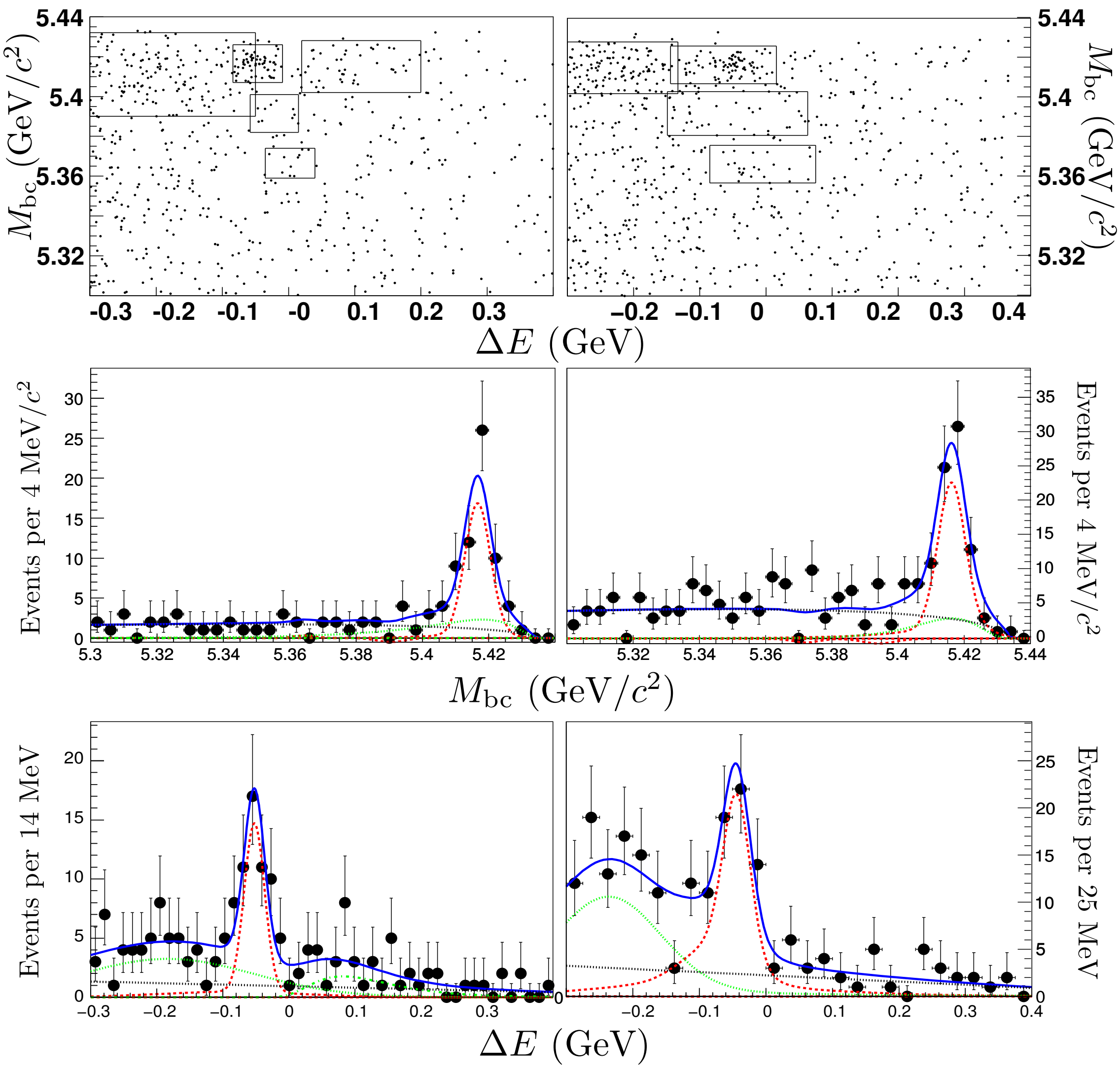

Figure 4.13: Top: $M_{\rm bc}$ and ΔE distributions of selected $B_s^0 \to D_s^{*-}\pi^+$ (left) and $B_s^0 \to D_s^-\rho^+$ (right) candidates; the solid boxes show the regions where signals and specific B_s^0 backgrounds are expected. Middle: $M_{\rm bc}$ distribution in the ΔE range of the $B_s^*\bar{B}_s^*$ signal region. Bottom: ΔE distribution in the $M_{\rm bc}$ range of the $B_s^*\bar{B}_s^*$ signal region. The blue curves show the total fitted function, while the red-dashed (green-dotted, black-dash-dotted) curves show the signal (specific B_s^0 background, continuum) component of the fit.

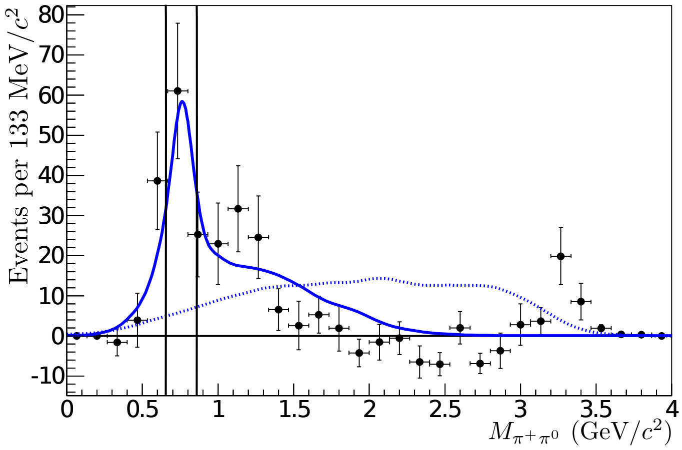

Figure 4.14: Mass of the ρ^+ candidate in the data for the fitted $B_s^0 \to D_s^- \rho^+$ signal in the $B_s^* \bar{B}_s^*$ region. The vertical lines show the restricted region used in the nominal analysis. The solid (dotted) curve presents the resonant $B_s^0 \to D_s^- \rho^+$ (non-resonant $B_s^0 \to D_s^- \pi^+ \pi^0$) shapes from the MC, both normalised to the total number of signal events. The statistical uncertainty of the MC shapes is not shown.

tions:

$$\varepsilon_{\mathrm{L}} = \left(\sum \varepsilon \mathcal{B}\right)_{\mathrm{L}} = [2.66 \pm 0.04(\varepsilon) \pm 0.17(\mathcal{B})] \times 10^{-3} \quad \text{for } f_{\mathrm{L}} = 1\,, \tag{4.44}$$

$$\varepsilon_{\mathrm{T}} = \left(\sum \varepsilon \mathcal{B}\right)_{\mathrm{T}} = [2.68 \pm 0.04(\varepsilon) \pm 0.17(\mathcal{B})] \times 10^{-3} \quad \text{for } f_{\mathrm{L}} = 0\,. \tag{4.45}$$

The signal yields, $N^L_{B_s^* \bar{B}_s^*}$ and $N^T_{B_s^* \bar{B}_s^*}$, are related to the branching fraction and the fraction of longitudinal polarisation via the relations :

$$f_{\mathrm{L}} = \frac{1}{\frac{N^T_{B_s^* \bar{B}_s^*}}{\varepsilon_{\mathrm{T}}} / \frac{N^L_{B_s^* \bar{B}_s^*}}{\varepsilon_{\mathrm{L}}} + 1} = 1.05^{+0.08}_{-0.10}(\mathrm{stat})\,, \tag{4.46}$$

$$\mathcal{B}(B_s^0 \to D_s^{*-} \rho^+) = \frac{\frac{N^T_{B_s^* \bar{B}_s^*}}{\varepsilon_{\mathrm{T}}} + \frac{N^L_{B_s^* \bar{B}_s^*}}{\varepsilon_{\mathrm{L}}}}{N_{B_s^0} \times F_{B_s^* \bar{B}_s^*}} = (11.5 \pm 2.0(\mathrm{stat})) \times 10^{-3}\,. \tag{4.47}$$

4.6.2 Check of the statistical uncertainty of f_{L}

Because the f_{L} estimate is close to the maximal physical value, its statistical uncertainty may not be Gaussian. In order to check that, we look at the distribution of the f_{L} values returned by the fit for approximately 1800 pseudo-experiments generated with 78 longitudinal-only signal events and 272 background events. The input value of $f_{\mathrm{L}} = 1$ should be recovered by the fitting procedure if it is unbiased. For 68% of the pseudo-experiments, the f_{L} fit result lies in a 0.21-broad interval (Fig. 4.19). The standard deviation returned by the nominal fit (0.1) is therefore in a good agreement with the standard deviation of this set of pseudo-experiments.

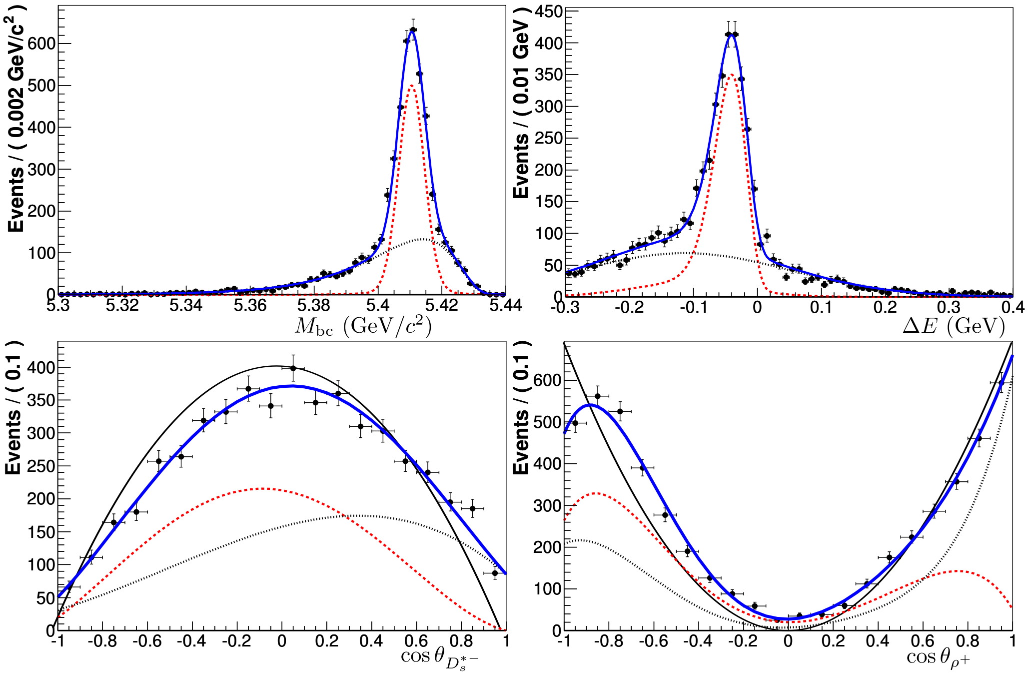

Figure 4.15: From left to right, and top to bottom: $M_{\rm bc}$, ΔE, $\cos\theta_{D_s^{*-}}$, $\cos\theta_{\rho^+}$ distributions for $B_s^0 \to D_s^{*-}\rho^+$ signal MC events, in the $B_s^*\bar{B}_s^*$ production mode, with full longitudinal polarisation. The dashed-red (dotted-black) curves describe the correctly (wrongly) reconstructed candidates. The solid black curves show the theoretical expectation (without detector effects) for the angular distributions (see Eq. (B.15)).

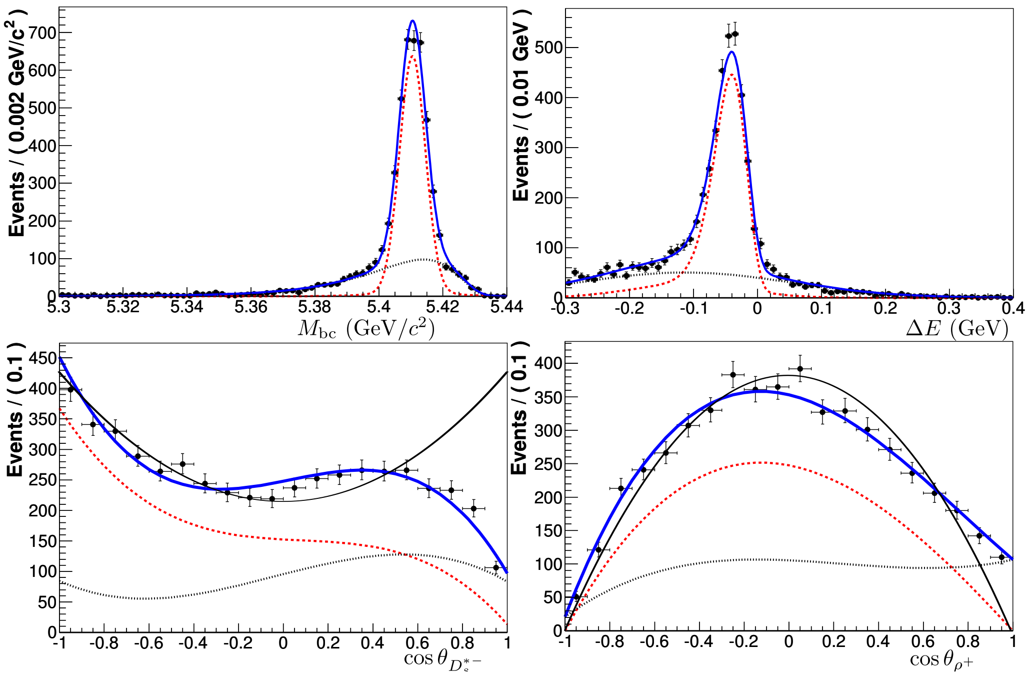

Figure 4.16: Same as Fig. 4.15, but for signal with full transverse polarisation.

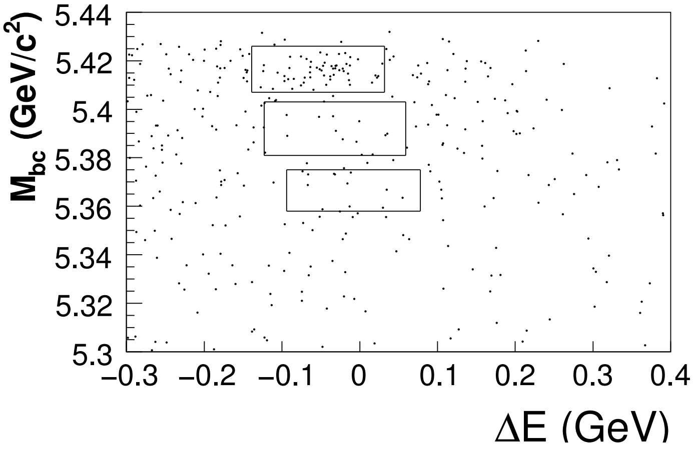

Figure 4.17: $(M_{\rm bc}, \Delta E)$ scatter plot of the $B_s^0 \to D_s^{*-}\rho^+$ candidates. The three boxes are the signal regions.

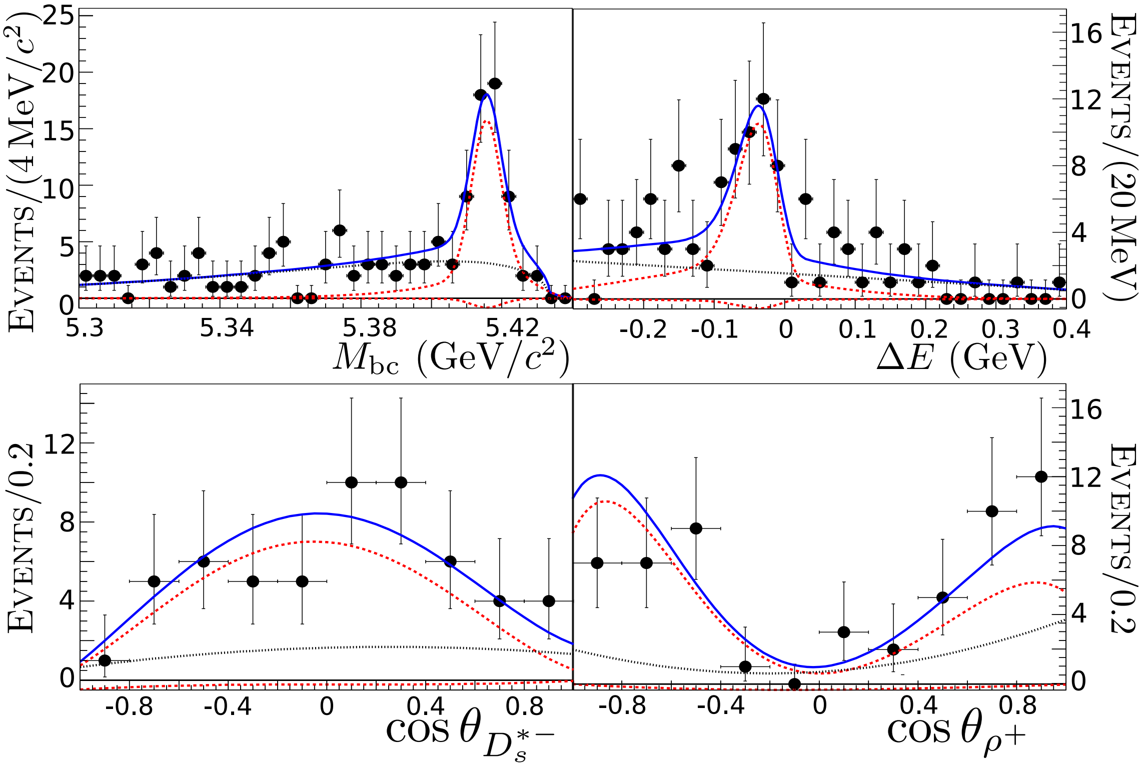

Figure 4.18: Projections for the $B_s^*\bar{B}_s^*$ signal box in the four fit variable ($M_{\rm bc}$, ΔE, $\cos\theta_{D_s^{*-}}$ and $\cos\theta_{\rho^+}$, from right to left, and from top to bottom). The blue curves show the fit result, while the black-dotted curves represent the background component. The large- (small-) yield red-dashed curve corresponds to the longitudinal (transverse) signal component.

4.6.3 Consistency checks

Using fast MC experiments, we have checked that the estimates of the continuum yield, signal yield and longitudinal polarisation fraction returned by the fit are unbiased.

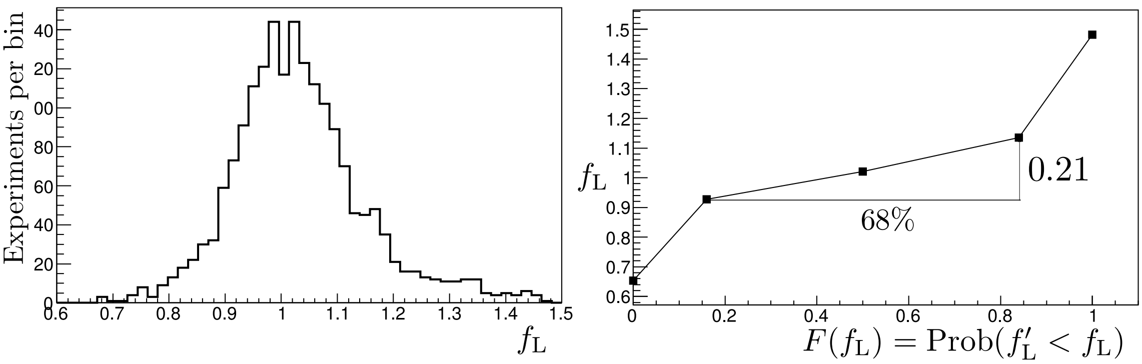

Figure 4.19: Left: distribution of the value of f_{L} returned by the fit of fast MC $B_s^0 \to D_s^{*-}\rho^+$ candidates with $f_{\mathrm{L}}^{\mathrm{input}} = 1$. Right: cumulative probability showing the $\pm 1\sigma$ interval, i.e. the interval that encompassed 68% of the f_{L} fit values.

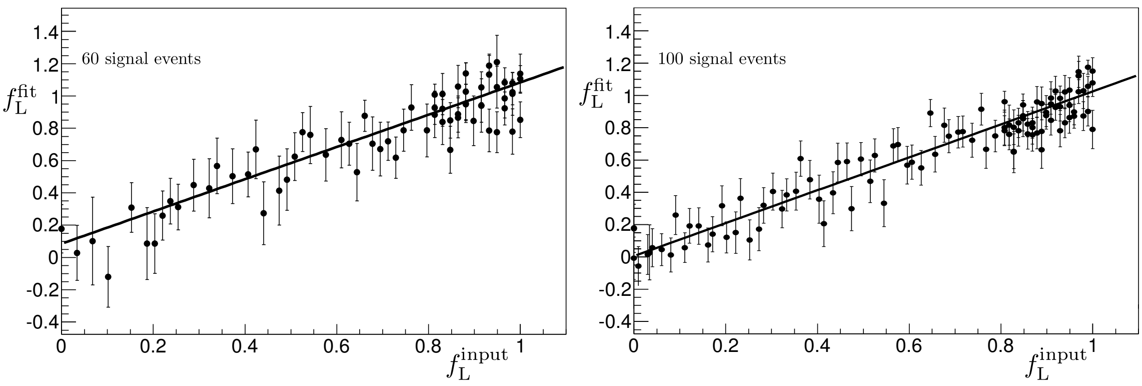

Figure 4.20: Value of f_{L} returned by the fit of $B_s^0 \to D_s^{*-}\rho^+$ candidates as a function of the true value of f_{L}. Left: pseudo experiments with 60 signal events. Right: pseudo experiments with 100 signal events.

First, pseudo-experiments with a fixed number of continuum events (270) and a fixed number of signal events (60 or 100) are generated with different f_{L} values. Because large f_{L} values are preferred by the data, half of the pseudo-experiments are concentrated in the region $f_{\mathrm{L}} > 0.8$. The results are shown in Fig. 4.20, where the fitted value, $f_{\mathrm{L}}^{\mathrm{fit}}$, is shown as a function of the true value $f_{\mathrm{L}}^{\mathrm{input}}$. With 60 signal events, the linear function $f_{\mathrm{L}}^{\mathrm{fit}} = f_{\mathrm{L}}^{\mathrm{input}}$ has $\chi^2/\mathrm{n.d.f.} = 97/67$, while the best linear function has $\chi^2/\mathrm{n.d.f.} = 64/65$ with $f_{\mathrm{L}}^{\mathrm{fit}} = (1.00 \pm 0.06) f_{\mathrm{L}}^{\mathrm{input}} + (0.09 \pm 0.05)$. With 100 signal events, the linear function $f_{\mathrm{L}}^{\mathrm{fit}} = f_{\mathrm{L}}^{\mathrm{input}}$ has $\chi^2/\mathrm{n.d.f.} = 116/99$, while The best linear function has $\chi^2/\mathrm{n.d.f.} = 112/97$ with $f_{\mathrm{L}}^{\mathrm{fit}} = (1.02 \pm 0.03) f_{\mathrm{L}}^{\mathrm{input}} + (0.00 \pm 0.03)$.

Secondly, pseudo-experiments with a fixed number of continuum events (270) and a fixed signal polarisation fraction of $f_{\mathrm{L}} = 1$ are generated with a number of signal events varying between 40 and 100 (Fig. 4.21 left). The linear function $N_{\mathrm{sig}}^{\mathrm{fit}} = N_{\mathrm{sig}}^{\mathrm{input}}$ has $\chi^2/\mathrm{n.d.f.} = 35/56$. The best linear function has $\chi^2/\mathrm{n.d.f.} = 33/54$ with $N_{\mathrm{sig}}^{\mathrm{fit}} = (1.12 \pm 0.09) N_{\mathrm{sig}}^{\mathrm{input}} + (-7.7 \pm 6.3)$.

Finally, pseudo-experiments with a fixed number of longitudinal-only signal events

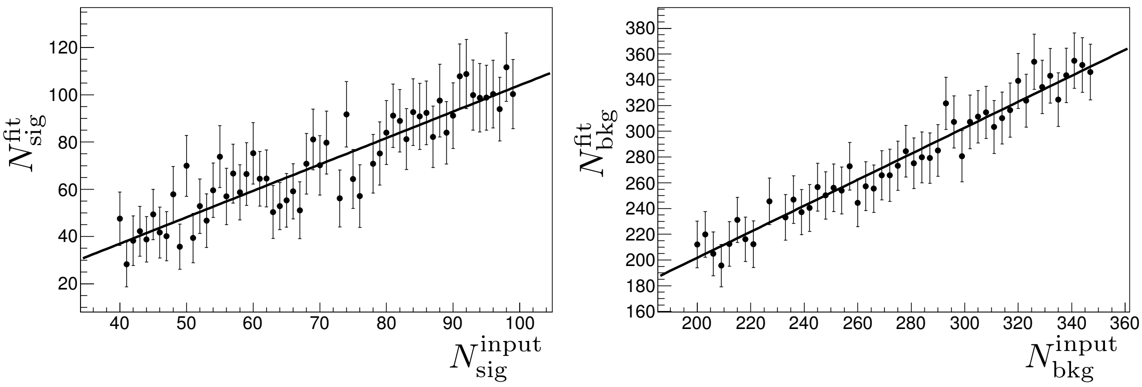

Figure 4.21: Number of signal events (left) and number of background events (right) returned by the fit of fast MC samples of longitudinally polarised $B_s^0 \to D_s^{*-}\rho^+$ candidates as a function of the input value.

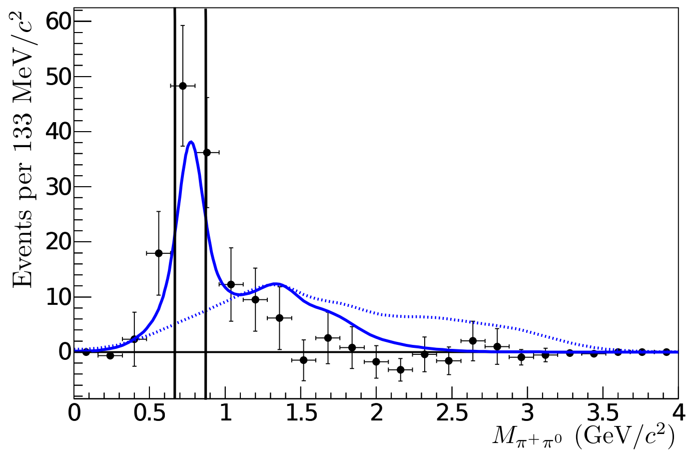

Figure 4.22: Mass of the ρ^+ candidate in the data for the fitted $B_s^0 \to D_s^{*-}\rho^+$ signal in the $B_s^*\bar{B}_s^*$ region. The vertical lines show the restricted region used in the nominal analysis. The solid (dotted) curve presents the resonant $B_s^0 \to D_s^{*-}\rho^+$ (non-resonant $B_s^0 \to D_s^{*-}\pi^+\pi^0$) shapes from the MC, both normalised to the total number of signal events. The statistical uncertainty of the MC shapes is not shown.

(80, $f_{\rm L} = 1$) are generated with a number of continuum events varying between 200 and 350 (Fig. 4.21 right). The linear function $N_{\rm bkg}^{\rm fit} = N_{\rm bkg}^{\rm input}$ has $\chi^2/\text{n.d.f.} = 15/46$. The best linear function has $\chi^2/\text{n.d.f.} = 14/44$ with $N_{\rm bkg}^{\rm fit} = (1.01 \pm 0.06)N_{\rm bkg}^{\rm input} + (-0.3 \pm 1.8)$.

Similarly to the $B_s^0 \to D_s^-\rho^+$ analysis and in order to confirm that the non resonant $B_s^0 \to D_s^{*-}\pi^+\pi^0$ decays are negligible in this analysis, we repeat the selection without any requirement on the ρ^+ mass. A simplified fitting procedure, consisting of a two-dimensional fit of the $M_{\rm bc}$ and ΔE distributions with only background and longitudinal signal components, is then applied, and the ρ^+ mass distribution for the signal in the $B_s^*\bar{B}_s^*$ region is extracted with the ${}_s\mathcal{P}lot$ method. Figure 4.22 shows that the ρ mass shape of the signal MC describes the data reasonably well. The signal shape accounts for both the correctly reconstructed and the wrongly reconstructed $B_s^0 \to D_s^{*-}\rho^+$ signal events.

4.7 Systematic uncertainties

4.7.1 Branching fraction systematics

Systematic errors for the branching fractions are calculated assuming that all the fixed parameters are uncorrelated. There are several sources of systematic uncertainties: particle identification, number of B_s^0, PDF shapes, candidate selection efficiencies, tracking efficiencies, D_s^- branching fractions, etc.

The dominant contribution is due to the number of B_s^0, and particularly to the parameter f_s (Eq. (3.39)). The uncertainty of f_s, 15%, affects directly any B_s^0 branching fraction measured, as explained in detail in the previous chapter. The normalisation is also affected by the integrated luminosity uncertainty, 1.3% [150], and the $\Upsilon(5S)$ production cross section, 4.6% (Eq. (3.6)).

The efficiency of the reconstruction of the charged tracks is taken from MC simulations. Based on data/MC comparison [206], a systematic uncertainty of 1% per track is assigned, i.e. 4% in total for all the modes presented here.

The particle identification efficiency obtained from MC is assigned a systematic uncertainty of 1.43% (1.72%) for each identified charged kaon (pion) [157]. An average error for the three D_s^- channels, weighted by $\varepsilon \times \mathcal{B}$ (efficiency×branching fraction of the D_s^- channel), is propagated.

Modes with a photon and/or a neutral pion have an additional systematic uncertainty of 1.7% per neutral pion and 2.0% per photon not used as a π^0 daughter.

The statistical uncertainties on the MC reconstruction efficiencies, and those on the D_s^- branching fractions are propagated to the branching fraction results.

The systematic error on the efficiency of the R_2 and $\cos\theta_{D_s^-}$ cuts is evaluated by repeating the complete[11] $B_s^0 \to D_s^-\pi^+$ analysis with different cut values. Figure 4.23 presents the results. Taking the maximal and the minimal deviations, a systematic error of 4.8% is added for the $B_s^0 \to D_s^-\pi^+$ and $B_s^0 \to D_s^{\mp}K^{\pm}$ analyses and 2.0% for the others which don't have a cut on the D_s^- decay angle. These systematic are estimated only with the clean $B_s^0 \to D_s^-\pi^+$ analysis and assumed to be comparable in all analyses.

The following procedure is used to obtain the systematic errors due to the PDF shape uncertainties: for each fixed parameter of the fit, the fit is done again with this parameter shifted by $+1\sigma$ and by -1σ. The resulting changes in the fit results are added in quadrature to obtain the total systematics. The systematic uncertainties on the $F_{B_s^{(*)}\bar{B}_s^{(*)}}$ are only affected by the PDF shape uncertainties and are evaluated in the same way.

4.7.2 Systematics on the masses

As 90% of the signal comes from the $B_s^*\bar{B}_s^*$ region, the masses are mostly determined by the two relations of Eqs. (4.4) and (4.3). The propagation of the error on E_{b}^* can be done

[11] Because of a too low statistics, for $R_2 < 0.25$, the parameters $F_{B_s^*\bar{B}_s^*}$ and $F_{B_s^*\bar{B}_s^0}$ are fixed (to the values we found for the nominal cut).

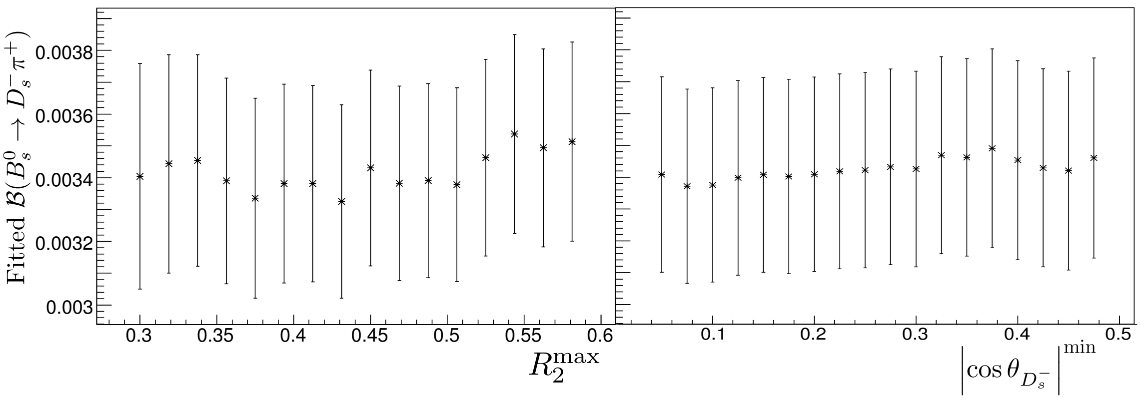

Figure 4.23: Left: fitted $\mathcal{B}(B_s^0 \to D_s^- \pi^+)$ as a function of the R_2 cut value, with statistical errors only. Right: fitted $\mathcal{B}(B_s^0 \to D_s^- \pi^+)$ as a function of the D_s^- decay angle cut value, with statistical errors only.

by inverting these relations, expressed with $E_{B_s^0}$, $p_{B_s^0}$ and E_{b}^*:

$$m_{B_s^0} = \sqrt{E_{B_s^0}^{*2} - p_{B_s^0}^{*2}} = \sqrt{\left(\Delta E + E_{\mathrm{b}}^*\right)^2 + \left(M_{\mathrm{bc}}^2 - E_{\mathrm{b}}^{*2}\right)} = \sqrt{E_{B_s^0}^{*2} - p_{B_s^0}^{*2}}\,, \tag{4.48}$$

$$m_{B_s^*} = M_{\mathrm{bc}} = \sqrt{E_{\mathrm{b}}^{*2} - p_{B_s^0}^{*2}}\,. \tag{4.49}$$

The relative errors on $E_{B_s^0}^*$ and $p_{B_s^0}^*$ are around 1.45×10^{-4}, due to momentum normalisation uncertainties[12].

The B_s^0 mass is measured from the reconstructed four-momentum of the B_s^0 candidates. It is therefore only sensitive to the above-mentioned momentum calibration uncertainties. The $B_s^0 \to D_s^- \pi^+$ fitting procedure is repeated with momenta shifted by $\pm 1\sigma$. The resulting shift of the B_s^0 mass is $^{+0.66}_{-0.65}$ MeV/c^2. A rounded systematic error of ± 0.7 MeV/c^2 is assigned to the B_s^0 mass measurement.

Because the B_s^* decays are not reconstructed, the B_s^* mass is measured with the help of the beam energy and by approximating its momentum with that of its B_s^0 daughter. The three sources of the B_s^* mass systematic uncertainty are

- the beam energy uncertainty,

$$\left|\frac{\partial m_{B_s^*}}{\partial E_{\mathrm{b}}^*}\right| \delta E_{\mathrm{b}}^* = \frac{E_{\mathrm{b}}^*}{m_{B_s^*}} \delta E_{\mathrm{b}}^* \approx \delta E_{\mathrm{b}}^* = \pm 0.5 \ \mathrm{MeV}/c^2 \ \text{(Eq. (2.1))}\,; \tag{4.50}$$

- the approximation of $p_{B_s^*}$ by $p_{B_s^0}$ resulting in an uncertainty of $\pm 0.14\ \mathrm{MeV}/c^2$ (Sec. 4.1);

- the momentum calibration:

$$\frac{\partial m_{B_s^*}}{\partial p_{B_s^0}} \delta p_{B_s^0} = \frac{p_{B_s^0}}{m_{B_s^*}} \delta p_{B_s^0} \approx 0.01 \ \mathrm{MeV}/c^2\,; \tag{4.51}$$

[12] $M_{J/\Psi} - M_{J/\Psi}^{\mathrm{PDG}}$ is measured to be -0.29 ± 0.16 MeV/c^2 in data. The uncertainty is chosen to be $(0.29 + 0.16)\,/M_{J/\Psi}^{\mathrm{PDG}} \approx 1.45 \times 10^{-4}$.

- and discrepancy detected in MC sample (Sec. 4.1): $\pm 0.44\ \mathrm{MeV}/c^2$.

The quadratic sum of these three contributions, $\pm 0.68\ \mathrm{MeV}/c^2$, is quoted as the B_s^* mass systematic error[13].

A quick cross check of the centre-of-mass value reported in Sec. 2.3.1 were performed: we reconstructed $B^+ \to \bar{D}^0(\to K^+\pi^-)\pi^+$ in $\Upsilon(5S)$ data (Fig. 4.24). The region $B^*\bar{B}^*$ was expected to be dominant[14], by comparison with the B_s^0 sector. A peak in M_{bc} should occur near the B^* mass. The PDG value for it is $m_{B^*}^{\mathrm{PDG}} = 5325.1 \pm 0.5\ \mathrm{MeV}/c^2$ [37]. MC studies shows that the peak in $B^*\bar{B}^*$ region is $2.2 \pm 0.1\ \mathrm{MeV}/c^2$ *higher* than the input B^{*+} mass. The peak in M_{bc} for $B^*\bar{B}^*$ region was fitted to be $5328.1 \pm 1.1\ \mathrm{MeV}/c^2$, by removing the $2.2 \pm 0.1\ \mathrm{MeV}/c^2$ bias, we estimated the B^* mass to be $m_{B^*} = 5325.9 \pm 1.1\ \mathrm{MeV}/c^2$. It is $0.8 \pm 1.2\ \mathrm{MeV}/c^2$ higher than the PDG value. Even though statistical error is high, this check shows that the beam energy chosen for the $m_{B_s^*}$ calculation is correct, within errors.

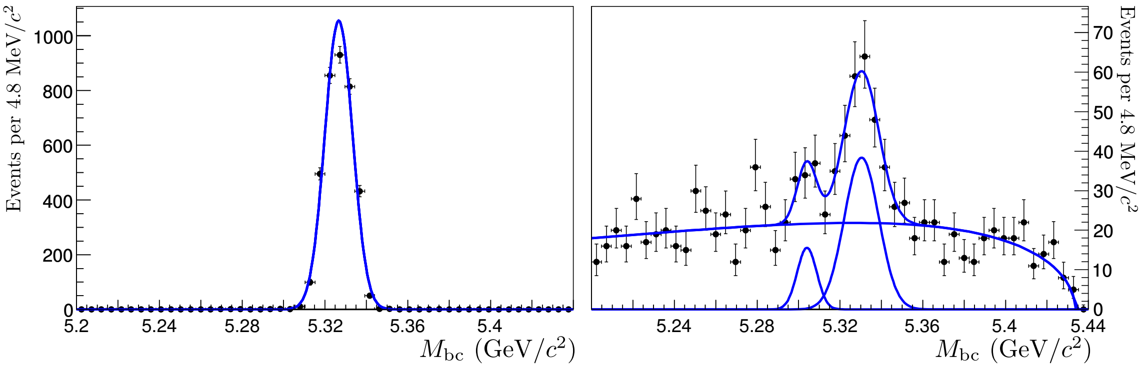

Figure 4.24: M_{bc} distributions (in GeV/c^2) for fully reconstructed $B^+ \to \bar{D}^0(\to K^+\pi^-)\pi^+$ candidates. On the left side, candidates selected in signal MC from $\Upsilon(5S) \to B^{+*}B^{-*}$ decays fitted with a Gaussian distribution. On the right side, candidates in $\Upsilon(5S)$ Belle data, fitted with an Argus shape, and two Gaussian distributions. All the parameters are free. The larger peak corresponds to $B^*\bar{B}^*$ region, while the smaller corresponds to the $B^*\bar{B}$ one. The candidate selection is as following: D^0 candidate with a mass between $1.85\ \mathrm{GeV}/c^2$ and $1.885\ \mathrm{GeV}/c^2$, $R_2 < 0.35$ and ΔE between -0.1 GeV and 0.

The mass B_s^0 determination using B_s^0 modes with a ρ^+ seems to be significantly biased and the results of our mass measurements are those obtained only with the cleaner $B_s^0 \to D_s^-\pi^+$ analysis.

4.7.3 Systematic effect on the $B_s^0 \to D_s^\mp K^\pm$ signal significance

The Cabibbo-suppressed $B_s^0 \to D_s^\mp K^\pm$ mode has a tiny signal with a statistical significance between 3σ and 4σ. It is important to include systematic uncertainties in the estimate of the signal significance.

The total systematics (mostly due to PDF shape uncertainties) on the $B_s^0 \to D_s^\mp K^\pm$ signal yield of Eq. (4.27) is evaluated to be ± 0.2. The curve of the maximum fitted like-

[13] This value differs from that reported in Ref. [10] ($\pm 0.5\ \mathrm{MeV}/c^2$) in which the $0.44\ \mathrm{MeV}/c^2$ uncertainty were omitted.

[14] The measurement of the $\Upsilon(5S)$ event composition reported in Sec. 3.1.2 confirmed it afterwards.

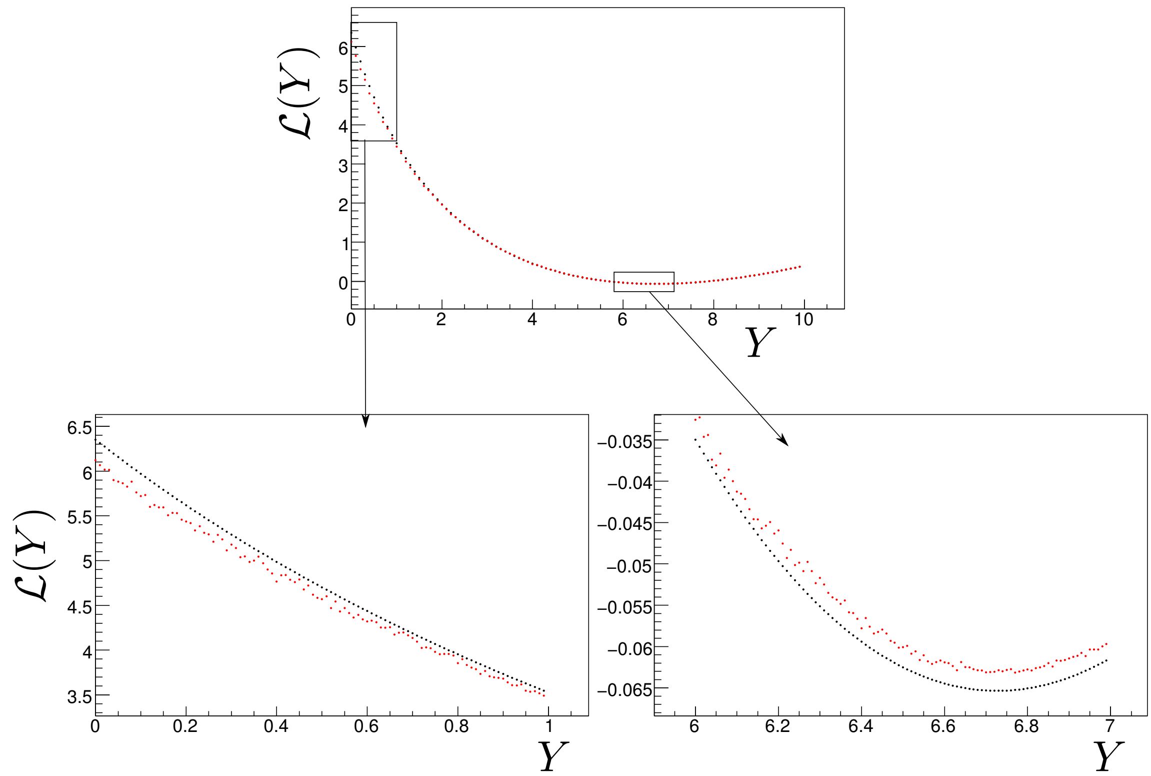

Figure 4.25: Minimised value of $-\log \mathcal{L}_{\text{fit}}$ (black) and $-\log \mathcal{L}_{\text{tot}}$ (red) as a function of the $B_s^0 \to D_s^{\mp}K^{\pm}$ signal yield Y. The three plots show different Y ranges.

lihood as function of the signal yield (Y) is convoluted with a Gaussian g with a mean corresponding to the fitted value and a width corresponding to the total systematics:

$$\mathcal{L}_{\text{tot}}(Y) = \int dy\ \mathcal{L}_{\text{fit}}(y)g(Y-y) \approx \frac{1}{m}\sum_{k=1}^{m} \mathcal{L}_{\text{fit}}(Y_k)\,, \tag{4.52}$$

where Y_k are values taken randomly following a Gaussian distribution with mean $Y_{\text{data}} = 6.7$ and standard deviation 0.2. The number of values $m = 300$ is large enough to ensure a proper estimation of the integral. Figure 4.25 presents the numerical convolution of the $-\ln \mathcal{L}$ function.

By taking the difference between the minimum value of $-\ln \mathcal{L}_{\text{tot}}(Y_{\text{data}})$ and the value at $Y = 0$, we find the significance including systematics to be

$$S(B_s^0 \to D_s^{\mp}K^{\pm}) = \sqrt{2\,(\ln \mathcal{L}_{\text{tot}}(Y_{\text{data}}) - \ln \mathcal{L}_{\text{tot}}(0))} = 3.5\,\sigma\,, \tag{4.53}$$

while the corresponding statistical significance computed from $\mathcal{L}_{\text{fit}}$ is 3.6σ.

4.7.4 Systematics on the $B_s^0 \to D_s^{*-}\rho^+$ fraction of longitudinal polarisation

The systematic uncertainty from the fitting procedure is evaluated in the same way as described above for the branching fraction. The possible discrepancy, between data and

MC, of the fraction of wrongly-reconstructed $B_s^0 \to D_s^{*-}\rho^+$ signal is propagated as an additional systematic uncertainty estimation on $f_{\rm L}$. The total systematic uncertainty on $f_{\rm L}$ is estimated to be $^{+0.03}_{-0.04}$.

4.8 Summary and Discussion

We studied five exclusive B_s^0 decays with one $D_s^{(*)-}$ meson, resulting in a new evidence of the $B_s^0 \to D_s^{\mp}K^{\pm}$ decay mode and the first observations of the $B_s^0 \to D_s^{*-}\pi^+$, $B_s^0 \to D_s^-\rho^+$ and $B_s^0 \to D_s^{*-}\rho^+$ decay modes. The following measurements are obtained:

$$
\begin{aligned}
F_{B_s^*\bar{B}_s^*} &= \left(90.1^{+3.8}_{-4.0}(\text{stat}) \pm 0.2(\text{syst})\right)\%\,, && (4.54)\\
F_{B_s^*\bar{B}_s^0} &= \left(7.3^{+3.3}_{-3.0}(\text{stat}) \pm 0.1(\text{syst})\right)\%\,, && (4.55)\\
F_{B_s^0\bar{B}_s^0} &= 1 - F_{B_s^*\bar{B}_s^*} - F_{B_s^*\bar{B}_s^0} = \left(2.6^{+2.6}_{-2.5}\right)\%\,, && (4.56)\\
m(B_s^0) &= 5364.4 \pm 1.3(\text{stat}) \pm 0.7(\text{syst})\ \text{MeV}/c^2\,, && (4.57)\\
m(B_s^*) &= 5416.4 \pm 0.4(\text{stat}) \pm 0.7(\text{syst})\ \text{MeV}/c^2\,, && (4.58)\\
\mathcal{B}(B_s^0 \to D_s^-\pi^+) &= (3.60 \pm 0.33(\text{stat}) \pm 0.42(\text{syst}) \pm 0.54(f_s)) \times 10^{-3}\,, && (4.59)\\
\mathcal{B}(B_s^0 \to D_s^{\mp}K^{\pm}) &= (2.4 \pm 1.1(\text{stat}){\pm}0.3(\text{syst}) \pm 0.4(f_s)) \times 10^{-4}\,, && (4.60)\\
\mathcal{B}(B_s^0 \to D_s^{*-}\pi^+) &= (2.3 \pm 0.4(\text{stat}) \pm 0.3(\text{syst}) \pm 0.3(f_s)) \times 10^{-3}\,, && (4.61)\\
\mathcal{B}(B_s^0 \to D_s^-\rho^+) &= (8.2 \pm 1.1(\text{stat}) \pm 1.1(\text{syst}) \pm 1.2(f_s)) \times 10^{-3}\,, && (4.62)\\
\mathcal{B}(B_s^0 \to D_s^{*-}\rho^+) &= (11.5 \pm 2.0(\text{stat}) \pm 1.6(\text{syst}) \pm 1.7(f_s)) \times 10^{-3}\,, && (4.63)\\
f_{\rm L}(B_s^0 \to D_s^{*-}\rho^+) &= 1.05^{+0.08}_{-0.10}(\text{stat})^{+0.03}_{-0.04}(\text{syst})\,, && (4.64)
\end{aligned}
$$

where the first (second) quoted uncertainey is statistical (systematic). The uncertainty due to f_s, when present, is quoted separately. Details on the systematic uncertainties of the branching fraction measurements are given in Table 4.16, which summarises all mass and branching fraction results.

The fitted values of the $B_s^0 \to D_s^-\pi^+$ and $B_s^0 \to D_s^{\mp}K^{\pm}$ branching fractions are in line with expectations and compatible with the CDF measurements [205, 207]. The branching fraction ratios, in which several systematic uncertainties cancel (in particular the large uncertainty on the number of produced B_s^0 mesons), are measured to be

$$
\begin{aligned}
\frac{\mathcal{B}(B_s^0 \to D_s^{\mp}K^{\pm})}{\mathcal{B}(B_s^0 \to D_s^-\pi^+)} &= 0.065^{+0.035}_{-0.029} \pm 0.004\,, && (4.65)\\
\frac{\mathcal{B}(B_s^0 \to D_s^{*-}\pi^+)}{\mathcal{B}(B_s^0 \to D_s^-\pi^+)} &= 0.65^{+0.15}_{-0.13} \pm 0.05\,, && (4.66)\\
\frac{\mathcal{B}(B_s^0 \to D_s^-\rho^+)}{\mathcal{B}(B_s^0 \to D_s^-\pi^+)} &= 2.3 \pm 0.4 \pm 0.2\,, && (4.67)\\
\frac{\mathcal{B}(B_s^0 \to D_s^{*-}\rho^+)}{\mathcal{B}(B_s^0 \to D_s^-\pi^+)} &= 3.2 \pm 0.6 \pm 0.2\,, && (4.68)\\
\frac{\mathcal{B}(B_s^0 \to D_s^{*-}\rho^+)}{\mathcal{B}(B_s^0 \to D_s^-\rho^+)} &= 1.4 \pm 0.3 \pm 0.1\,, && (4.69)
\end{aligned}
$$

where only the systematic uncertainties from MC statistics, selection cuts and PDF shapes, are retained. When the two selected modes do not involve the same particle identification requirements or branching fractions, the corresponding systematic errors are also kept: for instance, the uncertainties from the photon identification and from the $D_s^{*-} \to D_s^-\gamma$ branching fraction are included in the ratio $\mathcal{B}(B_s^0 \to D_s^{*-}\pi^+)/\ \mathcal{B}(B_s^0 \to D_s^-\pi^+)$, etc.

Table 4.17 compares our branching fraction measurements with predictions from various theoretical models [208–210], as well as with measurements and predictions of the B^0 counterpart decays. A very coherent picture emerges without significant discrepancies. Similarly, the large value of f_L measured in $B_s^0 \to D_s^{*-}\rho^+$ decays, also compared in Table 4.17, yields no surprise as the available prediction and the measurement with $B^0 \to D^{*-}\rho^+$ decays agree reasonable well with it.

Our measurement of the fraction $F_{B_s^*\bar{B}_s^*}$ is fully compatible with the result of the analysis of the $1.86\ \mathrm{fb}^{-1}$ Belle dataset [4], but more precise. This fraction is larger than theoretical predictions (70%, see discussion in Ref. [4]).

The fraction $F_{B_s^*\bar{B}_s^0}$ (Eq. (4.55)) is measured for the first time, providing only weak evidence of $B_s^*\bar{B}_s^0$ events at the $\Upsilon(5S)$. As to the fraction $F_{B_s^0\bar{B}_s^0} = 1 - F_{B_s^*\bar{B}_s^*} - F_{B_s^*\bar{B}_s^0}$, it is found to be compatible with 0 (Eq. (4.56)).

The fitted value of the B_s^0 mass in $B_s^0 \to D_s^-\pi^+$ events is fully compatible with the PDG average[15], $5366.6{\pm}0.9\ \mathrm{MeV}/c^2$ [211]. The B_s^* mass is completely compatible with that of a previous Belle analysis, $5418 \pm 1 \pm 3\ \mathrm{MeV}/c^2$ [4], and shows an acceptable 2.5σ deviation with the CLEO measurement, $5411.7 \pm 1.6 \pm 0.6\ \mathrm{MeV}/c^2$ [174]. The mass difference[16] $m_{B_s^*} - m_{B_s^0} = 52.0 \pm 1.6\ \mathrm{MeV}/c^2$ is 3.8σ larger than the PDG average for $m_{B^{*0}} - m_{B^0}$, $45.78{\pm}0.35\ \mathrm{MeV}/c^2$ [37]. Heavy quark symmetry models predict $m_{B_s^*} - m_{B_s^0} = m_{B^{*0}} - m_{B^0}$ (Sec. 1.7.1).

[15]This is the PDG 2008 average, because our measurements are included in the PDF updates since.

[16]The fit correlation between $m_{B_s^*}$ and $m_{B_s^0}$, +0.158, is included in the error.

Table 4.16: Summary of the branching fraction and mass measurements performed with exclusive B_s^0 decay modes. From top to bottom line: signal yield for the $B_s^*\bar{B}_s^*$ production mode with signal significance (including systematics only for $B_s^0 \to D_s^-\pi^+$ and $B_s^0 \to D_s^\mp K^\pm$); reconstruction efficiency including sub-decay branching fractions; branching fraction as measured from the signal yields, with statistical, systematic (without f_s contribution) and f_s uncertainties; B_s^0 and B_s^* masses measured from the signal mean values, only for comparison (the final mass measurements are only those obtained with $B_s^0 \to D_s^-\pi^+$ events). The bottom part of the table gives details about the systematic uncertainties affecting the branching fraction measurements.

	$B_s^0 \to D_s^-\pi^+$	$B_s^0 \to D_s^\mp K^\pm$	$B_s^0 \to D_s^{*-}\pi^+$	$B_s^0 \to D_s^-\rho^+$	$B_s^0 \to D_s^{*-}\rho^+$
$N_{B_s^*\bar{B}_s^*}$ (significance)	145^{+14}_{-13} (21σ)	$6.7^{+3.4}_{-2.7}$ (3.5σ)	$53.4^{+10.3+2.4}_{-9.4\ -2.6}$ (8.4σ)	$92.2^{+14.2+4.3}_{-13.2-4.2}$ (10.6σ)	$77.7^{+14.6}_{-13.3} \pm 3.3$ (9.1σ)
$\sum \varepsilon\mathcal{B}$ (10^{-3})	$15.8 \pm 0.2 \pm 1.0$	$11.2 \pm 0.2 \pm 0.7$	$9.13 \pm 0.15 \pm 0.59$	$4.40 \pm 0.10 \pm 0.28$	$2.67 \pm 0.03 \pm 0.17$
$\mathcal{B}$ (10^{-3})	$3.6 \pm 0.3 \pm 0.4 \pm 0.5$	$0.24 \pm 0.11 \pm 0.03 \pm 0.04$	$2.3 \pm 0.4 \pm 0.3 \pm 0.3$	$8.2 \pm 1.1 \pm 1.1 \pm 1.2$	$11.5 \pm 2.0 \pm 1.6 \pm 1.7$
$m_{B_s^0}$ (MeV$/c^2$)	$5364.4 \pm 1.3 \pm 0.7$	—	$5364.4^{+5.5+0.6}_{-3.4-0.8}$	$5372.3^{+4.2}_{-4.1} \pm 0.7$	$5379.2^{+7.0+0.3}_{-6.6-0.7}$
$m_{B_s^*}$ (MeV$/c^2$)	$5416.4 \pm 0.4 \pm 0.7$	—	$5416.7 \pm 0.6^{+0.2}_{-0.1}$	$5416.1 \pm 0.7 \pm 0.1$	$5415.7 \pm 0.8 \pm 0.1$
Relative systematic uncertainties (%)					
–f_s	15.1	15.1	15.1	15.1	15.1
–Others:	11.5	12.6	12.6	12.8	12.7
L_{int}	1.3	1.3	1.3	1.3	1.3
$\sigma(e^+e^- \to \Upsilon(5S))$	4.6	4.6	4.6	4.6	4.6
$F_{B_s^*\bar{B}_s^*}$	—	4.3	4.3	4.3	4.3
D_s^- branching fractions	6.3	6.3	6.4	6.4	6.4
selection efficiency	4.8	4.8	2.0	2.0	2.0
tracking efficiency	4.0	4.0	4.0	4.0	4.0
$\pi^\pm/K^\pm$ ID efficiency	5.4	5.2	5.4	5.4	5.4
γ ID efficiency	—	—	2.0	—	2.0
π^0 ID efficiency	—	—	—	1.7	1.7
PDF shapes	1.0	3.0	4.6	4.7	4.3
MC statistics	1.2	1.4	1.6	2.3	1.5

Table 4.17: Comparison between measurements and theoretical predictions in the heavy-quark effective theory with factorisation hypothesis (HQET+f) [208], in the covariant light-front quark model (cLFHQ) [209] and in the perturbative quantum chromo-dynamics approach (pQCD) [210]. The experimental values are those reported in this work averaged with other existing measurements. The B^0 counterpart decays are shown for comparison. Check also Refs. [212–217] for further theory speculations.

Quantity	HQET+f [208]	cLFQM [209]	pQCD [210]	Measurement
$\mathcal{B}(B^0 \to D^-\pi^+)$ (10^{-3})	2.5	—	2.7 ± 0.9	2.68 ± 0.13 [37]
$\mathcal{B}(B_s^0 \to D_s^-\pi^+)$ (10^{-3})	2.8	—	2.0 ± 1.1	3.6 ± 0.8 (This work)
$\mathcal{B}(B_s^0 \to D_s^{\mp}K^{\pm})(10^{-4})$	2.1	—	1.7 ± 0.9	2.4 ± 1.2 (This work)
$\mathcal{B}(B^0 \to D^{*-}\pi^+)$ (10^{-3})	2.6	—	2.6 ± 0.9	2.76 ± 0.13 [37]
$\mathcal{B}(B_s^0 \to D_s^{*-}\pi^+)$ (10^{-3})	2.8	3.5 ± 0.4	1.9 ± 1.1	2.3 ± 0.6 (This work)
$\mathcal{B}(B^0 \to D^-\rho^+)$ (10^{-3})	6.6	—	6.7 ± 2.3	7.8 ± 1.3 [37]
$\mathcal{B}(B_s^0 \to D_s^-\rho^+)$ (10^{-3})	7.5	—	4.7 ± 2.6	8.2 ± 2.0 (This work)
$\mathcal{B}(B^0 \to D^{*-}\rho^+)$ (10^{-3})	8.7	—	7.5 ± 2.6	6.8 ± 0.9 [37]
$\mathcal{B}(B_s^0 \to D_s^{*-}\rho^+)$ (10^{-3})	8.9	11.8 ± 3.2	5.2 ± 3.0	11.5 ± 3.1 (This work)
$f_{\mathrm{L}}(B^0 \to D^{*-}\rho^+)$	—	—	0.85	0.885 ± 0.020 [218]
$f_{\mathrm{L}}(B_s^0 \to D_s^{*-}\rho^+)$	—	—	0.87	$1.05^{+0.09}_{-0.11}$ (This work)

Conclusion

In this thesis, several original analyses performed with the Belle $\Upsilon(5S)$ dataset have been presented. From our study of B_s^0 decaying into one $D_s^{(*)-}$ and a light meson, we report the first observation of three new Cabibbo-allowed decay modes: $B_s^0 \to D_s^{*-}\pi^+$, $B_s^0 \to D_s^-\rho^+$ and $B_s^0 \to D_s^{*-}\rho^+$.

$$
\begin{aligned}
m_{B_s^0} &= 5364.4 \pm 1.3(\mathrm{stat}) \pm 0.7(\mathrm{syst})\ \mathrm{MeV}/c^2 \\
m_{B_s^*} &= 5416.4 \pm 0.4(\mathrm{stat}) \pm 0.7(\mathrm{syst})\ \mathrm{MeV}/c^2 \\
F_{B_s^*\bar{B}_s^*} &= \sigma(e^+e^- \to B_s^*\bar{B}_s^*)/\sigma(e^+e^- \to B_s^{(*)}\bar{B}_s^{(*)}) \\
&= \left(90.1^{+3.8}_{-4.0}(\mathrm{stat}) \pm 0.2(\mathrm{syst})\right)\%\,, \\
F_{B_s^*\bar{B}_s^0} &= \sigma(e^+e^- \to B_s^*\bar{B}_s^0)/\sigma(e^+e^- \to B_s^{(*)}\bar{B}_s^{(*)}) \\
&= \left(7.3^{+3.3}_{-3.0}(\mathrm{stat}) \pm 0.1(\mathrm{syst})\right)\%\,, \\
F_{B_s^0\bar{B}_s^0} &= \sigma(e^+e^- \to B_s^0\bar{B}_s^0)/\sigma(e^+e^- \to B_s^{(*)}\bar{B}_s^{(*)}) = \left(2.6^{+2.6}_{-2.5}\right)\%\,, \\
\mathcal{B}(B_s^0 \to D_s^-\pi^+) &= (3.60 \pm 0.33(\mathrm{stat}) \pm 0.42(\mathrm{syst}) \pm 0.54(f_s)) \times 10^{-3}\,, \\
\mathcal{B}(B_s^0 \to D_s^{\mp}K^{\pm}) &= (2.4 \pm 1.1(\mathrm{stat}){\pm}0.3(\mathrm{syst}) \pm 0.4(f_s)) \times 10^{-4}\,, \\
\mathcal{B}(B_s^0 \to D_s^{*-}\pi^+) &= (2.3 \pm 0.4(\mathrm{stat}) \pm 0.3(\mathrm{syst}) \pm 0.3(f_s)) \times 10^{-3}\,, \\
\mathcal{B}(B_s^0 \to D_s^-\rho^+) &= (8.2 \pm 1.1(\mathrm{stat}) \pm 1.1(\mathrm{syst}) \pm 1.2(f_s)) \times 10^{-3}\,, \\
\mathcal{B}(B_s^0 \to D_s^{*-}\rho^+) &= (11.5 \pm 2.0(\mathrm{stat}) \pm 1.6(\mathrm{syst}) \pm 1.7(f_s)) \times 10^{-3}\,, \\
f_{\mathrm{L}}(B_s^0 \to D_s^{*-}\rho^+) &= 1.05^{+0.08}_{-0.10}(\mathrm{stat})^{+0.03}_{-0.04}(\mathrm{syst})\,.
\end{aligned}
$$

These competitive measurements are in agreement with less precise results obtained by other particle physics experiment (when they exist), and are in line with theoretical expectations.

The branching fraction precision is limited by the poor knowledge of the B_s^0 production fraction. Our newly-implemented analysis exploiting the sign correlation of lepton pairs from semi-leptonic $B_{(s)}$ decays provides the most precise measurement of the ratio of the B_s^0 production fraction (f_s) over the non-strange B meson production fraction ($f_{u,d}$),

$$
\frac{f_s}{f_{u,d}} = \frac{\sigma(e^+e^- \to B_s^{(*)}\bar{B}_s^{(*)})}{\sigma(e^+e^- \to B^{(*)}\bar{B}^{(*)}(X))} = (38.6 \pm 5.6)\%\,.
$$

However this result is dominated by systematic uncertainties and its precision is affected by the complexity of the fitting procedure and by the limited knowledge of the composition of non-strange B events. An averaging procedure has been implemented to combine all existing measurement of $B_{(s)}$ production measurements at the $\Upsilon(5S)$ energy. Including our dilepton result, the world average of the $B_{(s)}$ production fractions is

$$\begin{aligned} f_s &= \frac{\sigma(e^+e^- \to B_s^{(*)}\bar{B}_s^{(*)})}{\sigma(e^+e^- \to b\bar{b})} = \left(23.4^{+2.3}_{-2.4}\right)\%\,, \\ f_{u,d} &= \frac{\sigma(e^+e^- \to B^{(*)}\bar{B}^{(*)}(X))}{\sigma(e^+e^- \to b\bar{b})} = \left(72.5^{+2.3}_{-2.8}\right)\%\,, \\ f_{\not B} &= 1 - f_{u,d} - f_s = \left(4.1^{+3.4}_{-0.5}\right)\%\,. \end{aligned}$$

This work shows the large potential of the Belle $\Upsilon(5S)$ sample and the physics at this energy is very rich. Our implementation of the B mixing for C-even $B^0_{(s)}\bar{B}^0_{(s)}$ pairs in the event generator, as well as the measurement of the $\Upsilon(5S)B_s^{(*)}\bar{B}_s^{(*)}$ production fractions are two significant improvements towards a more realistic Monte Carlo event generator at the $\Upsilon(5S)$ energy, and will help future research at Belle and at super B factories.

Since the beginning of this work, many other interesting results with B_s^0 mesons have been obtained by the Belle collaborators, providing new and competitive results for many decay modes, such as the first observation of a B_s^0 baryonic decay, $B_s^0 \to \Lambda_c^+\pi^-\bar{\Lambda}$ [219], or those involving $b \to c\bar{c}s$ transitions, like $B_s^0 \to J/\psi\eta^{(\prime)}$ [220], $B_s^0 \to J/\psi f_0$ [221] and the measurement of $\Delta\Gamma_s^{CP}/\Gamma_s$ with $B_s^0 \to D_s^{(*)+}D_s^{(*)-}$ events [222]. Hadron collider experiments, where the statistic is much larger than at B factories and where time-dependent studies are possible, also significantly contribute to the B_s^0 studies. However, the environment of e^+e^- collisions allows for analysing B_s^0 modes involving neutral pions or photon in their final states. Our discovery of the three $B_s^0 \to D_s^{*-}\pi^+$, $B_s^0 \to D_s^-\rho^+$ and $B_s^0 \to D_s^{*-}\rho^+$ decays demonstrates the unique feature.

In addition, e^+e^- collisions at $\Upsilon(5S)$ energy can also be used for bottomonium studies or for novel methods with non-strange B mesons. Surprisingly, the nature of the so-called $\Upsilon(5S)$ resonance is not well known, and large production of bottomonium resonance below the open-beauty threshold has been measured: beside the anomalously large $\Upsilon(nS), n = 1, 2, 3$ production [151, 223], several new bottomonium resonances have been observed, such as the $h_b(1P)$ and $h_b(2P)$ [172], or the charged $Z_b(10610)$ and $Z_b(10650)$ [224]. Finally, the feasibility of measuring the CKM angle ϕ_1 (β) with the so-called $B - \pi$ tagging [219] shows the potential of non-strange B studies at the $\Upsilon(5S)$ energy, in addition of being important for the dilepton measurements of $f_s/f_{u,d}$. The construction of next-generation of B factories [225] has already started and the first collisions in an upgraded Belle detector are expected to be delivered by 2014. In the light of the now firmly-established potential of $\Upsilon(5S)$ data, these new experiments should definitely dedicate a significant running time at this energy.

Remerciements

Ce travail n'aurait pas été rendu possible sans l'aide déterminante de plusieurs personnes auxquelles je souhaiterais exprimer ici ma reconaissance.

Ma gratitude va tout particulièrement au directeur de cette thèse, M. le Professeur Olivier Schneider, qui, avec beaucoup de patience et d'enthousiasme, a su me guider pendant ces quelques années passées dans le monde fascinant de la physique des particules.

Je remercie MM. Jean Wicht et Tagir Aushev pour leur aide précieuse tout au long de mon travail au sein de l'expérience Belle. Je remercie également tous les membres de l'expérience avec lesquels j'ai eu l'occasion d'être en contact, que ce soit ou cours d'un séminaire, d'un *shift* ou par courriel.

J'aimerais aussi remercier toutes les personnes qui m'ont rendu la vie si facile au laboratoire de physique des hautes énergie de l'EPFL, notamment son directeur, M. le Professeur Aurelio Bay, ainsi que ses deux secrétaires, Mmes Erika Lüthi et Esther Hofmann qui sont (presque) toujours au courant de (presque) tout. Le service informatique central (DIT) de l'EPFL, par l'intermédiaire de M. Jean-Claude Berney, son directeur, et de MM. Japhet Bagilishya et Jacques Menu, m'a été d'une grande aide en me donnant accès à de considérables ressources informatiques. Je remercie également les membres du jury de cette thèse pour l'accueil qu'ils ont donné à ce travail.

Enfin, je dois beaucoup à ma famille pour son soutient, et tout spécialement à ma femme qui a dû (et qui continue à) me supporter.

R. Louvot
Londres, novembre 2011.

Appendix A

Oscillations and simulation of $B_q^0\bar{B}_q^0$ meson pairs

A.1 Formulae

A $B_q^0\bar{B}_q^0$ meson pair produced in e^+e^- collisions does not oscillate in the same way as a free neutral meson (Sec. 1.7.2). Starting from Eqs. (1.69) and (1.70) with

$$z_q = x_q + iy_q = \frac{\Delta m_q + \frac{i}{2}\Delta\Gamma_q}{\Gamma_q}\,, \tag{A.1}$$

the time evolution of an incoherent $B_q^0\bar{B}_q^0$ pair at $t = 0$ is given by

$$\begin{aligned}
\left|B_q^0(t_1)\bar{B}_q^0(t_2)\right\rangle_0 = \left|B_q^0(t_1)\right\rangle \otimes \left|\bar{B}_q^0(t_2)\right\rangle = e^{-\Gamma_q(t_1+t_2)/2}e^{-im_q(t_1+t_2)}\times \qquad\qquad (\mathrm{A.2})\\
\Bigg(\cos\frac{\Gamma_q z_q t_1}{2}\cos\frac{\Gamma_q z_q t_2}{2}\left|B_q^0\bar{B}_q^0\right\rangle - \sin\frac{\Gamma_q z_q t_1}{2}\sin\frac{\Gamma_q z_q t_2}{2}\left|\bar{B}_q^0 B_q^0\right\rangle \\
-i\frac{p}{q}\cos\frac{\Gamma_q z_q t_1}{2}\sin\frac{\Gamma_q z_q t_2}{2}\left|B_q^0 B_q^0\right\rangle - i\frac{q}{p}\sin\frac{\Gamma_q z_q t_1}{2}\cos\frac{\Gamma_q z_q t_2}{2}\left|\bar{B}_q^0\bar{B}_q^0\right\rangle\Bigg)\,,\\
\left|\bar{B}_q^0(t_1)B_q^0(t_2)\right\rangle_0 = \left|\bar{B}_q^0(t_1)\right\rangle \otimes \left|B_q^0(t_2)\right\rangle = e^{-\Gamma_q(t_1+t_2)/2}e^{-im_q(t_1+t_2)}\times \qquad\qquad (\mathrm{A.3})\\
\Bigg(-\sin\frac{\Gamma_q z_q t_1}{2}\sin\frac{\Gamma_q z_q t_2}{2}\left|B_q^0\bar{B}_q^0\right\rangle + \cos\frac{\Gamma_q z_q t_1}{2}\cos\frac{\Gamma_q z_q t_2}{2}\left|\bar{B}_q^0 B_q^0\right\rangle \\
-i\frac{p}{q}\sin\frac{\Gamma_q z_q t_1}{2}\cos\frac{\Gamma_q z_q t_2}{2}\left|B_q^0 B_q^0\right\rangle - i\frac{q}{p}\cos\frac{\Gamma_q z_q t_1}{2}\sin\frac{\Gamma_q z_q t_2}{2}\left|\bar{B}_q^0\bar{B}_q^0\right\rangle\Bigg)\,.
\end{aligned}$$

However, in e^+e^- collisions, the neutral B pairs are produced in coherent C eigenstates and the quantum state has to be properly symmetrised [24] according the C eigenvalue.

A C-even ($\eta = +1$) or C-odd ($\eta = -1$) state can be written as

$$\begin{aligned}\left|B_q^0(t_1)\bar{B}_q^0(t_2)\right\rangle_\eta &= \frac{1}{\sqrt{2}}\left(\left|B_q^0(t_1)\bar{B}_q^0(t_2)\right\rangle_0 + \eta\left|\bar{B}_q^0(t_1)B_q^0(t_2)\right\rangle_0\right) \\ &= \frac{1}{\sqrt{2}}e^{-\frac{1}{2}\Gamma_q(t_1+t_2)}e^{-im_q(t_1+t_2)}\times \\ &\quad\left(-i\sin\frac{\Gamma_q z_q}{2}(t_1+\eta t_2)\left(\eta\frac{p}{q}\left|B_q^0B_q^0\right\rangle + \frac{q}{p}\left|\bar{B}_q^0\bar{B}_q^0\right\rangle\right)\right. \\ &\quad\left. + \cos\frac{\Gamma_q z_q}{2}(t_1+\eta t_2)\left(\left|B_q^0\bar{B}_q^0\right\rangle + \eta\left|\bar{B}_q^0B_q^0\right\rangle\right)\right)\,.\end{aligned} \tag{A.4}$$

The time-integrated normalisation of these states ($\eta = -1, 0, 1$) is

$$\begin{aligned}N_\eta = &\iint\left(\left|\left\langle\bar{B}_q^0B_q^0|B_q^0(t_1)\bar{B}_q^0(t_2)\right\rangle_\eta\right|^2 + \left|\left\langle B_q^0\bar{B}_q^0|B_q^0(t_1)\bar{B}_q^0(t_2)\right\rangle_\eta\right|^2\right. \\ &\left. + \left|\left\langle B_q^0B_q^0|B_q^0(t_1)\bar{B}_q^0(t_2)\right\rangle_\eta\right|^2 + \left|\left\langle\bar{B}_q^0\bar{B}_q^0|B_q^0(t_1)\bar{B}_q^0(t_2)\right\rangle_\eta\right|^2\right)dt_1dt_2 \\ = &\frac{1+\eta y_q^2}{\Gamma_q^2\left(1-y_q^2\right)^2}\,,\end{aligned} \tag{A.5}$$

where $\eta = 0$ for incoherent states and $\eta = \pm1$ for coherent states. The probabilities for the two neutral B mesons to decay with the same flavours or opposite flavours are

$$\begin{aligned}\mathrm{Prob}(B_q^0B_q^0) + \mathrm{Prob}(\bar{B}_q^0\bar{B}_q^0)_\eta &= \frac{1}{N_\eta}\iint\left(\left|\left\langle B_q^0B_q^0|B_q^0(t_1)\bar{B}_q^0(t_2)\right\rangle_\eta\right|^2\right. \\ &\quad\left. + \left|\left\langle\bar{B}_q^0\bar{B}_q^0|B_q^0(t_1)\bar{B}_q^0(t_2)\right\rangle_\eta\right|^2\right)dt_1dt_2 \\ &= \begin{cases}\frac{1}{N_\eta}\iint e^{-\Gamma_q(t_1+t_2)}\left|\sin\frac{\Gamma_q z_q}{2}(t_2+\eta t_1)\right|^2 dt_1dt_2\,, & \text{if } \eta = \pm1 \\ \frac{1}{N_\eta}\iint e^{-\Gamma_q(t_1+t_2)}\left|\cos\frac{\Gamma_q z_q}{2}t_1\sin\frac{\Gamma_q z_q}{2}t_2\right|^2 dt_1dt_2\,, & \text{if } \eta = 0\end{cases} \\ &= \frac{\left(x_q^2+y_q^2\right)\left(x_q^2-y_q^2+2+\eta+\eta x_q^2y_q^2\right)}{2\left(1+\eta y_q^2\right)\left(1+x_q^2\right)^2}\,.\end{aligned} \tag{A.6}$$

Similarly,

$$\begin{aligned}\mathrm{Prob}(B_q^0\bar{B}_q^0) + \mathrm{Prob}(\bar{B}_q^0B_q^0)_\eta &= \frac{1}{N_\eta}\iint\left(\left|\left\langle\bar{B}_q^0B_q^0|B_q^0(t_1)\bar{B}_q^0(t_2)\right\rangle_\eta\right|^2\right. \\ &\quad\left. + \left|\left\langle B_q^0\bar{B}_q^0|B_q^0(t_1)\bar{B}_q^0(t_2)\right\rangle_\eta\right|^2\right)dt_1dt_2 \\ &= \frac{x_q^4+y_q^4+(2-\eta)\left(x_q^2-y_q^2\right)+\eta x_q^2y_q^2\left(x_q^2-y_q^2+4\right)+2}{2\left(1+\eta y_q^2\right)\left(1+x_q^2\right)^2} \\ &= 1 - \mathrm{Prob}(B_q^0B_q^0 + \bar{B}_q^0\bar{B}_q^0)_\eta\,.\end{aligned} \tag{A.7}$$

A.2 Simulation of $B_q^0 \bar{B}_q^0$ mixing at the $\Upsilon(5S)$

A.2.1 Preamble

This section details the implementation of the B mixing in EvtGen. This is the documentation for the PHSP_BB_MIX and PHSP_B_MIX decay models included in the Belle library (from b20090127_0910 patch 36)

So far, the event generator EvtGen has only used the model VSS_BMIX designed to handle $\Upsilon(4S) \to B^0 \bar{B}^0$ events, i.e. $B^0 \bar{B}^0$ pairs with $C = -1$. As detailed in Chapter 3, at the $\Upsilon(5S)$ energy, more types of events involving neutral $B_{(s)}$ mesons exist and have to be simulated:

- $B^0_{(s)} \bar{B}^0_{(s)}$ pairs coming from $\Upsilon(5S) \to B^0_{(s)} \bar{B}^0_{(s)}$ or $\Upsilon(5S) \to B^{*0}_{(s)} \bar{B}^{*0}_{(s)}$ oscillate in an entangled way with $C = -1$.
- $B^0_{(s)} \bar{B}^0_{(s)}$ pairs coming from $\Upsilon(5S) \to B^{*0}_{(s)} \bar{B}^0_{(s)}$ or $\Upsilon(5S) \to B^0_{(s)} \bar{B}^{*0}_{(s)}$ oscillate in an entangled way with $C = +1$
- $B^0 \bar{B}^0$ pairs coming from $\Upsilon(5S) \to B^{(*)0} \bar{B}^{(*)0} \pi(\pi)$ 3,4-body decays oscillate with $C = +1$ or $C = -1$.
- single neutral B^0 mesons coming from $\Upsilon(5S) \to B^{(*)0} B^{(*)-} \pi^+(\pi^0)$ or $\Upsilon(5S) \to \bar{B}^{(*)0} B^+$ decays oscillate without entanglement.

In order to improve the decay generator, two decay models have been written, based on VSS_BMIX[1]:

- PHSP_BB_MIX for $\Upsilon(5S) \to B^0_{(s)} \bar{B}^0_{(s)}(X)$ decays. It takes as input the C eigenvalue of the $B^0_{(s)} \bar{B}^0_{(s)}$ pair and the mixing parameter, $\Delta m_{(s)}$.
- PHSP_B_MIX for $\Upsilon(5S) \to B^0 B^- X^+$ and $\Upsilon(5S) \to \bar{B}^0 B^+ X^-$ decays. The only parameter is the mixing parameter, Δm.

These very same models are also used for decays where one of the B meson is replaced with the corresponding excited state.

While these models implement the correct proper-time dependence and time-integrated mixing probabilities and should be sufficiently accurate for our purpose, they are far from perfect and should be used with care. The principal limitations are the following:

- All daughters of the $\Upsilon(5S)$ are assumed to be spinless (not correct for $B^*_{(s)}$).
- The B^{*0} undergoes mixing with the same properties as the B^0 and then decay to a B^0 with no lifetime. This solution is chosen for implementation simplicity, but the $B^{*0} \to B^0 \gamma$ vertices are displaced from their true position.
- The model cannot generate decays with initial state radiation, $e^+e^- \to \gamma_{\rm ISR} b\bar{b}, b\bar{b} \to B^{(*)} \bar{B}^{(*)}(X)$.
- The implementation is somewhat tricky: we need to define B^* mesons with no spin and with the B lifetime, B mesons with zero lifetime, etc.

[1] The names PHSP_BB_MIX and PHSP_B_MIX should have been VSS_BB_MIX and VSS_B_MIX...

A.2.2 Implementation

The new models are largely derived from the `VSS_BMIX` source code and can handle only spinless daughters. The files can be found in a local copy of the three EvtGen packages (evtgenutil, belleEvtGenBase, belleEvtGenModels) in the EvtGen directory. There are two new files for implementing the new models:

- `./src/belleEvtGenModels/src/EvtPHSPBMix.cc`
- `./src/belleEvtGenModels/belleEvtGenModels/EvtPHSPBMix.hh`

and minor modifications of three other files

- `./src/belleEvtGenModels/src/EvtModelReg.cc`. This is where all the possible decay models are declared.
- `./src/belleEvtGenBase/src/EvtParticle.cc`. B_s^0 mixing was hard-coded in the software core code with a time-integrated probability of 50%. This part of the file has been commented out because our new models can decay the B_s^0 pairs as well as the B^0 pairs by changing the value of the Δm mixing parameter. The time-integrated probability for the B_s^0 pairs has not changed, but the time-dependence is now included.
- `./src/evtgenutil/src/EvtGen.cc`. This is only for an additional printout (in the logfile) when launching EvtGen.

A.2.3 How to use it

The “make” command should work out-of-the-box. The module `./bin/evtgen.so` should be used. It should also be checked that it is linked with `./lib/so/{libevtgenutil.so, libbelleEvtGenBase.so, libbelleEvtGenModels.so}`.

Particle definition A few changes are needed in the particle definition table (PDT) file in order to always have spinless daughters and correct lifetimes for the mixing. The modifications are (see `~louvot/belle/fs/mcprod/script/evt_RL.pdl`):

- `B0` and `anti-B0` with zero lifetime;
- `(anti-)B0long`[2] has the B^0 properties (with non-zero lifetime) and decays to `B0`;
- `(anti-)B0heavy` is a B^{*0} with the B^0 lifetime and without spin; it decays to `B0 gamma`;
- there are also spinless B^{*+}, `B*+nospin` that decay to “normal” `B*+`;
- the same modifications are made for B_s^0 and B_s^* (`(anti-)Bs0heavy` and `(anti-)Bs0long`);
- the standard DECAY.DEC can be used, provided that the decay of these new particles is added. (for example, at the end of ~louvot/belle/fs/mcprod/script/DECAY_RL.DEC).

[2]These names are misleading: long and heavy have absolutely no relation with the mass eigenstates of the $B^0\bar{B}^0$ system. B0long is a B0 with a non-zero lifetime, B0heavy has the same spin and lifetime as a B^0, but more heavy (B^* mass).

Decay definition Appendix A.2.5 shows a full example of a generic $e^+e^- \to b\bar{b}$ decay file. The syntax of the PHSP_BB_MIX and PHSP_B_MIX lines is as follows:

- Two neutral B mesons:

  BR B01 B02 PI1 PI2 anti-B01 anti-B02 PHSP_BB_MIX Δm C;

  The parameters BR, Δm and C are the branching fraction, the mixing parameter, $\Delta m = m_{\mathrm{H}} - m_{\mathrm{L}}$ and the C-parity of the B01–B02 pair, respectively. If the second daughter, B02, is the antiparticle of the first one, B01, the anti-B01 and anti-B02 parameters must be omitted. Finally, the third and fourth daughter, PI1 and PI2, must be specified only in case of 3- or 4-body decay. The following examples show the description of the $\Upsilon(5S) \to B^{*0}\bar{B}^{*0}$, $B^{*0}\bar{B}^0 + B^0\bar{B}^{*0}$ and $B^0\bar{B}^0$ decays,

```
0.19687  B0heavy   anti-B0heavy                                  PHSP_BB_MIX  dm_B0  -1 ;
0.03595  B0heavy   anti-B0long          anti-B0heavy   B0long    PHSP_BB_MIX  dm_B0  +1 ;
0.03595  B0long    anti-B0heavy         anti-B0long    B0heavy   PHSP_BB_MIX  dm_B0  +1 ;
0.02886  B0long    anti-B0long                                   PHSP_BB_MIX  dm_B0  -1 ;
```

  $\Upsilon(5S) \to B_s^*\bar{B}_s^*, B_s^*\bar{B}_s^0 + B_s^0\bar{B}_s^*$ and $B_s^0\bar{B}_s^0$ decays,

```
0.17389  B_s0heavy  anti-B_s0heavy                                 PHSP_BB_MIX  dm_Bs  -1 ;
0.00704  B_s0heavy  anti-B_s0long        anti-B_s0heavy  B_s0long   PHSP_BB_MIX  dm_Bs  +1 ;
0.00704  B_s0long   anti-B_s0heavy       anti-B_s0long   B_s0heavy  PHSP_BB_MIX  dm_Bs  +1 ;
0.00502  B_s0long   anti-B_s0long                                  PHSP_BB_MIX  dm_Bs  -1 ;
```

  $\Upsilon(5S) \to B^{*0}\bar{B}^{*0}\pi^0, B^{*0}\bar{B}^0\pi^0 + B^0\bar{B}^{*0}\pi^0$ and $B^0\bar{B}^0\pi^0$ decays:

```
0.00181  B0heavy   anti-B0heavy  pi0                            PHSP_BB_MIX  dm_B0  -1 ;
0.00637  B0heavy   anti-B0long   pi0    anti-B0heavy   B0long   PHSP_BB_MIX  dm_B0  +1 ;
0.00637  B0long    anti-B0heavy  pi0    anti-B0long    B0heavy  PHSP_BB_MIX  dm_B0  +1 ;
0.00006  B0long    anti-B0long   pi0                            PHSP_BB_MIX  dm_B0  -1 ;
```

  and $\Upsilon(5S) \to B^0\bar{B}^0\pi^0\pi^0, B^0\bar{B}^0\pi^+\pi^-$ decays:

```
0.00000  B0long    anti-B0long   pi0  pi0                       PHSP_BB_MIX  dm_B0  -1 ;
0.00000  B0long    anti-B0long   pi+  pi-                       PHSP_BB_MIX  dm_B0  -1 ;
```

- One neutral B:

  BR B0 B+/- PI1 PI2 anti-B0 PHSP_B_MIX Δm;

  The parameters BR and Δm have the same meaning as before. The optional fourth daughter, PI2, is for the 4-body decays. B0 is the neutral $B_{(s)}^{(*)0}$, anti-B0 is its antiparticle. The following lines will generate $\Upsilon(5S) \to B^{*0}B^-\pi^+$, $B^+\bar{B}^{*0}\pi^-$, $B^0B^{*-}\pi^+$ and $B^{*+}\bar{B}^0\pi^-$ decays:

```
0.01274  B0heavy       B-          pi+    anti-B0heavy          PHSP_B_MIX  dm_B0   ;
0.01274  anti-B0heavy  B+          pi-    B0heavy               PHSP_B_MIX  dm_B0   ;
0.01274  B0long        B*-nospin   pi+    anti-B0long           PHSP_B_MIX  dm_B0   ;
0.01274  anti-B0long   B*+nospin   pi-    B0long                PHSP_B_MIX  dm_B0   ;
```

  and $\Upsilon(5S) \to B^0B^-\pi^+\pi^0, \bar{B}^0B^+\pi^-\pi^0$ decays:

```
0.00000  B0long       B-    pi+  pi0                            PHSP_BB_MIX  dm_B0  -1 ;
0.00000  anti-B0long  B+    pi-  pi0                            PHSP_BB_MIX  dm_B0  -1 ;
```

These decay models are used to write a realistic $e^+e^- \to b\bar{b}$ decay file (see below).

A.2.4 Check of the generated events

For several $\Upsilon(5S)$ decay modes, we generated 100k events with the code described above and the decay file in appendix. The fractions of $BB + \bar{B}\bar{B}$ events show an excellent agreement with the expectations [14].

As mentioned above, Appendix A.2.5 shows the detail of the realistic decay file for generic $\Upsilon(5S) \to b\bar{b}$. Two MC samples generated with this decay file are studied:

- "Lausanne": A run-independent sample of 15.2 million events (~ 50.3 fb^{-1}), generated in Lausanne;
- "KEK": Most of one stream of the official MC for the $\Upsilon(5S)$ data, made with exactly the same generator and decay file and representing 31.8 millions events ($\sim$ 105 fb^{-1}).

Table A.1 shows the measured f_s values in these two samples (see Sec. 3.4 for the formulae). The sample is therefore correctly generated, and the formula provides coherent results.

Sample		SS	OS	f_s
"Lausanne"	$B\bar{B}$ pairs	2'970'812	11'802'876	19.39 ± 0.03
	ll pairs	115'879	546'948	19.34 ± 0.19
"KEK"	$B\bar{B}$ pairs			19.36 ± 0.03
	ll pairs			19.86 ± 0.13

Table A.1: Number of same- and opposite-flavour B pairs and same- and opposite-sign signal dileptons in the EvtGen output for two MC samples. The f_s value is obtained from the formula of Sec. 3.4, with $\mathcal{B}(B \to X\, l\, \nu_l) = 1$ ("$B\bar{B}$ flavour" counting) or the original MC input parameter ("ll sign" counting).

After this check at the generator level, the detector response is simulated with the full-detector simulation made with Geant.

A.2.5 The $\Upsilon(5S) \to b\bar{b}$ Decay file

Fractions are discussed in Sec. 3.1.2.

```
##Generic Y(5S)->bbar
#RL 2010 03 31
#input: (all in %)
#PDG09:
#fs=19.3
#
#Belle Bs->Ds pi (PRL 102,021801)
#N_Bs*Bs*/N_Bs(*)Bs(*)=90.1
#N_Bs*Bs/N_Bs(*)Bs(*)=7.3
#N_BsBs/N_Bs(*)Bs(*)=2.6
#
#Belle Y(5S)->B+/B0 (1003.5885)
#f(B*B*)=37.5
#f(B*B)=13.7
#f(BB)=5.5
#f(B*B*pi)=1.0
#f(B*Bpi)=7.3
#f(BBpi)=0.0
#f(B(*)B(*)pi(pi))=17.5 --> f(redidual)=9.2
```

```
#-> rescalled to
#f(B(*)B(*)(X)) = 100 - f_s - BR(Y(5S)->Y(nS)hh)=77.9
#
#
#
#Belle Y(5S)->Y(nS)pipi (PRL 100,112001)
#BR(Y(5S)->Y(1S)pi+pi-)=0.53
#BBR(Y(5S)->Y(1S)K+K-)=0.06
#BR(Y(5S)->Y(2S)pi+pi-)=0.78
#BR(Y(5S)->Y(3S)pi+pi-)=0.48
#
#Isospin conservation:
#BR(Y(5S)->Y(nS)pi0pi0)=0.5 BR(Y(5S)->Y(nS)pi+pi-)
#BR(Y(5S)->Y(nS)K0 K0b)=BR(Y(5S)->Y(nS)K+K-)
#
#f(B*B*pi)= 1/3 f(B+ B0b pi-) + 1/3 f(B0 B- pi+) + 1/6 f(B+ B- pi0) + 1/6 f(B0 B0b pi0) (same for f(BBpi))
#f(B*Bpi)= 1/3 (1/2 f(B*+ B0b pi-) + 1/2 f(B+ B0*b pi-)) + 1/3 etc...
#
#Asumption:
#redidual -> ISR Y(5S)->Y(4S) gamma
#
#

Alias myUpsilon(4S) Upsilon(4S)

##mixing parameter

Define dm_B0 0.508e12
Define dm_Bs 17.77e12

Decay Upsilon(5S)

# Bs SUM=0.19300-


0.17389   B_s0heavy    anti-B_s0heavy                                       PHSP_BB_MIX  dm_Bs  -1 ;

0.00704   B_s0heavy    anti-B_s0long          anti-B_s0heavy  B_s0long     PHSP_BB_MIX  dm_Bs  +1 ;
0.00704   B_s0long     anti-B_s0heavy         anti-B_s0long   B_s0heavy    PHSP_BB_MIX  dm_Bs  +1 ;

0.00502   B_s0long     anti-B_s0long                                        PHSP_BB_MIX  dm_Bs  -1 ;

# B* B* SUM=0.39376--

0.19687   B0heavy      anti-B0heavy                                         PHSP_BB_MIX  dm_B0  -1 ;
0.19687   B*+          B*-                                                  PHSP                   ;

# B* B  SUM=0.14379+
0.03595   B0heavy      anti-B0long            anti-B0heavy    B0long       PHSP_BB_MIX  dm_B0  +1 ;
0.03595   B0long       anti-B0heavy           anti-B0long     B0heavy      PHSP_BB_MIX  dm_B0  +1 ;
0.03595   B*+          B-                                                   PHSP                   ;
0.03595   B+           B*-                                                  PHSP                   ;

# B B  SUM=0.05772
0.02886  B+            B-                                                   VSS                    ;
0.02886  B0long        anti-B0long                                          PHSP_BB_MIX  dm_B0  -1 ;

# B* B* pi SUM=0.01084
0.00181  B0heavy       anti-B0heavy  pi0                                    PHSP_BB_MIX  dm_B0  -1 ;
0.00181  B*+           B*-           pi0                                    PHSP;

0.00361  B0heavy       B*-nospin     pi+      anti-B0heavy                  PHSP_B_MIX  dm_B0   ;
0.00361  anti-B0heavy  B*+nospin     pi-      B0heavy                       PHSP_B_MIX  dm_B0   ;

# B* B pi SUM=0.07641+++
0.00637  B*+           B-            pi0           PHSP;
0.00637  B+            B*-           pi0           PHSP;

0.00637  B0heavy       anti-B0long   pi0      anti-B0heavy    B0long      PHSP_BB_MIX  dm_B0  +1 ;
0.00637  B0long        anti-B0heavy  pi0      anti-B0long     B0heavy     PHSP_BB_MIX  dm_B0  +1 ;

0.01274  B0heavy       B-            pi+      anti-B0heavy                  PHSP_B_MIX  dm_B0   ;
0.01274  anti-B0heavy  B+            pi-      B0heavy                       PHSP_B_MIX  dm_B0   ;
0.01274  B0long        B*-nospin     pi+      anti-B0long                   PHSP_B_MIX  dm_B0   ;
0.01274  anti-B0long   B*+nospin     pi-      B0long                        PHSP_B_MIX  dm_B0   ;

#B B pi SUM=0.00037-
0.00006  B0long        anti-B0long   pi0                                   PHSP_BB_MIX  dm_B0  -1 ;
0.00006  B+            B-            pi0                                   PHSP;

0.00012  B0long        B-            pi+      anti-B0long                  PHSP_B_MIX  dm_B0   ;
0.00012  anti-B0long   B+            pi-      B0long                       PHSP_B_MIX  dm_B0   ;


# Residual  SUM=0.09606
0.09606 myUpsilon(4S) gamma PHSP;

# non-BB SUM=0.02805
```

```
0.00530  Upsilon       pi+        pi-           PHSP;
0.00265  Upsilon       pi0        pi0           PHSP;
0.00780  Upsilon(2S)   pi+        pi-           PHSP;
0.00390  Upsilon(2S)   pi0        pi0           PHSP;
0.00480  Upsilon(3S)   pi+        pi-           PHSP;
0.00240  Upsilon(3S)   pi0        pi0           PHSP;
0.00060  Upsilon       K+         K-            PHSP;
0.00060  Upsilon       K0         anti-K0       PHSP;

Enddecay

Decay myUpsilon(4S)
0.5  B+            B-                                                  VSS                    ;
0.5  B0long        anti-B0long                                         PHSP_BB_MIX  dm_B0  -1 ;
Enddecay


End
```

Appendix B

Helicity and angular distributions

B.1 Helicity formalism

The helicity of a particle is the value of its spin projection along its momentum (Eq. (1.4)). It has the property to be invariant under rotation. This property makes the decay angular distributions easy to compute [226]. If a decay has a non-uniform angular distribution, the continuum can be distinguished from the signal by using angular observables. This section presents the theoretical way to obtain the expected distributions. For a two-body decay $P \to Q_1 Q_2$, the amplitude can be written as the product of a complex number, A_{λ_1,λ_2} and a D function [226]:

$$\mathcal{A}\left(P \to Q_1 Q_2\right) = D^{J*}_{M,\lambda_1-\lambda_2}\left(\varphi_P, \theta_P, -\varphi_P\right) A_{\lambda_1,\lambda_2}\,, \tag{B.1}$$

where[1]

$$D^{J*}_{m_1,m_2}\left(\alpha,\beta,\gamma\right) = e^{i\alpha m_1} d^J_{m_1,m_2}(\beta) e^{i\gamma m_2} \tag{B.2}$$

is the $SU(2)$ representation of the rotation as function of the Euler angles (α,β,γ), J the spin of the decaying particle P, M its projection on the z axis, and λ_1 and λ_2 are the helicities of the two daughters Q_1 and Q_2. The two angles θ_P and φ_P are the polar and azimuthal angles of a chosen daughter[2] in the frame of the mother. The z axis is defined as the momentum direction of the mother P, in the lab frame. Three specific cases are considered below, involving spin-0 scalar (S), spin-1 vector (V) particles and photons.

B.2 The decay $D_s^- \to \phi\pi^-, \phi \to K^+K^-$

In the decay chain $D_s^0 \to \phi\pi^-, \phi \to K^+K^-$, all the particles are pseudo-scalar mesons, except the ϕ which is a vector meson. The decay amplitude is

$$\begin{aligned}\mathcal{A}(D_s^- \to \phi(\to K^+K^-)\pi^-) = {} & D^{J_{D_s^-}*}_{\lambda_{D_s^-},\lambda_\phi-\lambda_{\pi^-}}\left(\varphi_{D_s^-}, \theta_{D_s^-}, -\varphi_{D_s^-}\right) A_{\lambda_\phi,\lambda_{\pi^-}} \\ & \times D^{J_\phi *}_{\lambda_\phi,\lambda_{K^+}-\lambda_{K_-}}\left(\varphi_\phi, \theta_\phi, -\varphi_\phi\right) B_{\lambda_{K^+},\lambda_{K^-}}\,.\end{aligned} \tag{B.3}$$

[1] The symbol * indicates the complex conjugation.

[2] The other one has $\theta' = \pi - \theta$ and $\varphi' = \varphi + \pi$.

Since $J_{D_s^-} = J_{K^\pm} = J_{\pi^-} = 0$ and $J_\phi = 1$, $M_{D_s^-}$, λ_{π^-} and $\lambda_{K^\pm}$ vanish as well as[3] λ_ϕ; this leads to

$$A(D_s^- \to \phi(\to K^+K^-)\pi^-) = A_{0,0}B_{0,0}D^{0*}_{0,0}(\varphi_{D_s^-}, \theta_{D_s^-}, -\varphi_{D_s^-})D^{1*}_{0,0}(\varphi_\phi, \theta_\phi, -\varphi_\phi)\,. \quad \text{(B.4)}$$

$D^0_{0,0}$ being a constant, the differential decay rate is proportional to[4]

$$\frac{\mathrm{d}\Gamma}{\mathrm{d}\,(\cos\theta_\phi)} \sim \left|D^{1*}_{0,0}(\varphi_\phi, \theta_\phi, -\varphi_\phi)\right|^2 = \left|d^1_{0,0}(\theta_\phi)\right|^2 = \cos^2\theta_\phi\,. \quad \text{(B.5)}$$

This result is similar for the $D_s^- \to K^{*0}K^-, K^{*0} \to K^+\pi^-$ and the $B_s^0 \to D_s^-\rho^+, \rho^+ \to \pi^+\pi^0$ decays, by considering $\theta_{K^{*0}}$ and θ_{ρ^+}, respectively.

B.3 The decay $B_s^0 \to D_s^{*-}\pi^+, D_s^{*-} \to D_s^-\gamma$

The decay $B_s^0 \to D_s^{*-}(\to D_s^-\gamma)\pi^+$ is governed by the amplitude

$$\begin{aligned}\mathcal{A}(B_s^0 \to D_s^{*-}(\to D_s^-\gamma)\pi^+) = {} & D^{J_{B_s^0}*}_{\lambda_{B_s^0}, \lambda_{D_s^{*-}} - \lambda_{\pi^+}}(\varphi_{B_s^0}, \theta_{B_s^0}, -\varphi_{B_s^0})A_{\lambda_{D_s^{*-}}, \lambda_{\pi^+}} \\ & \times D^{J_{D_s^{*-}}*}_{\lambda_{D_s^{*-}}, \lambda_{D_s^-} - \lambda_\gamma}(\varphi_{D_s^{*-}}, \theta_{D_s^{*-}}, -\varphi_{D_s^{*-}})B_{\lambda_{D_s^-}, \lambda_\gamma}\,.\end{aligned} \quad \text{(B.6)}$$

Since $J_{B_s^0} = J_{D_s^-} = 0$ and $J_{D_s^{*-}} = J_\gamma = 1$, the helicities $\lambda_{B_s^0}$, $\lambda_{D_s^-}$, λ_{π^+} and $\lambda_{D_s^{*-}}$ vanish. There are only two possible helicities for the photon ($\lambda_\gamma = \pm 1$), leading to

$$\begin{aligned}\mathcal{A}(B_s^0 \to D_s^{*-}(\to D_s^-\gamma)\pi^+) = {} & D^{0*}_{0,0}(\varphi_{B_s^0}, \theta_{B_s^0}, -\varphi_{B_s^0})A_{0,0} \\ & \times D^{1*}_{0,-\lambda_\gamma}(\varphi_{D_s^{*-}}, \theta_{D_s^{*-}}, -\varphi_{D_s^{*-}})B_{0,\lambda_\gamma}\,.\end{aligned} \quad \text{(B.7)}$$

The differential decay rate is then proportional to $\sum_{\lambda_\gamma}\left|d^1_{0,\lambda_\gamma}(\theta_{D_s^{*-}})B_{0,\lambda_\gamma}\right|^2$. When the γ polarisation is not measured, the parity is conserved by the electromagnetic force, therefore $|B_{0,-1}|^2 = |B_{0,1}|^2$. Finally the decay rate is proportional to[5]

$$\frac{\mathrm{d}\Gamma}{\mathrm{d}\left(\cos\theta_{D_s^{*-}}\right)} \sim |B_{0,1}|^2\left(\left|d^1_{0,1}(\theta_{D_s^{*-}})\right|^2 + \left|d^1_{0,-1}(\theta_{D_s^{*-}})\right|^2\right) \sim 1 - \cos^2\theta_{D_s^{*-}}\,. \quad \text{(B.8)}$$

B.4 The decay $B_s^0 \to D_s^{*-}\rho^+, D_s^{*-} \to D_s^-\gamma, \rho^+ \to \pi^+\pi^0$

The $B_s^0 \to D_s^{*-}\rho^+$ mode is a decay of a pseudo-scalar meson into two vector particles. The decay can be characterised by three angles (Fig. B.1): the D_s^{*-} polarisation angle, $\theta_{D_s^{*-}}$, is the supplement of the angle between the B_s^0 and the D_s^- momenta in the D_s^{*-} frame; the ρ^+ polarisation angle, θ_{ρ^+}, is the supplement of the angle between the B_s^0 and the π^+ momenta in the ρ^+ frame; and χ is the angle of the ρ^+ decay plane with respect to the D_s^{*-} decay plane in the B_s^0 frame.

[3] In the mother's frame, the projection of the relative angular momentum between the two daughters on the momentum direction of one daughter is zero.

[4] The explicit expressions of the d functions are tabulated for example in Ref. [37].

[5] The angular distribution for the non-strange counterpart of $B_s^0 \to D_s^{*-}\pi^+$, $B^0 \to D^*(2010)^-\pi^+$ is proportional to $\cos^2\theta_{D^*}$ because the $D^*(2010)^-$ decays into two scalars, D and π.

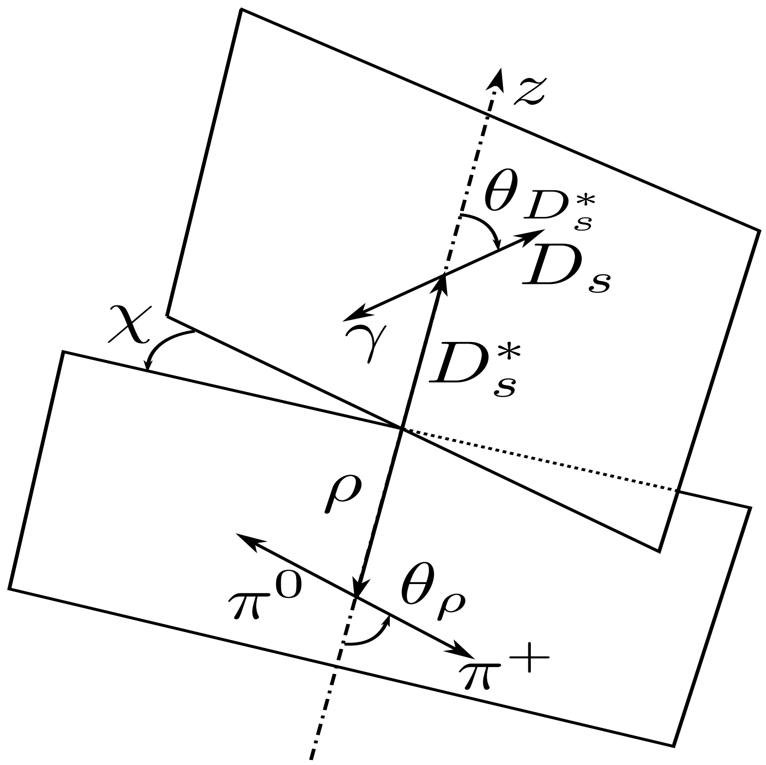

Figure B.1: Definition of the three angles characterising the $B_s^0 \to D_s^{*-}\rho^+$ decay. The D_s^{*-} and ρ^+ helicity angles are defined in their respective rest frames.

The conservation of the projection of the total angular momentum can be written as

$$0 = M(B_s^0) = s_z(D_s^{*-}) + s_z(\rho^+) + l_z = \lambda_{D_s^{*-}} - \lambda_{\rho^+}\,, \tag{B.9}$$

where $l_z = 0$ because z is the direction of the daughters' momenta (see note 3 on page 136). We define

$$\lambda = \lambda_{D_s^{*-}} = \lambda_{\rho^+}\,, \tag{B.10}$$

which can take the values $-1, 0, +1$. Therefore three polarisations are possible. We need to sum the decay amplitudes over these three "internal" helicities. In addition, the photon has two possible polarisations $\lambda_\gamma = \pm 1$. When it is not measured, the two decay widths should be added.

The total decay amplitude as function of the two helicities λ and λ_γ is a product of three decay amplitudes[6],

$$\begin{aligned}\mathcal{A}(\lambda, \lambda_\gamma) &= \mathcal{A}_{B_s^0 \to D_s^{*-}\rho^+}(\lambda) \times \mathcal{A}_{D_s^{*-} \to D_s^-\gamma}(\lambda, \lambda_\gamma) \times \mathcal{A}_{\rho^+ \to \pi^+\pi^0}(\lambda) & \text{(B.11)}\\ &= A_{\lambda,\lambda} D^{*0}_{0,0}(\phi_{B_s^0}, \theta_{B_s^0}, -\phi_{B_s^0}) \times B_{0,\lambda_\gamma} D^{*1}_{\lambda,-\lambda_\gamma}(\phi_{D_s^{*-}}, \theta_{D_s^{*-}}, -\phi_{D_s^{*-}}) \\ &\quad \times C_{0,0} D^{*1}_{-\lambda,0}(\phi_{\rho^+}, \theta_{\rho^+}, -\phi_{\rho^+})\,. & \text{(B.12)}\end{aligned}$$

[6] The spin projection along z is $+\lambda$ for D_s^{*-} and $-\lambda$ for ρ^+, see Eqs. (B.9) and (B.10).

The azimuthal origin is set by[7] $\phi_{D_s^{*-}} = 0$. In this way, the angle χ is simply $\phi_{\rho^+} = \chi$. Defining $H_\lambda = A_{\lambda,\lambda}$, we have

$$\mathcal{A}(\lambda, \lambda_\gamma) \propto H_\lambda B_{0,\lambda_\gamma} d^1_{\lambda,-\lambda_\gamma}(\theta_{D_s^{*-}}) d^1_{-\lambda,0}(\theta_{\rho^+}) e^{-i\lambda\chi} \,. \tag{B.13}$$

As before, the electromagnetic decay $D_s^{*-} \to D_s^- \gamma$ conserves the parity P, and the constant factor is the same for the two photon polarities, $|B_{0,1}|^2 = |B_{0,-1}|^2$. We are left with only the three helicity amplitudes H_λ. The distribution is obtained after simple algebraic calculation[8]:

$$\begin{aligned}
\frac{\mathrm{d}^3\Gamma}{\mathrm{d}\cos\theta_{D_s^{*-}}\,\mathrm{d}\cos\theta_{\rho^+}\,\mathrm{d}\chi} &\propto \sum_{\lambda_\gamma=-1,+1} \left| \sum_{\lambda=-1,0,+1} \mathcal{A}(\lambda,\lambda_\gamma) \right|^2 \\
&\propto 4\,|H_0|^2 \sin^2\theta_{D_s^{*-}} \cos^2\theta_{\rho^+} \\
&\quad + \left(|H_+|^2 + |H_-|^2\right)\left(1+\cos^2\theta_{D_s^{*-}}\right)\sin^2\theta_{\rho^+} \\
&\quad + \left(\Re\left(H_0H_+^* + H_0H_-^*\right)\cos\chi + \Im\left(H_0H_-^* - H_0H_+^*\right)\sin\chi\right) \\
&\qquad\qquad \times \sin 2\theta_{D_s^{*-}} \sin 2\theta_{\rho^+} \\
&\quad -2\left(\Re\left(H_+H_-^*\right)\cos 2\chi + \Im\left(H_+H_-^*\right)\sin 2\chi\right)\sin^2\theta_{D_s^{*-}}\sin^2\theta_{\rho^+}\,,
\end{aligned} \tag{B.14}$$

or[9], after integrating over χ and normalising to Γ,

$$\frac{\mathrm{d}^2\Gamma}{\mathrm{dcos}\,\theta_{D_s^{*-}}\mathrm{dcos}\,\theta_{\rho^+}} = \Gamma \times f_L \times \frac{\left(1-\cos^2\theta_{D_s^{*-}}\right)\cos^2\theta_{\rho^+}}{8/9} \tag{B.15}$$

$$+\Gamma \times (1-f_L) \times \frac{\left(1+\cos^2\theta_{D_s^{*-}}\right)\sin^2\theta_{\rho^+}}{32/9}\,, \tag{B.16}$$

where f_L is the longitudinal polarisation fraction defined as

$$f_L = \frac{|H_0|^2}{|H_+|^2 + |H_0|^2 + |H_-|^2}\,. \tag{B.17}$$

Given this non-constant distribution, $\cos\theta_{D_s^{*-}}$ and $\cos\theta_{\rho^+}$ can be used as observables in order to distinguish between longitudinally- and transversely-polarised decays.

---

[7] A consistency check shows that the choice $\phi_{\rho^+} = 0$, $\phi_{D_s^{*-}} = -\chi$ leads to the same result.

[8] The helicity of the D_s^+ and ρ^+, λ, is not an observable: hence the amplitudes are summed over its three values. In contrast, the helicity of the photon λ_γ is not measured, but could be: thus the probabilities (square of the amplitude modulus) are summed over the two values of λ_γ. For a similar calculation, see Ref. [218]. The difference between the $B_s^0 \to D_s^{*-}\rho^+$ and $B \to D^*\rho^+$ decays is that the D_s^{*-} decays into a photon ($\lambda = \pm 1$) and a pseudo-scalar meson ($\lambda = 0$), while the D^* decays into two pseudo-scalar mesons ($\lambda = 0$).

[9] Our calculation gives the same result as that obtained in Ref. [227] for the study of decay $B^0 \to D_s^{*+}V^-$, $V = \rho, K^*$.

Appendix C

Articles in Physical Review Letters

Measurement of the Decay $B_s^0 \to D_s^- \pi^+$ and Evidence for $B_s^0 \to D_s^{\mp} K^{\pm}$ in e^+e^- Annihilation at $\sqrt{s} \approx 10.87$ GeV

R. Louvot,[18] J. Wicht,[9] O. Schneider,[18] I. Adachi,[9] H. Aihara,[42] K. Arinstein,[1] V. Aulchenko,[1] T. Aushev,[18,13] A. M. Bakich,[38] V. Balagura,[13] A. Bay,[18] V. Bhardwaj,[33] U. Bitenc,[14] A. Bondar,[1] A. Bozek,[27] M. Bračko,[20,14] T. E. Browder,[8] A. Chen,[24] B. G. Cheon,[7] R. Chistov,[13] I.-S. Cho,[47] Y. Choi,[37] J. Dalseno,[9] M. Danilov,[13] M. Dash,[46] A. Drutskoy,[3] W. Dungel,[11] S. Eidelman,[1] N. Gabyshev,[1] P. Goldenzweig,[3] B. Golob,[19,14] H. Ha,[16] J. Haba,[9] K. Hayasaka,[22] H. Hayashii,[23] M. Hazumi,[9] Y. Hoshi,[41] W.-S. Hou,[26] H. J. Hyun,[17] T. Iijima,[22] K. Inami,[22] A. Ishikawa,[34] H. Ishino,[43,*] R. Itoh,[9] M. Iwasaki,[42] N. J. Joshi,[39] D. H. Kah,[17] J. H. Kang,[47] N. Katayama,[9] H. Kawai,[2] T. Kawasaki,[29] H. Kichimi,[9] S. K. Kim,[36] Y. I. Kim,[17] Y. J. Kim,[6] K. Kinoshita,[3] S. Korpar,[20,14] P. Križan,[19,14] P. Krokovny,[9] R. Kumar,[33] A. Kuzmin,[1] Y.-J. Kwon,[47] S.-H. Kyeong,[47] J. S. Lange,[5] J. S. Lee,[37] M. J. Lee,[36] S. E. Lee,[36] T. Lesiak,[27,4] J. Li,[8] A. Limosani,[21] S.-W. Lin,[26] D. Liventsev,[13] F. Mandl,[11] A. Matyja,[27] S. McOnie,[38] T. Medvedeva,[13] K. Miyabayashi,[23] H. Miyake,[32] H. Miyata,[29] Y. Miyazaki,[22] R. Mizuk,[13] T. Mori,[22] E. Nakano,[31] M. Nakao,[9] S. Nishida,[9] O. Nitoh,[45] S. Ogawa,[40] T. Ohshima,[22] S. Okuno,[15] H. Ozaki,[9] G. Pakhlova,[13] C. W. Park,[37] H. K. Park,[17] R. Pestotnik,[14] L. E. Piilonen,[46] H. Sahoo,[8] Y. Sakai,[9] J. Schümann,[9] A. J. Schwartz,[3] A. Sekiya,[23] K. Senyo,[22] M. E. Sevior,[21] M. Shapkin,[12] J.-G. Shiu,[26] J. B. Singh,[33] A. Somov,[3] S. Stanič,[30] M. Starič,[14] K. Sumisawa,[9] T. Sumiyoshi,[44] M. Tanaka,[9] G. N. Taylor,[21] Y. Teramoto,[31] I. Tikhomirov,[13] K. Trabelsi,[9] S. Uehara,[9] T. Uglov,[13] Y. Unno,[7] S. Uno,[9] Y. Usov,[1] G. Varner,[8] K. Vervink,[18] C. C. Wang,[26] C. H. Wang,[25] P. Wang,[10] X. L. Wang,[10] Y. Watanabe,[15] R. Wedd,[21] E. Won,[16] B. D. Yabsley,[38] Y. Yamashita,[28] M. Yamauchi,[9] Z. P. Zhang,[35] V. Zhilich,[1] V. Zhulanov,[1] T. Zivko,[14] A. Zupanc,[14] N. Zwahlen,[18] and O. Zyukova[1]

(Belle Collaboration)

[1]*Budker Institute of Nuclear Physics, Novosibirsk*
[2]*Chiba University, Chiba*
[3]*University of Cincinnati, Cincinnati, Ohio 45221*
[4]*T. Kościuszko Cracow University of Technology, Krakow*
[5]*Justus-Liebig-Universität Gießen, Gießen*
[6]*The Graduate University for Advanced Studies, Hayama*
[7]*Hanyang University, Seoul*
[8]*University of Hawaii, Honolulu, Hawaii 96822*
[9]*High Energy Accelerator Research Organization (KEK), Tsukuba*
[10]*Institute of High Energy Physics, Chinese Academy of Sciences, Beijing*
[11]*Institute of High Energy Physics, Vienna*
[12]*Institute of High Energy Physics, Protvino*
[13]*Institute for Theoretical and Experimental Physics, Moscow*
[14]*J. Stefan Institute, Ljubljana*
[15]*Kanagawa University, Yokohama*
[16]*Korea University, Seoul*
[17]*Kyungpook National University, Taegu*
[18]*École Polytechnique Fédérale de Lausanne (EPFL), Lausanne*
[19]*Faculty of Mathematics and Physics, University of Ljubljana, Ljubljana*
[20]*University of Maribor, Maribor*
[21]*University of Melbourne, School of Physics, Victoria 3010*
[22]*Nagoya University, Nagoya*
[23]*Nara Women's University, Nara*
[24]*National Central University, Chung-li*
[25]*National United University, Miao Li*
[26]*Department of Physics, National Taiwan University, Taipei*
[27]*H. Niewodniczanski Institute of Nuclear Physics, Krakow*
[28]*Nippon Dental University, Niigata*
[29]*Niigata University, Niigata*
[30]*University of Nova Gorica, Nova Gorica*
[31]*Osaka City University, Osaka*
[32]*Osaka University, Osaka*

 © 2009 The American Physical Society

[33]Panjab University, Chandigarh
[34]Saga University, Saga
[35]University of Science and Technology of China, Hefei
[36]Seoul National University, Seoul
[37]Sungkyunkwan University, Suwon
[38]University of Sydney, Sydney, New South Wales
[39]Tata Institute of Fundamental Research, Mumbai
[40]Toho University, Funabashi
[41]Tohoku Gakuin University, Tagajo
[42]Department of Physics, University of Tokyo, Tokyo
[43]Tokyo Institute of Technology, Tokyo
[44]Tokyo Metropolitan University, Tokyo
[45]Tokyo University of Agriculture and Technology, Tokyo
[46]Virginia Polytechnic Institute and State University, Blacksburg, Virginia 24061
[47]Yonsei University, Seoul

(Received 15 September 2008; revised manuscript received 20 November 2008; published 13 January 2009)

We have studied $B_s^0 \to D_s^- \pi^+$ and $B_s^0 \to D_s^\mp K^\pm$ decays using 23.6 fb^{-1} of data collected at the $\Upsilon(5S)$ resonance with the Belle detector at the KEKB e^+e^- collider. This highly pure $B_s^0 \to D_s^- \pi^+$ sample is used to measure the branching fraction, $\mathcal{B}(B_s^0 \to D_s^- \pi^+) = [3.67^{+0.35}_{-0.33}(\mathrm{stat})^{+0.43}_{-0.42}(\mathrm{syst}) \pm 0.49(f_s)] \times 10^{-3}$ ($f_s = N_{B_s^{(*)}\bar{B}_s^{(*)}}/N_{b\bar{b}}$) and the fractions of B_s^0 event types at the $\Upsilon(5S)$ energy, in particular $N_{B_s^*\bar{B}_s^*}/N_{B_s^{(*)}\bar{B}_s^{(*)}} = (90.1^{+3.8}_{-4.0} \pm 0.2)\%$. We also determine the masses $M(B_s^0) = (5364.4 \pm 1.3 \pm 0.7)$ MeV$/c^2$ and $M(B_s^*) = (5416.4 \pm 0.4 \pm 0.5)$ MeV$/c^2$. In addition, we observe $B_s^0 \to D_s^\mp K^\pm$ decays with a significance of 3.5σ and measure $\mathcal{B}(B_s^0 \to D_s^\mp K^\pm) = [2.4^{+1.2}_{-1.0}(\mathrm{stat}) \pm 0.3(\mathrm{syst}) \pm 0.3(f_s)] \times 10^{-4}$.

DOI: 10.1103/PhysRevLett.102.021801 PACS numbers: 13.25.Hw, 13.25.Gv, 14.40.Gx, 14.40.Nd

The decay $B_s^0 \to D_s^- \pi^+$ [1] has a relatively large branching fraction and is a primary normalization mode at hadron colliders, where the absolute production rate of B_s^0 mesons is difficult to measure directly. It proceeds dominantly via a Cabibbo-favored tree process. The decay $B^0 \to D^- \pi^+$ proceeds through the same tree process but may also have additional contributions from W exchange, so a comparison of the partial widths of the two decays can give insight into the poorly known W-exchange process. The Cabibbo-suppressed mode $B_s^0 \to D_s^\mp K^\pm$ is mediated by $b \to c$ and $b \to u$ tree transitions of similar order ($\sim \lambda^3$, in the Wolfenstein parametrization [2]), which raises the possibility of measuring time-dependent CP-violating effects [3]. It has recently become possible to produce B_s^0 events from e^+e^- collisions at the $\Upsilon(5S)$ resonance in sufficiently large numbers to achieve interesting and competitive measurements. $\Upsilon(5S)$ events may also be used to determine precisely the masses of B_s^* and B_s^0; the mass difference can be compared with that of B^{*0} and B^0 to test heavy-quark symmetry [4], which predicts equality between them. Properties of the $\Upsilon(5S)$ such as the fraction of events containing a B_s^0 and the relative proportions of $B_s^0\bar{B}_s^0$, $B_s^*\bar{B}_s^0$, and $B_s^*\bar{B}_s^*$ provide additional tests of heavy-quark theories [5,6].

In this Letter, we report measurements performed with fully reconstructed $B_s^0 \to D_s^- \pi^+$ and $B_s^0 \to D_s^\mp K^\pm$ decays in $L_{\mathrm{int}} = (23.6 \pm 0.3)$ fb^{-1} of data collected with the Belle detector at the KEKB asymmetric-energy (3.6 GeV on 8.2 GeV) e^+e^- collider [7] operated at the $\Upsilon(5S)$ resonance. The beam energy in the center-of-mass (c.m.) frame is measured to be $E_b^* = \sqrt{s}/2 = 5433.5 \pm 0.5$ MeV with $\Upsilon(5S) \to \Upsilon(1S)\pi^+\pi^-$, $\Upsilon(1S) \to \mu^+\mu^-$ decays [8]. The total $b\bar{b}$ cross section at the $\Upsilon(5S)$ energy has been measured to be $\sigma_{b\bar{b}}^{\Upsilon(5S)} = (0.302 \pm 0.014)$ nb [9], which includes B^0, B^+, and B_s^0 events. Three B_s^0 production modes are kinematically allowed: $B_s^0\bar{B}_s^0$, $B_s^*\bar{B}_s^0$, and $B_s^*\bar{B}_s^*$. The B_s^* decays electromagnetically to B_s^0, emitting a photon with energy $E_\gamma \sim 53$ MeV. The fraction of $b\bar{b}$ events containing a $B_s^{(*)}\bar{B}_s^{(*)}$ pair has been measured to be $f_s = N_{B_s^{(*)}\bar{B}_s^{(*)}}/N_{b\bar{b}} = (19.5^{+3.0}_{-2.3})\%$ [9]. The number of B_s^0 mesons in the sample is thus $N_{B_s^0} = 2 \times L_{\mathrm{int}} \times \sigma_{b\bar{b}}^{\Upsilon(5S)} \times f_s = (2.78^{+0.45}_{-0.36}) \times 10^6$. The B_s^0 production mode ratios are defined as $f_{B_s^*\bar{B}_s^*} = N_{B_s^*\bar{B}_s^*}/N_{B_s^{(*)}\bar{B}_s^{(*)}}$, $f_{B_s^*\bar{B}_s^0} = N_{B_s^*\bar{B}_s^0}/N_{B_s^{(*)}\bar{B}_s^{(*)}}$, and $f_{B_s^0\bar{B}_s^0} = N_{B_s^0\bar{B}_s^0}/N_{B_s^{(*)}\bar{B}_s^{(*)}}$. The Belle Collaboration previously measured $f_{B_s^*\bar{B}_s^*} = (93^{+7}_{-9})\%$ [10].

The Belle detector is a large-solid-angle magnetic spectrometer that consists of a silicon vertex detector, a central drift chamber (CDC), an array of aerogel threshold Cherenkov counters (ACC), a barrel-like arrangement of time-of-flight (TOF) scintillation counters, and an electromagnetic calorimeter composed of CsI(Tl) crystals located inside a superconducting solenoid coil that provides a 1.5 T magnetic field. An iron flux return located outside of the coil is instrumented to detect K_L^0 and to identify muons. The detector is described in detail elsewhere [11].

Reconstructed charged tracks are required to have a maximum impact parameter with respect to the nominal interaction point of 0.5 cm in the radial direction and 3 cm

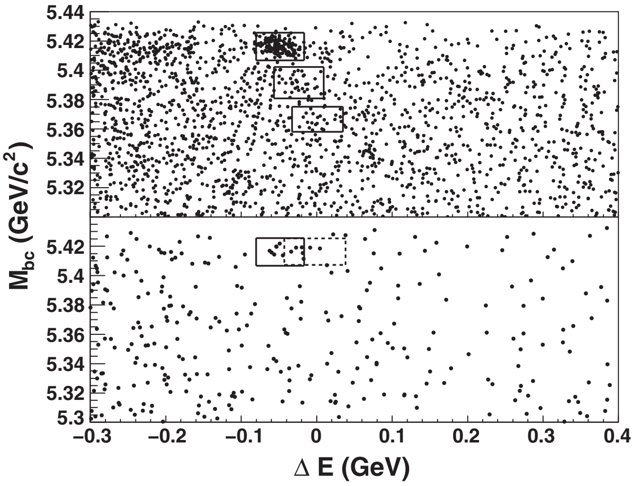

FIG. 1. $(M_{bc}, \Delta E)$ scatter plots for $B_s^0 \to D_s^- \pi^+$ (top) and $B_s^0 \to D_s^\mp K^\pm$ (bottom) candidates. The three boxes in the top plot are the $\pm 2.5\sigma$ signal regions ($B_s^* \bar{B}_s^*$, $B_s^* \bar{B}_s^0$, and $B_s^0 \bar{B}_s^0$, from top to bottom) while those in the bottom plot are the $\pm 2.5\sigma$ $B_s^* \bar{B}_s^*$ regions for signal (solid) and for $B_s^0 \to D_s^- \pi^+$ background (dashed).

in the beam-axis direction. A likelihood ratio $\mathcal{R}_{K/\pi} = \mathcal{L}_K/(\mathcal{L}_\pi + \mathcal{L}_K)$ is built using ACC, TOF, and CDC (dE/dx) measurements. A track is identified as a pion if $\mathcal{R}_{K/\pi} < 0.6$ or as a kaon otherwise. With this selection, the identification efficiency for pions (kaons) is about 91% (85%), while the fake rate is about 9% (14%).

Neutral kaons are reconstructed via the decay $K_S^0 \to \pi^+\pi^-$ with no identification requirements for the two charged pions. The K_S^0 candidates are required to have an invariant mass within ± 7.5 MeV/c^2 ($\pm 4\sigma$) of the nominal K_S^0 mass (all nominal mass values are taken from Ref. [12]). Requirements on the K_S^0 vertex displacement from the interaction point and on the difference between vertex and K_S^0 flight directions are applied. The criteria are described in detail elsewhere [13]. The K^{*0} (ϕ) candidates are reconstructed via the decay $K^{*0} \to K^+\pi^-$ ($\phi \to K^+K^-$) with an invariant mass within ± 50 MeV/c^2 (± 12 MeV/c^2) of the nominal mass.

Candidates for D_s^- are reconstructed in the three modes $D_s^- \to \phi\pi^-$, $D_s^- \to K^{*0}K^-$, and $D_s^- \to K_S^0 K^-$ and required to have mass within ± 15 MeV/c^2 ($\pm 3\sigma$) of the nominal D_s^- mass for $B_s^0 \to D_s^- \pi^+$ and within ± 8 MeV/c^2 for $B_s^0 \to D_s^\mp K^\pm$. Following Ref. [10], the signals for $B_s^0 \to D_s^- \pi^+$ and $B_s^0 \to D_s^\mp K^\pm$ are observed using two variables: the beam-constrained mass of the B_s^0 candidate $M_{bc} = \sqrt{E_b^{*2} - \vec{p}_{B_s^0}^{*2}}$ and the energy difference $\Delta E = E_{B_s^0}^* - E_b^*$, where $(E_{B_s^0}^*, \vec{p}_{B_s^0}^*)$ is the four-momentum of the B_s^0 candidate expressed in the c.m. frame. We select candidates with $M_{bc} > 5.3$ GeV/c^2 and $-0.3 < \Delta E < 0.4$ GeV. In each event the B_s^0 candidate with the D_s^- mass closest to its nominal value is selected for further analysis; only ≈1% of events have more than one candidate.

TABLE I. Parametrization of M_{bc} and ΔE mean values.

Signal	Mean of $(M_{bc}, \Delta E)$
$B_s^* \bar{B}_s^*$	$(m_{B_s^*}, \sqrt{E_b^{*2} - (m_{B_s^*}^2 - m_{B_s^0}^2)} - E_b^*)$
$B_s^* \bar{B}_s^0$	$(\sqrt{(m_{B_s^*}^2 + m_{B_s^0}^2)/2 - [(m_{B_s^*}^2 - m_{B_s^0}^2)/4E_b^*]^2}, -\frac{m_{B_s^*}^2 - m_{B_s^0}^2}{4E_b^*})$
$B_s^0 \bar{B}_s^0$	$(m_{B_s^0}, 0)$

Further selection criteria are developed using Monte Carlo (MC) samples based on EVTGEN [14] and GEANT [15] detector simulation. The most significant source of background is continuum events, $e^+e^- \to u\bar{u}, d\bar{d}, s\bar{s}, c\bar{c}$. In addition, for the $B_s^0 \to D_s^\mp K^\pm$ mode there is also a large background from $B_s^0 \to D_s^- \pi^+$, where the π^+ is misidentified as a K^+. The expected continuum background, N_{bkg}, is estimated using MC-generated continuum events representing three times the data. The expected signal, N_{sig}, is obtained assuming $\mathcal{B}(B_s^0 \to D_s^- \pi^+) = 3.0 \times 10^{-3}$ and $f_{B_s^* \bar{B}_s^*} = 93\%$ for the $B_s^0 \to D_s^- \pi^+$ analysis and $\mathcal{B}(B_s^0 \to D_s^\mp K^\pm) = 3.7 \times 10^{-4}$ for the $B_s^0 \to D_s^\mp K^\pm$ analysis. For $B_s^0 \to D_s^\mp K^\pm$, we assume the values of $\mathcal{B}(B_s^0 \to D_s^- \pi^+)$ and $f_{B_s^* \bar{B}_s^*}$ obtained in the $B_s^0 \to D_s^- \pi^+$ analysis.

To improve signal relative to background, criteria are chosen to maximize $N_{sig}/\sqrt{N_{sig} + N_{bkg}}$, evaluated in the $B_s^* \bar{B}_s^*$ signal region (Fig. 1). Two topological variables are used. First, we use the ratio of the second and zeroth Fox-Wolfram moments [16], R_2, which has a broad distribution between zero and one for jetlike continuum events and is concentrated in the range below 0.5 for the more spherical signal events. Candidates for $B_s^0 \to D_s^- \pi^+$ ($B_s^0 \to D_s^\mp K^\pm$) are required to have $R_2 < 0.5$ (<0.4). We then use the helicity angle θ_{hel} of the $D_s^- \to \phi\pi^-$ ($D_s^- \to K^{*0}K^-$) decays, defined as the angle between the momentum of the positive daughter of the ϕ (K^{*0}) and the momentum of the D_s^- in the ϕ (K^{*0}) rest frame; for signal decays consisting in a spin-0 particle decaying into a spin-1 particle and a spin-0 particle, the distribution is $\propto \cos^2\theta_{hel}$, while for combinatorial background under D_s signal it is flat. Candidates for $D_s^- \to \phi\pi^-$ and $D_s^- \to K^{*0}K^-$ are required to satisfy $|\cos\theta_{hel}| > 0.2$ (>0.35) for the

TABLE II. Signal efficiencies, yields (N), and significances (S).

$\Upsilon(5S)$ mode	$\sum_k \varepsilon_k \mathcal{B}_k$	N	S
$B_s^0 \to D_s^- \pi^+$ mode		161 ± 15	
$B_s^* \bar{B}_s^*$	1.58%	145_{-13}^{+14}	21.0σ
$B_s^* \bar{B}_s^0$	1.58%	$11.8_{-5.0}^{+5.8}$	2.7σ
$B_s^0 \bar{B}_s^0$	1.56%	$4.0_{-3.7}^{+4.6}$	1.1σ
$B_s^0 \to D_s^\mp K^\pm$ mode			
$B_s^* \bar{B}_s^*$	1.12%	$6.7_{-2.7}^{+3.4}$	3.5σ

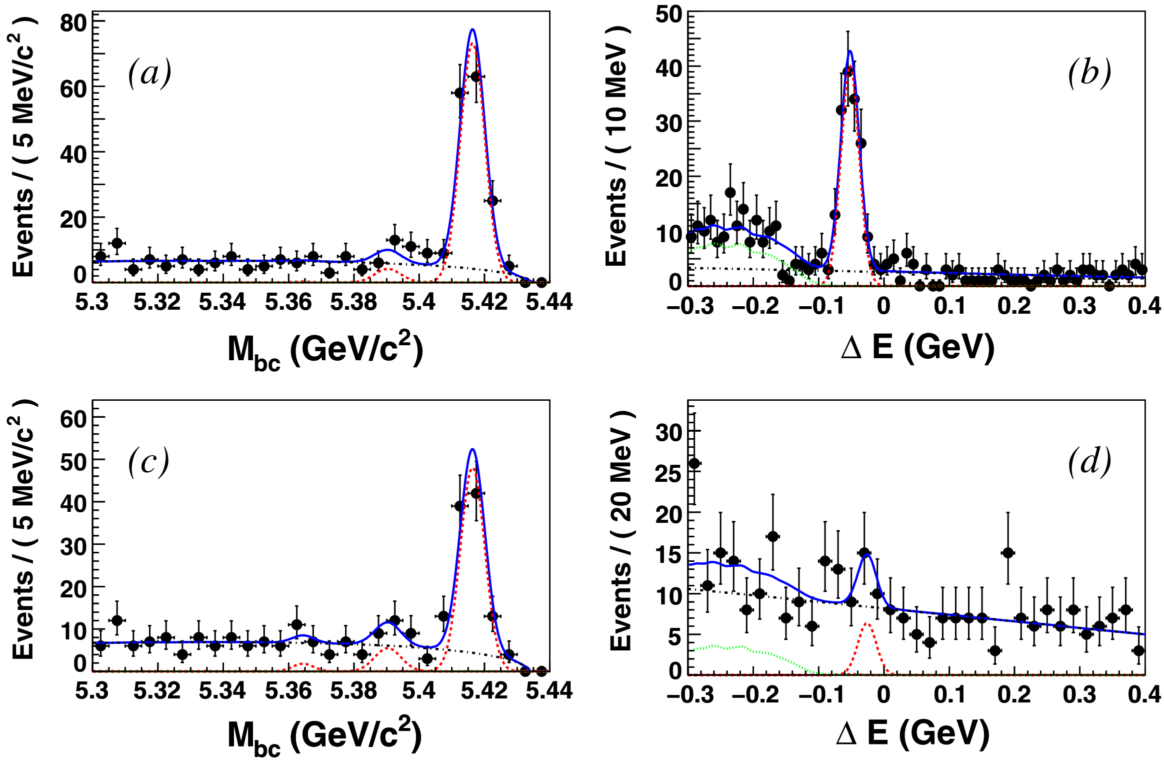

FIG. 2 (color online). (a) $M_{\rm bc}$ distribution of the $B_s^0 \to D_s^- \pi^+$ candidates with ΔE in the $B_s^* \bar{B}_s^*$ signal region $[-80, -17]$ MeV. (b) ΔE distribution of the $B_s^0 \to D_s^- \pi^+$ candidates with $M_{\rm bc}$ in the $B_s^* \bar{B}_s^*$ signal region $[5.41, 5.43]$ GeV$/c^2$. The different fitted components are shown with dashed curves for the signal, dotted curves for the $B_s^0 \to D_s^{*-} \pi^+$ background, and dash-dotted curves for the continuum. (c),(d) show the same distributions but using the $B_s^* \bar{B}_s^0$ signal region ($\Delta E \in [-57, 9]$ MeV and $M_{\rm bc} \in [5.38, 5.40]$ GeV$/c^2$).

$B_s^0 \to D_s^- \pi^+$ ($B_s^0 \to D_s^\mp K^\pm$) mode. These two selections reject 43% (73%) of the continuum while retaining 95% (85%) of the $B_s^0 \to D_s^- \pi^+$ ($B_s^0 \to D_s^\mp K^\pm$) signal. MC studies show that background from B^+ and B^0 decays is small and flat enough to be described together with the continuum events for the $B_s^0 \to D_s^- \pi^+$ mode and is negligible for the $B_s^0 \to D_s^\mp K^\pm$ mode. The most relevant background from B_s^0 decays is $B_s^0 \to D_s^{*-} \pi^+$.

For each mode, a two-dimensional unbinned extended maximum likelihood fit [17] in $M_{\rm bc}$ and ΔE is performed on the selected candidates, which are shown in Fig. 1. Each signal probability density function (PDF) is described by a sum of two Gaussians. For the $B_s^0 \to D_s^- \pi^+$ analysis, all three B_s^0 production modes ($B_s^* \bar{B}_s^*$, $B_s^* \bar{B}_s^0$, and $B_s^0 \bar{B}_s^0$) are fitted simultaneously. For the $B_s^0 \to D_s^\mp K^\pm$ mode, only the $B_s^* \bar{B}_s^*$ component is taken into account. The resolutions for $M_{\rm bc}$ and ΔE are estimated from MC simulation and scaled by a common factor (one for each variable) left free in the $B_s^0 \to D_s^- \pi^+$ fit. Approximating $p^*_{B_s^*}$ with $p^*_{B_s^0}$ in the $B_s^* \to B_s^0 \gamma$ decay, the mean values are parametrized, as shown in Table I, as functions of the B_s^0 and B_s^* masses, which are also left free in the $B_s^0 \to D_s^- \pi^+$ fit. The continuum (together with possible B^+ and B^0 background) is modeled with an ARGUS function [18] for $M_{\rm bc}$ and a linear function for ΔE. A nonparametric two-dimensional PDF, obtained from MC simulation with the kernel-estimation method [19], is used to describe the shape of the $B_s^0 \to D_s^{*-} \pi^+$ background.

For the $B_s^0 \to D_s^- \pi^+$ mode, the three signal yields are expressed as a function of three free parameters, $\mathcal{B}(B_s^0 \to D_s^- \pi^+)$, $f_{B_s^* \bar{B}_s^*}$, and $f_{B_s^* \bar{B}_s^0}$, with the relations

TABLE III. Relative systematic uncertainties (in %) for $\mathcal{B}(B_s^0 \to D_s^- \pi^+)$ and $\mathcal{B}(B_s^0 \to D_s^\mp K^\pm)$.

Source	$B_s^0 \to D_s^- \pi^+$		$B_s^0 \to D_s^\mp K^\pm$	
Integrated luminosity	+1.3	−1.3	+1.4	−1.2
$\sigma_{b\bar{b}}^{\Upsilon(5S)}$	+4.8	−4.4	+5.0	−4.4
f_s	+13.3	−13.3	+13.6	−13.4
$f_{B_s^* \bar{B}_s^*}$	...		+4.8	−4.1
D_s^- branching fractions	+6.6	−6.1	+6.8	−5.9
Efficiencies (MC stat.)	+1.2	−1.2	+1.5	−1.3
Efficiencies (R_2, cos$\theta_{\rm hel}$)	+4.8	−4.8	+4.8	−4.8
$\pi^\pm$, $K^\pm$ identification	+5.4	−5.4	+5.2	−5.2
Track reconstruction	+4.0	−4.0	+4.0	−4.0
PDF shapes	+1.0	−1.0	+3.3	−2.7
Total	+17.8	−17.5	+19.0	−18.1

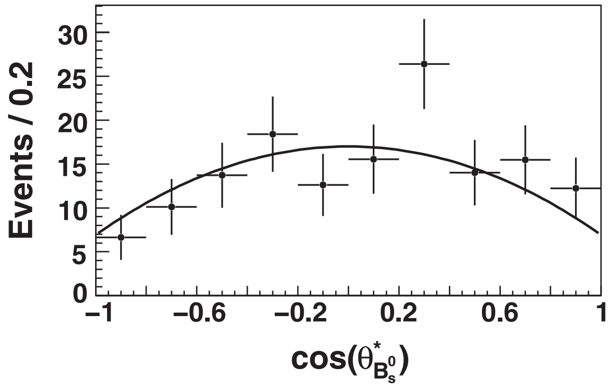

FIG. 3. Fitted distribution of the cosine of the angle between the B^0_s momentum and the beam axis in the c.m. frame for the $\Upsilon(5S) \to B^*_s \bar{B}^*_s$ signal.

$N_M = N_{B^0_s} \mathcal{B}(B^0_s \to D^-_s \pi^+) f_M \sum_k \varepsilon^M_k \mathcal{B}_k$, where M is one of the three $B^{(*)}_s \bar{B}^{(*)}_s$-pair production modes and k runs over the D^-_s modes; the third fraction is defined as $f_{B^0_s \bar{B}^0_s} = 1 - f_{B^*_s \bar{B}^*_s} - f_{B^*_s \bar{B}^0_s}$. The values of $\sum_k \varepsilon^M_k \mathcal{B}_k$, which are the total D^-_s branching fractions [12] weighted by the reconstruction efficiencies, are listed in Table II.

Figure 2 shows the $M_{\rm bc}$ and ΔE projections in the $B^*_s \bar{B}^*_s$ and in the $B^*_s \bar{B}^0_s$ regions of the data, together with the fitted function. In the $M_{\rm bc}$ distribution, the three signal components are present due to overlap of the signal boxes; the peak on the right (middle, left) is due to $B^*_s \bar{B}^*_s$ ($B^*_s \bar{B}^0_s$, $B^0_s \bar{B}^0_s$) production. Table II presents the fitted signal yields as well as the significance defined by $S = \sqrt{2\ln(\mathcal{L}_{\rm max}/\mathcal{L}_0)}$, where $\mathcal{L}_{\rm max}$ ($\mathcal{L}_0$) is the value at the maximum (with the corresponding yield set to zero) of the likelihood function convolved with a Gaussian distribution that represents the systematic errors.

Systematic uncertainties on the branching fractions are shown in Table III. Those on $f_{B^*_s \bar{B}^*_s}$ and $f_{B^*_s \bar{B}^0_s}$ are mainly due to PDF uncertainties. Those due to the beam energy, the momentum calibration, and the $p^*_{B^*_s} \approx p^*_{B^0_s}$ approximation are propagated as systematics on the B^*_s mass and B^0_s mass. The momentum normalization uncertainties are much more important in the latter case because the measured energy of the B^0_s candidate is used instead of the beam energy.

We measure the branching fraction $\mathcal{B}(B^0_s \to D^-_s \pi^+) = [3.67^{+0.35}_{-0.33}({\rm stat})^{+0.43}_{-0.42}({\rm syst}) \pm 0.49(f_s)] \times 10^{-3}$, where the largest systematic uncertainty, due to f_s, is quoted separately, the fraction $f_{B^*_s \bar{B}^*_s} = (90.1^{+3.8}_{-4.0} \pm 0.2)\%$ and the two fitted masses $m_{B^0_s} = (5364.4 \pm 1.3 \pm 0.7)$ MeV$/c^2$ and $m_{B^*_s} = (5416.4 \pm 0.4 \pm 0.5)$ MeV$/c^2$. These four measurements supersede the previous Belle values [10]. We obtain for the first time values for the two fractions $f_{B^*_s \bar{B}^0_s} = (7.3^{+3.3}_{-3.0} \pm 0.1)\%$ and $f_{B^0_s \bar{B}^0_s} = (2.6^{+2.6}_{-2.5})\%$, using the correlation (-0.77) between $f_{B^*_s \bar{B}^*_s}$ and $f_{B^*_s \bar{B}^0_s}$.

Our branching fraction is compatible with the CDF result [12,20], and is slightly higher (1.3σ) than $\mathcal{B}(B^0 \to D^- \pi^+)$ [12]. The value of $f_{B^*_s \bar{B}^*_s}$ is significantly larger than the theoretical expectation of $\approx 70\%$ [5,6]. The B^0_s mass is compatible with the world average value [12], while our value for the B^*_s mass is 2.6σ larger than the result from CLEO [21]. The mass difference obtained, $m_{B^*_s} - m_{B^0_s} = 52.0 \pm 1.5$ MeV$/c^2$, is 4.0σ larger than the world average of $m_{B^{*0}} - m_{B^0}$ [12], while heavy-quark symmetry predicts equal values [4].

The distribution of the angle between the B^0_s momentum and the beam axis in the c.m. frame is of theoretical interest [5] and is presented in Fig. 3 for the signal events in the $B^*_s \bar{B}^*_s$ region, using the $_s$Plot method [22]. A fit to a $1 + a\cos^2\theta^*_{B^0_s}$ distribution returns $\chi^2/(\text{number of degrees of freedom}) = 8.74/8$ and $a = -0.59^{+0.18}_{-0.16}$. It has been checked that the signal efficiency does not depend on this angle. We naively expect $a = -0.27$ by summing over all the possible polarization states.

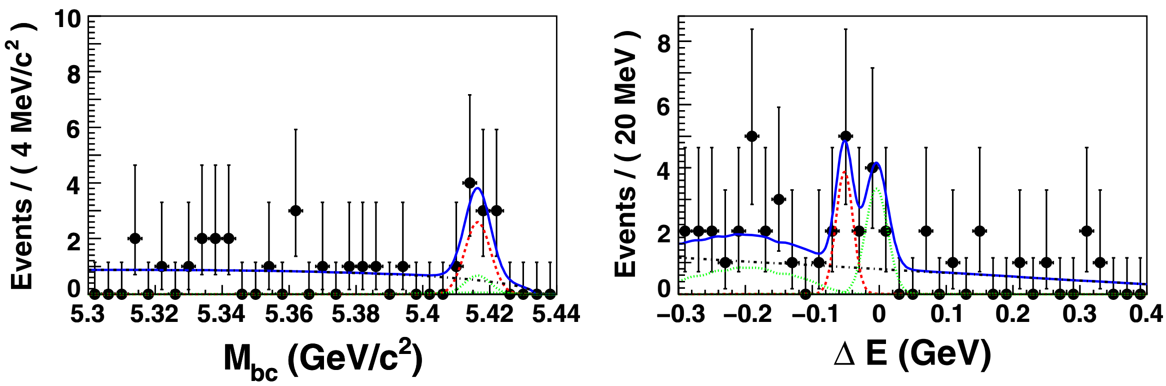

FIG. 4 (color online). Left: $M_{\rm bc}$ distribution of $B^0_s \to D^\mp_s K^\pm$ candidates with ΔE in the $B^*_s \bar{B}^*_s$ signal region. Right: ΔE distribution of the $B^0_s \to D^\mp_s K^\pm$ candidates with $M_{\rm bc}$ in the $B^*_s \bar{B}^*_s$ signal region; the left (right) peak is the $B^0_s \to D^\mp_s K^\pm$ ($B^0_s \to D^-_s \pi^+$) component. The dashed curves, dotted curves, and dash-dotted curves represent the signal, $B^0_s \to D^{(*)-}_s \pi^+$ backgrounds, and continuum, respectively.

For the $B_s^0 \to D_s^{\mp} K^{\pm}$ mode, mean values and resolutions for $B_s^0 \to D_s^{\mp} K^{\pm}$ and $B_s^0 \to D_s^- \pi^+$ components are calibrated using the results of the $B_s^0 \to D_s^- \pi^+$ fit. The four yields (signal, continuum, $B_s^0 \to D_s^- \pi^+$, and $B_s^0 \to D_s^{*-} \pi^+$) are allowed to float, but, due to the very small contribution of $B_s^0 \to D_s^{*-} \pi^+$, the ratio between the yields of $B_s^0 \to D_s^{*-} \pi^+$ and $B_s^0 \to D_s^- \pi^+$ is fixed from a fit to data without kaon identification.

The fit results are shown in Fig. 4 and Table II. Systematic errors are presented in Table III. We find $6.7^{+3.4}_{-2.7}$ signal events (3.5σ), corresponding to $\mathcal{B}(B_s^0 \to D_s^{\mp} K^{\pm}) = [2.4^{+1.2}_{-1.0}(\mathrm{stat}) \pm 0.3(\mathrm{syst}) \pm 0.3(f_s)] \times 10^{-4}$, using the previously fitted value of $f_{B_s^* \bar{B}_s^*}$. In the ratio $\mathcal{B}(B_s^0 \to D_s^{\mp} K^{\pm})/\mathcal{B}(B_s^0 \to D_s^- \pi^+) = (6.5^{+3.5}_{-2.9})\%$, the errors are dominated by the low $B_s^0 \to D_s^{\mp} K^{\pm}$ statistics.

In summary, a large $B_s^0 \to D_s^- \pi^+$ signal is observed and six physics parameters are measured: the branching fraction $\mathcal{B}(B_s^0 \to D_s^- \pi^+) = [3.67^{+0.35}_{-0.33}(\mathrm{stat})^{+0.43}_{-0.42}(\mathrm{syst}) \pm 0.49(f_s)] \times 10^{-3}$, the fractions of the B_s^0 pair production modes at the $\Upsilon(5S)$ energy, $f_{B_s^* \bar{B}_s^*} = (90.1^{+3.8}_{-4.0} \pm 0.2)\%$, $f_{B_s^* \bar{B}_s^0} = (7.3^{+3.3}_{-3.0} \pm 0.1)\%$, $f_{B_s^0 \bar{B}_s^0} = (2.6^{+2.6}_{-2.5})\%$, and the masses $m_{B_s^*} = (5416.4 \pm 0.4 \pm 0.5)\ \mathrm{MeV}/c^2$, $m_{B_s^0} = (5364.4 \pm 1.3 \pm 0.7)\ \mathrm{MeV}/c^2$. In addition, evidence (3.5σ) for the $B_s^0 \to D_s^{\mp} K^{\pm}$ decay is obtained, leading to a measurement $\mathcal{B}(B_s^0 \to D_s^{\mp} K^{\pm}) = [2.4^{+1.2}_{-1.0}(\mathrm{stat}) \pm 0.3(\mathrm{syst}) \pm 0.3(f_s)] \times 10^{-4}$.

We thank the KEKB group for excellent operation of the accelerator, the KEK cryogenics group for efficient solenoid operations, and the KEK computer group and the NII for valuable computing and SINET3 network support. We acknowledge support from MEXT and JSPS (Japan); ARC and DEST (Australia); NSFC (China); DST (India); MOEHRD, KOSEF and KRF (Korea); KBN (Poland); MES and RFAAE (Russia); ARRS (Slovenia); SNSF (Switzerland); NSC and MOE (Taiwan); and DOE (U.S.A.).

*Now at: Okayama University, Okayama.

[1] Unless specified otherwise, charge-conjugated modes are implied throughout the Letter.

[2] L. Wolfenstein, Phys. Rev. Lett. **51**, 1945 (1983).
[3] R. Aleksan, I. Dunietz, and B. Kayser, Z. Phys. C **54**, 653 (1992). See also R. Fleicher, Nucl. Phys. **B671**, 459 (2003); S. Nandi and U. Nierste, Phys. Rev. D **77**, 054010 (2008).
[4] W. A. Bardeen, E. J. Eichten, and C. T. Hill, Phys. Rev. D **68**, 054024 (2003).
[5] A. G. Grozin and M. Neubert, Phys. Rev. D **55**, 272 (1997).
[6] N. A. Törnqvist, Phys. Rev. Lett. **53**, 878 (1984).
[7] S. Kurokawa and E. Kikutani, Nucl. Instrum. Methods Phys. Res., Sect. A **499**, 1 (2003).
[8] K.-F. Chen *et al.* (Belle Collaboration), Phys. Rev. Lett. **100**, 112001 (2008). We obtain $\sqrt{s} = m_{\Upsilon(1S)} + \Delta M$, where $m_{\Upsilon(1S)}$ is the nominal $\Upsilon(1S)$ mass [12] and ΔM is the measured $M_{\mu^+\mu^-\pi^+\pi^-} - M_{\mu^+\mu^-}$.
[9] A. Drutskoy *et al.* (Belle Collaboration), Phys. Rev. Lett. **98**, 052001 (2007); G. S. Huang *et al.* (CLEO Collaboration), Phys. Rev. D **75**, 012002 (2007). These two published values of $\sigma_{b\bar{b}}^{\Upsilon(5S)}$ are averaged. Experimental f_s values are also given by both of them; the average is given in Ref. [12].
[10] A. Drutskoy *et al.* (Belle Collaboration), Phys. Rev. D **76**, 012002 (2007).
[11] A. Abashian *et al.* (Belle Collaboration), Nucl. Instrum. Methods Phys. Res., Sect. A **479**, 117 (2002).
[12] C. Amsler *et al.* (Particle Data Group), Phys. Lett. B **667**, 1 (2008).
[13] F. Fang, Ph.D. thesis, University of Hawaii, 2003.
[14] D. J. Lange, Nucl. Instrum. Methods Phys. Res., Sect. A **462**, 152 (2001).
[15] CERN Application Software Group, CERN Program Library Long Write-up W5013, 1993.
[16] G. C. Fox and S. Wolfram, Phys. Rev. Lett. **41**, 1581 (1978).
[17] R. Barlow, Nucl. Instrum. Methods Phys. Res., Sect. A **297**, 496 (1990).
[18] H. Albrecht *et al.* (ARGUS Collaboration), Phys. Lett. B **185**, 218 (1987).
[19] K. Cranmer, Comput. Phys. Commun. **136**, 198 (2001).
[20] A. Abulencia *et al.* (CDF Collaboration), Phys. Rev. Lett. **98**, 061802 (2007).
[21] O. Aquines *et al.* (CLEO Collaboration), Phys. Rev. Lett. **96**, 152001 (2006).
[22] M. Pivk and F. R. Le Diberder, Nucl. Instrum. Methods Phys. Res., Sect. A **555**, 356 (2005).

Observation of $B_s^0 \to D_s^{*-}\pi^+$ and $B_s^0 \to D_s^{(*)-}\rho^+$ and Measurement of the $B_s^0 \to D_s^{*-}\rho^+$ Longitudinal Polarization Fraction

R. Louvot,[19] O. Schneider,[19] T. Aushev,[19,12] K. Arinstein,[1,33] A. M. Bakich,[39] V. Balagura,[12] E. Barberio,[23] A. Bay,[19] K. Belous,[11] M. Bischofberger,[25] A. Bondar,[1,33] A. Bozek,[29] M. Bračko,[21,13] T. E. Browder,[7] P. Chang,[28] Y. Chao,[28] A. Chen,[26] K.-F. Chen,[28] P. Chen,[28] B. G. Cheon,[6] C.-C. Chiang,[28] I.-S. Cho,[47] Y. Choi,[38] M. Danilov,[12] M. Dash,[46] A. Drutskoy,[3] S. Eidelman,[1,33] P. Goldenzweig,[3] B. Golob,[20,13] H. Ha,[17] J. Haba,[8] T. Hara,[8] Y. Horii,[42] Y. Hoshi,[41] W.-S. Hou,[28] Y. B. Hsiung,[28] H. J. Hyun,[18] T. Iijima,[24] K. Inami,[24] R. Itoh,[8] M. Iwabuchi,[47] M. Iwasaki,[43] Y. Iwasaki,[8] N. J. Joshi,[40] D. H. Kah,[18] J. H. Kang,[47] P. Kapusta,[29] N. Katayama,[8] T. Kawasaki,[31] C. Kiesling,[22] H. J. Kim,[18] H. O. Kim,[18] J. H. Kim,[16] M. J. Kim,[18] Y. J. Kim,[5] K. Kinoshita,[3] B. R. Ko,[17] P. Kodyš,[2] S. Korpar,[21,13] P. Križan,[20,13] P. Krokovny,[8] T. Kumita,[44] Y.-J. Kwon,[47] S.-H. Kyeong,[47] J. S. Lange,[4] M. J. Lee,[37] S.-H. Lee,[17] J. Li,[7] C. Liu,[36] A. Matyja,[29] S. McOnie,[39] K. Miyabayashi,[25] H. Miyata,[31] Y. Miyazaki,[24] G. B. Mohanty,[40] M. Nakao,[8] H. Nakazawa,[26] S. Nishida,[8] K. Nishimura,[7] O. Nitoh,[45] T. Ohshima,[24] S. Okuno,[14] S. L. Olsen,[37,7] P. Pakhlov,[12] G. Pakhlova,[12] H. Palka,[29] H. Park,[18] H. K. Park,[18] R. Pestotnik,[13] M. Petrič,[13] L. E. Piilonen,[46] A. Poluektov,[1,33] M. Prim,[15] M. Röhrken,[15] S. Ryu,[37] H. Sahoo,[7] Y. Sakai,[8] C. Schwanda,[10] A. J. Schwartz,[3] K. Senyo,[24] M. E. Sevior,[23] M. Shapkin,[11] V. Shebalin,[1,33] C. P. Shen,[7] J.-G. Shiu,[28] J. B. Singh,[35] P. Smerkol,[13] A. Sokolov,[11] S. Stanič,[32] M. Starič,[13] T. Sumiyoshi,[44] G. N. Taylor,[23] Y. Teramoto,[34] K. Trabelsi,[8] S. Uehara,[8] Y. Unno,[6] S. Uno,[8] G. Varner,[7] K. E. Varvell,[39] K. Vervink,[19] C. H. Wang,[27] M.-Z. Wang,[28] P. Wang,[9] J. Wicht,[8] E. Won,[17] B. D. Yabsley,[39] Y. Yamashita,[30] Z. P. Zhang,[36] T. Zivko,[13] and O. Zyukova[1,33]

(Belle Collaboration)

[1]*Budker Institute of Nuclear Physics, Novosibirsk*
[2]*Faculty of Mathematics and Physics, Charles University, Prague*
[3]*University of Cincinnati, Cincinnati, Ohio 45221*
[4]*Justus-Liebig-Universität Gießen, Gießen*
[5]*The Graduate University for Advanced Studies, Hayama*
[6]*Hanyang University, Seoul*
[7]*University of Hawaii, Honolulu, Hawaii 96822*
[8]*High Energy Accelerator Research Organization (KEK), Tsukuba*
[9]*Institute of High Energy Physics, Chinese Academy of Sciences, Beijing*
[10]*Institute of High Energy Physics, Vienna*
[11]*Institute of High Energy Physics, Protvino*
[12]*Institute for Theoretical and Experimental Physics, Moscow*
[13]*J. Stefan Institute, Ljubljana*
[14]*Kanagawa University, Yokohama*
[15]*Institut für Experimentelle Kernphysik, Karlsruher Institut für Technologie, Karlsruhe*
[16]*Korea Institute of Science and Technology Information, Daejeon*
[17]*Korea University, Seoul*
[18]*Kyungpook National University, Taegu*
[19]*École Polytechnique Fédérale de Lausanne (EPFL), Lausanne*
[20]*Faculty of Mathematics and Physics, University of Ljubljana, Ljubljana*
[21]*University of Maribor, Maribor*
[22]*Max-Planck-Institut für Physik, München*
[23]*University of Melbourne, School of Physics, Victoria 3010*
[24]*Nagoya University, Nagoya*
[25]*Nara Women's University, Nara*
[26]*National Central University, Chung-li*
[27]*National United University, Miao Li*
[28]*Department of Physics, National Taiwan University, Taipei*
[29]*H. Niewodniczanski Institute of Nuclear Physics, Krakow*
[30]*Nippon Dental University, Niigata*
[31]*Niigata University, Niigata*
[32]*University of Nova Gorica, Nova Gorica*
[33]*Novosibirsk State University, Novosibirsk*
[34]*Osaka City University, Osaka*

0031-9007/10/104(23)/231801(6) © 2010 The American Physical Society

[35]Panjab University, Chandigarh
[36]University of Science and Technology of China, Hefei
[37]Seoul National University, Seoul
[38]Sungkyunkwan University, Suwon
[39]School of Physics, University of Sydney, NSW 2006
[40]Tata Institute of Fundamental Research, Mumbai
[41]Tohoku Gakuin University, Tagajo
[42]Tohoku University, Sendai
[43]Department of Physics, University of Tokyo, Tokyo
[44]Tokyo Metropolitan University, Tokyo
[45]Tokyo University of Agriculture and Technology, Tokyo
[46]IPNAS, Virginia Polytechnic Institute and State University, Blacksburg, Virginia 24061
[47]Yonsei University, Seoul
(Received 27 March 2010; published 8 June 2010)

First observations of the $B_s^0 \to D_s^{*-}\pi^+$, $B_s^0 \to D_s^-\rho^+$ and $B_s^0 \to D_s^{*-}\rho^+$ decays are reported together with measurements of their branching fractions: $\mathcal{B}(B_s^0 \to D_s^{*-}\pi^+) = [2.4^{+0.5}_{-0.4}(\mathrm{stat}) \pm 0.3(\mathrm{syst}) \pm 0.4(f_s)] \times 10^{-3}$, $\mathcal{B}(B_s^0 \to D_s^-\rho^+) = [8.5^{+1.3}_{-1.2}(\mathrm{stat}) \pm 1.1(\mathrm{syst}) \pm 1.3(f_s)] \times 10^{-3}$ and $\mathcal{B}(B_s^0 \to D_s^{*-}\rho^+) = [11.9^{+2.2}_{-2.0}(\mathrm{stat}) \pm 1.7(\mathrm{syst}) \pm 1.8(f_s)] \times 10^{-3}$ ($f_s = N_{B_s^{(*)}\bar{B}_s^{(*)}}/N_{b\bar{b}}$). From helicity-angle distributions, we measured the longitudinal polarization fraction in $B_s^0 \to D_s^{*-}\rho^+$ decays to be $f_L(B_s^0 \to D_s^{*-}\rho^+) = 1.05^{+0.08}_{-0.10}(\mathrm{stat})^{+0.03}_{-0.04}(\mathrm{syst})$. These results are based on a 23.6 fb^{-1} data sample collected at the $\Upsilon(5S)$ resonance with the Belle detector at the KEKB e^+e^- collider.

DOI: 10.1103/PhysRevLett.104.231801 PACS numbers: 13.25.Hw, 12.39.Hg, 13.25.Gv, 13.88.+e

The measurement of exclusive $B_s^0 \to D_s^{(*)-}h^+$ [1] ($h^+ = \pi^+$ or ρ^+) decays is an important milestone in the study of the poorly known decay processes of the B_s^0 meson. In Refs. [2–5] Belle confirmed the large potential of B factories for B_s^0 investigations due to the low multiplicities of charged and neutral particles and high reconstruction efficiencies. We have now observed three new exclusive B_s^0 modes with relatively large branching fractions and neutral particles such as photons or π^0's in their final states. The leading amplitude for the four $B_s^0 \to D_s^{(*)-}\pi^+$ and $B_s^0 \to D_s^{(*)-}\rho^+$ modes is a $b \to c$ tree diagram of order λ^2 (in the Wolfenstein parameterization [6] of the CKM quark-mixing matrix [7]) with a spectator s quark. The study of B_s^0 decays provides useful tests of the heavy-quark theories that predict, based on an $SU(3)$ symmetry, similarities between B_s^0-meson decay modes and their corresponding B^0-meson counterparts. These include the unitarized quark model [8], the heavy-quark effective theory (HQET) [9–12], and a more recent approach based on chiral symmetry [13]. Our B_s^0 branching fraction results can be used to normalize measurements of B_s^0 decays made at hadron collider experiments, where the number of B_s^0 mesons produced has a substantial systematic uncertainty.

The decay $B_s^0 \to D_s^{*-}h^+$ is mediated by the same tree diagram as $B^0 \to D^{*-}h^+$, but with a spectator s quark. The contribution of the strongly suppressed W-exchange diagram is expected to be negligibly small. Moreover, the helicity amplitudes in $B \to VV$ decays can be used to test the factorization hypothesis [12,14]. The relative strengths of the longitudinal and transverse states can be measured with an angular analysis of the decay products. In the helicity basis, the expected $B_s^0 \to D_s^{*-}\rho^+$ differential decay width is

$$\frac{d^2\Gamma(B_s^0 \to D_s^{*-}\rho^+)}{d\cos\theta_{D_s^{*-}}\, d\cos\theta_{\rho^+}} \propto 4f_L \sin^2\theta_{D_s^{*-}}\cos^2\theta_{\rho^+} + (1-f_L)(1+\cos^2\theta_{D_s^{*-}})\sin^2\theta_{\rho^+}, \tag{1}$$

where $f_L = |H_0|^2/\sum_\lambda |H_\lambda|^2$ is the longitudinal polarization fraction, H_λ ($\lambda = \pm 1, 0$) are the helicity amplitudes, and $\theta_{D_s^{*-}}$ (θ_{ρ^+}) is the helicity angle of the D_s^{*-} (ρ^+) defined as the supplement of the angle between the B_s^0 and the D_s^- (π^+) momenta in the D_s^{*-} (ρ^+) frame.

Here we report measurements performed with fully reconstructed $B_s^0 \to D_s^{*-}\pi^+$, $B_s^0 \to D_s^-\rho^+$ and $B_s^0 \to D_s^{*-}\rho^+$ decays in a data set corresponding to an integrated luminosity of $L_{\mathrm{int}} = (23.6 \pm 0.3)$ fb^{-1} collected with the Belle detector at the KEKB asymmetric-energy (3.6 GeV on 8.2 GeV) e^+e^- collider [15] operated at the $\Upsilon(5S)$ resonance [$\sqrt{s} = (10867.0 \pm 1.0)$ MeV [5]]. The total $b\bar{b}$ cross section at the $\Upsilon(5S)$ energy has been measured to be $\sigma_{b\bar{b}}^{\Upsilon(5S)} = (0.302 \pm 0.014)$ nb [2,16]. Three B_s^0 production modes are kinematically allowed at the $\Upsilon(5S)$: $B_s^*\bar{B}_s^*$, $B_s^*\bar{B}_s^0 + B_s^0\bar{B}_s^*$, and $B_s^0\bar{B}_s^0$. The B_s^* decays to B_s^0, emitting a photon with energy $E_\gamma \sim 50$ MeV. The fraction of $b\bar{b}$ events containing a $B_s^{(*)}\bar{B}_s^{(*)}$ pair has been measured to be $f_s = N_{B_s^{(*)}\bar{B}_s^{(*)}}/N_{b\bar{b}} = (19.3 \pm 2.9)\%$ [17]. The fraction of $B_s^{(*)}\bar{B}_s^{(*)}$ events containing a $B_s^*\bar{B}_s^*$ pair is predominant and has been measured with $B_s^0 \to D_s^-\pi^+$ events to be $f_{B_s^*\bar{B}_s^*} = (90.1^{+3.8}_{-4.0} \pm 0.2)\%$ [5]. The number of B_s^0 mesons produced in the dominant $B_s^*\bar{B}_s^*$ production mode is thus $N_{B_s^0} = 2L_{\mathrm{int}}\sigma_{b\bar{b}}^{\Upsilon(5S)} f_s f_{B_s^*\bar{B}_s^*} = (2.48 \pm 0.41) \times 10^6$.

The Belle detector is a large-solid-angle magnetic spectrometer that consists of a silicon vertex detector, a central drift chamber (CDC), an array of aerogel threshold Cherenkov counters (ACC), a barrel-like arrangement of time-of-flight scintillation counters (TOF), and an electromagnetic calorimeter comprised of CsI(Tl) crystals (ECL) located inside a superconducting solenoid coil that provides a 1.5 T magnetic field. An iron flux-return located outside of the coil is instrumented to detect K_L^0 and to identify muons. The detector is described in detail elsewhere [18].

Reconstructed charged tracks are required to have a maximum impact parameter with respect to the nominal interaction point of 0.5 cm in the radial direction and 3 cm in the beam-axis direction. A likelihood ratio $\mathcal{R}_{K/\pi} = \mathcal{L}_K/(\mathcal{L}_\pi + \mathcal{L}_K)$ is constructed using ACC, TOF and CDC (ionization energy loss) measurements. A track is identified as a charged pion if $\mathcal{R}_{K/\pi} < 0.6$ or as a charged kaon otherwise. With this selection, the momentum-averaged identification efficiency for pions (kaons) is about 91% (86%), while the momentum-averaged rate of kaons (pions) identified as pions (kaons) is about 9% (14%).

Photons are reconstructed using ECL energy clusters within the polar angle acceptance 17° to 150° that are not associated with a charged track and that have an energy deposit larger than 50 MeV. A photon candidate is retained only if the ratio of the energy deposited in the array of the central 3×3 cells is more than 85% of that in the array of 5×5 cells. Neutral pions are reconstructed via the $\pi^0 \to \gamma\gamma$ decay with photon pairs having an invariant mass within ± 13 MeV$/c^2$ of the π^0 mass. A mass-constrained fit is then applied to the π^0 candidates.

Neutral kaons are reconstructed via the decay $K_S^0 \to \pi^+\pi^-$ with no $\mathcal{R}_{K/\pi}$ requirements for the two charged pions. The K_S^0 candidates are required to have an invariant mass within ± 7.5 MeV$/c^2$ of the K_S^0 mass. Requirements are applied on the K_S^0 vertex displacement from the interaction point (IP) and on the difference between the K_S^0 flight directions obtained from the K_S^0 momentum and from the decay vertex and IP. The criteria are described in detail elsewhere [19]. The K^{*0} (ϕ, ρ^+) candidates are reconstructed via the decay $K^{*0} \to K^+\pi^-$ ($\phi \to K^+K^-$, $\rho^+ \to \pi^+\pi^0$) with an invariant mass within ± 50 MeV$/c^2$ ($\pm$ 12 MeV$/c^2$, ± 100 MeV$/c^2$) of their nominal values. Candidates for D_s^- are reconstructed in the three modes $D_s^- \to \phi\pi^-$, $D_s^- \to K^{*0}K^-$, and $D_s^- \to K_S^0 K^-$ and are required to have a mass within ± 10 MeV$/c^2$ of the D_s^- mass. The D_s^{*-} candidates are reconstructed via the decay $D_s^{*-} \to D_s^-\gamma$ by adding a photon candidate to a D_s^- candidate. The $D_s^-\gamma$ pair is required to have a mass difference $m(D_s^-\gamma) - m(D_s^-)$ within ± 13 MeV$/c^2$ of the $D_s^{*-} - D_s^-$ mass difference. All mass values are those reported in Ref. [17], and the applied mass windows correspond to $\pm$(3–4)σ around these values; the mass resolution, σ, is obtained from Monte Carlo (MC) signal simulations.

The $B_s^0 \to D_s^{*-}\pi^+$ and $B_s^0 \to D_s^-\rho^+$ candidates are reconstructed using two variables: the beam-energy-constrained mass of the B_s^0 candidate $M_{\rm bc} = \sqrt{E_b^{*2} - \vec{p}_{B_s^0}^{\,*2}}$, and the energy difference $\Delta E = E_{B_s^0}^* - E_b^*$, where ($E_{B_s^0}^*$, $\vec{p}_{B_s^0}^{\,*}$) is the four-momentum of the B_s^0 candidate and E_b^* is the beam energy, both expressed in the center-of-mass frame. The two angles $\theta_{D_s^{*-}}$ and θ_{ρ^+} are used as additional observables for the $B_s^0 \to D_s^{*-}\rho^+$ candidate. We select candidates with $M_{\rm bc} > 5.3$ GeV$/c^2$ and -0.3 GeV $< \Delta E < 0.4$ GeV.

Further selection criteria are developed using MC samples based on the EVTGEN [20] event generator and the GEANT [21] full-detector simulation. The most significant source of background is continuum processes, $e^+e^- \to q\bar{q}$ ($q = u$, d, s, c). In addition, peaking backgrounds can arise from specific B_s^0 decays. Using a MC sample of $e^+e^- \to B_s^{(*)}\bar{B}_s^{(*)}$ events corresponding to 3 times the integrated luminosity, we find that $B_s^0 \to D_s^-\pi^+$ and $B_s^0 \to D_s^-\rho^+$ events make a significant contribution to the background in the $B_s^0 \to D_s^{*-}\pi^+$ analysis. However, they are well separated from the signal in the ΔE distribution. If a $B_s^0 \to D_s^-\pi^+$ decay is combined with an extra photon, the energy is larger than the signal; the four charged tracks of a $B_s^0 \to D_s^-\rho^+$ event can be selected with an additional photon giving a B_s^0 candidate with a smaller energy. Similarly, $B_s^0 \to D_s^{*-}\rho^+$ decays give a significant contribution to the $B_s^0 \to D_s^-\rho^+$ analysis at lower energies. For the $B_s^0 \to D_s^{*-}\rho^+$ analysis, there is no significant peaking background. MC studies show that, for the three modes, all the other background sources (mainly B^0 and B^+ events) are smooth and small enough to be well described by the same shape that is used for the continuum. The contribution of nonresonant $B_s^0 \to D_s^{(*)-}\pi^+\pi^0$ decays is studied by relaxing the $(\pi^+\pi^0)$ mass ($M_{\pi\pi}$) requirement and doing a two-dimensional fit in $M_{\rm bc}$ and ΔE (see below). The signal $M_{\pi\pi}$ distribution is then obtained using the $_s$Plot method [22]. The resulting $M_{\pi\pi}$ spectrum shows no indication of $B_s^0 \to D_s^{(*)-}\pi^+\pi^0$ decays (consistent with results for $B^0 \to D^{(*)+}\pi^0\pi^-$ [23]), and we neglect this component in our fit.

To improve signal significance, criteria for each of the three B_s^0 modes are chosen to maximize $N_{\rm sig}/\sqrt{N_{\rm sig} + N_{\rm bkg}^{q\bar{q}} + N_{\rm bkg}^{\rm peak}}$, evaluated in the $\pm 2.5\sigma$ $B_s^*\bar{B}_s^*$ signal region in the ($M_{\rm bc}$, ΔE) plane. The expected continuum background, $N_{\rm bkg}^{q\bar{q}}$, is estimated using MC-generated continuum events corresponding to 3 times the data. The expected signal, $N_{\rm sig}$, and peaking background, $N_{\rm bkg}^{\rm peak}$, are obtained assuming $\mathcal{B}(B_s^0 \to D_s^-\pi^+) = \mathcal{B}(B_s^0 \to D_s^{*-}\pi^+) = 3.3 \times 10^{-3}$ [17] and $\mathcal{B}(B_s^0 \to D_s^-\rho^+) = \mathcal{B}(B_s^0 \to D_s^{*-}\rho^+) = 7.0 \times 10^{-3}$ [9]. The efficiencies of exclusive B_s^0 decays are determined using MC simulations.

To suppress the continuum background, we use the ratio of the second and zeroth Fox-Wolfram moments [24], R_2.

This variable has a broad distribution between zero and one for jetlike continuum events and is concentrated in the range below 0.5 for the more spherical signal events. This property allows an efficient continuum reduction with a low systematic uncertainty ($\sim 2\%$). Candidates for $B_s^0 \to D_s^{*-}\pi^+$ ($B_s^0 \to D_s^-\rho^+$ and $B_s^0 \to D_s^{*-}\rho^+$) are required to have $R_2 < 0.5$ (< 0.35). This selection rejects 40% (69%, 64%) of the background while retaining 93% (82%, 86%) of the $B_s^0 \to D_s^{*-}\pi^+$ ($B_s^0 \to D_s^-\rho^+$, $B_s^0 \to D_s^{*-}\rho^+$) signal.

After the event selection described above, about 15%, 15%, and 28% of $D_s^{*-}\pi^+$, $D_s^-\rho^+$ and $D_s^{*-}\rho^+$ candidate events, respectively, have multiple candidates. We select one candidate per event according to the following criteria. The D_s^+ with the mass closest to the nominal value is preferred. The D_s^{*+} formed with the preferred D_s^+ and with the mass difference $m(D_s^*) - m(D_s)$ closest to the nominal value is preferred. The $B_s^0 \to D_s^{*-}\pi^+$ candidate with the preferred D_s^{*-} and the π^+ with the best $\mathcal{R}_{K/\pi}$ is retained. The preferred ρ^+ is the one with the π^0 mass (before the mass-constrained fit) closest to the nominal value and the π^+ with the best $\mathcal{R}_{K/\pi}$. The $B_s^0 \to D_s^-\rho^+$ ($B_s^0 \to D_s^{*-}\rho^+$) candidate with the preferred D_s^- (D_s^{*-}) and the preferred ρ^+ is retained. After this selection, in MC signal simulations, 76%, 68% and 51% (64%) of the selected $B_s^0 \to D_s^{*-}\pi^+$, $B_s^0 \to D_s^-\rho^+$ and longitudinally (transversally) polarized $B_s^0 \to D_s^{*-}\rho^+$ candidates are correctly reconstructed.

The $B_s^0 \to D_s^{*-}\pi^+$ and $B_s^0 \to D_s^-\rho^+$ signals are extracted from a two-dimensional unbinned extended maximum likelihood fit [25] in $M_{\rm bc}$ and ΔE. The three decays of the $\Upsilon(5S)$ ($B_s^*\bar{B}_s^*$, $B_s^*\bar{B}_s^0 + B_s^0\bar{B}_s^*$ and $B_s^0\bar{B}_s^0$) are considered. Each signal probability density function (PDF) is described with sums of Gaussian or so-called "Novosibirsk functions" [26]; the latter function is used to describe the distribution if it is asymmetrical around its central value. Each signal PDF is composed of two components with their respective proportions fixed, representing the correctly and the incorrectly reconstructed candidates. In a simulated signal event, a candidate is correctly (incorrectly) reconstructed when the selected decay products do (do not) match the true combination. The fractions of correctly reconstructed candidates are fixed from MC samples and their uncertainties are included in the systematic error. The $M_{\rm bc}$ and ΔE resolutions for $B_s^0 \to D_s^{*-}\pi^+$ ($B_s^0 \to D_s^-\rho^+$ and $B_s^0 \to D_s^{*-}\rho^+$) are calibrated by a multiplying factor measured with the $B_s^0 \to D_s^-\pi^+$ [5] ($B^0 \to D^{*-}\rho^+$) signal. The mean values of $M_{\rm bc}$ and ΔE for the three B_s^0 production modes (6 parameters) are related to two floating parameters corresponding to the B_s^0 and B_s^* meson masses [27]. The peaking background PDFs are analytically defined and fixed from specific MC samples. The continuum (together with possible B^+ and B^0 background) is modeled with an ARGUS function [28] for $M_{\rm bc}$ and a linear function for ΔE. The endpoint of the ARGUS function is fixed to the beam energy, while the two other parameters are left free. All the yields can float.

For the $B_s^0 \to D_s^{*-}\rho^+$ candidates, we perform a four-dimensional fit using the two observables $\cos\theta_{D_s^{*-}}$ and $\cos\theta_{\rho^+}$ in addition to $M_{\rm bc}$ and ΔE. Only the main B_s^0 production mode is considered ($B_s^*\bar{B}_s^*$), and three components are used in the likelihood: the transverse and longitudinal signals, and the background. We define the PDF for $M_{\rm bc}$ and ΔE in the same way as described above, while the angular distributions are analytically described with polynomials of order up to five. The shape parameters are floated for the background PDF but are fixed for the two signal PDFs.

The fitted signal yields are listed in Table I, while Figs. 1 and 2 show the observed distributions in the $B_s^*\bar{B}_s^*$ signal region with the projections of the fit result. The significance is defined by $S = \sqrt{2\ln(\mathcal{L}_{\rm max}/\mathcal{L}_0)}$, where $\mathcal{L}_{\rm max}$ ($\mathcal{L}_0$) is the value at the maximum (with the corresponding yield set to zero) of the likelihood function convolved with a Gaussian distribution that represents the systematic errors of the yield. The linearity of the floating parameters in the region near the results has been extensively checked with MC simulations, as well as the statistical uncertainty

TABLE I. Total efficiencies (ε), signal yields (N_S) with statistical errors, and significance (S) including systematic uncertainties, for the three measured modes.

Mode	Prod. mode	ε (%)	N_S	S
	$B_s^*\bar{B}_s^*$	9.13	$53.4^{+10.3}_{-9.4}$	7.1σ
$B_s^0 \to D_s^{*-}\pi^+$	$B_s^*\bar{B}_s^0 + B_s^0\bar{B}_s^*$	$\cdots$	$-1.9^{+4.0}_{-2.9}$	$\cdots$
	$B_s^0\bar{B}_s^0$	$\cdots$	$2.9^{+3.9}_{-3.0}$	$\cdots$
	$B_s^*\bar{B}_s^*$	4.40	$92.2^{+14.2}_{-13.2}$	8.2σ
$B_s^0 \to D_s^-\rho^+$	$B_s^*\bar{B}_s^0 + B_s^0\bar{B}_s^*$	$\cdots$	$-4.0^{+5.2}_{-3.7}$	$\cdots$
	$B_s^0\bar{B}_s^0$	$\cdots$	$-3.0^{+5.7}_{-4.0}$	$\cdots$
$B_s^0 \to D_s^{*-}\rho^+$	$B_s^*\bar{B}_s^*$	$\cdots$	$77.8^{+14.5}_{-13.4}$	7.4σ
Longitudinal component		2.66	$81.3^{+16.0}_{-14.9}$	$\cdots$
Transverse component		2.68	$-3.5^{+8.0}_{-6.1}$	$\cdots$

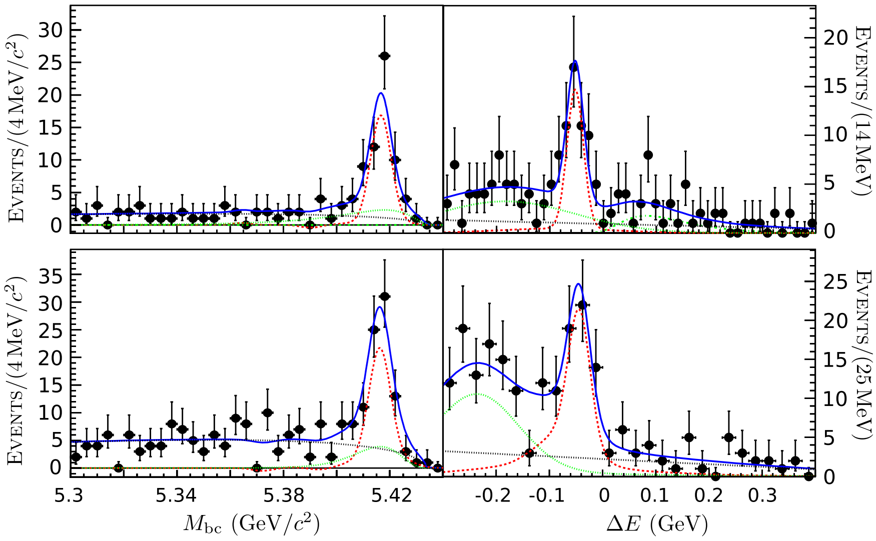

FIG. 1 (color online). Left (right): $M_{\rm bc}$ (ΔE) distributions for the $B_s^0 \to D_s^{*-}\pi^+$ (top) and $B_s^0 \to D_s^-\rho^+$ (bottom) candidates with ΔE ($M_{\rm bc}$) restricted to the $\pm 2.5\sigma$ $B_s^*\bar{B}_s^*$ signal region. The blue solid curve is the total PDF, while the green (black) dotted curve is the peaking (continuum) background and the red dashed curve is the signal. The errors bars correspond to the Poissonian standard deviation.

of $f_L(B_s^0 \to D_s^{*-}\rho^+)$, which lies near the limit of the physically allowed range (0–1).

The dominance of the $\Upsilon(5S) \to B_s^*\bar{B}_s^*$ mode is confirmed. For better precision, we therefore extract the branching fractions (BFs) using only the yields in this mode. Table II shows the values obtained with the relations $\mathcal{B} = N_S/(N_{B_s^0} \times \varepsilon)$, for the $B_s^0 \to D_s^{*-}\pi^+$ and $B_s^0 \to D_s^-\rho^+$ modes. The values for $\mathcal{B}(B_s^0 \to D_s^{*-}\rho^+)$ and $f_L = 1.05^{+0.08}_{-0.10}(\text{stat})^{+0.03}_{-0.04}(\text{syst})$ are obtained by floating these two parameters in a fit where the longitudinal (transverse) yield is replaced by the relation $N_{B_s^0} \times \mathcal{B} \times f_L \times \varepsilon_L$ ($N_{B_s^0} \times \mathcal{B} \times (1 - f_L) \times \varepsilon_T$), with $N_{B_s^0}$, ε_T and ε_L being fixed. Since the transverse yield fluctuated to a negative central value, $f_L > 1$. The corresponding Feldman-Cousins [29] 68% confidence interval is [0.93, 1.00].

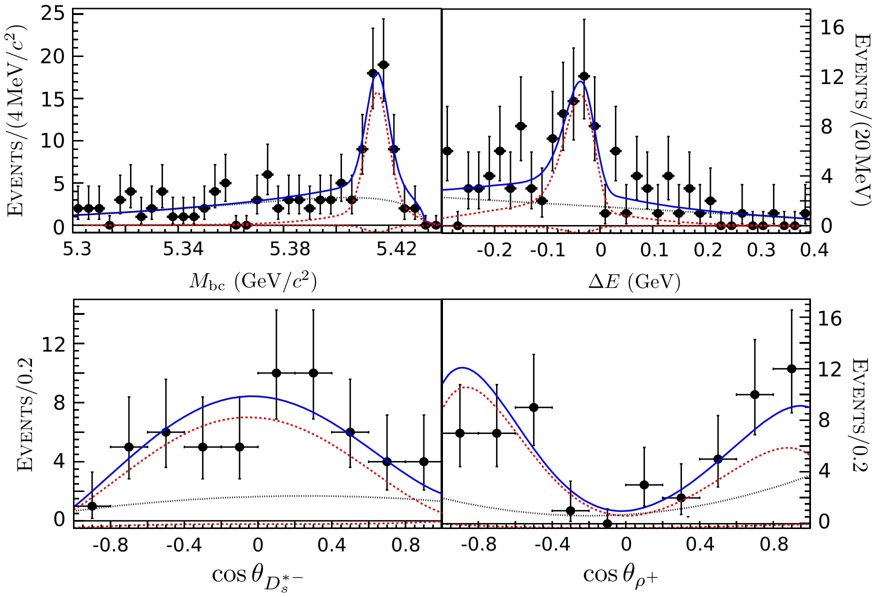

FIG. 2 (color online). Distributions for the $B_s^0 \to D_s^{*-}\rho^+$ candidates. Top: $M_{\rm bc}$ and ΔE distributions, as in Fig. 1. Bottom: helicity distributions of the D_s^{*-} (left) and ρ^+ (right) with $M_{\rm bc}$ and ΔE restricted to the $B_s^*\bar{B}_s^*$ kinematic region. The components of the total PDF (blue solid line) are shown separately: the black dotted curve is the background and the two red dashed curves are the signal. The large (small) signal shape corresponds to the longitudinal (transverse) component.

TABLE II. Top: measured BF values with statistical, systematic (without f_s) and f_s uncertainties, and HQET predictions from the factorization hypothesis [11]. Bottom: BF ratios where several systematic uncertainties cancel out. We use our previous measurement of $\mathcal{B}(B_s^0 \to D_s^- \pi^+)$ [5].

Mode	$\mathcal{B}$ (10^{-3})	HQET (10^{-3})
$B_s^0 \to D_s^{*-}\pi^+$	$2.4^{+0.5}_{-0.4} \pm 0.3 \pm 0.4$	2.8
$B_s^0 \to D_s^- \rho^+$	$8.5^{+1.3}_{-1.2} \pm 1.1 \pm 1.3$	7.5
$B_s^0 \to D_s^{*-}\rho^+$	$11.9^{+2.2}_{-2.0} \pm 1.7 \pm 1.8$	8.9

Ratios
$\mathcal{B}(B_s^0 \to D_s^{*-}\pi^+)/\mathcal{B}(B_s^0 \to D_s^- \pi^+) = 0.65^{+0.15}_{-0.13} \pm 0.07$
$\mathcal{B}(B_s^0 \to D_s^- \rho^+)/\mathcal{B}(B_s^0 \to D_s^- \pi^+) = 2.3 \pm 0.4 \pm 0.2$
$\mathcal{B}(B_s^0 \to D_s^{*-}\rho^+)/\mathcal{B}(B_s^0 \to D_s^- \pi^+) = 3.2 \pm 0.6 \pm 0.3$
$\mathcal{B}(B_s^0 \to D_s^{*-}\rho^+)/\mathcal{B}(B_s^0 \to D_s^- \rho^+) = 1.4 \pm 0.3 \pm 0.1$

The common systematic uncertainties on the BFs are due to the errors on the integrated luminosity (1.3%), $\sigma_{b\bar{b}}^{\Upsilon(5S)}$ (4.6%), f_s (15.0%), $f_{B_s^*\bar{B}_s^*}^*$ (4.3%), the D_s^- BFs (6.4%), the R_2 cut (2.0%), the tracking efficiency (4.0%) and the charged-particle identification (5.4%). In addition, uncertainties due to the MC statistics (1.6%, 2.3%, 1.5%), the neutral-particle identification (8.8%, 5.4%, 8.8%) and the PDF shapes (4.6%, 4.7%, 4.3%) depend on the ($B_s^0 \to D_s^{*-}\pi^+$, $B_s^0 \to D_s^- \rho^+$, $B_s^0 \to D_s^{*-}\rho^+$) mode. The systematic errors on f_L are due to the uncertainties in PDF shapes.

Our values for the BFs are in good agreement with predictions based on HQET and the factorization approximation [11]. The large value of $f_L(B_s^0 \to D_s^{*-}\rho^+)$ is consistent with the value measured for $B^0 \to D^{*-}\rho$ decays [30] and with the predictions of Refs. [9,31].

In summary, we report the first observation of three CKM-favored exclusive B_s^0 decay modes, we extract their branching fractions, and, for $B_s^0 \to D_s^{*-}\rho^+$, we measure the longitudinal polarization fraction. Our results are consistent with theoretical predictions based on HQET [11] and are similar to analogous B^0 decay branching fractions. The dominance of the unexpectedly large $\Upsilon(5S) \to B_s^*\bar{B}_s^*$ mode [5] is confirmed.

We thank the KEKB group for excellent operation of the accelerator, the KEK cryogenics group for efficient solenoid operations, and the KEK computer group and the NII for valuable computing and SINET3 network support. We acknowledge support from MEXT, JSPS and Nagoya's TLPRC (Japan); ARC and DIISR (Australia); NSFC (China); MSMT (Czechia); DST (India); MEST, NRF, NSDC of KISTI, and WCU (Korea); MNiSW (Poland); MES and RFAAE (Russia); ARRS (Slovenia); SNSF (Switzerland); NSC and MOE (Taiwan); and DOE (USA).

[1] Unless specified otherwise, charge-conjugated modes are implied throughout.
[2] A. Drutskoy *et al.* (Belle Collaboration), Phys. Rev. Lett. **98**, 052001 (2007).
[3] A. Drutskoy *et al.* (Belle Collaboration), Phys. Rev. D **76**, 012002 (2007).
[4] J. Wicht *et al.* (Belle Collaboration), Phys. Rev. Lett. **100**, 121801 (2008).
[5] R. Louvot *et al.* (Belle Collaboration), Phys. Rev. Lett. **102**, 021801 (2009).
[6] L. Wolfenstein, Phys. Rev. Lett. **51**, 1945 (1983).
[7] M. Kobayashi and T. Maskawa, Prog. Theor. Phys. **49**, 652 (1973); N. Cabibbo, Phys. Rev. Lett. **10**, 531 (1963).
[8] N. A. Törnqvist, Phys. Rev. Lett. **53**, 878 (1984).
[9] J. L. Rosner, Phys. Rev. D **42**, 3732 (1990).
[10] B. Block and M. Shifman, Nucl. Phys. B **389**, 534 (1993).
[11] A. Deandrea *et al.*, Phys. Lett. B **318**, 549 (1993).
[12] T. Mannel, W. Roberts, and Z. Ryzak, Phys. Lett. B **259**, 359 (1991).
[13] W. A. Bardeen, E. J. Eichten, and C. T. Hill, Phys. Rev. D **68**, 054024 (2003).
[14] J. G. Körner and G. R. Goldstein, Phys. Lett. B **89**, 105 (1979).
[15] S. Kurokawa and E. Kikutani, Nucl. Instrum. Methods Phys. Res., Sect. A **499**, 1 (2003), and other articles included in this volume.
[16] G. S. Huang *et al.* (CLEO Collaboration), Phys. Rev. D **75**, 012002 (2007).
[17] C. Amsler *et al.* (Particle Data Group), Phys. Lett. B **667**, 1 (2008).
[18] A. Abashian *et al.* (Belle Collaboration), Nucl. Instrum. Methods Phys. Res., Sect. A **479**, 117 (2002).
[19] F. Fang, Ph.D. thesis, University of Hawaii, 2003.
[20] D. J. Lange, Nucl. Instrum. Methods Phys. Res., Sect. A **462**, 152 (2001).
[21] CERN Application Software Group, CERN Program Library Report No. W5013, 1993.
[22] M. Pivk and F. R. Le Diberder, Nucl. Instrum. Methods Phys. Res., Sect. A **555**, 356 (2005).
[23] M. S. Alam *et al.* (CLEO Collaboration), Phys. Rev. D **50**, 43 (1994).
[24] G. C. Fox and S. Wolfram, Phys. Rev. Lett. **41**, 1581 (1978).
[25] R. Barlow, Nucl. Instrum. Methods Phys. Res., Sect. A **297**, 496 (1990).
[26] The Novosibirsk function is defined as $f(x) = \exp[-\frac{1}{2} \times (\ln^2\{1 + \Lambda(x - x_0)\}/\tau^2 + \tau^2)]$ with $\Lambda = \sinh(\tau\sqrt{\ln 4})/(\sigma\sqrt{\ln 4})$. The parameters represent the mean (x_0), the width (σ) and the tail asymmetry (τ).
[27] See Table I of Ref. [5] for the detailed parameterization.
[28] H. Albrecht *et al.* (ARGUS Collaboration), Phys. Lett. B **185**, 218 (1987).
[29] G. J. Feldman and R. D. Cousins, Phys. Rev. D **57**, 3873 (1998).
[30] S. E. Csorna *et al.* (CLEO Collaboration), Phys. Rev. D **67**, 112002 (2003).
[31] A. Ali *et al.*, Z. Phys. C **1**, 269 (1979).

Bibliography

[1] A. Abashian *et al.* (Belle Collaboration), "The Belle Detector," *Nucl. Instrum. Methods Phys. Res., Sect. A* **479**, 117 (2002).

[2] S. Kurokawa and E. Kikutani, "Overview of the KEKB accelerators," *Nucl. Instrum. Methods Phys. Res., Sect. A* **499**, 1 (2003).

[3] A. Drutskoy *et al.* (Belle Collaboration), "Measurement of Inclusive D_s, D^0, and J/ψ Rates and Determination of the $B_s^{(*)}\bar{B}_s^{(*)}$ Production Fraction in $b\bar{b}$ Events at the $\Upsilon(5S)$ Resonance," *Phys. Rev. Lett.* **98**, 052001 (2007).

[4] A. Drutskoy *et al.* (Belle Collaboration), "Measurements of Exclusive B_s^0 decays at the $\Upsilon(5S)$ Resonance," *Phys. Rev. D* **76**, 012002 (2007).

[5] R. Fleischer, N. Serra and N. Tuning, "New Strategy for B_s Branching Ratio Measurements and the Search for new Physics in $B_s^0 \to \mu^+\mu^-$," *Phys. Rev. D* **82**, 034038 (2010).

[6] O. Schneider and F. Teubert, "A Possible Contribution from Belle to Search for New Physics in $B_s^0 \to \mu^+\mu^-$?" unpublished (2008). Available at http://kds.kek.jp/getFile.py/access? contribId=19& resId=0& materialId=0& confId=2099.

[7] R. Aleksan, I. Dunietz and B. Kayser, "Determining the CP-violating phase γ," *Z. Phys. C* **54**, 653 (1992).

[8] R. Louvot, J. Wicht and T. Aushev, "Study of the Decay $B_s \to D_s\pi$ and Search for $B_s \to D_sK$ at the $\Upsilon(5S)$," Belle Note #1036, unpublished (2008).

[9] R. Louvot, "Study of the Decays $B_s^0 \to D_s^{*-}\pi^+$ and $B_s^0 \to D_s^{(*)-}\rho^+$ at the $\Upsilon(5S)$," Belle Note #1104v1.0, unpublished (2009).

[10] R. Louvot *et al.* (Belle Collaboration), "Measurement of the Decay $B_s^0 \to D_s^-\pi^+$ and Evidence for $B_s^0 \to D_s^{\mp}K^{\pm}$ in e^+e^- Annihilation at $\sqrt{s} \approx 10.87$ GeV," *Phys. Rev. Lett.* **102**, 021801 (2009), reproduced in Appendix C.

[11] R. Louvot *et al.* (Belle Collaboration), "Observation of $B_s^0 \to D_s^{*-}\pi^+$ and $B_s^0 \to D_s^{(*)-}\rho^+$ and Measurement of the $B_s^0 \to D_s^{*-}\rho+$ Longitudinal Polarization Fraction," *Phys. Rev. Lett.* **104**, 231801 (2010), reproduced in Appendix C.

[12] D. Asner *et al.* (Heavy Flavor Averaging Group), "Averages of b-hadron, c-hadron, and τ-lepton Properties," arXiv:1010.1589v2 [hep-ex] (2010).

[13] R. Sia and S. Stone, "Model independent methods for determining $\mathcal{B}(\Upsilon(5S) \to B_s^{(*)}\bar{B}_s^{(*)})$," *Phys. Rev. D* **74**, 031501 (2006), Erratum *ibid.* **80**, 039901 (2009).

[14] R. Louvot, O. Schneider and T. Aushev, "Prospects for Precise Measurement of B_s^0 Branching Fractions," Belle Note #1140, unpublished (2010); available at `http://lphe.epfl.ch/louvot/bnote_1140.pdf`.

[15] R. Louvot, "Simulation and Measurement of Same- and Opposite-sign Dilepton at the $\Upsilon(5S)$," Belle Note #1174, unpublished (2010).

[16] S. Weinberg, "A Model of Leptons," *Phys. Rev. Lett.* **19**, 1264 (1967).

[17] S.L. Glashow, "Partial-symmetries of Weak Interactions," *Nucl. Phys.* **22**, 579 (1961).

[18] A. Salam *in* N. Svartholm, *Elementary Particle Theory* (Almqvist & Wiksell, Stockholm, 1968).

[19] M. Gell-Mann, "A Schematic Model of Baryons and Mesons," *Phys. Lett.* **8**, 214 (1964).

[20] G. Zweig, CERN Report 8419/TH.412 (1964) *in* D.B. Lichtenberg and S.P. Rosen "Developments in the Quark Theory of Hadrons, A Reprint Collection, Vol. I: 1964–1978", Hadronic Press (Mass.), 1980.

[21] P. Langacker, *The Standard Model and Beyond* (CRC Press, 2009).

[22] J.-P. Derendinger, *Théorie Quantique des Champs* (PPUR, Lausanne (in French), 2008).

[23] D. Griffiths, *Introduction to Elementary Particles* (Wiley, 2008).

[24] I.I. Bigi and A.I. Sanda, *CP violation* (Cambridge university press, Cambridge, 2009).

[25] G.C. Branco, L. Lavoura and J.P. Silva, *CP violation* (Clarendon Press, Oxford, 1999).

[26] E. Neother, "Invariante Variationsprobleme," *Nachr. d. König. Gesellsch. d. Wiss. zu Göttingen, Math-phys. Klasse* **1918**, 235 (1918), English translation: arXiv:physics/0503066v1 [physics.hist-ph] (2005.

[27] T.D. Lee and C.N. Yang, "Question of Parity Conservation in Weak Interactions," *Phys. Rev.* **104**, 254 (1956).

[28] C.S. Wu *et al.*, "Experimental Test of Parity Conservation in Beta Decay," *Phys. Rev.* **105**, 1413 (1957).

[29] B.L. Ioffe, L.B. Okun and A.P. Rudik, "The Problem of Parity Non-conservation in Weak Interactions," *Sov. Phys. JETP* **5**, 328 (1957).

[30] T.D. Lee, R. Oehme and C.N. Yang, "Remarks on Possible Noninvariance under Time Reversal and Charge Conjugation," *Phys. Rev.* **106**, 340 (1957).

[31] R.L. Garwin, L.M. Lederman and M. Weinrich, "Observation of the Failure of Conservation of Parity and Charge Conjugation in Meson Decay: the Magnetic Moment of the Free Muon," *Phys. Rev.* **105**, 1415 (1957).

[32] J.H. Christenson *et al.*, "Evidence for the 2π Decay of the K_2^0 Meson," *Phys. Rev. Lett.* **13**, 138 (1964).

[33] J. Schwinger, "The Theory of Quantized Fields. I," *Phys. Rev.* **82**, 914 (1951).

[34] A. Angelopoulos *et al.* (CPLEAR Collaboration), "First Direct Observation of Time-reversal Non-invariance in the Neutral-kaon System," *Phys. Lett. B* **444**, 43 (1998).

[35] A.D. Sakharov, "Violation of CP Invariance, C Asymmetry, and Baryon Asymmetry of the Universe," *Pis'ma Zh. Eksp. Teor. Fiz.* **5**, 32 (1967), [*JETP Lett.* **5**, 24 (1967)]; Reprint in *Sov. Phys. Ups.* **34**, 392 (1991).

[36] C. Jarlskog and E. Shabalin, "On Searches for CP, T, CPT and C Violation in Flavour-Changing and Flavour-Conserving Interactions," *Phys. Scripta T* **99**, 23 (2002).

[37] K. Nakamura *et al.* (Particle Data Group), "Review of Particle Physics," *J. Phys. G* **37**, 075021 (2010), and 2011 web update.

[38] M. Bander, "Theory of Quark Confinement," *Phys. Rep.* **75**, 205 (1981).

[39] E. Fermi, "Versuch einer Theorie der β-Strahlen. I," *Z. Phys.* **88**, 161 (1934), (in German). Translated in F.L. Wilson, "Fermi's Theory of β Decay", *Am. J. Phys.* **36**, 1150 (1968).

[40] R.P. Feynman and M. Gell-Mann, "Theory of Fermi Interaction," *Phys. Rev.* **109**, 193 (1958).

[41] J.J. Sakurai, "Mass Reversal and weak Interactions," *Nuov. Cim.* **7**, 649 (1958).

[42] M. Gell-Mann, "The Interpretation of the New Particles as Displaced Charge Multiplets," *Nuov. Cim.* **4**, 848 (1956).

[43] K. Nishijima, "Charged Independence of Theory of V Particles," *Prog. Theor. Phys.* **13**, 285 (1955).

[44] C. Kiefer, "Quantum Gravity: General Introduction and Recent Developments," *Ann. Phys. (Leipzig)* **15**, 129 (2006).

[45] A. Adhtekar, "The Winding Road to Quantum Gravity," *Current Sci.* **89**, 2064 (2005).

[46] J.W. Rohlf, *Modern Physics from α to Z^0* (Wiley cop., New York, 1994).

[47] P.A.M. Dirac, "The Quantum Theorie of the Electron," *Proc. Roy. Soc. Lond. A* **117**, 610 (1928).

[48] M. Sher, "Electroweak Higgs Potential and Vacuum Stability," *Phys. Rep.* **179**, 273 (1989).

[49] J. Goldstone, A. Salam and S. Weinberg, "Broken Symmetries," *Phys. Rev.* **127**, 965 (1962).

[50] H. Yukawa, "Models and Methods in the Meson Theory," *Rev. Mod. Phys.* **21**, 474 (1949).

[51] S. Schael *et al.* (ALEPH, DELPHI, L3, OPAL, SLD Collaborations and LEP EW, SLD EW-HF Working Groups), "Precision Electroweak Measurements on the Z Resonance," *Phys. Rep.* **427**, 257 (2006), Updates available at `http://lepewwg.web.cern.ch`.

[52] J.L. Lagrange, *Mécanique Analytique* (Jean Gaby, Sceaux (in French), 1989) Reprint of *Méchanique Analitique* par M. de la Grange, Veuve Desaint, Paris (1788).

[53] A. Einstein, "Die Grundlage der allgemeinen Relativitätstheorie," *Ann. d. Phys.* **354**, 769 (1916), in German, English transl. in Ref. [228].

[54] C.N. Yang and R.L. Mills, "Conservation of Isotopic Spin and Isotopic Gauge Invariance," *Phys. Rev.* **96**, 191 (1954).

[55] M. Kobayashi and T. Maskawa, "CP-violation in the Renormalizable Theory of Weak Interaction," *Prog. Theor. Phys.* **49**, 652 (1973).

[56] L.L. Chau and W.Y. Keung, "Comments on the Parametrization of the Kobayashi-Maskawa Matrix," *Phys. Rev. Lett.* **53**, 1802 (1984).

[57] M. Bona *et al.*, "The 2004 UTfit collaboration report on the status of the unitarity triangle in the standard model," *J. High Energy Phys.* **7**, 28 (2005), updated results for summer 2010, available at `http://www.utfit.org`.

[58] J. Charles *et al.* (CKMfitter Group), "CP violation and the CKM matrix: assessing the impact of the asymmetric B factories," *Eur. Phys. J. C* **41**, 1 (2005), updated results for summer 2010, available at `http://ckmfitter.in2p3.fr`.

[59] N. Cabibbo, "Unitary Symmetry and Leptonic Decays," *Phys. Rev. Lett.* **10**, 531 (1963).

[60] L. Wolfenstein, "Parametrization of the Kobayashi-Maskawa Matrix," *Phys. Rev. Lett.* **51**, 1945 (1983).

[61] F. De Bernardis *et al.*, "Improved Limit on the Neutrino Mass with CMB and Redshift-dependent Halo Bias-mass Relations from SDSS, DEEP2, and Lyman-break Galaxies," *Phys. Rev. D* **78**, 083535 (2008).

[62] M. Antonelli *et al.*, "Flavor Physics in the Quark Sector," *Phys. Rep.* **494**, 197 (2010).

[63] T. Aaltonen *et al.* (CDF Collaboration), "First Flavor-Tagged Determination of Bounds on Mixing-Induced CP Violation in $B_s^0 \to J/\psi\phi$ Decays," *Phys. Rev. Lett.* **100**, 161802 (2008).

[64] V.M. Abazov *et al.* (D0 Collaboration), "Measurement of B_s^0 Mixing Parameter from the Flavor-Tagged Decay $B_s^0 \to J/\psi\phi$," *Phys. Rev. Lett.* **101**, 241801 (2008).

[65] C. Jarlskog, "Commutator of the Quark Mass Matrix in the Standard Model Electroweak Model and a Measure of Maximal CP Nonconservation," *Phys. Rev. Lett.* **55**, 1039 (1985).

[66] C. Jarlskog, "A Basis Independent Formulation of the Connection Between Quark Mass Matrix, CP Violation and Experiment," *Z. Phys. C* **29**, 491 (1985).

[67] C. Jarlskog and R. Story, "Unitary Polygons and CP Violation Areas and Phases in the Standard Electroweak Model," *Phys. Lett. B* **208**, 268 (1988).

[68] A.G. Grozin, *Heavy Quark Effective Theory* (Springer, 2004).

[69] M. Neubert, "Heavy-quark Symmetry," *Phys. Rep.* **245**, 259 (1994).

[70] J.C. Collins and D.E. Soper, "The Theorems of Perturbative QCD," *Ann. Rev. Nucl. Part. Sci.* **37** (1987).

[71] R. Fleischer, N. Serra and N. Tuning, "Tests of Factorization and $SU(3)$ Relations in B Decays into Heavy-light Final States," *Phys. Rev. D* **83**, 014017 (2011).

[72] B. Block and M. Shifman, "Nonfactorizable Amplitudes in Weak Nonleptonic Decays of Heavy Mesons," *Nucl. Phys. B* **389**, 534 (1993).

[73] A.M. Badalian, B.L.G. Bakker and I.V. Danilkin, "Hyperfine Splittings in Bottomonium and the $B_q(q = n, s, c)$ Mesons," *Phys. Rev. D* **81**, 071502 (2010), Erratum *ibid.* **81**, 099902 (2010).

[74] E. Eichten *et al.*, "Charmonium: Comparison with Experiment," *Phys. Rev. D* **21**, 203 (1980).

[75] M. Di Pierro and E. Eichten, "Excited Heavy-light Systems and Hadronic Transitions," *Phys. Rev. D* **64**, 114004 (2001).

[76] I. Peruzzi *et al.*, "Observation of a Narrow Charged State at 1876 MeV/c^2 Decaying to an Exotic Combination of $K\pi\pi$," *Phys. Rev. Lett.* **37**, 569 (1976).

[77] G. Goldhaber *et al.*, "Observation in e^+e^- Annihilation of a Narrow State at 1865 MeV/c^2 Decaying to $K\pi$ and $K\pi\pi\pi$," *Phys. Rev. Lett.* **37**, 255 (1976).

[78] R. Brandelik *et al.* (DASP Collaboration), "Production Characteristics of the F Meson," *Phys. Lett. B* **80**, 412 (1979).

[79] C. Bebek *et al.*, “Evidence for New-Flavor Production at the $\Upsilon(4S)$,” *Phys. Rev. Lett.* **46**, 84 (1981).

[80] K. Chadwick *et al.*, “Decay of b-Flavored Hadrons to Single-Muon and Dimuon Final States,” *Phys. Rev. Lett.* **46**, 88 (1981).

[81] S. Behrends *et al.*, “Observation of Exclusive Decay Modes of b-Flavored Mesons,” *Phys. Rev. Lett.* **50**, 881 (1983).

[82] K. Han *et al.*, “Observation of B^* Production in e^+e^- Interactions above the b-Flavor Threshold,” *Phys. Rev. Lett.* **55**, 36 (1985).

[83] J. Lee-Franzini *et al.* (CUSB Collaboration), “Hyperfine splitting of B mesons and B_s^0 production at the $\Upsilon(5S)$,” *Phys. Rev. Lett.* **65**, 2947 (1990).

[84] B. Aubert *et al.* (BaBar Collaboration), “Dalitz plot analysis of $B^- \to D^+\pi^-\pi^-$,” *Phys. Rev. D* **79**, 112004 (2009).

[85] K. Abe *et al.* (Belle Collaboration), “Study of $B^- \to D^{**0}\pi^-(D^{**0} \to D^{(*)+}\pi^-)$ Decays,” *Phys. Rev. D* **69**, 112002 (2004).

[86] J.M. Link *et al.* (FOCUS Collaboration), “Measurement of Masses and Widths of Excited Charm Mesons D_2^* and Evidence for Broad States,” *Phys. Lett. B* **586**, 11 (2004).

[87] A. Kuzmin *et al.* (Belle Collaboration), “Study of $\bar{B}^0 \to D^0\pi^+\pi^-$ Decays,” *Phys. Rev. D* **76**, 012006 (2007).

[88] K. Abe *et al.* (Belle Collaboration), “Observation of the $D_1(2420) \to D\pi^+\pi^-$ Decays,” *Phys. Rev. Lett.* **94**, 221805 (2005).

[89] P. Abreu *et al.* (DELPHI Collaboration), “First Evidence for a Charm Radical Excitation, $D^{*'}$,” *Phys. Lett. B* **426**, 231 (1998).

[90] T. Aaltonen *et al.* (CDF Collaboration), “Measurement of Resonance Parameters of Orbitally Excited Narrow B^0 Mesons,” *Phys. Rev. Lett.* **102**, 102003 (2009).

[91] V.M. Abazov *et al.* (D0 Collaboration), “Properties of $L = 1$ B_1 and B_2^* Mesons,” *Phys. Rev. Lett.* **99**, 172001 (2007).

[92] V.M. Abazov *et al.* (D0 Collaboration), “Observation and Properties of the Orbitally Excited B_{s2}^* Meson,” *Phys. Rev. Lett.* **100**, 082002 (2008).

[93] T. Aaltonen *et al.* (CDF Collaboration), “Observation of Orbitally Excited B_s Mesons,” *Phys. Rev. Lett.* **100**, 082001 (2008).

[94] V. Weisskopf and E. Wigner, “Berechnung der natürlichen Linienbreite auf Grund der Diracschen Lichttheorie,” *Z. Phys.* **63**, 54 (1930), in German.

[95] V. Weisskopf and E. Wigner, “Über die natürliche Linienbreite in der Strahlung des harmonischen Oszillators,” *Z. Phys.* **65**, 18 (1930), in German.

[96] S.W. Lin *et al.* (Belle Collaboration), "Difference in Direct Charge-parity Violation between Charged and Neutral B Meson Decays," *Nature (London)* **452**, 332 (2008).

[97] B. Aubert *et al.* (BaBar Collaboration), "Observation of CP Violation in $B^0 \to K^-\pi^+$ and $B^0 \to \pi^+\pi^-$," *Phys. Rev. Lett.* **99**, 021603 (2007).

[98] H. Ishino *et al.* (Belle Collaboration), "Observation of Direct CP Violation in $B^0 \to \pi^+\pi^-$ Decays and Model-Independent Constraints on the Quark-Mixing Angle ϕ_2," *Phys. Rev. Lett.* **98**, 211801 (2007).

[99] A. Giri *et al.*, "Determining γ Using $B^\pm \to DK^\pm$ with Multibody D Decays," *Phys. Rev. D* **68**, 054018 (2003).

[100] R.H. Dalitz, "On the Analysis of τ-meson data and the Nature of the τ-meson," *Philos. Mag.* **44**, 1068 (1953).

[101] D. Atwood, I. Dunietz and A. Soni, "Enhanced CP Violation with $B \to KD^0(\bar{D}^0)$ Modes and Extraction of the Cabibbo-Kobayashi-Maskawa Angle γ," *Phys. Rev. Lett.* **78** (1997).

[102] D. Atwood, I. Dunietz and A. Soni, "Improved Method for Observing CP Violation in $B^\pm \to KD$ and Measuring the CKM phase γ," *Phys. Rev. D* **63**, 036005 (2001).

[103] M. Gronau and D. Wyler, "On Determining a Weak Phase from Charged B Decay Asymmetries," *Phys. Lett. B* **265**, 483 (1991).

[104] M. Gronau and D. London, "How to Determine all the Angles of the Unitary Triangle from $B_d \to DK_S$ and $B_s^0 \to D\phi$," *Phys. Lett. B* **253**, 483 (1991).

[105] R. Fleicher, "New Strategies to Obtain Insights into CP Violation through $B_s \to D_s^\pm K^\mp, D_s^{*\pm} K^\mp, \ldots$ and $B_d \to D^\pm \pi^\mp, D^{*\pm}\pi^\mp, \ldots$ Decays," *Nucl. Phys. B* **671**, 459 (2003).

[106] M. Artuso, E. Barberio and S. Stone, "B Meson Decays," *PMC phys. A* **3**, 3 (2009).

[107] K.F. Chen *et al.* (Belle Collaboration), "Observation of Time-Dependent CP Violation in $B^0 \to \eta' K^0$ Decays and Improved Measurement of CP Asymmetries in $B^0 \to \phi K^0$, $K_S^0 K_S^0 K_S^0$ and $B^0 \to J/\psi K^0$ Decays," *Phys. Rev. Lett.* **98**, 031802 (2007).

[108] B. Aubert *et al.* (BaBar Collaboration), "Measurement of the CP Asymmetry Amplitude $\sin 2\beta$ with B^0 Mesons," *Phys. Rev. Lett.* **89**, 201802 (2002).

[109] K. Abe *et al.* (Belle Collaboration), "Improved Measurement of Mixing-induced CP Violation in the Neutral B Meson System," *Phys. Rev. D* **66**, 071102 (2002).

[110] A.J. Bevan *et al.* (UTfit Collaboration), "Update of the Unitary Triangle Analysis," *Proceedings of Science*, POS(ICHEP 2010)270 (2010), arXiv:1010.5089v1 [hep-ph].

[111] K. Hara *et al.* (Belle Collaboration), "Evidence for $B^- \to \tau^-\bar{\nu}_\tau$ with a Semileptonic Tagging Method," *Phys. Rev. D* **82**, 071101 (2010).

[112] B. Aubert *et al.* (BaBar Collaboration), "Search for $B^+ \to \tau^+\nu_\tau$ Decays with Hadronic B Tag," *Phys. Rev. D* **77**, 011107 (2008).

[113] B. Aubert *et al.* (BaBar Collaboration), "Search for $B^+ \to l^+\nu_l$ Recoiling against $B^- \to D^0 l^- \bar{\nu}_l X$," *Phys. Rev. D* **81**, 051101 (2010).

[114] V.M. Abazov *et al.* (D0 Collaboration), "Evidence for an Anomalous Like-sign Dimuon Charge Asymmetry," *Phys. Rev. Lett.* **105**, 081801 (2010), *id.*, *Phys. Rev. D* **82**, 032001 (2010).

[115] T. Aaltonen *et al.* (CDF Collaboration), "Invariant Mass Distribution of Jet Pairs Produced in Association with a W Boson in $p\bar{p}$ Collisions at $\sqrt{s} = 1.96$ TeV," *Phys. Rev. Lett.* **106**, 171801 (2011), and update at `http://www-cdf.fnal.gov/physics/ewk/2011/wjj/7_3.html`.

[116] V.M. Abazov *et al.* (D0 Collaboration), "Bounds on an Anomalous Dijet Resonance in W + Jets Production in $p\bar{p}$ Collisions at $\sqrt{s} = 1.96$ TeV," *Phys. Rev. Lett.* **107**, 011804 (2011).

[117] A. Nisati and V. Sharma, "Higgs searches at ATLAS and CMS," (2011), Talks at the XXV international symposium on lepton photon interactions at high energies, Mumbai, India, 22-27 August 2011.

[118] Y. Fukuda *et al.* (Super-Kamiokande Collaboration), "Evidence for Oscillation of Atmospheric Neutrinos," *Phys. Rev. Lett.* **81**, 1562 (1998).

[119] T. Kajita, "Discovery of Neutrino Oscillations," *Rep. Prog. Phys.* **69**, 1607 (2006).

[120] Z. Maki, M. Nakagawa and S. Sakata, "Remarks on the Unified Model of Elementary Particles," *Prog. Theor. Phys.* **28**, 870 (1962).

[121] J. Dunkley *et al.*, "The Atacama Cosmology Telescope: Cosmological Parameters from the 2008 Power Spectra," arXiv:1009.0866v1 [astro-ph.CO] (2010).

[122] W.S. Hou, "Source of CP Violation for the Baryon Asymmetry of the Universe," *Chin. J. Phys.* **47**, 134 (2009).

[123] M.E. Peskin, "Song of the Electroweak Penguin," *Nature (London)* **452**, 293 (2008).

[124] E. Lunghi and A. Soni, "Possible Evidence for the Breakdown of the CKM-paradigm of CP-violation," *Phys. Lett. B* **697**, 323 (2011).

[125] D.N. Spergel *et al.*, "Three-Year *Wilkinson Microwave Anisotropy Probe (WMAP)* Observations: Implication for Cosmology," *Astrophys. J. Suppl. Ser.* **170**, 377 (2007).

[126] J.E. Kim and G. Carosi, "Axions and the Strong CP Problem," *Rev. Mod. Phys.* **82**, 557 (2010).

[127] R.D. Peccei and H.R. Quinn, "CP Conservation in the Presence of Pseudoparticles," *Phys. Rev. Lett.* **38**, 1440 (1977).

[128] S. Nandi and A. Soni, "Constraining the Mixing Matrix for Standard Model with Four Generations: Time Dependent and Semi-leptonic CP Asymmetries in B_d^0, B_s and D^0," arXiv:1011.6091v2 [hep-ph] (2010).

[129] E. Lunghi and A. Soni, "Demise of CKM and its Aftermath," arXiv:1104.2117v1 [hep-ph] (2011), talk presented at Moriond EW 2011.

[130] N. Arkani-Hamed, S. Dimopoulos and G. Dvali, "The Hierarchy Problem and New Dimensions at a Millimeter," *Phys. Lett. B* **429**, 263 (1998).

[131] L. Randall and R. Sundrum, "Large Mass Hierarchy from a Small Extra Dimension," *Phys. Rev. Lett.* **83**, 3370 (1999).

[132] L. Randall and R. Sundrum, "An Alternative to Compactification," *Phys. Rev. Lett.* **83**, 4690 (1999).

[133] M. Bauer *et al.*, "Flavor Physics in the Randall-Sundrum Model: II. Tree-level Weak-interaction Processes," *J. High Energy Phys.* **09(2010)**, 017 (2010).

[134] J. Ellis *et al.*, "Supersymmetric Relics from the Big Bang," *Nucl. Phys. B* **238**, 453 (1984).

[135] J. Ellis *et al.*, "Supersymmetric Dark Matter in Light of WMAP," *Phys. Lett. B* **565**, 176 (2003).

[136] S.L. Glashow, "Towards a Unified Theory: Threads in a Tapestry," *Rev. Mod. Phys.* **52**, 539 (1980).

[137] J. Ellis, "Searching for Particle Physics Beyond the Standard Model at the LHC and Elsewhere," arXiv:1102.5009v1 [hep-ph] (2011).

[138] T.E. Browder *et al.*, "New Physics at a Super Flavor Factory," *Rev. Mod. Phys.* **81**, 1887 (2009).

[139] G. Finocchiaro, "The Super$B$ Project," *Proceedings of Science*, POS(HQL 2010)080 (2010), arXiv:1012.2449v1 [hep-ex].

[140] A. Lenz *et al.* (CKMfitter Group), "Anatomy of New Physics in $B-\bar{B}$ Mixing," *Phys. Rev. D* **83**, 036004 (2011).

[141] I. Dunietz, R. Fleischer and U. Nierste, "In Pursuit of New Physics with B_s Decays," *Phys. Rev. D* **63**, 114015 (2001).

[142] G. Herten, "The First Year of the Large Hadron Collider: A Brief Review," *Mod. Phys. Lett. A* **26**, 843 (2011).

[143] T. Abe *et al.*, "Compensation of the Crossing Angle with Crab Cavities at KEKB," Proceedings of the 22nd Particle Accelerator Conference, Albuquerque, USA (June 2007); arXiv:0706.3248v1 [hep-ex] (2007).

[144] Y. Ushiroda, "Belle Silicon Vertex Detectors," *Nucl. Instrum. Methods Phys. Res., Sect. A* **511**, 6 (2003).

[145] T. Ziegler, "The Belle Silicon Vertex Detector Trigger," *Nucl. Instrum. Methods Phys. Res., Sect. A* **511**, 153 (2003).

[146] Z. Natkaniec *et al.*, "Status of the Belle Silicon Vertex Detector," *Nucl. Instrum. Methods Phys. Res., Sect. A* **560**, 1 (2006).

[147] M. Nakano *et al.* (Belle Collaboration), "Measurement of the $B \to K^*\gamma$ Branching Fractions and Asymmetries," *Phys. Rev. D* **69**, 112001 (2004).

[148] Y. Chao *et al.* (Belle Collaboration), "Observation of $B^0 \to \pi^0\pi^0$," *Phys. Rev. Lett.* **94**, 181803 (2005).

[149] B. Casey, "HadronB," Belle Note #390, unpublished (2001).

[150] V. Zhilich *et al.*, "Offline Luminosity Measurements from the Belle Detector," Belle Note #453v2.2, unpublished (2001), and Belle luminosity webpage.

[151] K.F. Chen *et al.* (Belle Collaboration), "Observation of Anomalous $\Upsilon(1S)\pi^+\pi^-$ and $\Upsilon(2S)\pi^+\pi^-$ Production near the $\Upsilon(5S)$ Resonance," *Phys. Rev. Lett.* **100**, 112001 (2008).

[152] K.F. Chen, "Observation of $\Upsilon(1S)\pi^+\pi^-$ and $\Upsilon(2S)\pi^+\pi^-$ States in e^+e^- Annihilation at $\sqrt{s} \sim 10.87$ GeV," Belle Note #1030, unpublished (2008).

[153] G.C. Fox and S. Wolfram, "Observables for the Analysis of Event Shapes in e^+e^- Annihilation and Other Processes," *Phys. Rev. Lett.* **41**, 1581 (1978).

[154] H. Hamasaki *et al.* (Belle KID group), "Kaon identification in belle," *Belle Note #321, unpublished* (2000).

[155] K. Hanagaki *et al.*, "Electron Identification in Belle," *Nucl. Instrum. Methods Phys. Res., Sect. A* **485**, 490 (2002).

[156] A. Abashian *et al.*, "Muon Identification in the Belle Experiment at KEKB," *Nucl. Instrum. Methods Phys. Res., Sect. A* **491**, 69 (2002).

[157] S. Nishida, "Study of Kaon and Pion Identification Using Inclusive D^* Sample," Belle Note #779v0.3, unpublished (2005).

[158] L. Hinz *et al.*, "Lepton Efficiency and Systematic Error for Experiments 21 to 27," Belle Note #777, unpublished (2004.

[159] L. Hinz, "Lepton ID Efficiency Correction and Systematic Error," Belle Note #954, unpublished (2006).

[160] C. Park, "New Corrections of Energy and Angles of Photons," Belle Note #469, unpublished (2001).

[161] H.W. Kim *et al.*, "Photon Detection Efficiency Using Radiative Bhabha Sample," Belle Note #499v0.1, unpublished (2002).

[162] S.W. Lin, P. Chang and H.C. Huang, "Update of π^0 Systematics Using Inclusive η (78/fb)," Belle Note #645, unpublished (2003).

[163] J.M. Torres-Rincon and F.J. Llanes-Estrada, "Heavy Quark Fluorescence," *Phys. Rev. Lett.* **105**, 022003 (2010).

[164] B. Aubert *et al.* (BaBar Collaboration), "Measurement of the $e^+e^- \to b\bar{b}$ Cross Section between $\sqrt{s} = 10.54$ and 11.20 GeV," *Phys. Rev. Lett.* **102**, 012001 (2009).

[165] G.S. Huang *et al.* (CLEO Collaboration), "Measurement of $\mathcal{B}(\Upsilon(5S) \to B_s^{(*)}\bar{B}_s^{(*)})$ using ϕ Mesons," *Phys. Rev. D* **75**, 012002 (2007).

[166] A. Drutskoy *et al.* (Belle Collaboration), "Measurement of $\Upsilon(5S)$ Decays to B^0 and B^+ Mesons," *Phys. Rev. D* **81**, 112003 (2010).

[167] Y.A. Simonov and A.I. Veselov, "Bottomonium $\Upsilon(5S)$ Decays into BB and $BB\pi$," *JETP Lett.* **88**, 7 (2008).

[168] A. Ali, "Theory Overview on Spectroscopy," Talk presented at the 13th international conference on B-physics at hadron machines, April 2011, Amsterdam; arXiv:1108.2197v1 [hep-ph].

[169] A. Ali *et al.*, "A Case for Hidden $b\bar{b}$ Tetraquarks Based on $e^+e^- \to b\bar{b}$ Cross Section Between $\sqrt{s} = 10.54$ and 11.20 GeV," *Phys. Lett. B* **684**, 28 (2010).

[170] A. Ali and C. Hambrock, "Tetraquark Interpretation of the Belle Data on the Anomalous $\Upsilon(1S)\pi^+\pi^-$ and $\Upsilon(2S)\pi^+\pi^-$ Production near the $\Upsilon(5S)$ Resonance," *Phys. Rev. Lett.* **104**, 162001 (2010).

[171] A. Ali, C. Hambrock and S. Mishima, "Tetraquark-Based Analysis and Prediction of the Cross Sections and Distributions for the Processes $e^+e^- \to \Upsilon(1S)(\pi^+\pi^-, K^+K^-, \eta\pi^0)$ near $\Upsilon(5S)$," *Phys. Rev. Lett.* **106**, 092002 (2011).

[172] I. Adachi *et al.* (Belle Collaboration), "First Observation of the $h_b(1P)$ and $h_b(2P)$ Bottomonium States," arXiv:1103.3419v2 [hep-ex] (2011).

[173] B. Barish *et al.* (CLEO Collaboration), "Measurement of the B Semileptonic Branching Fraction with Lepton Tags," *Phys. Rev. Lett.* **76**, 1570 (1996).

[174] O. Aquines *et al.* (CLEO Collaboration), "Measurements of the Exclusive Decays of the $\Upsilon(5S)$ to B Meson Final States and Improved B_s^* Mass Measurement," *Phys. Rev. Lett.* **96**, 152001 (2006).

[175] M. Artuso *et al.* (CLEO Collaboration), "Evidence for $B_s^{(*)}\bar{B}_s^{(*)}$ Production at the $\Upsilon(5S)$ Resonance," *Phys. Rev. Lett.* **95**, 261801 (2005).

[176] W.M. Yao *et al.* (Particle Data Group), "Review of Particle Physics," *J. Phys. G* **33**, 1 (2006).

[177] R. Godang, private communication for the HFAG oscillation group.

[178] F. James, "Minuit; Function Minimization and Error Analysis," CERN Long Writeup D506 (1998).

[179] E. Barberio *et al.* (Heavy Flavor Averaging Group), "Average of b-hadron and c-hadron Properties at the End of 2007," arXiv:0808.1297v1 [hep-ex] (2008).

[180] A. Drutskoy, "Results and Prospects for $\Upsilon(5S)$ Running at B-factories," Talk presented at the 19th Hadron Collider Physics symposium, Galena, Illinois, USA (May 2008); arXiv:0807.3973v1 [hep-ex] (2008).

[181] K. Abe *et al.* (Belle Collaboration), "Measurement of the Inclusive $B_s^0 \to X^+l^-\nu$ Semileptonic Decay Branching Fraction," Belle-conf-0735, arXiv:0710.2548v1 [hep-ex] (2007).

[182] E. Nakano *et al.* (Belle Collaboration), "Charged Asymmetry of Same-sign Dileptons in $B^0 - \bar{B}^0$ Mixing," *Phys. Rev. D* **73**, 112002 (2006).

[183] N.C. Hastings *et al.* (Belle Collaboration), "Studies of $B^0 - \bar{B}^0$ Mixing Properties with Inclusive Dilepton Events," *Phys. Rev. D* **67**, 052004 (2003).

[184] K. Abe *et al.* (Belle Collaboration), "Measurement of $B_d^0 - \bar{B}_d^0$ Mixing Rate from the Time Evolution of Dilepton Events at the $\Upsilon(4S)$," *Phys. Rev. Lett.* **86**, 3228 (2001).

[185] R. Barlow, "Extended Maximum Likelihood," *Nucl. Instrum. Methods Phys. Res., Sect. A* **297**, 496 (1990).

[186] R. Barlow and C. Beeston, "Fitting Using Finite Monte Carlo Samples," *Comput. Phys. Commun.* **77**, 219 (1993).

[187] A. Nappi, "A Pitfall in the Use of Extended Likelihood for Fitting Fractions of Pure Samples in a Mixed Sample," *Comput. Phys. Commun.* **180**, 269 (2009).

[188] F. Fang, "Study of $K_S^0 \to \pi^+\pi^-$ Selection," *Belle Note #323, unpublished* (2000).

[189] F. Fang, "Measurement of Branching Fractions and CP Violation in $B \to \eta_c K$ and Observation of $B^\pm \to p\bar{p}K^\pm$," Ph.D. thesis, University of Hawaii (2003).

[190] D.J. Lange, "The EvtGen Particle Decay Simulation Package," *Nucl. Instrum. Methods Phys. Res., Sect. A* **462**, 152 (2001).

[191] CERN Application Software Group, "GEANT – Detector Description and Simulation Tool," (1993), CERN Program Library, W5013.

[192] K. Sumisawa *et al.* (Belle ϕ_2 Group), Belle Note #663, unpublished (2003).

[193] S.H. Lee *et al.* (Belle Collaboration), "Evidence for $B^0 \to \pi^0\pi^0$," *Phys. Rev. Lett.* **91**, 261801 (2003).

[194] R.A. Fisher, "The Use of Multiple Measurements in Taxonomic Problems," *Ann. Eugenics* **7**, 179 (1936).

[195] W. Verkerke and D. Kirkby, "The RooFit toolkit for Data Modeling," ArXiv:physics/0306116v1 [physics.data-an] (2003).

[196] R. Brun and F. Rademakers, "ROOT – An Object Oriented Data Analysis Framework," *Nucl. Instrum. Methods Phys. Res., Sect. A* **389**, 81 (1997).

[197] B. Aubert *et al.* (BaBar Collaboration), "Measurement of the $\tau^- \to \eta\pi^-\pi^+\pi^-\nu_\tau$ Branching Fraction and a Search for a Second-class Current in the $\tau^- \to \eta'(958)\pi^-\nu_\tau$ Decay," *Phys. Rev. D* **77**, 112002 (2008).

[198] N.J. Joshi, T. Aziz and K. Trabelsi, "Measurement of $\mathcal{B}R(B^0 \to D_s^* h)$," Belle Note #995v1.6, unpublished (2009).

[199] N.J. Joshi *et al.* (Belle Collaboration), "Measurement of the Branching Fractions for $B^0 \to D_s^{*+}\pi^-$ and $B^0 \to D_s^{*-}K^+$ Decays," *Phys. Rev. D* **81**, 031101 (2010).

[200] N.J. Joshi, T. Aziz and K. Trabelsi, "Branching fraction measurement for the $B^0 \to D_s^{*+}\rho^-$ Decay," Belle Note #1029, unpublished (2007). See also talk at the ϕ_3 meeting (June 25, 2009).

[201] K.S. Cranmer, "Kernel Estimation in High-energy Physics," *Comput. Phys. Commun.* **136**, 198 (2001).

[202] H. Albrecht *et al.* (ARGUS Collaboration), "Reconstruction of B Mesons," *Phys. Lett. B* **185**, 218 (1987).

[203] M. Pivk and F.R. Le Diberder, "${}_s$Plot: a Statistical Tool to Unfold Data Distributions," *Nucl. Instrum. Methods Phys. Res., Sect. A* **555**, 356 (2005).

[204] K. Kinoshita, private communication.

[205] T. Aaltonen *et al.* (CDF Collaboration), "First Observation of $\bar{B}_s^0 \to D_s^{\pm}K^{\mp}$ and Measurement of the Ratio of Branching Fractions $\mathcal{B}(\bar{B}_s^0 \to D_s^{\pm}K^{\mp})/\mathcal{B}(\bar{B}_s^0 \to D_s^{+}\pi^{-})$," *Phys. Rev. Lett.* **103**, 191802 (2009).

[206] P. Koppenburg, "A Measurement of the Track Finding Efficiency Using Partially Reconstructed D^* Decays," Belle Note #621v1.2, unpublished (2003).

[207] A. Abulencia *et al.* (CDF Collaboration), "Measurement of the Ratios of Branching Fractions $\mathcal{B}(B_s^0 \to D_s^-\pi^+\pi^+\pi^-)/\mathcal{B}(B^0 \to D^-\pi^+\pi^+\pi^-)$ and $\mathcal{B}(B_s^0 \to D_s^-\pi^+)/\mathcal{B}(B^0 \to D^-\pi^+)$," *Phys. Rev. Lett.* **98**, 061802 (2007).

[208] A. Deandrea *et al.*, "Two Body Non-leptonic Decays of B and B_s mesons," *Phys. Lett. B* **318**, 549 (1993).

[209] G. Li, F.L. Shao and W. Wang, "$B_s \to D_s(3040)$ Form Factors and B_s Decays into $D_s(3040)$," *Phys. Rev. D* **82**, 094031 (2010).

[210] R.H. Li, C.D. Lü and H. Zou, "$B(B_s) \to D_{(s)}P$, $D_{(s)}V$, $D_{(s)}^*$, and $D_{(s)}^*V$ Decays in the Perturbative QCD Approach," *Phys. Rev. D* **78**, 014018 (2008).

[211] C. Amsler *et al.* (Particle Data Group), "Review of Particle Physics," *Phys. Lett. B* **667**, 1 (2008).

[212] A. Ali *et al.*, "Nonleptonic Weak Decays of Bottom Mesons," *Z. Phys. C* **1**, 269 (1979).

[213] X.J. Chen *et al.*, "Form Factors of $B_s \to D_s^{(*)}$ in Salpeter Method and their Application to Non-leptonic Decays," arXiv:1106.3003v1 [hep-ph] (2011).

[214] T. Mannel, W. Roberts and Z. Ryzak, "Factorization Hypothesis and the Non-leptonic Decays of Heavy Hadrons," *Phys. Lett. B* **259**, 359 (1991).

[215] J. Bijnens and F. Hoogeveen, "Two-body Decays of B_s Mesons," *Phys. Lett. B* **283**, 434 (1992).

[216] P. Blasi *et al.*, "Phenomenology of B_s Decays," *Phys. Rev. D* **49**, 238 (1994).

[217] R.H. Li, C.D. Lü and Y.M. Wang, "Exclusive B_s Decays to the Charmed Mesons $D_s^+(1968, 2317)$ in the Standard Model," *Phys. Rev. D* **80**, 014005 (2009).

[218] S.E. Csorna *et al.* (CLEO Collaboration), "Measurement of the Branching Fractions and Helicity Amplitudes in $B \to D^*\rho$ Decays," *Phys. Rev. D* **67**, 112002 (2003).

[219] R. Louvot, "B_s^0 Decays at Belle," (2011), Talk at the 2011 Europhysics conference on high energy physics, Grenoble, France, 21-27 July 2011. Procedings to appear in *Proceedings of Science*, arXiv:1111.0333v1 [hep-ex] (2011).

[220] I. Adachi *et al.* (Belle Collaboration), "Observation of the Decay $B_s^0 \to J/\psi\eta$ and Evidence for $B_s^0 \to J/\psi\eta'$," Belle-conf-0902, arXiv:0912.1434v1 [hep-ex] (2009).

[221] J. Li *et al.* (Belle Collaboration), "Observation of $B_s^0 \to J/\psi f_0(980)$ and Evidence for $B_s^0 \to J/\psi f_0(1370)$," *Phys. Rev. Lett.* **106**, 121802 (2011).

[222] S. Esen *et al.* (Belle Collaboration), "Observation of $B_s^0 \to D_s^{(*)+} D_s^{(*)-}$ Using e^+e^- Collisions and a Determination of the B_s–$\bar{B}_s$ Width Difference $\Delta\Gamma_s$," *Phys. Rev. Lett.* **105**, 201802 (2010), updated result with 120 fb^{-1} shown at the meeting of the division of particles and field of the APS (DPF2011), August 2011.

[223] K.F. Chen *et al.* (Belle Collaboration), "Observation of an Enhancement in $e^+e^- \to \Upsilon(1S)\pi^+\pi^-$, $\Upsilon(2S)\pi^+\pi^-$, and $\Upsilon(3S)\pi^+\pi^-$ Production near $\sqrt{s} = 10.89$ GeV," *Phys. Rev. D* **82**, 091106 (2010).

[224] I. Adachi *et al.* (Belle Collaboration), "Observation of Two Charged Bottomonium-like Resonances," arXiv:1105.4583v1 [hep-ex] (2011); see also A. Bondar *et al.* (Belle Collaboration) "Observation of Two Charged Bottomonium-like Resonances in $\Upsilon(5S)$ Decays," arXiv:1110.2251v1 [hep-ex] (2011).

[225] P. Križan, "Plans for Future B Factories," arXiv:1103.1209v1 [hep-ex] (2011).

[226] J.D. Richman, "An Experimenter's Guide to the Helicity Formalism," DOE R&D report CALT-68-1148, unpublished, 1984.

[227] B. Aubert *et al.* (BaBar Collaboration), "Measurement of the Branching Fractions of the Rare Decays $B^0 \to D_s^{(*)+}\pi^-$, $B^0 \to D_s^{(*)+}\rho-$ and $B^0 \to D_s^{(*)-}K^{(*)+}$," *Phys. Rev. D* **78**, 032005 (2008).

[228] S. Hawking, *On the Shoulders of Giants* (Running Press, Philadelphia, 2003)

Remi LOUVOT

12/497 King's Road
Chelsea London SW10 0TU
+44 20 7352 5098
remi.louvot@gmail.com

Academic degrees
- 10/201 : PhD, physics / doctorat ès sciences
- 02/2008 : Master of science (MSc), physics / Ingénieur physicien dipl. EPF (GPA : 5.6/6)
- 06/2006 : Bachelor of science (BSc), physics (GPA : 5.2/6)
- 02/2002 : French Baccalauréat (A-level), science, with mention "good" (GPA>14/20)

Education
- 2003 - 2011 : Swiss federal institute of technology in Lausanne (EPFL), Switzerland
- 08/2010 : "SLAC summer institute" at Stanford University, USA
- 01/2010 : Swiss PhD winter school in particle physics in Ascona (TI), Switzerland.
- 2008/2009 : Scientific stay at the KEK laboratory near Tokyo, Japan (5 months in total)
- 06-09/2006 : "Summer student" at CERN, Geneva, Switzerland
- 2002 - 2003 : Preparatory class (MPSI) to engineer schools at Lycée Louis-le-Grand, Paris, France
- 1999 - 2002 : Secondary school, Lycée Sainte-Marie, La Roche sur Foron, France

Scientific activities
- Study of the B_s^0 meson in electron-positron collisions at the Υ(5S) energy with the Belle detector
- Peer-reviewed publications (as principal author)
  - R. Louvot *et al.* (Belle collaboration), *Physical Review Letters* **102**, 021801 (2009)
  - R. Louvot *et al.* (Belle collaboration), *Physical Review Letters* **104**, 231801 (2010)
- International physics conferences and other reports (see http://arxiv.org)
  - D. Asner *et al.*, Average of *b*-hadron, *c*-hadron and tau-lepton properties, arXiv:1010.1589
  - R. Louvot, talk presented at the 2011 Europhysics conf., Grenoble (France), arXiv:1111.0333
  - R. Louvot, talk presented at the "DISCRETE2010" symposium, Roma (Italy), arXiv:1101.5052
  - R. Louvot, talk presented at the "FPCP2010" conference, Turin (Italy), arXiv:1009.2605
  - R. Louvot, talk presented at the 2009 Europhysics conference, Krakow (Poland), arXiv:0909.2160
  - R. Louvot, talk presented at the Lake-Louise winter institute, Alberta (Canada), arXiv:0905.4345

Professional experiences
- UBS investment bank, London, UK
  - From 09/2011: Quantitative analytics graduate
- Swiss federal institute of Technology in Lausanne (EPFL), Lausanne, Switzerland
  - 09/2010-08/2011: Member of the council of the faculty for maths, physics and chemistry
  - 03/2008-08/2011: Scientific assistant in particle physics; academic research
  - 10/2004-02/2008: Assistant for several undergraduate courses: IT, maths and physics
  - 09/2006-02/2008: Member of the teaching committee for the physics section
- European organization for nuclear research (CERN), Geneva, Switzerland
  - Summer 2007: Summer programme designed for young European physicists

Personal situation
- 27-year old, married, Swiss and French citizenships